Geochronology and Structure of the Lupa Goldfield, Tanzania

CHRISTOPHER J.M. LAWLEY

Geochronology and Structure of the Lupa Goldfield, Tanzania

Christopher John Michael Lawley

A thesis submitted in partial fulfilment of the requirements for the degree of Doctor of Philosophy at Durham University

Department of Earth Sciences, Durham University
2012

Abstract

Gold occurrences in the Lupa goldfield, SW Tanzania, are typical of the orogenic Au deposit type. Auriferous quartz veins and mylonitic shear zones cross cut Archean granitoids (ca. 2740 Ma) and Paleoproterozoic felsic-mafic intrusions (1960–1880 Ma) comprising a Paleoproterozoic magmatic arc at the Tanzanian cratonic margin. Lu-Hf zircon results provide evidence for ca. 3.1 Ga basement beneath the Lupa goldfield and imply significant portions of the Ubendian Belt represent re-worked Archean crust. A greenschist facies metamorphic mineral assemblage overprints all of the magmatic phases and U-Pb dating of syn-metamorphic titanite hosted by a foliated Archean granitoid at ca. 1950 Ma suggests the onset of this tectono-thermal episode occurred during the Paleoproterozoic.

The majority of mineralization is hosted by a network of brittle-ductile and mylonitic shear zones, which record evidence for transpressional deformation of triclinic, or lower order, symmetry. Relacement of igneous feldspar (plagioclase and K feldspar) with intrinsically weaker phyllosilicates, during sericitization of the granitic wall rock, created the ideal conditions for strain localization and locally may have led to the onset of crystal plastic deformation processes. Continued feedback between fluid, rock and deformation generated interconnected networks of weak mylonitic shear zones that are subject to reactivation. Quartz veins are the other significant host for Au and possess geometries that imply mineralization occurred concurrently with episodic fluid pressure fluctuations.

Re-Os molybdenite, pyrite and chalcopyrite geochronology ages record a protracted metallogenic history and provide evidence for at least two mineralizing events at ca. 1940 and 1885 Ma. Each metallogenic event is represented in detail by a hydrothermal history that occurred at a time scale less than the resolution of the Re-Os method. High precision U-Pb zircon ages for the Saza Granodiorite overlap with Re-Os ages and provide unequivocal evidence for magmatism concomitant with sulphidation, however the wide range of Re-Os sulphide ages precludes a genetic relationship between any individual intrusion and Au. The goldfield-wide metallogenic event at ca. 1885 Ma occurred concurrently with eclogite facies metamorphism elsewhere in the Ubendian Belt and provides one of Earth's earliest examples of subduction processes temporally linked to orogenic Au deposit formation. Mesoproterozoic Re-Os ages (ca. 1125 Ma) correlated to the Kibaran/Irumide Orogenies and compatible with inferred Pb-loss events provide evidence for sulphidation during at least two discrete orogenic cycles and suggest mid-crustal mylonitic shear zones represent long-lived zones of structural weakness.

Table of Contents

Chapter Three

Re-Os Geochronology of Quartz Enclosed Ultrafine Molybdenite: Implications for Ore Geochronology

Chapter Four

Re-Os Molybdenite, Pyrite and Chalcopyrite Geochronology, Lupa Goldfield, SW Tanzania: Tracing Hydrothermal Fluid System Connectivity and Metallogenic Time Scales at Mid-Crustal Shear Zones Hosting Orogenic Au Deposits

Chapter Five

Fluid-Rock Interaction and Shear Zone Development in a Transpressional Setting: An example from the Lupa Goldfield, SW Tanzania

Chapter Six

U-Pb Titanite Geochronology: Implications for the Orogenic Au Deposit Model from the Lupa Goldfield, SW Tanzania

Chapter Seven

Conclusions, Mineral Exploration Implications and Future Research

Appendices

Chapter One

Chapter Two

Chapter Three

List of Figures

Chapter Two

Chapter Three

Chapter Four

Chapter Five

Chapter Six

Chapter Seven

List of Tables

Chapter Two

Chapter Three

Chapter Four

Chapter Five

Chapter Six

Declaration

I declare that this thesis, which I submit for the degree of Doctor of Philosophy at Durham University, is my own work and not substantially the same as any which has previously been submitted at this or any other university.

Christoher John Michael Lawley
Durham University
2012

Acknowledegments

My two academic supervisors, in conjunction with Helio Resource Corp., conceived the research project, secured funding and kindly offered me an opportunity to pursue a PhD. Dave Selby taught me the dark ways of Re-Os geochronology, allowed me to cut-my-teeth in his lab and gave me the freedom to explore the questions I was interested in — thank you for those chances and your unwavering commitment to the project. Jonathan Imber provided encouragement and acted as a source of un-ending things to try whilst preparing Chapter Five. Conversations with Bob Holdsworth, Gawen Jenkin, Richard Jones, Mark Pearce and Dave Holwell also greatly improved the thesis.

The NIGL team were incredibly supportive of the project and I am very thankful for my time there. Daniel Condon supervised the U-Pb work, provided the ID-TIMS analyses and was a source of salient advice on all things uranium-lead. Matthew Horstwood was 'instrumental' in making sure I got the most out of my days on site and provided valuable guidance on data presentation and interpretation. A special thank you also goes to Ian, Vanessa, Nicola, Tony, Steve and Adrian for all of their assistance in making Chapter Two possible.

Chris MacKenzie was actively involved in the project from the early stages and Helio Resource Corp. provided funding, logistical support and access to the exploration licenses/drill core — without which the PhD would not have been possible. Thank you to all of the Helio/Bafex staff for assistance, but I am particularly grateful for Mike Ashley, Oliver Jones, and Dan King's excellent company in the field. My time on site taught me that it is possible to get six people on a dirt bike, live pigs (± goats) make excellent backpacks, and that people make the place.

Thank you to my fellow grad students and department administrative/technical staff. In particular, thank you to the folks living on the lab floor - Chris Ottley, Joe Peterkin, and Geoff Nowell. My research group – Alan, Viv, Alex, Alice, and Sarah – made time in the lab a pleasure and were always there to answer my incessant questions.

Thank you to Mom, Dad, and Michelle for the Skype calls and forgiving my temporary absence as a son/brother. Time to come home.

And finally, thank you to my fiancé Kate — for proving every day that life is possible without geology.

“let er’ rip”

Leslie Nielson, 1926–2010

– Chapter One –

Introduction

1.1 Orogenic Au deposits and the need for a four-dimensional approach

Metamorphic belts are a major host for epigenetic Au deposits that have been variably classified as orogenic (Groves et al., 1998), mesothermal (Nesbitt et al., 1986), intrusion-related (Sillitoe and Thompson, 1998; Lang and Baker, 2001), quartz-carbonate greenstone-hosted (Dubé and Gosselin, 2007) and/or Archean lode Au deposits (Barnicoat et al., 1991; Hagemann and Cassidy, 2000). The orogenic Au deposit model was proposed as a unifying classification and is defined as shear and quartz-carbonate vein hosted, sulphide poor (< 5% pyrite ± pyrrhotite) and Au dominated deposits that result from structural focusing of low salinity H_2O-CO_2 (± CH_4) fluids at convergent margins (Groves et al., 1998). The deposits are temporally associated with periods of Earth's history dominated by convergent tectonics and spatially associated with accreted terranes within exhumed paleo-orogens (Goldfarb et al., 2005). Precambrian metamorphic belts host the largest examples of orogenic Au type deposits and are characterized by temporally distinct, but spatially overprinting metamorphic, structural, magmatic and metallogenic histories (Goldfarb et al., 2001).

Previous studies have demonstrated the exceptionally complex structural and geologic settings of these deposits and the exact mechanisms responsible for their formation remain equivocal (Groves et al., 2003). Many of the uncertainties regarding the formation of orogenic Au deposits are a consequence of the dearth of temporal constraints on the absolute timing of mineralization relative to tectono-magmatic events. This has led to the so-called 'intrusion-related' classification for deposits that are interpreted to be genetically related to igneous intrusions (Sillitoe and Thompson, 1998). Magmatic activity is a natural consequence of the subduction zone processes operating at the accretionary orogens where both deposit types are associated. As a result, distinguishing intrusion-related Au deposits from orogenic Au deposits is especially challenging in the absence of precise geochronologic constraints (Hart, 2005). The debate has important implications for mineral exploration efforts as each deposit model implies a distinct auriferous fluid source(s). Proponents of 'intrusion-related' deposit models predict that mineralization is associated with locally derived and magmatic hydrothermal fluids, whereas orogenic Au deposit models emphasize the importance of distal fluids of probable metamorphic origin. The source of fluid(s) and the role of magmatic activity in the formation Au deposits in metamorphic belts remain uncertain (Jia and Kerrich, 1999; Phillips and Powell, 2010).

The relative geologic histories of orogenic Au deposits are well described and have been the subject of comprehensive study (Hagemann and Cassidy, 2000). The results of this research have highlighted the intimate relationship between deformation, hydrothermal alteration and metallogenesis (Phillips and Powell, 2010). Whilst mutually cross cutting relationships between quartz veins and mylonitic shear zones provide evidence for broad contemporaneity between hydrothermal fluids and deformation, the absolute timing of these events are typically poorly constrained. Furthermore, the time scale(s) of orogenic Au deposit formation has not been addressed. Most orogenic Au deposits are hosted by mid-crustal shear zones and provide an opportunity to investigate the architecture and 'lifespans' of mid-crustal hydrothermal plumbing systems. The latter has important implications for the rheology and long-term weakening of crustal-scale faults. These large-scale faults also likely play a role in transporting hydrothermal fluids at depth to higher crustal levels where other ore deposits may develop (e.g., Hronsky, 2012).

The Lupa goldfield, SW Tanzania is one of eight litho-tectonic terranes comprising the Paleoproterozoic Ubendian Belt (Daly, 1988; Lenoir et al., 1994). Meso- and Neoproterozoic tectono-magmatic events correlated to the Kibaran and Pan-African orogenic cycles, respectively, overprint Paleoproterozoic Ubendian orogenesis (Boniface et al., 2012). All three orogenic cycles are in turn reactivated by tectonism related to the development of the western branch of the Tertiary East African Rift (Theunissen et al., 1996). The protracted history of the Ubendian Belt is recorded by regional-scale isotopic and structural studies with comparatively little geochronologic and geologic understanding of the Lupa goldfield specifically. Therefore, it remains unclear how Au mineralization in the Lupa goldfield relates to the tectono-magmatic evolution of the Ubendian Belt. Differentiating spatially overprinting, but temporally distinct orogenic events in the Ubendian Belt requires a precise temporal framework as part of a four-dimensional approach. This thesis attempts to address this issue by integrating several isotopic systems and multiple geochronometers with structural and lithologic mapping in order to develop a tectono-magmatic-metallogenic model for the Lupa goldfield.

Throughout the thesis the Au occurrences in the Lupa goldfield are defined as "orogenic Au deposits". The justification for this classification is built on the geochemical, structural and geochronologic data presented in the following thesis chapters. Our results demonstrate that Au is hosted by mylonitic shear zones and quartz veins at an evolving convergent margin concomitant with orogenesis and regional metamorphism. Furthermore, the geochronologic database developed as part of this thesis prelcudes any genetic relationship between all of the identified metallogenic events and any of the individual dated intrusive phases. The Au occurences therefore possess several of the defining characteristics of the orogenic Au deposit type and we suggest that this deposit model is the most favourable based on the available data.

1.2 Aims and Objectives

The Lupa goldfield has received very little scientific attention since the mid 20th century despite the region's importance as an important Au producer in Tanzania (Grantham, 1931, 1932,

1933; Teale et al., 1935; Gallagher, 1939; Harris, 1961; Van Straaten, 1984; Sango, 1988; Kuehen et al., 1990). As a result, many basic questions regarding the geologic setting of rocks comprising the Lupa goldfield remain unanswered. The impetus for this thesis is a renewed interest in the geology of the Lupa goldfield driven by Helio Resource Corp.'s mineral exploration successes. Recent drilling by Helio Resource Corp. highlighted the need to develop a detailed U-Pb and Re-Os geochronologic framework in order to constrain the absolute timing of major magmatic, tectonic and metallogenic events. In particular, the lack of geochronologic constraints made it unclear as to which ore deposit type the ore bodies in the Lupa goldfield belonged (orogenic Au vs. 'intrusion-related'). In this thesis, the precise timing of felsic-mafic magmatism is constrained by utilizing U-Pb zircon ID-TIMS geochronology in conjunction with U-Pb zircon LA-MC-ICP-MS geochronology. Lu-Hf zircon LA-MC-ICP-MS and U-Pb titanite ID-TIMS results provide additional constraints on the petrogenesis and timing of magmatic phases, whereas Re-Os sulphide geochronology constrained the timing of mineralization. Field observations, structural and lithologic mapping, petrography and lithgeochemistry are incorporated into this temporal framework in order to semi-quantify the tectono-thermal evolution of the Lupa goldfield. The project set out with the following three objectives:

- Establish the timing of magmatic phases and identify the geodynamic setting of the Lupa goldfield.
- Develop a temporal framework for metallogenesis
- Determine the structural setting of the Lupa goldfield and develop a genetic model for Au mineralization.

In addition to these three main objectives, the thesis also addresses several fundamental questions regarding the formation of orogenic Au deposits hosted by metamorphic belts:

- Are Precambrian orogenic Au deposits exclusively associated with allocthonous terranes?
- How connected are fluid conduits in the mid-crust? And on what time scale(s) do they operate?
- Are the brittle and ductile deformation processes that characterize auriferous shear zones truly contemporaneous?
- What is the timing relationship between Au, magmatism and metamorphism? How does the timing of these processes relate to the timing of subduction? And what does the time scale(s) of each these processes tell us about Au deposit formation?

1.3 Thesis Organization

The thesis is presented as five "journal-style" chapters with each chapter investigating at least one of the aims and objectives described above. Chapter one, 'Introduction', describes the thesis aims and organization, summarizes the individual contributions of the author and supervisors/collaborators to the overall thesis and introduces the concept of analytical

uncertainty. Chapter seven, 'Conclusions', explores the implications of the thesis results at varying scales of mineral exploration, summarizes the findings of the "journal-style" chapters and proposes areas of future research.

Chapter Two – Lithogeochemistry, Geochronology and Geodynamic Setting of the Lupa Terrane, Tanzania: Implications for the Extent of the Archean Tanzanian Craton

Chapter two sets out to constrain the timing of magmatic phases and the geodynamic setting of the Lupa goldfield. U-Pb zircon LA-MC-ICP-MS and ID-TIMS geochronology results are presented and integrated with Lu-Hf zircon LA-MC-ICP-MS analyses in order to understand the timing and petrogenesis of felsic-mafic intrusions. U-Pb, Lu-Hf and lithogeochemistry are integrated with field observations and a new geodynamic model for the Lupa goldfield is proposed. Chapter Two has been submitted to the journal Precambrian Research. I completed all of the fieldwork (four months on site), petrography, mineral separation (with the exception of CL098 which was completed by Quentin Crowley at Trinity College, Dublin), sample preparation, zircon imaging (supervised by Tony Milodowski), LA-MC-ICP-MS analyses, REE modeling, data synthesis, data interpretation, figure production and wrote the chapter. Daniel Condon completed the ID-TIMS analyses (I completed a portion of the chemistry) and assisted with data interpretation. Matthew Horstwood supervised the U-Pb zircon LA-MC-ICP-MS analyses and assisted with data interpretation. Ian Miller supervised the Lu-Hf zircon LA-MC-ICP-MS analyses and assisted with data interpretation. David Selby, Jonathan Imber and Quentin Crowley spent one week in the field. Activation Laboratories (Ancaster, Ontario, Canada) completed all lithogeochemistry analyses. The chapter benefitted from the editorial handling of David Selby, Jonathan Imber, Daniel Condon, Matthew Horstwood and Quentin Crowley.

Chapter Three - Re-Os Geochronology of Quartz Enclosed Ultrafine Molybdenite: Implications for Ore Geochronology

Molybdenite is the ideal Re-Os geochronometer because of its tendency to incorporate significant Re and exclude Os during crystallization (e.g., Stein et al., 2001). This property allows a Re-Os molybdenite model age to be calculated using a simplified isotope equation, $t = \ln(^{187}Os/^{187}Re + 1)/\lambda$; where t = model age, and $\lambda = ^{187}Re$ decay constant, 1.666×10^{-11}; Smoliar et al. 1996). Molybdenite in the Lupa goldfield is present as veins and ultrafine disseminations within Au-bearing quartz veins and hydrothermally altered granitoids. Conventional mineral separation techniques were inadequate to separate sufficient quantities of ultrafine molybdenite sample for Re-Os analysis. Chapter three outlines a novel chemical mineral separation technique, which takes advantage of the disparate solubility of silicates and sulfides in HF acid, in order to isolate ultrafine molybdenite from these difficult samples. The effects of HF exposure on Re-Os molybdenite systematics are tested by exposing four reference materials to HF and

comparing Re-Os molybdenite model ages before and after exposure. The HF approach is then applied to six ultrafine molybdenite samples from the Lupa goldfield. Chapter three is published with the journal Economic Geology (v. 107, p. 1499–1505). I completed mineral separation, chemistry, ID-TIMS analyses, data synthesis, data interpretation, figure production and wrote the chapter. David Selby assisted with data interpretation and the chapter benefitted from his editorial handling. Chris Ottley assisted with ICP-MS analyses.

Chapter Four – Re-Os Molybdenite, Pyrite and Chalcopyrite Geochronology, Lupa Goldfield, SW Tanzania: Tracing Hydrothermal Fluid System Connectivity and Metallogenic Time Scales at Mid-Crustal Shear Zones Hosting Orogenic Au Deposits

The timing of Au mineralization at orogenic Au deposits is typically constrained by U-Pb zircon dating of cross cutting dikes and/or host rocks. U-Pb zircon ID TIMS analyses possess exceptionally low analytical uncertainties, however cross cutting relationships rarely constrain the timing of Au mineralization to within tens of millions of years (e.g., Kerrich and Cassidy, 1994). Another approach taken by some authors has been to constrain the timing of quartz veining by U-Pb hydrothermal zircon (± titanite ± monazite) geochronology (e.g., Lin and Corfu, 2002; Ramussen et al., 2006). Hydrothermal zircons are not reported for a large number of orogenic deposits and the suitability of this approach is limited. Re-Os sulphide geochronology provides a feasible alternative to U-Pb geochronology by directly dating sulphides that are co-genetic with Au (Stein et al., 2000; Arne et al., 2001, Morelli et al., 2007; Selby et al., 2009; Kerr and Selby, 2012). Chapter four presents the results of a detailed Re-Os study of orogenic Au deposits that integrates several geochronometers (molybdenite, pyrite and chalcopyrite) in order to constrain the timing of sulphidation in the Lupa goldfield. The results of Chapter Four are used to investigate the time scale of orogenic Au deposit formation and to trace the connectivity and time scale(s) of fluid-conduits in the mid-crust. Chapter Four is submitted to the journal Economic Geology. I completed sample collection, mineral separation, chemistry, ID-TIMS analyses, data synthesis, data interpretation, figure production and wrote the chapter. David Selby completed three analyses (SZM01; SZM02 F1; SZM02-drill) and assisted with data interpretation. The chapter benefitted from the editorial handling of David Selby and Jonathan Imber.

Chapter Five – Fluid-Rock Interaction and Shear Zone Development in a Transpressional Setting: An example from the Lupa Goldfield, SW Tanzania

The structural settings of orogenic Au deposits have been well studied and are known to be exceptionally complex (Robert and Poulsen, 2001). Despite this complexity, the majority of deposits are interpreted within the context of simple and/or pure shear models and the implications of more complex styles of deformation on ore body geometry are rarely considered (for an exception see Dubé et al. 1989). Chapter Five presents the results of structural mapping,

micro-structural examination and shear zone geochemistry. The results suggest that the mylonitic shear zones followed a complex deformation path that is typical of transpressional and triclinic, or lower order, symmetry shear zones (Jiang and Williams, 1998). A model for shear zone development is proposed and the scale(s) at which transpressional strain partitioning occurs is discussed. Chapter Five is submitted to the journal Economic Geology. I completed the fieldwork, sample collection, structural mapping, serial slicing of oriented samples, petrography, ore body modelling, data synthesis, data interpretation, figure production and wrote the chapter. Jonathan Imber assisted with data interpretation and the chapter benefitted from his and David Selby's editorial handling. David Holwell completed the Computer X Ray Tomography at the University of Leicester.

Chapter Six – U-Pb Titanite Geochronology: Implications for the orogenic Au deposit model from the Lupa goldfield, SW Tanzania

Orogenic Au deposits are associated with crustal-scale shear zones and their subsidiary structures at paleo-convergent margins (Kerrich and Wyman, 1990; Sibson et al., 1988; Weinberg et al., 2004; Bierlein et al., 2009). Most deposits occur relatively late in the orogenic cycle and post-date the majority of metamorphism, magmatism and deformation (Witt and Vanderhor, 1998; Groves et al., 2000). The absolute age of metamorphism relative to mineralization and magmatism is poorly constrained at most goldfields due to the complex tectono-thermal history at paleo-orogens and the difficulty in reconstructing this thermal history from the rock record. One potential approach to this problem lies in the contrasting closure temperatures of accessory mineral phases, which record a distinct part of the paleo-orogen's thermal evolution. The U-Pb system lends itself to this approach due to the wide variety of U-bearing accessory mineral phases, which possess a range of closure temperatures and occur in a wide variety of rock types (e.g., Hawkins and Bowring, 1999; Crowley et al., 2009). For example, the titanite geochronometer possesses a high closure temperature (550–650ºC; Frost et al., 2000) and is typically used to "see through" low temperature metamorphic episodes and overprinting low-grade metamorphic events in order to date older igneous events and pro-grade metamorphism (e.g., Lucassen and Becchio, 2003). However, titanite neocrystallization during greenschist facies metamorphism is also demonstrated and can provide valuable information regarding the timing of metamorphic mineral growth (Aleinikoff et al., 2002). In Chapter Six, the increased reactivity of titanite relative to zircon at greenschist facies metamorphic conditions is exploited by comparing U-Pb zircon and U-Pb titanite ages for the same samples. These U-Pb titanite ID-TIMS ages are integrated with the U-Pb zircon (Chapter Two) and Re-Os sulphide (Chapter Four) ages for magmatism and mineralization, respectively. Therefore, this thesis presents a comprehensive geochronologic database that constrains the timing of each of the important geologic events important to orogenic Au deposit formation (magmatism, deformation and metamorphism). The complete dataset provides an opportunity to test the relative importance of different geologic events in the development of orogenic Au deposits

based on their absolute ages. Chapter Six is to be submitted to a peer-reviewed journal that has yet to be decided. I completed the mineral separation, data interpretation, figure production and wrote the chapter. Daniel Condon completed the U-Pb titanite ID-TIMS analyses and assisted with data interpretation. The chapter benefitted from the editorial handling of David Selby and Jonathan Imber

1.4 Presentation of research reported by this thesis

In addition to submitted and/or published chapters, thesis research has been presented as poster and oral conference presentations:

Lawley, C.J.M., Selby, D., Condon, D., Horstwood, M., Crowley, Q., Imber, J., and MacKenzie, C., 2012, Geochronology of gold, magmatism, and metamorphism at the Lupa goldfield, SW Tanzania: 34th International Geological Conference, Brisbane, August 5th to 10th, Student Oral Presentation.

Lawley, C.J.M., Imber, J., Selby, D., and MacKenzie, C., 2012, Structural setting of orogenic gold deposits in the Paleoproterozoic Lupa goldfield, SW Tanzania, 34th International Geological Conference, Brisbane, August 5th to 10th, Student Poster Presentation.

Lawley, C.J.M., Imber, J., Selby, D., and Mackenzie, C., 2011, Transpressional deformation and implications for ore body geometry of orogenic gold deposits: Applied Earth Science (Trans. Inst. Min. Metall. B), v. 120, p. 69.

Lawley, C.J.M., and Selby, D., 2011, Re-Os geochronology of quartz enclosed ultra-fine molybdenite: implications for ore geochronology: Applied Earth Science (Trans. Inst. Min. Metall. B), v. 120, p. 83.

Lawley, C.J.M., Selby, D., Condon, D.J., Horstwood, M.S.A., Crowley, Q.G., Imber, J., and MacKenzie, C., 2010, Geochronology of Granites and Gold in the Lupa Goldfield, Southwest Tanzania: Applied Earth Science (Trans. Inst. Min. Metall. B), v. 119, p. 87.

Lawley, C.J.M., Selby, D., and MacKenzie, C., 2011, Genetic constraints for the Lupa goldfield, SW Tanzania: Implications from Rhenium-Osmium pyrite and molybdenite geochronology: Fermor Conference, September 7-9th, London, Student Poster.

Lawley, C.J.M., Selby, D., Imber, J., Crowley, Q., and Mackenzie, C., 2010, Preliminary investigation into the structural and geologic setting of the Lupa Goldfield, Tanzania: Mineral Deposit Study Group Conference, January 6–7th, Glasgow, Student Poster.

1.5 A brief note on analytical uncertainty

A large proportion of this thesis is dedicated to presenting isotopic age determinations and a brief discussion on the intended meaning of these ages and their associated analytical uncertainties is required. All scientific measurements are associated with uncertainty in the measured property's true "value". In the case of geochronology, mass spectrometer measurements of radiogenic isotope ratios provide a means to calculate the crystallization age of specific minerals. Geochronologic age determinations are therefore associated with uncertainties that are

critical to assess the significance and geologic meaning of the determined ages. The source of uncertainty varies from geologic sampling (e.g., geologic heterogeneity), isotopic measurements (e.g., mass spectrometer measurements), and age calculations (e.g., assuming molybdenite does not possess common Os in Re-Os molybdenite model age calculations). In this thesis, analytical uncertainties are reported at two standard errors of the mean (i.e., two sigma; unless specified) and include but are not limited to uncertainty in sample weighing, spike calibration, isotopic composition and abundance of the blank, decay constant uncertainty and reproducibility of standards. The contributions of each individual analytical uncertainty were propagated following previously established protocols that are specific to each isotopic system (see individual Chapters for further discussion). For correlated analytical uncertainties, the assigned uncertainty is also reported with the error correlation function (rho; Ludwig, 2008). The assigned analytical uncertainty for each age is intended to encapsulate all sources of analytical scatter and thus any remaining data-point scatter is interpreted to reflect geologic heterogeneity.

Age determinations were calculated using Isoplot v. 4.15 (Ludwig, 2008) and are predominately based on reducing multiple age determinations to a single value (e.g., weighted average ages, isochron ages). In order to assess the suitability of this approach, calculated ages are reported with their respective Mean Square Weighted Deviation (MSWD). The MSWD represents the distribution of data points around the mean taking into account each data point uncertainty (Ludwig, 2008). A MSWD > 1 suggests the assigned analytical uncertainties do not account for the scatter of data points (excess data point scatter) and/or that the assigned analytical uncertainties underestimate the true analytical uncertainty, whereas a MSWD < 1 suggest the assigned analytical uncertainties overestimate the true analytical uncertainty. The acceptable range of MSWD values is dependent on the size of the dataset. In general, large datasets should possess MSWD ~ 1; whereas small datasets that possess minimal geologic scatter may possess MSWDs >>1. The presence or absence of "excess" data point scatter can only be tested outside of the assigned analytical uncertainties and datasets with MSWD ~ 1 may still possess geologic scatter that is unresolvable within the assigned analytical uncertainties.

1.6 References

Aleinikoff, J.N., Wintsch, R.P., Fanning, C.M., and Dorais, M.J., 2002, U-Pb geochronology of zircon and polygenetic titanite from the Glastonbury Complex, Connecticut, USA: an integrated SEM, EMPA, TIMS and SHRIMP study: Chemical Geology, v. 188, p. 125–147.

Arne, D.C., Bierlein, F.P., Morgan, J.W., and Stein H.J., 2001, Re-Os dating of sulphides associated with gold mineralization in central Victoria, Australia: Economic Geology, v. 96, p. 1455–1459.

Barnicoat, A.C., Fare, R.J., Groves, D.I., and McNaughton, N.J., 1991, Synmetamorphic lode-gold deposits in high-grade Archean settings: Geology, v. 19, p. 921–924.

Bierlein, F.P., Groves, D.I., and Cawood, P.A., 2009, Metallogeny of accretionary orogens: the connection between lithospheric processes and metal endowment: Ore Geology Reviews, v. 36, p. 282–292.

Boniface, N., Schenk, V., and Appel, P., 2012, Paleoproterozoic eclogites of MORB-type chemistry and three Proterozoic orogenic cycles in the Ubendian Belt (Tanzania): evidence from monazite and zircon geochronology, and geochemistry: Precambrian Research, v. 192–195, p. 16–33.

Crowley, J.L., Waters, D.J., Searle, M.P., and Bowring, S.A., 2009, Pleistocene melting and rapid exhumation of the Nanga Parbat massif, Pakistan: Age and P-T conditions of accessory mineral growth in migmatite and leucogranite: Earth and Planetary Science Letters, v. 288, p. 408–420.

Dubé, B., Poulsen, K.H., and Guha, J., 1989, The effects of layer anisotropy on auriferous shear zones: the Norbeau Mine, Quebec: Economic Geology, v. 84, p. 871–878.

Dubé, B., and Gosselin, P., 2007, Greenstone-hosted quartz-carbonate vein deposits, *in* Goodfellow, W.D., ed., Mineral Deposits of Canada: A Synthesis of Major Deposit-Types, District Metallogeny, the Evolution of Geological Provinces, and Exploration Methods: Geological Association of Canada, Mineral Deposits Division, Special Publication No. 5, p. 49–73.

Daly, M.C., 1988, Crustal shear zones in central Africa: a kinematic approach to Proterozoic tectonics: Episodes, v. 11, p. 5–11.

Jia, Y.F., and Kerrich, R., 1999, Nitrogen isotope systematics of mesothermal lode gold deposits: metamorphic, granitic, meteoric water, or mantle origin?: Geology, v. 27, p. 1051–1054.

Jiang, D., and Williams, P.F., 1998, High-strain zones: a unified model: Journal of Structural Geology, v. 20, p. 1105–1120.

Frost, B.R., Chamberlain, K.R., and Schumacher, J.C., 2000, Sphene (titanite): phase relations and role as a geochronometer: Chemical Geology, v. 172, p. 131–148.

Gallagher, D.R., 1939, Preliminary account of the geology of a portion of Lupa goldfield: Economic Geology, v. 34, p. 306–323.

Goldfarb, R.J., Groves, D.I., and Gardoll, S., 2001, Orogenic gold and geologic time: a global synthesis: Ore Geology Reviews, v. 18, p. 1–75.

Grantham, D.R., 1931, Lupa river goldfield: Min. Mag., v. 45, p. 265–276.

Grantham, D.R., 1932, Lupa goldfield: Bulletin of the Geological Survey of Tanganyika, v. 3, 34 p.

Grantham, D.R., 1933, The eastern extension of Lupa goldfield: Geological Survey of Tanganyika, short paper 11, 9 p.

Groves, D.I., Goldfarb, R.J., Gebre-Mariam, M., Hagemann, S.G., and Robert, F., 1998, Orogenic gold deposits: a proposed classification in the context of their crustal distribution and relationship to other gold deposit types: Ore Geology Reviews, v. 13, p. 7–27.

Groves, D.I., Goldfarb, R.J., Knox-Robinson, C.M., Ojala, J., Gardoll, S., Yun, G.Y., and Holyland, P., 2000, Late-kinematic timing of orogenic gold deposits and significance for computer-

based exploration techniques with emphasis on the Yilgarn Block, Western Australia: Ore Geology Reviews, v. 17, p. 1–38.

Groves, D.I., Goldfarb, R.J., Robert, F., and Hart, C.J., 2003, Gold deposits in metamorphic belts: overview of current understanding, outstanding problems, future research, and exploration significance: Economic Geology, v. 98, p. 1–29.

Harris, J.F., 1961, Summary of geology of Tanganyika: Geological Survey of Tanganyika Memoir, v. 1, p. 64–67.

Hart, C., 2005, Classifying, distinguishing and exploring for intrusion-related gold systems: The Gangue, Mineral Deposits Division Newsletter, v. 87, 2 p.

Hagemann, S.G., and Cassidy, K.F., 2000, Archean orogenic lode gold deposits: Reviews in Economic Geology, v. 13, p. 9–68.

Hawkins, D.P., and Bowring, S.A., 1999, U-Pb monazite, xenotime and titanite geochronological constraints on the prograde to post-peak metamorphic thermal history of Paleoproterozoic migmatites from the Grand Canyon, Arizona: Contributions to Mineralogy and Petrology, v. 134, p. 150–169.

Hronsky, J.M.A., Groves, D.I., Loucks, R.R., and Begg, G.C., 2012, A unified model for gold mineralisation in accretionary orogens and implications for regional-scale exploration targeting methods: Mineralium Deposita, v. 47, p. 339–358.

Kerr, A., and Selby, D., 2012, The timing of epigenetic gold mineralization on the Baie Verte Peninsula, Newfoundland, Canada: new evidence from Re-Os pyrite geochronology: Mineralium Deposita, v. 47, p. 325–327.

Kerrich, R., and Wyman, D., 1990, Geodynamic setting of mesothermal gold deposits: an association with accretionary tectonic regimes: Geology, v. 18, p. 882–885.

Kerrich, R., and Cassidy, K.F., 1994, Temporal relationships of lode gold mineralization to accretion, magmatism, metamorphism, and deformation — Archean to present: a review: Ore Geology Reviews, v. 9, p. 263–310.

Kuehn, S., Ogola, J., and Sango, P., 1990, Regional setting and nature of gold mineralization in Tanzania and southwest Kenya: Precambrian Research, v. 46, p. 71–82.

Lang, J.R., and Baker, T., 2001, Intrusion-related gold systems—the present level of understanding: Mineralium Deposita, v. 36, p. 477–489.

Lenoir, J.L., Liégeois, J.P., Theunissen, K., and Klerkx, J., 1994, The Palaeoproterozoic Ubendian shear Belt in Tanzania: geochronology and structure: Journal of African Earth Sciences, v. 19, p. 169–184.

Lin, S., and Corfu, F., 2002, Structural setting and geochronology of auriferous quartz veins at the High Rock Island Gold Deposit, Northwestern Superior Province, Manitoba, Canada: Economic Geology, v. 97, p. 43–57.

Lucassen, F., and Becchio, R., 2003, Timing of high-grade metamorphism: early Palaeozoic U-Pb formation ages of tianite indicate long-standing high-T conditions at the western

margin of Gondwana (Argentina, 26–29ºS): Journal of Metamorphic Geology, v. 21, p. 649–662.

Ludwig, K.R., 2008, User's manual for Isoplot 3.6: a geochronological toolkit for Microsoft Excel: Berkeley Geochronology Center Special Publication No. 4, 77 p.

Morelli, R., Creaser, R.A., Seltmann, R., Stuart, F.M., Selby, D., and Graupner, T., 2007, Age and source constraints for the giant Muruntau gold deposit, Uzbekistan, from coupled Re-Os-He isotopes in arsenopyrite: Geology, v. 35, p. 795–798.

Nesbitt, B.E., Murrowchick, J.B., and Muehlenbachs, K., 1986, Dual origin of lode-gold deposits in the Canadian Cordillera: Geology, v. 14, p. 506–509.

Phillips, G.N., and Powell, R., 2010, Formation of gold deposits a metamorphic devolatilization model: Journal of Metamorphic Geology, v. 28, p. 689–718.

Rasmussen, B., Sheppard, S., and Fletcher, I.R., 2006, Testing ore deposit models using in situ U-Pb geochronology of hydrothermal monazite: Paleoproterozoic gold mineralization in northern Australia: Geology, v. 34, p. 77–80.

Robert, F., and Poulsen, K.H., 2001, Vein formation and deformation in greenstone gold deposits, *in* Richards, J.P., and Tosdal, R.M., eds., Structural Controls on Ore Genesis: Society of Economic Geologists, Reviews in Economic Geology, v. 14, p. 111-155.

Sango, P.M., 1988, Structural and lithological controls of gold mineralization in the Lupa goldfield, Tanzania, *in* Ho, S.E., and Groves, D.I., Recent advances in understanding Precambrian gold deposits, Geology Department and University Extension, The University of Western Australia, Publication No. 12, p. 99–109.

Selby, D., Kelley, K.D., Hitzman, M.W., and Zieg, J., 2009, Re-Os sulphide (bornite, chalcopyrite, and pyrite) systematics of the carbonate-hosted copper deposits at Ruby Creek, southern Brooks Range, Alaska: Economic Geology, v. 104, p. 437–444.

Sibson, R.H., Robert, F., and Poulsen, H., 1988, High-angle reverse faults, fluid-pressure cycling, and mesothermal gold-quartz deposits: Geology, v. 16, p. 551–555.

Sillitoe, R.H., and Thompson, J.F.H., 1998, Intrusion-related vein gold deposits: types, tectono-magmatic settings and difficulties in distinction from orogenic gold deposits: Resource Geology, v. 48, p. 237–250.

Smoliar, M.I., Walker, R.J. and Morgan, J.W., 1996, Re-Os isotope constraints on the age of Group IIA, IIIA, IVA and IVB iron meteorites: Science, v. 271, p. 1099–1102.

Stein, H.J., Morgan, J.W., and Scherstén, A., 2000, Re-Os dating of low-level highly radiogenic (LLHR) sulphides: the Harnäs gold deposit, southwest Sweden, records continental-scale tectonic events: Economic Geology, v. 95, p. 1657–1671.

Stein, H.J., Markey, R.J., Morgan, J.W., Hannah, J.L., and Scherstén, A., 2001, The remarkable Re-Os chronometer in molybdenite; how and why it works: Terra Nova, v. 13, p. 479–486.

Teale, E.O., Eades, N.W., Harkin, D.A., Harpum, J.R., and Horne, R.G., 1935, Brief explanation of the geology of Irambo area, quarter degree sheet 245, Geological Survey of Tanganyika,

Dodoma.

Theunissen, K., Klerkx, J., Melnikov, A., and Mruma, A., 1996, Mechanisms of inheritance of rift faulting in the western branch of the east African Rift, Tanzania: Tectonics, v. 15, p. 776–790.

Van Straaten, V.P., 1984, Gold Mineralization in Tanzania – a review, *in* Foster, R.P., eds., Gold '82; the geology, geochemistry and genesis of gold deposits, A.A. Balkema, Rotterdam, p. 673–685.

Weinberg, R.F., Hodkiewicz, P.F., and Groves, D.I., 2004, What controls gold distribution in Archean terranes?: Geology, v. 32, p. 545–548.

Witt, W.K., and Vanderhor, F., 1998, Diversity within a unified model for Archaean gold mineralization in the Yilgarn Craton of Western Australia: an overview of the late-orogenic, structurally-controlled gold deposits: Ore Geology Reviews, v. 13, p. 29–64.

– Chapter Two –

Lithogeochemistry, Geochronology and Geodynamic Setting of the Lupa Terrane, Tanzania: Implications for the Extent of the Archean Tanzanian Craton

Chapter Two is submitted to the journal Precambrian Research

Collaborators: David Selby[1], Daniel J. Condon[2], Matthew Horstwood[2], Ian McDonald[2], Quentin Crowley[3] and Jonathan Imber[1]

[1]Department of Earth Sciences, Durham University, Science Labs, Durham, DH1 3LE, UK
[2]Natural Environment Research Council Isotope Geosciences Laboratory, British Geological Survey, Keyworth, Nottingham, NG12 5GG, UK
[3]School of Natural Sciences, Department of Geology, Trinity College, Dublin 2, Ireland

2.1 Introduction

Archean cratonic margins are complex geologic settings characterized by overprinting structural, magmatic and metamorphic events (e.g., Zhoa et al., 2002; Reddy and Evans, 2009). This is particularly apparent in the Ubendian and Usagaran metamorphic belts, which border the western and southern margins of the Tanzania Craton, respectively. Existing models for the Paleoproterozoic tectonic evolution of the Tanzanian cratonic margin invoke thrust-dominated accretion of terranes comprising the Usagaran Belt coupled with lateral accretion of terranes comprising the Ubendian Belt (Daly, 1988; Lenoir et al., 1994). However, recent geochronologic evidence suggests that the current configuration of the Ubendian Terranes are the product of at least three discrete orogenic events that are correlated to the Ubendian (2.1–1.8 Ga), Kibaran (1.4–1.0 Ga) and Pan-African (650–450 Ma) orogenic episodes (Hanson, 2003; Boniface et al., 2012; Boniface and Schenk, 2012). The Paleoproterozoic tectonic history of the Ubendian Belt and the Tanzanian cratonic margin therefore remains poorly understood due, in part, to Neoproterozoic and younger cover rocks, Meso- and Neoproterozoic metamorphic overprints and periodic reactivation of geologic structures from the Paleoproterozoic until the present day (Theunissen et al., 1996).

The Lupa Terrane is located adjacent to the Tanzanian Craton and is the least-understood of the eight litho-tectonic terranes comprising the Ubendian Belt (Fig. 2.1; Daly, 1988). Hitherto voluminous granitoids intruding the Lupa Terrane and obscuring the southern extent of the Tanzanian cratonic margin have been attributed to widespread Paleoproterozoic magmatic

activity related to the Ubendian Orogeny (e.g., Sommer et al., 2005). Herein major lithologies comprising the Lupa Terrane are characterized and dated, which places new constraints on the Paleoproterozoic geodynamic evolution of the Ubendian Belt. New U-Pb zircon LA-MC-ICP-MS ages, coupled with Lu-Hf zircon LA-MC-ICP-MS results, calls into question the SW extent of the Tanzanian cratonic margin (Manya, 2011). Establishing the extent of the Tanzanian Craton places important constraints on the prospectivity of SW Tanzania for deposits associated with Archean Cratons. The temporal and geologic setting of the Lupa Terrane are particularly important as it hosts a large number of orogenic Au deposits (Sango, 1988).

2.2 Geologic setting

2.2.1 Regional geology

The western margin of the Tanzanian Craton is separated from the Congo Craton and the Bangweulu Block by the ca. 600 km long and 150 km wide zone of granulite-greenschist facies meta-igneous and meta-sedimentary rocks known as the Ubendian Belt (McConnell, 1950; Sutton et al., 1954; Priem et al., 1979; Lenoir et al., 1994). Current tectonic models divide the Ubendian Belt into eight lithologic and structurally-defined terranes: Ubende, Wakole, Katuma, Ufipa, Mbozi, Lupa, Upangwa and Nyika (Fig. 2.1; Upangwa and Nyika are not shown in Fig. 2.1; Daly, 1988). Mesoproterozoic meta-sedimentary rocks, corresponding to the Muva Supergroup,

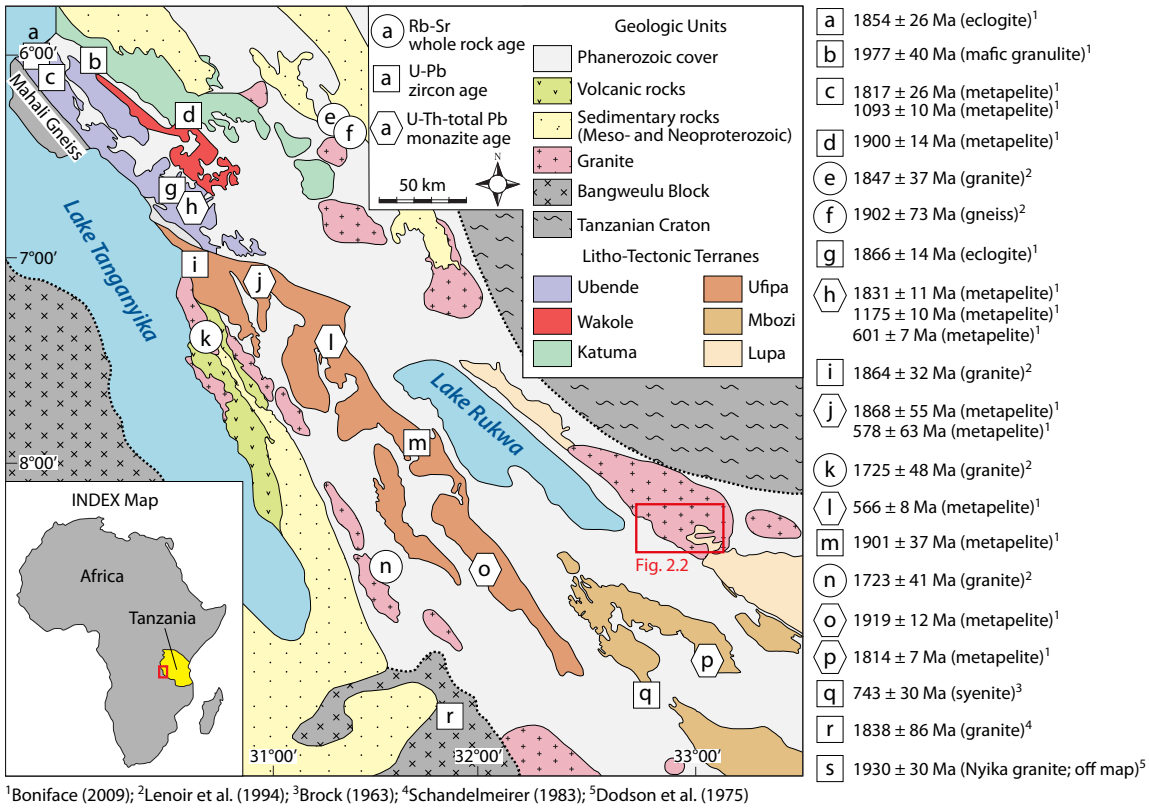

[1]Boniface (2009); [2]Lenoir et al. (1994); [3]Brock (1963); [4]Schandelmeirer (1983); [5]Dodson et al. (1975)

Figure 2.1 – Regional geologic map showing Ubendian Terranes and previously reported geochronology sample locations (modified from Smirnov et al., 1973).

unconformably overlie the Ubendian Belt and have been subsequently metamorphosed during the Kibaran Orogeny (Cahen et al., 1984). These rocks are in turn overlain by Neoproterozoic clastic sedimentary rocks corresponding to the Bukoban Supergroup (Cahen et al., 1984). Meso- and Neoproterozoic cover sequences blanket large areas of the Ubendian basement and obscure its northern and southern limits (Hanson, 2003).

The Ubendian Belt formed through a series of metamorphic and tectonic events that span ca. 300 Myr (Lenoir et al., 1994). The first tectonic event is constrained by U-Pb zircon and Rb-Sr whole rock dating of syntectonic magmatic intrusions at 2093–2048 Ma (Dodson et al., 1975; Lenoir et al., 1994; Ring et al., 1997). The 2.1–2.0 Ga Ubendian tectonic phase corresponds with a period of eclogite and granulite facies metamorphism, the development of a ductile E-W trending tectonic fabric and is concomitant with metamorphism in the adjacent Usagaran Belt (Lenoir et al., 1994; Collins et al., 2004). Eclogitic rocks with MORB-like chemistry from the Usagaran, dated at ca. 2.0 Ga, suggest that metamorphism and tectonism resulted from subduction zone processes analogous to modern-day accretionary margins and may have resulted from the collision between the Tanzanian and Congo Cratons and the Bangweulu Block (Möller et al., 1995). Structural evidence associated with the 2.1–2.0 Ga Ubendian tectonic phase is largely overprinted by later deformation, with the exception of the Mbozi Terrane (Theunissen et al., 1996).

The 2.1–2.0 Ga Ubendian tectonic phase is overprinted by a 1.9–1.8 Ga tectonic phase that produced the characteristic terrane-bounding NW-SE trending shear zones and amphibolite facies metamorphism (Lenoir et al., 1994). The exact timing of this deformation event is poorly constrained and is thought to have occurred at 1860 ± 23 Ma based on a weighted average age of U-Pb and whole rock Rb-Sr ages of late-kinematic granitoids (Lenoir et al., 1994; Fig. 2.1). This age overlaps within analytical uncertainty with a weighted average Ar-Ar barroisite cooling age of 1848 ± 6 Ma from a mafic tectonite that is also interpreted to record the 1.9–1.8 Ga Ubendian tectonic phase (Boven et al., 1999), whereas the Kate Granite post-dates the second Ubendian tectonic phase and suggests deformation occurred prior to ca. 1825 Ma (Rb-Sr whole rock; Schandelmeier, 1983). These Rb-Sr and Ar-Ar ages are younger than recent U-Pb (SIMS) zircon dating of eclogites with MORB-like chemistry that suggest high-pressure and low-temperature metamorphism, analogous to modern-day subduction zones, occurred within the Ubende Terrane at 1886 ± 16 and 1866 ± 14 Ma (Boniface et al., 2012). Paleoproterozoic granites and tectonites are in turn overprinted during Meso- and Neoproterozoic orogenic episodes (Theunissen et al., 1992; Ring et al., 1993; Ring et al., 1997; Theunissen et al., 1996). In particular, Meso- and Neoproterozoic-aged eclogites with MORB-like chemistry are thought to represent paleo-sutures and suggest that the current configuration of Ubendian Terranes is the result of at least three discrete orogenic cycles (Boniface, 2009; Boniface and Schenk, 2012). Our U-Pb ages place new geochronologic constraints on the timing of metamorphism, tectonism and magmatism in the Lupa Terrane and provide new evidence to support the Ubendian Belt's protracted Paleoproterozoic tectonic evolution.

2.2.2 Local geology

The geology of the Lupa Terrane has been variably described as comprising high-grade gneissic, high-grade schistose rocks and granitic gneisses (e.g., Grantham, 1931, 1932, 1933; Teale et al., 1935; Gallagher, 1939; Harris, 1961; Van Straaten, 1984; Daly, 1988; Sango, 1988; Lenoir et al., 1994). The extent of the Lupa Terrane is also unclear from the literature (e.g., Kimambo, 1984; Daly, 1988). For the purposes of this study the Lupa Terrane is assumed to be coincident with the extent of the Lupa goldfield which is defined as the triangular shaped block bounded by the Rukwa Rift Escarpment (or Lupa Border Fault; Kilembe and Rosendahl, 1992) to the west, the Mkondo Magnetic Lineament to the north (Marobhe, 1989) and the Usangu Escarpment to the east (Fig 2.2). The Rukwa and Usangu Escarpments represent Tertiary faults that are related to the East African Rift, whereas the nature of the Mkondo Magnetic Lineament is more cryptic (Fig. 2.2; Marobhe, 1989). The field area for the current study is located in the western portion of the Lupa Terrane and corresponds with the mineral exploration licenses currently controlled by Helio Resource (Fig. 2.3). These mineral exploration licenses contain a number of Au occurences that possess geologic similarities with the orogenic Au deposit type and include the Kenge and Porcupine ore bodies (e.g., Simpson, 2012; Chapter Five).

Hitherto geochronology of the Lupa Terrane has been limited to a K-Ar ages from a greisen and granite at 1802 ± 70 Ma and 1827 ± 70 (Cahen et al., 1984), respectively, and two poorly constrained U-Pb zircon ages from the Ilunga Syenogranite (1931 ± 44 Ma; MSWD = 110; n = 4) and Saza Granodiorite (1936 ± 47 Ma; MSWD = 230; n = 4; Mnali, 1999). The Ilunga and Saza granitoids intruded into what has been previously mapped as a "highly-deformed acid schist" (e.g., Kimambo, 1984) and "gneiss" (e.g., Grantham, 1932; Teale, 1935; van Straaten, 1984). We provide new geologic, geochemical evidence and geochronologic evidence to re-classify these rocks and propose a geodynamic setting to explain their occurrence.

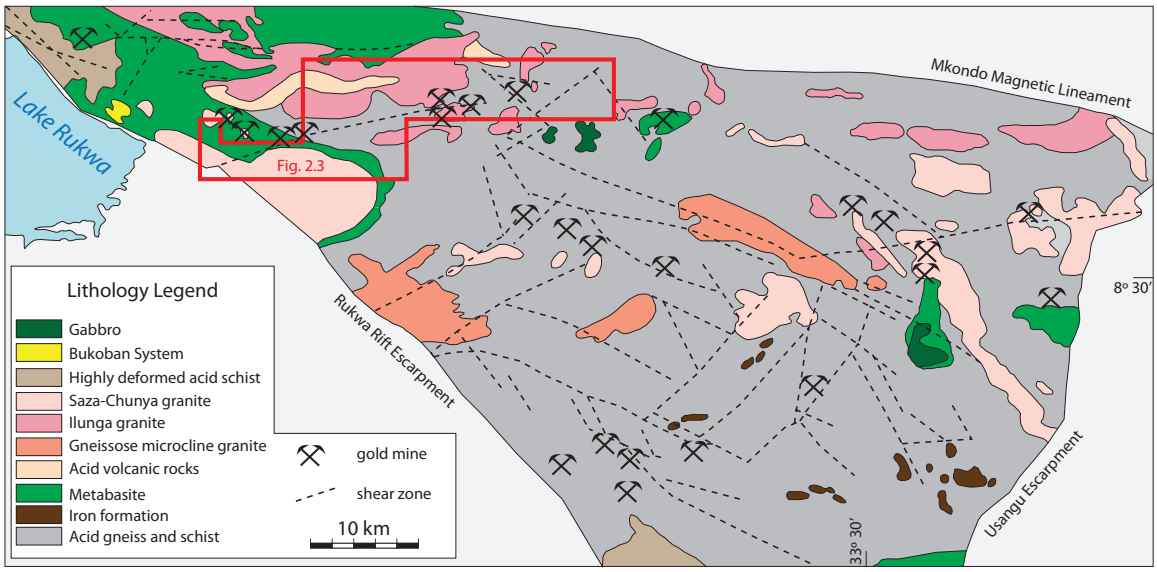

Figure 2.2 – Simplified geology of the Lupa goldfield (modified from Kimambo, 1984).

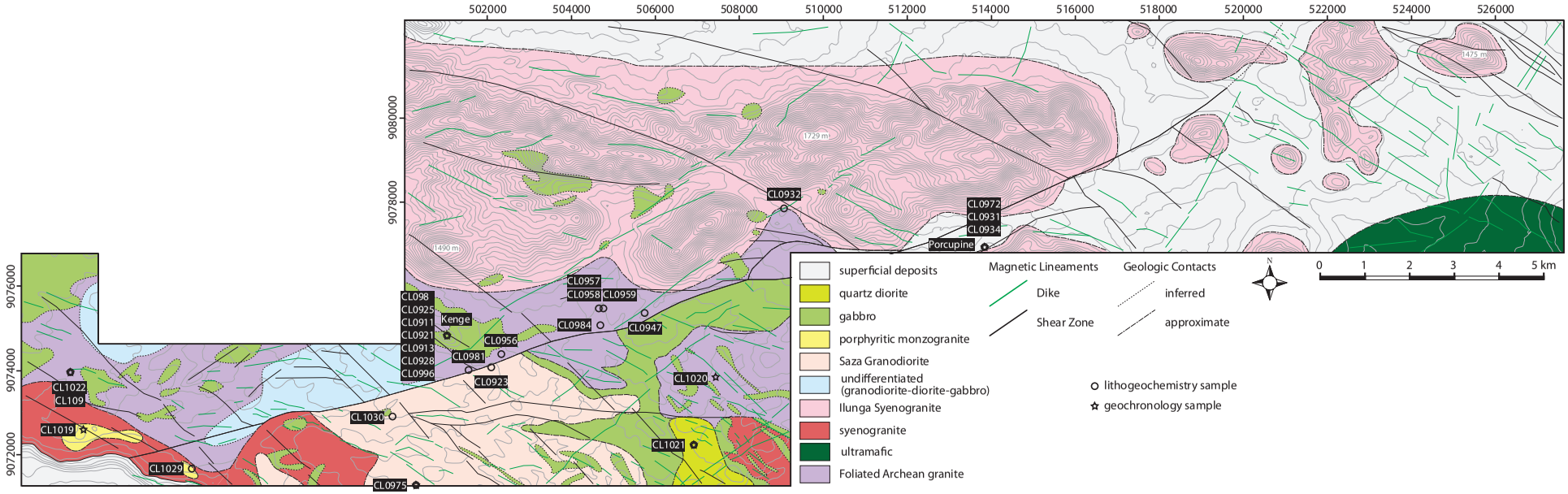

Figure 2.3 – Local geology map showing the location of geochronology and lithogeochemistry samples. Inferred lithologic contacts are based on a series of river traverses by the first author and are integrated with unpublished aeromagnetic and radiometric surveys, acquired from Helio Resource Corp., to interpret approximate lithologic contacts. Shear zone locations are based, in part, on mapping and correspond to negative magnetic anomalies, whereas dikes are buried and interpreted from linear magnetic highs. Contour lines are based on an unpublished digital elevation model by Helio Resource Corp. and are shown at 20 m intervals.

2.3 Analytical methods

2.3.1 Lithogeochemistry

A representative suite (23 samples) of magmatic phases were analyzed for major and trace elements using a combination of fusion inductively coupled plasma-mass spectrometry (ICP-MS) and instrumental neutron activation analysis (INAA) by Actlabs (Ancaster, Ontario; method 4E-Research). Sample aliquants for ICP-MS analysis were first mixed with a lithium metaborate-tetraborate flux and fused in order to ensure complete digestion of refractory minerals (e.g., zircon). As a result, fusion ICP-MS results are considered most representative and are used for plotting purposes. Detection limits for this assay package are in the low ppm and ppb range for most trace elements.

2.3.2 Zircon mineral separation

Zircons were separated from their host rock by crushing ~5 kg of rock in a jaw crusher and pulverizing in a disc mill before passing the sample through a 355 μm sieve. Samples were then placed on a Rogers shaking table and the heavy fraction dried (at 60ºC) before passing through a Frantz isodynamic magnetic separator. The non-magnetic fractions of each sample were then density separated using methylene iodide before handpicking, under ethanol, of the most crack- and inclusion-free grains.

2.3.3 U-Pb zircon ID-TIMS

All of the analyzed zircons have undergone the "chemical abrasion" (thermal annealing and subsequent leaching) pre-treatment technique (Mattinson, 2005) for the effective elimination of Pb-loss. This involved placing zircons in a muffle furnace at 900 ± 20°C for ~60 hours in quartz beakers before being transferred to 3ml Hex Savillex beakers, placed in a Parr vessel and leached in a ~5:1 mix of 29M HF + 30% HNO_3 for 12 hours at ~180°C. The acid solution was removed and fractions were rinsed in ultrapure H_2O, fluxed on a hot plate at ~80°C for an hour in 6 M HCl, ultrasonically cleaned for an hour and then placed back on the hot plate for an additional 30 min. The HCl solution was removed and the fractions (single zircon crystals or fragments) were selected, photographed (in transmitted light) and again rinsed (in ultrapure acetone) prior to being transferred to 300 μl Teflon FEP microcapsules and spiked with a mixed ^{233}U–^{235}U–^{205}Pb tracer. Zircon was dissolved in ~120 μl of 29 M HF with a trace amount of 30% HNO_3 with microcapsules placed in Parr vessels at ~220°C for 48 hours, dried to fluorides and then converted to chlorides at ~180°C overnight. U and Pb for all minerals were separated using standard HCl-based anion-exchange chromatographic procedures.

Isotope ratios were measured at the NERC Isotope Geosciences Laboratory (NIGL), UK, using a Thermo-Electron Triton Thermal Ionisation Mass-Spectrometer (TIMS). Pb and U were loaded together on a single Re filament in a silica-gel/phosphoric acid mixture. Pb was measured by peak-hopping on a single SEM detector. U isotopic measurements were made in static Faraday mode. Age calculations and uncertainty estimation (including U/Th disequilibrium) were based upon the algorithms of Schmitz and Schoene (2007) and plotted in

Isoplot (Ludwig, 2008).

2.3.4 U-Pb zircon LA-MC-ICP-MS

Laser Ablation Multi-Collector Inductively Coupled Plasma Mass Spectrometry (LA-MC-ICP-MS) was conducted at the NERC Isotope Geoscience Laboratory (NIGL). Zircon mineral separates were mounted in epoxy, polished and imaged using cathodoluminesence (CL) on a scanning electron microscope (SEM) at the British Geological Survey (with the exception of CL098 which was prepared at the School of Natural Sciences, Trinity College Dublin). CL imaging provided textural information that assisted zircon targeting. Zircons were ablated using a New Wave Research UP193SS Nd:YAG laser ablation system and an in-house built low-volume rapid washout ablation cell. Ablated material was transported from the ablation cell using a continuous flow of He gas to a Nu Plasma MC-ICP-MS equipped with a multi-ion-counting array. ^{207}Pb, ^{206}Pb and ^{204}Pb+Hg isotopes were measured on ion counters whereas U and Tl isotopes and ^{202}Hg were measured using Faraday Cups. Data were collected using the Nu Instrument's time resolved analysis software. Prior to analysis, the MC-ICP-MS was tuned and gains were measured using a Tl-^{235}U solution co-aspirated using a Nu Instruments DSN-100 desolvating nebuliser. At the start of each run an instrument zero was measured for 30s and was followed by three 30s ablations of three reference materials. The internationally recognized 91500 reference zircon (Weidenbeck et al., 1995) was used as the primary reference material, whereas Plešovice (Sláma et al., 2008) and GJ-1 (Jackson et al., 2004) were used as validation materials. All three matrix matched materials were used to monitor instrumental drift and 91500 was used to correct for instrumental drift. The nine standard ablations were followed by ca. twelve 30s sample ablations. Once data stability had been established, replicates were dropped to one to two for each reference materials. All ablations used a 25–30 μm static spot at 5 Hz and a fluence of 2.7 J/cm^2. During each analysis, the co-aspirated Tl-^{235}U solution was used to correct for instrumental mass bias and plasma induced elemental fractionation. The interference of ^{204}Hg on ^{204}Pb was monitored and corrected for by simultaneously measuring ^{202}Hg and assuming a ^{204}Hg/^{202}Hg = 0.229887. U-Pb data were processed using an in-house spread sheet at NIGL.

All presented ^{206}Pb/^{238}U dates (ID-TIMS and LA-ICP-MS) are calculated using the ^{238}U and ^{235}U decay constants of Jaffey et al. (1971). The consensus value of ^{238}U/^{235}U = 137.818 ± 0.045 (Hiess et al., 2012) was used in the data reduction calculations. Using this more accurate value with its associated uncertainty estimate has the effect of lowering ^{207}Pb/^{206}Pb dates of ca. 2 Ga by 0.8 ± 0.6 Myr, compared to ^{207}Pb/^{206}Pb dates calculated using the consensus value of ^{238}U/^{235}U = 137.88. For U–Pb dates of this age the ^{206}Pb/^{238}U dates are the most precise and robust. In contrast, the ^{207}Pb-based dates (^{207}Pb/^{235}U and ^{206}Pb/^{207}Pb) are considerably less precise and hence are only used to assess concordance of the U–Pb (zircon) systematics.

2.3.5 Lu-Hf zircon LA-MC-ICP-MS

Near concordant (>95% concordance) U-Pb zircon ablation sites from samples CL098,

CL109 and CL1020 were re-analyzed to measure their respective Lu-Hf isotopic compositions. Isotope analyses were carried out at the NIGL using a Thermo Scientific Neptune Plus MC-ICP-MS coupled to a New Wave Research UP193FX excimer laser ablation system and low-volume ablation cell. Helium was used as the carrier gas through the ablation cell with Ar make-up gas being connected via a T-piece and sourced from a Cetac Aridus II desolvating nebulizer. After initial set-up and tuning, a 2% HNO_3 solution was aspirated during the ablation analyses. Lutetium (^{175}Lu), ytterbium (^{172}Yb, ^{173}Yb) and hafnium (^{177}Hf, ^{178}Hf, ^{179}Hf and ^{180}Hf) isotopes were measured simultaneously during static 30s ablation analyses (50 μm; fluence = 8–10 J/cm^2). A standard–sample–standard bracketing technique, using reference zircon 91500, was used to monitor accuracy of internally corrected Hf isotope ratios and instrumental drift with respect to the Lu/Hf ratio. Hf reference solution JMC475 was analyzed during the analytical session to allow normalisation of the laser ablation Hf isotope data. Correction for ^{176}Yb on

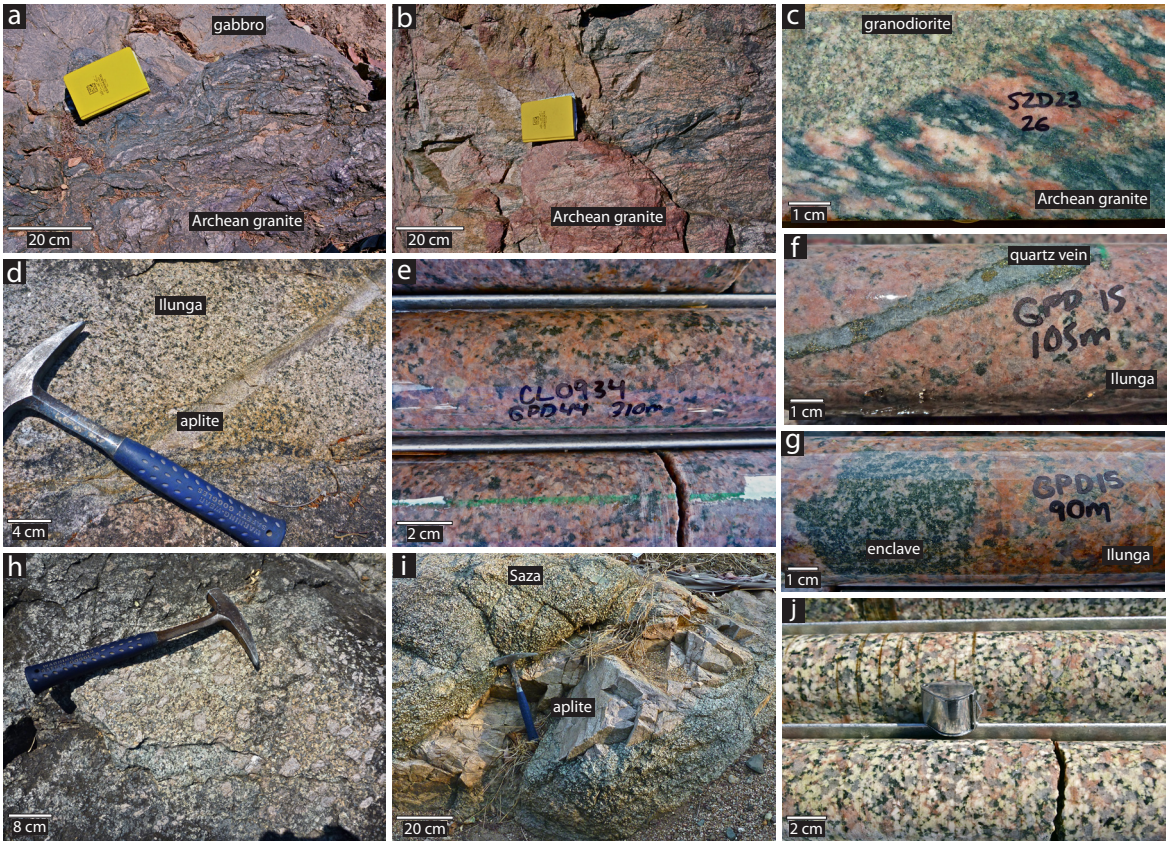

Figure 2.4 – (a) Folded banding in Archean granite in sharp contact with non-foliated gabbroic dike; (b) well developed banding in foliated granite; (c) foliated Archean granitoid (CL098) cross cut by non-foliated granodiorite dike (CL0911); (d) weathered surface of Ilunga Syenogranite that gives surface outcrops a grey appearance. When fresh, modally dominant pink K feldspar crystals are visible. Narrow aplitic dike observed crosscutting the Ilunga Syenogranite; (e) Ilunga Syenogranite in drill core from Porcupine ore body; (f) gold- and pyrite-bearing quartz vein cross cutting Ilunga Syenogranite; (g) mafic enclave suggesting the Ilunga Syenogranite is pre-dated by mafic intrusions; (h) porphyritic monzogranite showing characteristic K feldspar phenocrysts; (i) Saza Granodiorite cross cut by aplite dike. The pitted weathered profile is typical of Saza Granodiorite outcrops; (j) Saza Granodiorite in drill core (CL1030).

the ^{176}Hf peak was made using reverse-mass-bias correction of the $^{176}Yb/^{173}Yb$ ratio (0.7941) empirically derived using Hf mass bias corrected Yb-doped JMC475 solutions following the principles of Nowell & Parrish (2001). ^{176}Lu interference on the ^{176}Hf peak was corrected by using the measured ^{175}Lu and assuming $^{176}Lu/^{175}Lu = 0.02653$.

2.4 Results and data interpretation

2.4.1 Lithologies

All rocks within the field area have undergone hydrothermal alteration and greenschist facies metamorphism. Thus, all rock names are metamorphic and for the remaining discussion all rock names should have the prefix "meta-" (Figs. 2.4, 2.5 and 2.6). Non-foliated felsic-mafic magmatic rocks intrude into a pervasively deformed granitic unit (Fig. 2.4a, b and c). This tectonic fabric varies in development at the outcrop scale but alternating chlorite rich and quartz-feldspar rich bands locally give the foliated granitoid a banded appearance. Crystal plastic deformation of quartz (e.g., undulose extinction) is observed in all samples and a lack of similar deformation processes in the other mineral constituents suggests deformation and metamorphism did not exceed greenschist facies temperature and pressure conditions (Fig. 2.6d; Chapter Five). The comparatively low-grade metamorphism inferred for the foliated granitoids is in contrast to the high-grade rocks that are characteristic of other Ubendian Terranes (Lenoir et al., 1994). Rocks lacking this pervasive tectonic fabric have been classified according to the IUGS classification scheme (LeMaitre, 2002). Two granitoids, the Saza Granodiorite and Ilunga Syenogranite (named after their outcrop localities adjacent to the town of Saza and the Ilunga Hills, respectively), are exceptions and their IUGS names are accompanied by the prefix Saza and Ilunga, respectively as a result of their regional significance (Fig. 2.4). Intermediate and

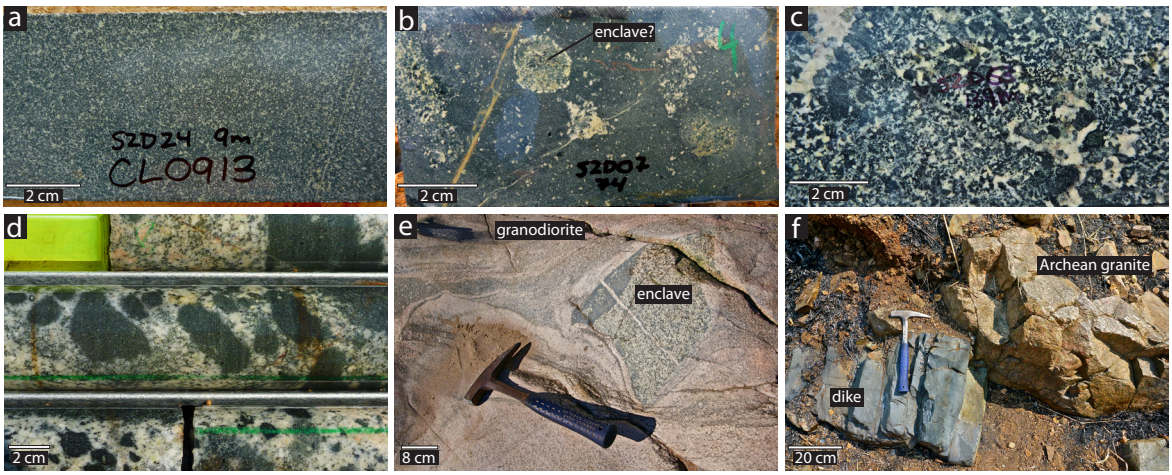

Figure 2.5 – (a) Typical example of the diorite-gabbro suite in core; (b) finer grained example of diorite-gabbro suite with more felsic enclaves; (c) plagioclase-amphibole intergrowths in diorite; (d) core photo of an example of the undifferentiated diorite-gabbro-granodiorite unit (Fig. 2.2) showing variable grain-size and modal mineralogy at hand sample scale; (e) complex and poly-phase mafic enclave hosted by granodiorite. Note ductile flow evidence around the enclave; (f) late fine-grained and alkaline dike (CL0956) cross cutting foliated Archean granitoid.

mafic rocks are difficult to classify using the IUGS scheme because the primary mineralogy has been partially to completely replaced by amphibole (± relict pyroxene) and plagioclase (Fig. 2.5). The large range of amphibole content (modes 15–60%) coupled with the large range of SiO_2 (50–60% SiO_2; see below) and Mg# (44–73; see below) suggests that these rocks represent a compositional spectrum of protoliths. Modal mineralogy for amphibole-plagioclase rocks is variable at the outcrop scale and these rocks are termed the diorite-gabbro suite in the following lithogeochemistry discussion (Mnali, 2002). Sample locations, descriptions and modal mineralogy are presented in Table 2.1.

2.4.2 Lithology descriptions

Foliated granitoids outcrop in the southern portion of the field area (Fig. 2.3). K feldspar, quartz and plagioclase are the dominant mineral assemblage with lesser amounts of chlorite ± calcite ± titanite ± epidote. However, foliated granitoids exhibit a wide range of modal mineralogy (e.g., the modal mineralogy of foliated granitoids ranges from syenogranite to monzogranite) and likely represent several different lithologies, but have been grouped based on a distinct deformation fabric that is absent in the other identified granitoids. This characteristic foliation is defined by alternating quartz-feldspar and chlorite rich bands, which gives the rock a

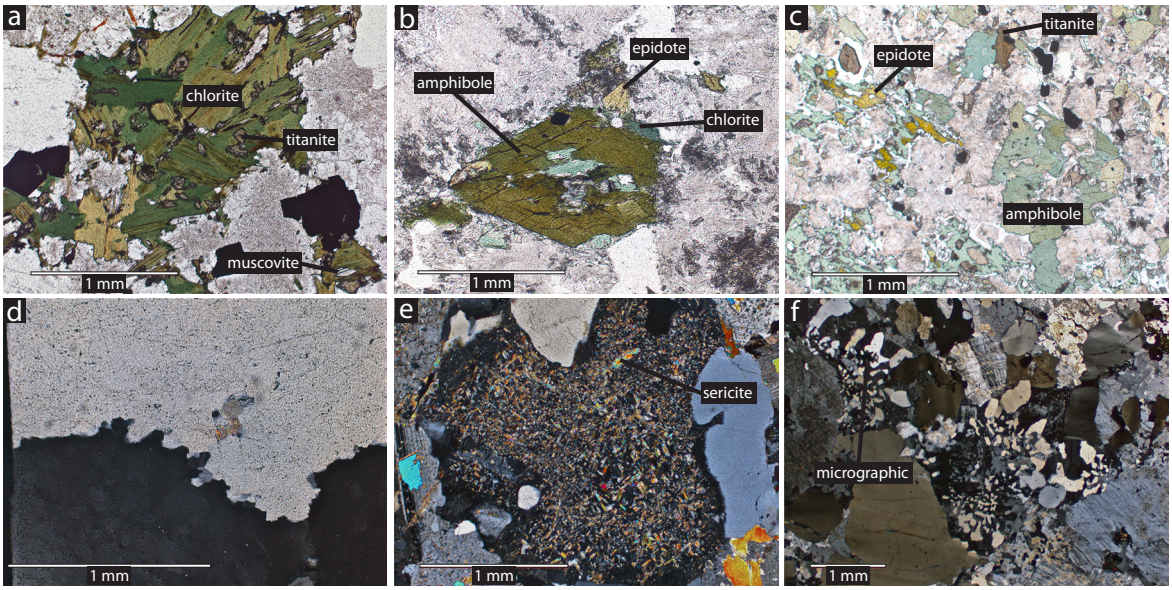

Figure 2.6 – (a) Transmitted light photomicrograph of primary Fe-Mg minerals in foliated Archean granite that have been replaced by chlorite, titanite, epidote and opaques (SZD23 at 32 m); (b) transmitted light photomicrograph of rare relict amphibole in a granodiorite dike that has been overprinted by chlorite and epidote (SZD24 at 27 m); (c) transmitted light photomicrograph of diorite dike showing characteristic mineral assemblage of amphibole, plagioclase, quartz, titanite and epidote (504690, 9075531); (d) crossed nicols transmitted light photomicrograph of recrystallized quartz grain boundaries in foliated Archean granitoid. Quartz crystals also locally possess undulatory extinction and subgrain development (SZD23 at 32 m); (e) crossed nicols transmitted light photomicrograph of sericitized plagioclase (SZD71 at 10 m); (f) crossed nicols transmitted light photomicrograph of micrographic texture in Ilunga Syenogranite. Locally, Ilunga Syenogranite samples possess gradational contacts with aplite dikes and are characterized by abundant feldspar intergrowth textures (GPD15 at 105 m).

banded to "gneissic" appearance (Fig. 2.4b). Compositional banding is accompanied by crystal plastic deformation of quartz (Chapter Five) and both characteristics are dissimilar to the mineralogy and deformation processes that are typical of the auriferous mylonites (Chapter Five) and high-grade rocks from other Ubendian Terranes (Lenoir et al., 1994). Non-foliated granitoids, dioritic-gabbroic intrusions/dikes and aplitic dikes are observed cross cutting foliated granitoids and suggest that fabric development occurred prior to widespread magmatism in the field area (Fig. 2.4c). Mylonitic shear zones, quartz veins and associated hydrothermal alteration (e.g., silicification and sericitization) are observed cross cutting and/or overprinting foliated granitoids (Chapters Four and Five). These cross cutting relationships suggest that foliated granitoids represent the oldest lithology in the field area.

The Ilunga Syenogranite represents the dominant lithology in the northern portion of the field area and corresponds with a topographic high referred to as the Ilunga Hills (Fig. 2.3). K feldspar, quartz and plagioclase comprise the primary mineral assemblage with lesser amounts of chloritized biotite (typically less than 10% modal abundance). The Ilunga Syenogranite is typically equigranular and coarse grained, but locally grades into finer grained and more K feldspar rich zones with aplitic texture. The finer grain size and change in modal mineralogy is also accompanied with quartz-feldspar intergrowths in thin section (Fig. 2.6f). K feldspar-plagioclase intergrowths are also locally observed in thin section and are unique to the Ilunga Syenogranite within the field area. Very few igneous contacts between the Ilunga Syenogranite and other lithologies were observed aside from cross cutting diorite-gabbroic intrusions at the top of the Ilunga Hills, which coupled with mafic enclaves suggests diorite-gabbroic intrusions/dikes pre- and post-date the Ilunga Syenogranite. The Ilunga Syenogranite is also cross cut by narrow aplite dikes and auriferous mylonitic shear zones (Chapters Four and Five). Several mineral alteration assemblages (e.g., sericitization and silicification; Chapter Four) are also observed overprinting the primary mineral assemblage.

Syenogranite outcrops in the southeastern portion of the field area, but is predominately delineated by Helio Resource Corp.'s unpublished radiometric survey (Fig. 2.3; Appendix 1). K feldspar, quartz and plagioclase are the dominant minerals with lesser amounts of chloritized biotite. Auriferous mylonites and intermediate-mafic dikes cross cut the syenogranite in the southeast portion of the map.

The regionally significant Saza Granodiorite outcrops in the southern portion of the field area as a coarse grained and equigranular intrusion (Fig. 2.3). Quartz, plagioclase and K feldspar comprise the dominant mineral assemblage with lesser amounts of chloritized biotite and hornblende (Fe-Mg minerals generally constitute less than 5% modal abundance). Sericite, calcite and epidote are also observed overprinting the primary mineral assemblage. Abundant diorite-gabbroic enclaves/xenoliths, coupled with cross cutting dioritic-gabbroic dikes/intrusions, suggests that the Saza Granodiorite was pre- and post-dated by dioritic-gabbroic magmatism (Fig. 2.5e). The Saza Granodiorite is also cross cut by auriferous mylonitic shear zones (Chapters Four and Five) and aplite dikes.

The porphyritic monzogranite is a distinct granitoid outcropping in the SW corner of

Table 2.1 - Sample locations and descriptions

Sample	Location[1]		Method	Lithology	Modal Mineralogy[2]				Accessory Minerals	Petrographic Features
	Easting	Northing			Q	K	P	Mafic		
CL098	SZD23 (32 m)		LA-ICP-MS							
CL109	492100	9073992	LA-ICP-MS						± chlorite ± sericite	quartz exhibits undulatory extinction and subgrains;
CL1020	507450	9073893	LA-ICP-MS	Foliated Archean granite	18	43	24	15	± epidote ± titanite	plagioclase twins are bent; chlorite pseudomorphing
CL0925	SZD26 (8 m)		ICP-MS						± opaques ± zircon	amphibole (?); pervasive sericitization
CL0947	SZD172 (77 m)		ICP-MS							
CL0911	SZD24 (27 m)		TIMS						± chlorite ± sericite	
CL0921	SZD71 (11 m)		ICP-MS	granodiorite	34	9	53	4	± epidote ± titanite	feldpar sericitization, relict amphibole; minor
CL0958	504690	9075531	ICP-MS						± zircon ± opaques	perthite; quartz ehibits undulatory extinction
CL0972	GPD16 (135 m)		TIMS							
CL0931	GPD10 (22 m)		ICP-MS						± chlorite ± sericite	microcline twinning; perthitic exsolution;
CL0932	509253	9077615	ICP-MS	Ilunga Syenogranite	34	45	15	6	± epidote ± titanite	micrographic intergrowths; quartz exhibits
CL0934	GPD44 (310 m)		ICP-MS						± zircon ± opaques	undulatory extinction
CL0959	504761	9075308	ICP-MS							
CL0975	500237	9071994	TIMS	Saza Granodiorite	25	11	55	9	± chlorite ± amphibole	relict amphibole; abundant chloritization and
CL1030	499339	9073205	ICP-MS						± sericite ± titanite	sericitization
CL1019	492287	9072472	LA-ICP-MS	porphyritic monzogranite	26	44	19	10	± chlorite ± sericite	K feldspar megacrysts; abundant chlortiization and
CL1029	494893	9071545	ICP-MS						± titanite ± opaques	sericitization
CL1021	506889	9072207	LA-ICP-MS	quartz diorite	11	0	68	21	± amphibole ± chlorite ± titanite ± opaques	chloritized amphibole; interstial and fine grained quartz
CL1022	492115	9073982	LA-ICP-MS							
CL0913	SZD24 (9 m)		ICP-MS							
CL0923	SZD26 (35 m)		ICP-MS						± amphibole ± chlorite	chloritized amphibole; albite twins; minor fine
CL0928	SZD7 (74)		ICP-MS	diorite-gabbro	3	0	62	35	± epidote ± clinozoisite	grained and interstial quartz; sericitization of
CL0957	504690	9075531	ICP-MS						± titanite ± opaques	plagioclase; epidote, calcite, clinozoisite, and titanite
CL0981	501536	9074051	ICP-MS						± calcite ± apatite	are a spatially related alteration assemblage;
CL0984	504758	9075081	ICP-MS							abundant calcite veins
CL0956	502293	9074496	ICP-MS	late dikes	0	0	56	44	± OPX ± CPX	localized chlorite-serpentine(?) alteration veinlets
CL0996	SZD63 (192 m)		ICP-MS						± chlorite ± serpentine(?)	

[1] eastings and northings are reported as UTM coordinates (WGS84, Zone 36S); SZD and GPD drill holes are from the Kenge and Porcupine targets, respectively

[2] modal mineralogy is an average value based on point counting 2–5 thin sections (300 points counted per thin section)

the field area (Fig. 2.3). The granitoid was differentiated based on the abundance of K feldspar megacrysts, which locally approach 3 cm in diameter (Fig. 2.4h). The porphyritic monzogranite was observed cross cutting the foliated granitoid but no other igneous contacts were observed. Epidote, sericite, chlorite and calcite collectively overprint the primary quartz-plagioclase-K feldspar-biotite mineral assemblage. Porphyritic monzogranite float was also observed during river traverses across the eastern part of the field area and may suggest additional outcropping examples of this unit are un-mapped.

A variety of granodiorite-tonalite dikes/intrusions were observed across the field area that are not distinguishable on the unpublished radiometric survey flow by Helio Resource Corp. and could not be correlated across to other river traverses. As a result, these are not plotted on the simplified geology map (Fig. 2.3). Quartz and plagioclase are the dominant primary minerals with lesser amounts of chloritized biotite and rare chloritized amphibole (chlorite typically constitutes <10% modal abundance). Granodiorite-tonalite dikes are observed cross cutting foliated granitoids and diorite-gabbroic intrusions. The temporal relationship between granodiorite-tonalite and dioritic-gabbroic intrusions is complicated by abundant evidence for magma mixing textures, which suggest that both rock suites are broadly contemporaneous. This is particularly apparent in the western portion of the field area where felsic segregations, which possess modal compositions similar to granodiorite-tonalite intrusions, are observed within dioritic-gabbroic intrusions (Fig. 2.2). Granodiorite-tonalite dikes/intrusions are differentiated from the Saza Granodiorite based on the finer grain size and the lower modal abundance of K feldspar of the former.

Dioritic-gabbroic dikes and intrusions represent a significant proportion of the field area and are typically observed cross cutting and intruding granitoids (Fig. 2.3). Amphibole and plagioclase are the dominant minerals, whereas chlorite, epidote and calcite are typically present as accessory phases (Fig. 2.6c). Rare relict pyroxene crystals are also observed and are variably altered by a chlorite ± epidote ± titanite ± calcite alteration assemblage. A more siliceous and leucocratic variant of the diorite-gabbro suite was mapped in the southeast corner of the field area (Fig. 2.3; quartz diorite) and is also distinguishable in Helio Resource Corp.'s unpublished radiometric survey. The presence of diorite-gabbroic enclaves/xenoliths in all of the identified granitoids is consistent with multiple dioritic-gabbroic intrusive events. However, dioritic-gabbroic dikes are observed cross cutting the youngest granitoids and suggest that intermediate-mafic dikes at least locally represent the youngest magmatic event.

2.4.3 Lithogeochemistry results

For lithogeochemical results see Appendix 2 and Figs. 2.7, 2.8, 2.9 and 2.10. Hydrothermal alteration and greenschist facies metamorphism are ubiquitous features of Lupa lithologies. Petrographic evidence such as partial to complete replacement of feldspars with sericite (± calcite) and partial to complete replacement of Fe-Mg minerals with amphibole (± chlorite, ± epidote, ± clinozoisite, ± titanite, ± calcite, ± opaques) are likely related to this regional metamorphic event (Fig. 2.6). Chemical alteration is also inferred from large variations in certain

major elements and Large Ion Lithophile Elements (LILE) which are considered to be more mobile during hydrothermal alteration and metamorphism (Cs, Rb, Ba, Sr and Pb; Grant, 2005). High Field Strength Elements (HFSE; Ti, Zr, Y, Nb, Hf, Ta, U and Th), transition elements (Ni, Cr, V and Sc) and Rare Earth Elements (REE; La, Ce, Pr, Nd, Sm, Eu, Gd, Tb, Dy, Ho, Er, Tm, Yb, Lu) are least disturbed by hydrothermal processes (Floyd and Winchester, 1975; Winchester and Floyd, 1977). Thus, the following discussion is focused on trace elements that are considered to be more representative of protolith composition.

The trace element composition of the felsic lithologies can be qualitatively divided into three REE patterns (inset Fig. 2.8a) and all phases share similar trace element patterns normalized to primitive mantle (Fig. 2.8a). Saza Granodiorite (CL1030; CL0975), granodiorite samples (CL0911; CL0921; CL0958) and porphyritic monzogranite (CL1029) possess Light Rare Earth Element (LREE) enrichment (La/Sm_{CN} = 5.2–11.7) and concave-up trends in the Medium and Heavy Rare Earth Elements (MREE and HREE, respectively). This pattern is in contrast to the REE pattern of foliated granite samples (CL098; CL0925; CL0947), which possess LREE enrichment (La/Sm_{CN} = 3.8–8.1), steeply dipping patterns towards the HREE (La/Yb_{CN} = 20.9–64.6) and minor negative Eu anomalies (Eu/Eu* = 0.7–0.9). The third qualitatively distinct REE pattern is shown by the Ilunga Syenogranite (CL0931; CL0932; CL0934; CL0959), which exhibits LREE enrichment (La/Sm_{CN} = 2.9–5.3), deep negative Eu anomalies (Eu/Eu* = 0.08–0.36) and flat MREE and HREE patterns (Gd/Yb_{CN} = 0.9–1.3). On trace element plots normalized to primitive mantle, all felsic phases possess LILE enrichment, gently-dipping patterns towards the REE and are characterized by large negative Nb and Ti anomalies (Nb/Th_{CN} = 0.1–0.6; Ti/Sm_{CN} = 0.0–0.3; Fig. 2.8b).

The trace element compositions of the intermediate and mafic magmatic phases can be qualitatively divided into two trace element groups (Fig. 2.8c and d). The diorite-gabbro suite (CL1021; CL1022; CL0913; CL0923; CL0928; CL0957; CL0981; CL0984) possess LREE enrichment (La/Sm_{CN} = 2.1–4.0) and gently-dipping slopes towards the HREE (La/Yb_{CN} = 3.0–19.9) and minor positive Eu (Eu/Eu* = 1.5–1.1) anomalies. This distinctive REE profile is

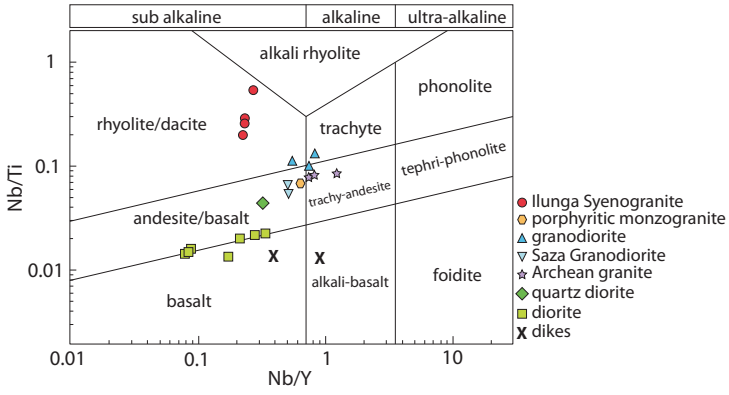

Figure 2.7 – Trace element rock classification diagram (modified from Pearce, 1996a). See text for discussion.

complimented by LILE enrichment relative to HFSE, large negative Nb anomalies (Nb/Th_{CN} = 0.1–0.2) and small negative Ti anomalies (Ti/Sm_{CN} = 0.2–1.2; only CL1022 has a positive Ti anomaly). Two samples, CL0956 and CL0996, are dikes that cross cut foliated granitoids and the diorite-gabbro suite, respectively and preserve their original clinopyroxene and orthopyroxene mineralogy. This suggests that these two dikes post-date greenschist facies metamorphism and are potentially the youngest rocks in the field area. These samples do not possess negative Nb

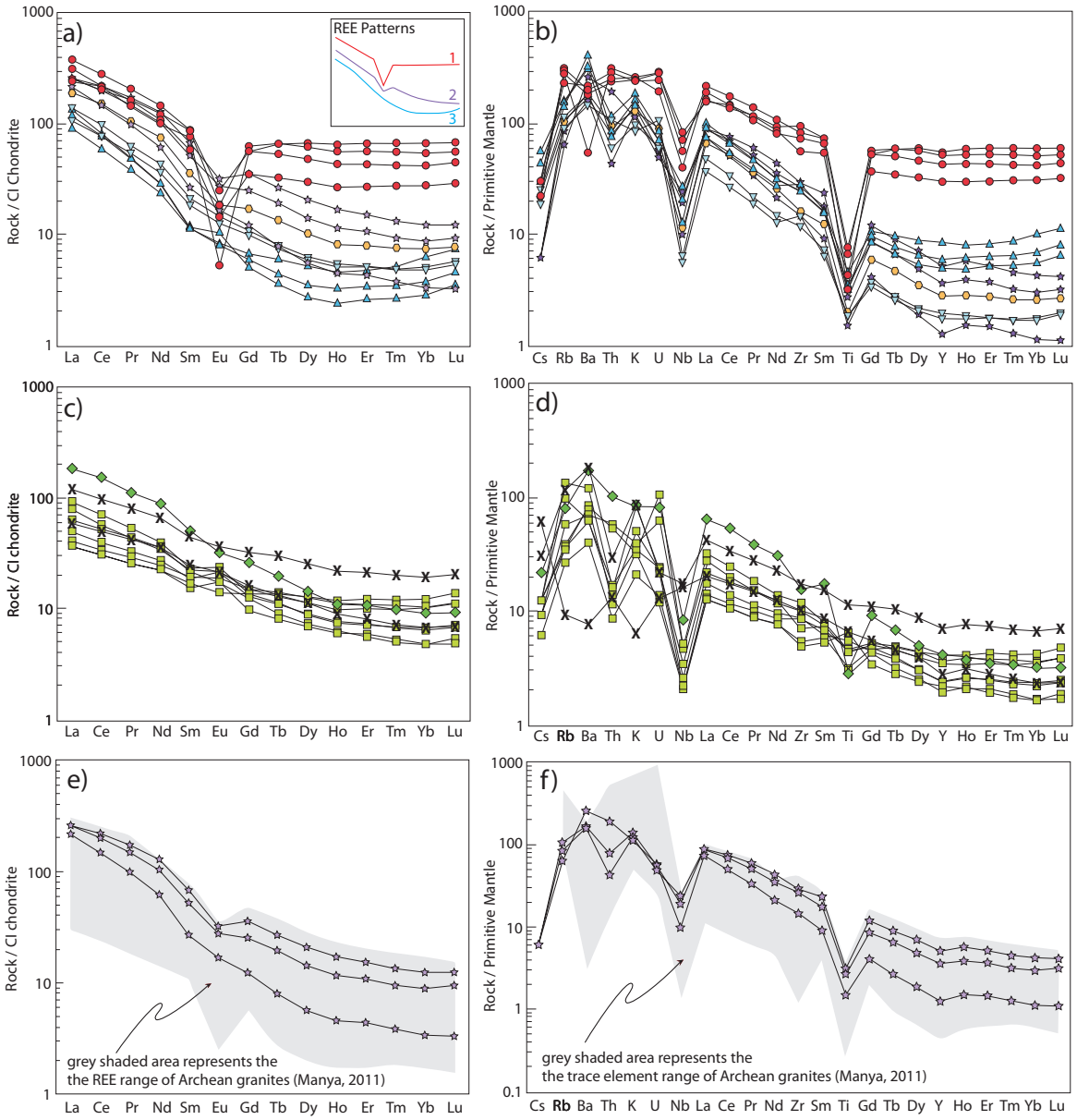

Figure 2.8 – (a–b) REE and trace element plots plot of felsic phases normalized to CL chondrite and primitive mantle, respectively (Sun and McDonough, 1989); (c–d) REE and trace element plots of intermediate-mafic phases normalized to CL chondrite and primitive mantle, respectively (Sun and McDonough, 1989); (e–f) REE and trace element plots of foliated Archean granitoids normalized to CI chondrite and primitive mantle, respectively (Sun and McDonough, 1989). Grey shadings area represents the range of Archean granitoid compositions from the Tanzanian Craton (Manya, 2011). Sample symbols are the same as Fig. 2.6.

or Ti anomalies which is a consistent pattern shown by all other igneous phases in the sample suite. In addition, sample CL0956 possess an alkaline major element chemistry (K_2O wt. % + Na_2O wt. % = 6 % at 50 wt. % SiO_2) which contrasts with the calc-alkaline nature of all the other magmatic phases. The timing and petrogenetic significance of these late dikes is unclear.

2.4.4 REE modelling

Our REE modelling used the non-modal melting equation of Shaw (1970) to assess whether the diorite-gabbro suite could have formed from mantle sources with compositions typical of volcanic arcs (e.g., McKenzie and O'Nions, 1991; Fig. 2.9). We chose primitive mantle (PM; Sun and McDonough, 1989) and the depleted mid-ocean ridge basalt (DMM; McKenzie and O'Nions, 1991) as starting compositions and then calculated the REE concentrations of melts at increasing degrees of partial melting. N-MORB and E-MORB (Sun and McDonough, 1989) are also plotted for reference. Mineral/matrix partition coefficients are from McKenzie and O'Nions (1991); whereas mineral modes and melt-modes for garnet lherzolite and spinel lherzolite are from Walter (1998) and Kinzler (1997), respectively.

Our results suggest that, even at low degrees of partial melting (<1%), the LREE composition of the diorite gabbro suite cannot be explained by non-modal melting (Shaw, 1970) of depleted mid-ocean ridge basalt or primitive mantle sources (Fig. 2.9a). Partial melting of spinel lherzolite sources produce magmas with Sm/Yb ratios similar to the source, whereas partial melting of a garnet lhzerolite with residual garnet produces melts with higher Sm/Yb ratios than the DMM-PM "mantle" array (Fig. 2.9b). The diorite-gabbro suite of this study

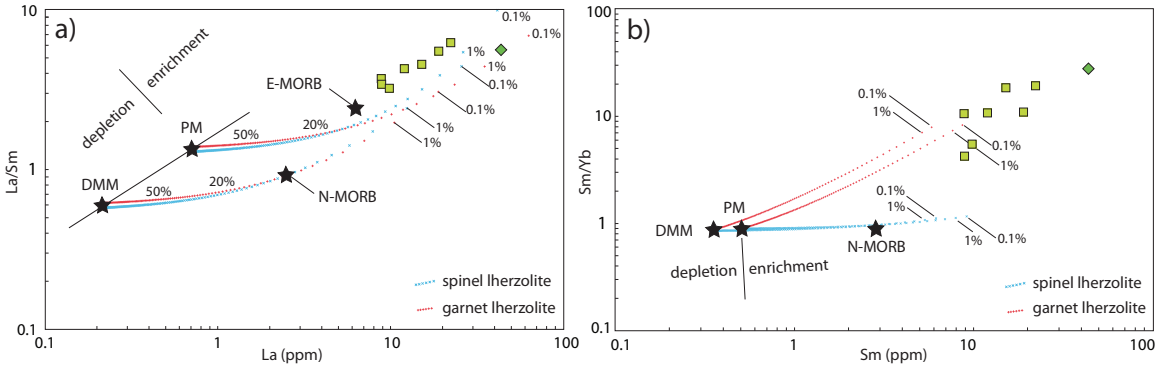

Figure 2.9 – (a) La vs. La/Sm plot of diorite-gabbro suite. (b) Sm vs. Sm/Yb plot of diorite gabbro suite. Melting curves are from the non-modal batch melting equations of Shaw (1970). The modelling used spinel lherzolite (with mode = $olivine_{53}$ + $orthopyroxene_{27}$ + $clinopyroxene_{17}$ + $spinel_3$; melt mode = $olivine_6$ + $orthopyroxene_{28}$ + $clinopyroxene_{67}$ + $spinel_{11}$; Kinzler, 1997) and garnet lherzolite (with mode = $olivine_{60}$ + $orthopyroxene_{20}$ + $clinopyroxene_{10}$ + $garnet_{10}$; melt mode = $olivine_3$ + $orthopyroxene_{16}$ + $clinopyroxene_{88}$ + $garnet_9$; Walter, 1998) sources with depleted mantle (DMM; McKenzie and O'Nions, 1991) and primitive mantle (PM; Sun and McDonough, 1989) compositions. Mineral/matrix partition coefficients are from McKenzie and O'Nions (1991). N-MORB and E-MORB compositions were taken from Sun and McDonough (1989). The solid line represents the mantle array and is defined using the DMM and PM compositions. Lithology sample symbols are the same as Fig. 2.6.

possesses Sm/Yb ratios greater than even small degrees of partial melting of these potential mantle sources and is displaced from the mantle array (Fig. 2.9b). Thus, the diorite-gabbro suite requires a REE enriched source (e.g., a more differentiated source) and/or REE enrichment during magma-crust interaction. Furthermore, depleted Nb/Ta (18–5) and enriched Zr/Hf ratios (50–39) relative to chondritic values (Nb/Ta = 17.6; Zr/Hf = 36.3) suggest that these rocks are not mantle-derived magmas (Green, 2006). Volcanic arcs are thought to possess depleted mantle sources that may be enriched in LILE and REE by a subduction component and/or interaction with the crust (Pearce, 1996a), whereas continental arcs are known to have sources that vary in composition from the upper mantle (i.e, fertile MORB mantle) to more enriched mantle (Pearce and Parkinson, 1993). Alternatively, REE enrichment within the diorite-gabbro suite may be due to the melting of a differentiated source in the lower crust. The exact source

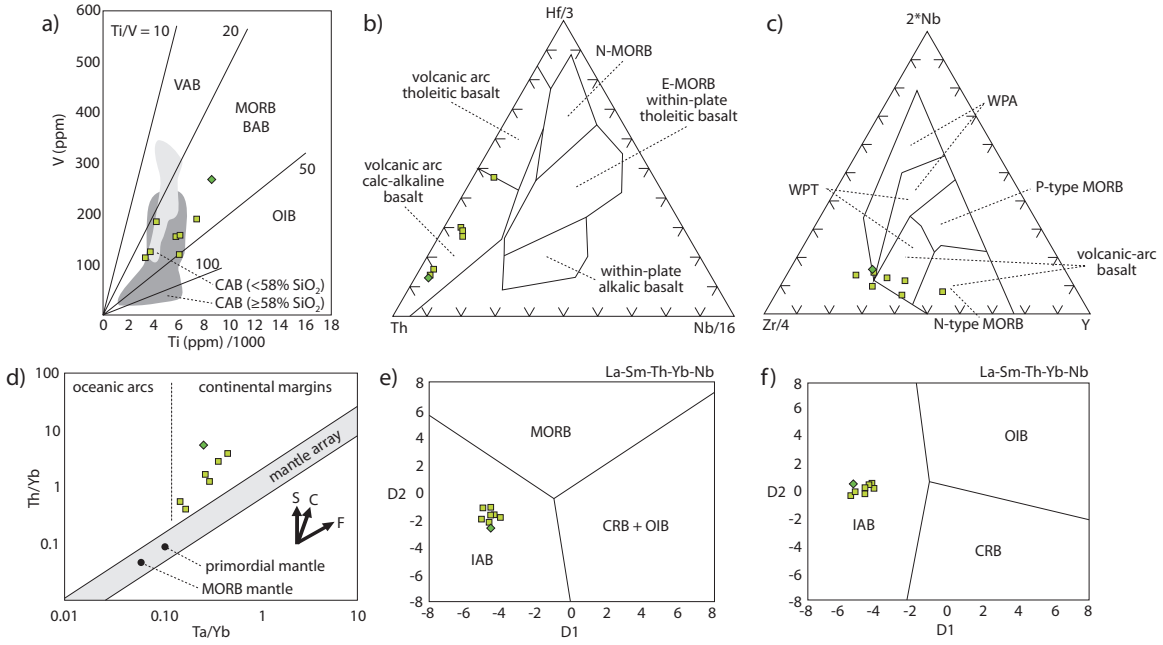

Figure 2.10 – Intermediate-mafic tectonic discrimination diagrams. (a) Basaltoid tectonic discrimination diagram modified from Shervais (1982). VAB = volcanic arc basalt, MORB = mid-ocean ridge basalt, BAB = back-arc basin basalt, OIB = ocean island basalt, CAB = continental arc basalt; (b) basaltoid tectonic discrimination diagram modified from Wood (1980). N-MORB = normal-mid ocean ridge basalt; (c) basaltoid tectonic discrimination diagram modified from Meschede (1986). WPT = within-plate tholeitic basalt, WPA = within-plate alkalic basalt, P-type MORB = primitive mid-ocean ridge basalt, N-type MORB = normal-type mid-ocean ridge basalt; (d) basaltoid tectonic discrimination diagram modified from Pearce (1983). S = subduction zone enrichment trend, C = crustal contamination trend, F = fractional crystallization trend (F = 0.5); (e) log-transformed basaltoid discrimination diagram modified from Agrawal et al. (2008). DF1=0.3518 Log(La/Th) + 0.6013 Log(Sm/Th) - 1.3450 Log(Yb/Th) + 2.1056 Log(Nb/Th) - 5.4763; and DF2 = -0.3050 Log(La/Th) - 1.1801 Log(Sm/Th) + 1.6189 Log(Yb/Th) + 1.2260 Log(Nb/Th) - 0.9944. MORB = mid-ocean ridge basalts, IAB = island arc basalt, CRB = continental rift basalt, OIB = ocean island basalt; (f) log-transformed basaltoid discrimination diagrams modified from Agrawal et al. (2008). DF1 = 0.5533 Log(La/Th) + 0.2173 Log(Sm/Th) - 0.0969 Log(Yb/Th) + 2.0454 Log(Nb/Th) - 5.6305 and DF2 = -2.4498 Log(La/Th) + 4.8562 Log(Sm/Th) - 2.1240 Log(Yb/Th) - 0.1567 Log(Nb/Th) + 0.94. IAB = island arc basalt, OIB = ocean island basalt, CRB = continental rift basalt. Lithology symbols are the same as Fig. 2.6.

of the diorite-gabbro suite is unclear because of a lack of petrogenetic constraints on melting processes, however our REE modelling results are consistent with the trace element evidence (discussed in more detail below) that supports the involvement of crust-magma interaction.

2.4.5 U-Pb zircon ID-TIMS results

For all U-Pb zircon results see Appendix 2 and Fig. 2.11. Our interpreted crystallization ages are reported in Table 2.2 and were calculated using Isoplot v. 4.15 (Ludwig, 2008). The preferred crystallization age for each of the three samples is a weighted average $^{207}Pb/^{206}Pb$ age of concordant analyses because these zircons exhibit the least evidence of disturbance and are the most likely to record crystallization ages. Sample CL0972 is a zircon mineral separate from the Ilunga Syenogranite that hosts the Porcupine ore body. Concordant zircons from CL0972 yield a weighted average $^{207}Pb/^{206}Pb$ age of 1959.6 ± 1.0 (MSWD = 1.4; n = 5). Sample CL0975 is a zircon mineral separate from the Saza Granodiorite. Concordant zircons from this sample yield a weighted average $^{207}Pb/^{206}Pb$ age of 1934.5 ± 1.0 (MSWD = 1.7; n = 5). Sample CL0911 is a zircon mineral separate from a non-foliated granodiorite dike that is observed cross cutting the foliated granitoid at the Kenge ore body (CL098 dated by LA-MC-ICP-MS; Fig. 2.4c). Concordant zircons from sample CL0911 yield a weighted average $^{207}Pb/^{206}Pb$ age of 1958.5 ± 1.3 (MSWD = 0.41; n = 2), consistent with the less precise upper intercept date of 1964.6 ± 5.4 (MSWD = 3.6; n = 5). The lower intercept age of 1126 ± 150 Ma (MSWD = 3.6; n = 5) could represent a Pb-loss event during the Mesoproterozoic that is consistent with the timing of the Kibaran Orogeny (Boniface et al., 2012). In addition to determining the crystallization age of CL0911, U-Pb ages also constrain the maximum age of deformation for CL098 (see section

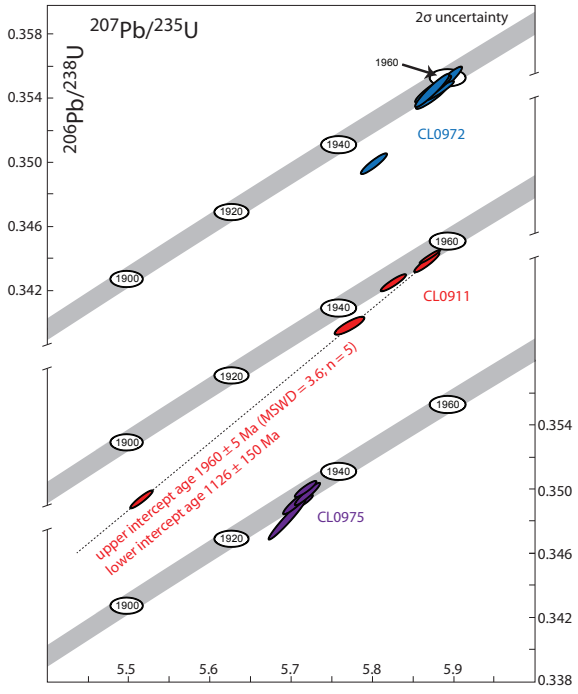

Figure 2.11 – Concordia plots for CL0911, CL0972 and CL0975, respectively. See text for discussion.

4.5).

2.4.6 U-Pb zircon LA-MC-ICP-MS results

All cathodoluminesence images (CL) and ablation spot locations, reference material analyses and sample results are provided in Appendix 2. Concordia plots of the data are shown in Figs. 2.13 and 2.14. Our preferred crystallization ages are reported in Table 2 and were calculated using Isoplot v. 4.15 (Ludwig, 2008). Zircons possess euhedral crystal shapes and complex magmatic oscillatory zoning characterized by truncated and resorbed growth phases. Zircon recrystallization is also suspected in weakly luminescent zircon zones that lack oscillatory zoning (Fig. 2.12).

Sample CL098 is a foliated granitoid that hosts the Kenge Au ore body. Twenty six ablation analyses were measured from seventeen zircons. Two of these analyses (zircons 12-1 and 18-2) possessed significant common lead (1.7–3.8% $f^{206}Pbc$) and are therefore not shown in Fig. 2.13a, b. The remaining twenty-four analyses constrain a Model-2 York fit regression with an upper intercept age of 2725 ± 8 Ma and lower intercept age of 337 ± 470 Ma (MSWD = 3.9; n = 24). We consider the fifteen concordant (100 ± 2% concordance) analyses to reflect the best determination of the actual crystallization age of the sample and yield a weighted average $^{207}Pb/^{206}Pb$ age of 2723 ± 10 Ma (± 40 2SD; MSWD = 5.8; n = 17). The large MSWD implies the assigned analytical uncertainties do not account for the observed U-Pb age range. Therefore, our dataset likely contains multiple zircon populations that possess similar but distinct ages that partially overlap within analytical uncertainty of individual analyses.

Sample CL109 is a foliated granitoid with a well-developed S- and L-fabric. Thirty seven ablation spots from seventeen zircons were analyzed. The majority of imaged zircons from CL109 possess a bright and very-narrow rim that was not possible to analyse with a 25 μm spot size (Fig. 2.12a). Three of these zircons (zircons C5-1, C6-1 and H1-2) possess significant common lead (1.5–1.8% $f^{206}Pbc$) and are not shown in Fig. 2.13a, b. The remaining zircons constrain a

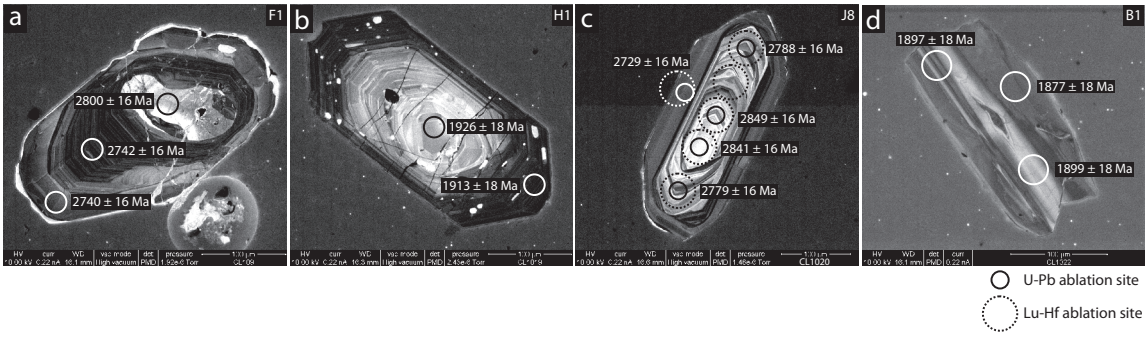

Figure 2.12 – (a) Cathodoluminesence image of zircon F1 from CL109 showing ablation spots and concordant $^{207}Pb/^{206}Pb$ ages; (b) cathodoluminesence image of zircon H1 from CL1019 showing ablation spots and concordant $^{207}Pb/^{206}Pb$ ages; (c) cathodoluminesence image of zircon J8 from CL1020 showing U-Pb and Lu-HF ablation spots and concordant $^{207}Pb/^{206}Pb$ ages; (e) cathodoluminesence image of zircon B1 from CL1022 showing ablation spots and concordant $^{207}Pb/^{206}Pb$ ages.

Model-2 York fit regression with an upper intercept age of 2754 ±14 Ma and lower intercept age at 512 ± 140 Ma (MSWD = 16; n = 34). The large MSWD reflects considerable scatter along the discordia curve and is indicative of complex and non-zero Pb-loss. The youngest $^{207}Pb/^{206}Pb$ ages correspond to what appear from CL images to be recrystallized zircons; however several of the younger $^{207}Pb/^{206}Pb$ ages correspond with magmatically zoned and pristine portions of the zircons. One of these analyses (J2-1) overlaps multiple growth zones, corresponds to a brightly-luminescent margin of the zircon and possesses an anomalously low $^{207}Pb/^{206}Pb$ age at 2620 ± 17 Ma. If this analysis is excluded, a weighted average $^{207}Pb/^{206}Pb$ age for the remaining most concordant zircons (>98% concordance) is 2758 ± 9 Ma (± 28 2SD; MSWD = 2.8; n = 11). The weighted average possesses a MSWD >1 and we interpret this to reflect multiple zircon populations included within the weighted average calculation.

Sample CL1020 is a foliated granitoid with a weakly developed tectonic fabric. Fifty two ablation analyses were measured from eighteen zircon crystals. Seven of these analyses (G2-1, G2-2, C5-1, H9-1, I1-2, Z4-1 and Z7 2) possessed significant common lead (1.5–4.6% $f^{206}Pbc$) and are not shown in Fig. 2.13a, b. Concordant $^{207}Pb/^{206}Pb$ ages (>95% concordance) possess a 150 Myr age range that likely reflects at least two disparate age components and each has likely undergone non-zero Pb-loss. CL imaging provides textural support for an inherited zircon component with the oldest zircons corresponding to highly luminescent and resorbed zircon cores (Fig. 2.12c). The age of this older population is unclear as inherited zircons are suspected to have undergone non-zero Pb-loss, however a weighted average $^{207}Pb/^{206}Pb$ age of the five oldest and most concordant (100 ± 2% concordance) zircons that correspond to texturally distinct zircon zones represents a minimum age estimate of inherited zircons at 2846 ± 7 Ma (± 9 2SD;

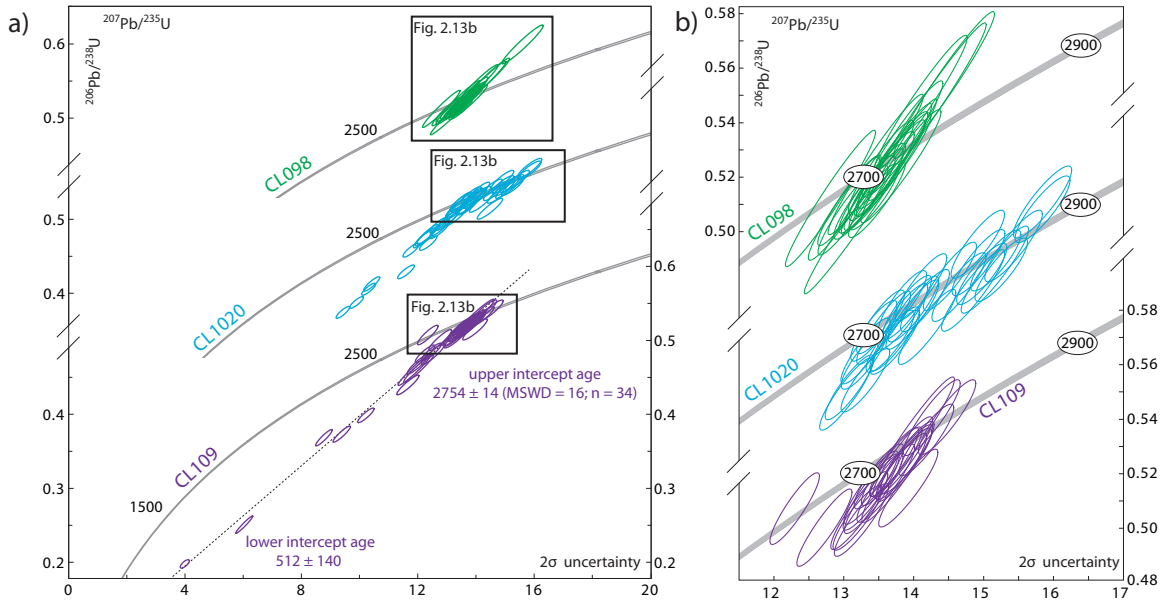

Figure 2.13 – (a,b) Concordia plots of all Archean LA-MC-ICP-MS zircon analyses and concordant (>95% concordance) analyses, respectively. See text for discussion.

MSWD = 0.31; n = 5). The crystallization age of CL1020 is similarly open to interpretation as the younger age population likely includes inherited zircons that have undergone non-zero Pb-loss; however, a weighted average $^{207}Pb/^{206}Pb$ age of the fourteen most concordant (100 ± 2% concordance) zircons corresponding to magmatically zoned zircons provides our best estimate for the crystallization age of CL1020 at 2739 ± 10 Ma (± 35 2SD; MSWD = 4.6; n = 14).

Sample CL1019 is a porphyritic monzogranite that possesses K-feldspar megacrysts (locally several cm in diameter), which distinguish this lithology from the other granitic phases in the field. Thirty two ablations from sixteen zircons were analyzed. Seven of these analyses (A10-1; B3-1; B10-1; C1-1; C4-1; E2-1; G10-1) contained significant concentrations of common Pb (1.9–2.7% $f^{206}Pbc$) and are not included in Fig. 2.14a, b. Two of the remaining twenty five analyses are from zircon G1 and possess significantly older U-Pb ages (ca. 700 Myr). One of these analyses is near-concordant (96% concordance) and provides a $^{207}Pb/^{206}Pb$ age of 2671 ± 17 Ma. This zircon possesses a resorbed and highly luminescent centre and weakly luminescent margin. The textural and isotopic evidence suggest that this zircon is consistent with an inherited zircon component that was derived from Archean basement (e.g., CL098, CL109 and CL1020). All other CL1019 zircons analyses possess Proterozoic U-Pb ages and constrain a Model-2 York fit regression with an upper intercept age of 1948 ± 16 Ma and lower intercept age of 87 ± 150 Ma (MSWD = 13; n = 23). The high MSWD reflects significant scatter about the discordia curve that is likely related to Pb-loss and a range of concordant U-Pb ages that may suggest multiple zircon populations were included in the regression. Concordant analyses are most likely to reflect the true crystallization age of the sample and a weighted average $^{207}Pb/^{206}Pb$ age of the most concordant (>98% concordance) and Proterozoic zircons is 1942 ± 14 Ma (± 35 2SD; MSWD = 3.3; n = 8).

Sample CL1021 is a quartz diorite intrusion adjacent to the Saza granodiorite (CL0975). Thirty ablation spots were analysed from 14 zircon grains. Three of these analyses (J1-23, J1-24 and D9-16) possessed large counts of common lead (1.5–2.1% $f^{206}Pbc$) and are not presented in the concordia plots (Fig. 2.14a, b) or discussed further. The remaining zircons constrain a Model-2 York fit regression with an upper intercept age of 1907 ± 27 Ma and lower intercept age of 524 ± 140 Ma (MSWD = 5.8; n = 27). The dataset likely contains multiple zircon

Table 2.1 - Interpreted U-Pb crystallization ages

Sample	Lithology	Method	Interpreted crystallization ages (Ma)	±
CL0975	Saza Granodiorite	ID-TIMS	1934.5[a]	1.0
CL0972	Ilunga Syenogranite	ID-TIMS	1959.6[a]	1.1
CL0911	granodiorite dike	ID-TIMS	1958.5[a]	1.3
CL098	Archean granite	LA-MC-ICP-MS	2723[a]	10
CL1020	Archean granite	LA-MC-ICP-MS	2739[a]	10
CL109	Archean granite	LA-MC-ICP-MS	2758[a]	9
CL1019	porphyritic monzogranite	LA-MC-ICP-MS	1942[a]	14
CL1021	quartz diorite	LA-MC-ICP-MS	1891[b]	17
CL1022	gabbroic dike	LA-MC-ICP-MS	1880[b]	17

[a]weighted average $^{207}Pb/^{206}Pb$ age of concordant zircons
[b]upper intercept age from Model-2 York fit regression

populations that are unresolvable within the assigned analytical uncertainties based on the 107 Myr range of near-concordant (>95% concordance) $^{206}Pb/^{238}U$ ages coupled with the high MSWD of the upper intercept age (Fig. 2.14b). Our best approximation to the crystallization of CL1021 is the upper intercept age of all the analyzed zircons (except for those with excessive common lead and analysis J1-25 which plots significantly below discordia) at 1891 ± 17 Ma (MSWD = 4.8; n = 26).

Sample CL1022 is a massive gabbroic dike that is observed cross cutting a foliated granitoid (CL109). Twenty one ablation spots from ten zircons were analyzed and constrain a Model-2 York fit regression with an upper intercept age at 1880 ± 17 Ma and lower intercept at age 469 ± 81 Ma (MSWD = 4.9; n = 21). Near-concordant (>95% concordant) zircons possess a 160 Myr range of $^{206}Pb/^{238}U$ ages and imply our dataset contain multiple zircon populations (Fig. 2.14b). Our best approximation of the crystallization age of CL1022 is the upper intercept age of all analyzed zircons at 1880 ± 17 Ma (MSWD = 4.9; n = 21). The interpreted crystallization age also constrains the timing of crystallization and provides a maximum possible age for deformation within the foliated granitoid (CL109).

2.4.7 Lu-Hf zircon LA-MC-ICP-MS results

Three Archean foliated granitoid samples (CL098, CL109 and CL1020) were selected for LA-MC-ICP-MS Lu-Hf isotopic analysis. These samples were chosen because of their unexpected Archean ages and their poorly constrained petrogenetic history. Only near-concordant (>95% concordance) zircon analyses were selected for Lu-Hf analysis and, in the majority of cases, the Lu-Hf ablation sites were centred on top of the pre-existing U-Pb

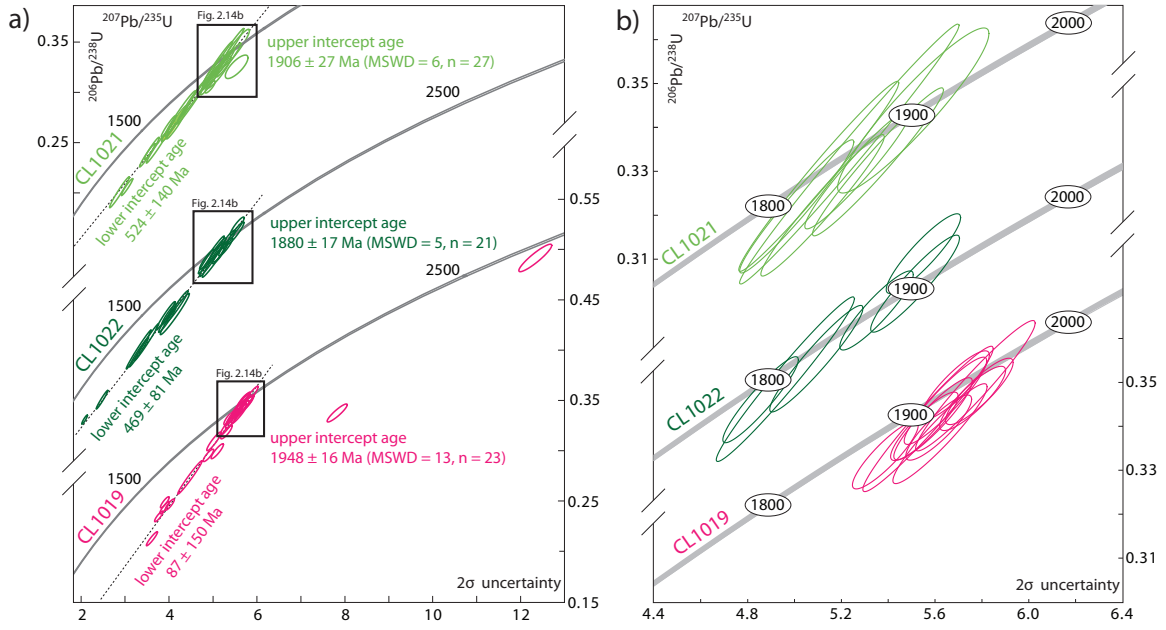

Figure 2.14 – (a–b) Concordia plots of all Proterozoic LA-MC-ICP-MS zircon analyses and concordant (>95% concordance) analyses, respectively. See text for discussion.

ablation site (Fig. 2.12). For zircons where this was not possible (e.g., zircon growth zones were too thin), the Lu-Hf ablation site was repositioned adjacent to the U-Pb ablation site in what is assumed to be a coeval growth zone of the zircon. For ablation sites, CL images, reference material analyses and sample results see Appendix 2.

Zircon crystals incorporate a small amount of ^{176}Lu during crystallization which decays to ^{176}Hf. As a result, each measured $^{176}Hf/^{177}Hf$ ratio needs to be corrected for the interpreted crystallization age of the sample ($^{176}Hf/^{177}Hf_{initial}$). We approached this problem by using the $^{207}Pb/^{206}Pb$ age of the ablation site and the measured $^{176}Lu/^{177}Hf$ ratios to correct for the corresponding $^{176}Hf/^{177}Hf$ analysis. Normalizing $^{176}Hf/^{177}Hf_{initial}$ ratios to the $^{176}Hf/^{177}Hf$ value of the present-day bulk earth ($^{176}Hf/^{177}Hf_{p} = 0.28295$; Patchett and Tatsumoto, 1980) allows the calculation of εHf [($^{176}Hf/^{177}Hf_{initial}$ / $^{176}Hf/^{177}Hf_{present\ day\ earth}$) x 10^4]. Crustal residence ages were calculated following a 2-stage model age approach. The calculated $^{176}Hf/^{177}Hf_{initial}$ ratio of the zircon at the time of growth ($^{207}Pb/^{206}Pb$ zircon age) and an average crustal $^{176}Lu/^{177}Hf$ ratio of 0.012 (Vervoort et al., 1999) were used to project back to the time of intersection with depleted

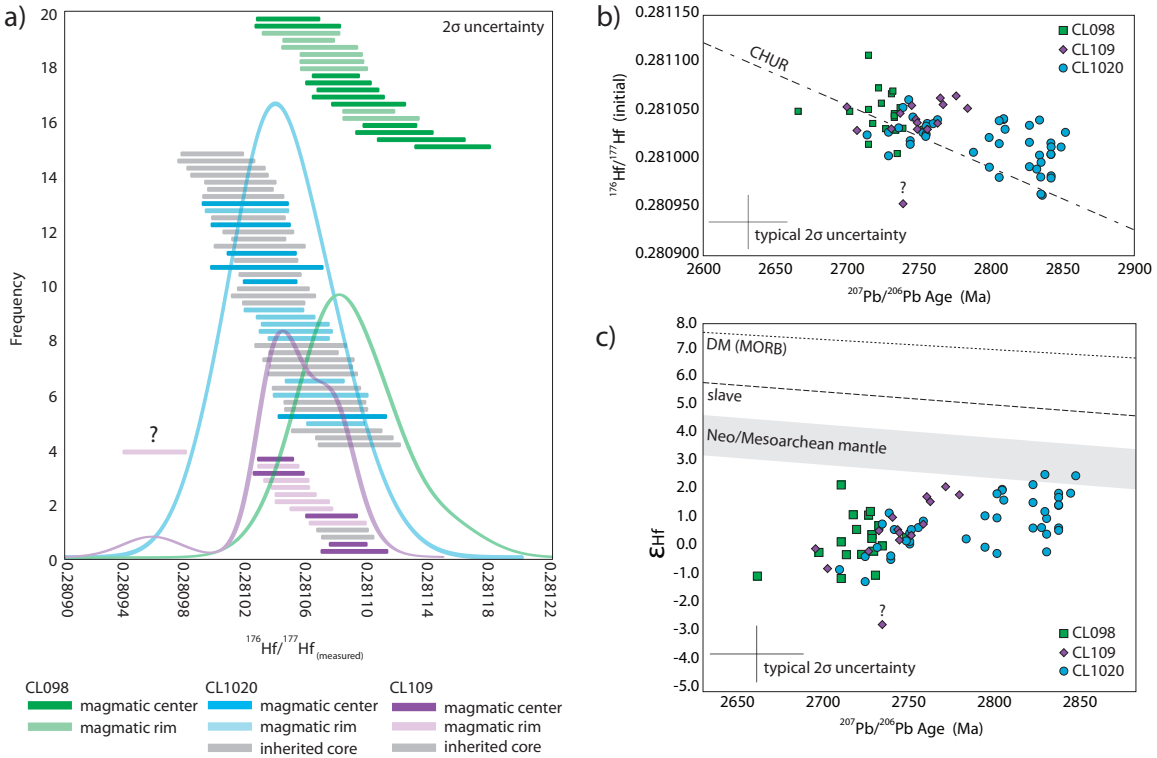

Figure 2.15 – (a) Measured $^{176}Hf/^{177}Hf$ ratios from CL098, CL109 and CL1020. Overlying individual analyses are the probability distributions for each sample. Samples CL098 and CL1020 possess approximately normal $^{176}Hf/^{177}Hf$ ratios distributions, whereas CL109 possesses a weakly bi-modal distribution. (b) Calculated $^{176}Hf/^{177}Hf_{initial}$ ratios for sample CL098, CL109 and CL1020 plotted against each analyses corresponding $^{207}Pb/^{206}Pb$ age. The CHUR evolution line and typical 2σ uncertainty for an individual analysis are also shown. (c) Calculated εHf for samples CL098, CL109 and CL1020 plotted against the corresponding $^{207}Pb/^{206}Pb$ age for each analysis. DM (MORB source depleted mantle, Griffin et al., 2000), Slave Craton mantle (Pietranik et al., 2008) and Neo-Mesoarchean mantle (Shirey et al., 2008) are also plotted. The typical 2σ uncertainty on individual $^{207}Pb/^{206}Pb$ ages and εHf values are also shown.

mantle (with $^{176}Lu/^{177}Hf$ = 0.0384, $^{176}Hf/^{177}Hf$ = 0.28325; Chauvel and Blichert-Toft, 2001)

Forty-two Lu-Hf analyses were performed on fourteen zircons from sample CL1020 (Fig. 2.15a). The $^{176}Hf/^{177}Hf$ analyses possess an approximately normal distribution and overlap within analytical uncertainty at the 2σ uncertainty level. Inherited zircons possess identical $^{176}Hf/^{177}Hf_{initial}$ values (arithmetic average = 0.281010 ± 0.000045 at 2SD, n =26) within uncertainty but are generally lower than zircons that are thought to represent crystallization of CL1020 at ca. 2740 Ma (arithmetic average = 0.281032 ± 0.000029 at 2SD, n = 16).

Nineteen Lu-Hf analyses were performed on twelve concordant zircons from CL098. $^{176}Hf/^{177}Hf$ analyses possess an approximately normal distribution and largely overlap within analytical uncertainty at the 2σ uncertainty level (Fig. 2.15a). An arithmetic average of $^{176}Hf/^{177}Hf_{initial}$ for this sample is 0.281048 ± 0.000046 (2SD, n =19).

Fifteen Lu-Hf analyses were performed on ten concordant zircons from CL109. One Lu-Hf analysis (H1-2) possesses an anomalously low $^{176}Hf/^{177}Hf$. The significance of this value is unclear and is not included in the following discussion but is plotted in Fig. 2.15. The remaining $^{176}Hf/^{177}Hf$ analyses possess a weakly bi-modal distribution (Fig. 15a). $^{176}Hf/^{177}Hf_{initial}$ values are largely within analytical uncertainty of each other (arithmetic average = 0.281047 ± 0.000025 at 2SD, n = 14) and the $^{176}Hf/^{177}Hf_{initial}$ values of CL098 (0.281048) and CL1020 (0.281032). The four oldest U-Pb analyses possess the highest $^{176}Hf/^{177}Hf_{initial}$ values and overlap with $^{176}Hf/^{177}Hf_{initial}$ values of interpreted inherited zircon cores from CL1020 at the 2σ uncertainty level.

2.4.8 Interpretation of complex inheritance and Pb-loss systematics

Concordant LA-MC-ICP-MS U-Pb zircon analyses possess age ranges that exceed the analytical uncertainty of the individual measurements (e.g., near-concordant zircons from CL1022 possess a 160 Myr range; Figs. 2.13 and 2.14). Reference material analyses, run as part of our standard-sample-standard bracketing protocol, overlap within analytical uncertainty and suggest that our analytical methodology cannot explain this age range and that real geologic scatter exists in our samples. The cause of the concordant U-Pb zircon age range can be constrained by integrating the U-Pb and Lu-Hf analyses with CL imaging for the same ablation pits. Previous studies provide empirical evidence to suggest the U-Pb and Lu-Hf isotopic systems are decoupled during metamorphism (e.g., Gerdes and Zeh, 2009; Kemp et al., 2009; Whitehouse and Kemp, 2010). As a result, the $^{176}Hf/^{177}Hf_{initial}$ remains unchanged even for zircons that exhibit U-Pb evidence for Pb-loss. The oldest $^{207}Pb/^{206}Pb$ ages from CL1020 correspond to highly luminescent and resorbed zircon cores that are interpreted to be inherited xenocrysts. Lu-Hf isotopic data supports this interpretation as $^{207}Pb/^{206}Pb$ ages <2740 Ma possesses $^{176}Hf/^{177}Hf_{initial}$ ratios identical to zircons with $^{207}Pb/^{206}Pb$ ages at ca. 2740 Ma, whereas inherited zircons with $^{207}Pb/^{206}Pb$ ages >2740 Ma possess generally less radiogenic $^{176}Hf/^{177}Hf_{inititial}$ ratios. Our results possess considerable overlap, but generally less radiogenic, $^{176}Hf/^{177}Hf_{initial}$ values of inherited and magmatic zircons suggest the source of inherited zircons may have had a dissimilar Lu-Hf composition compared to the source of magmatic zircons.

Conversely, younger zircons that possess identical $^{176}Hf/^{177}Hf_{initial}$ ratios have likely undergone non-zero Pb-loss.

2.5 Discussion

2.5.1 Archean granitoid petrogenesis

The results demonstrate that granites previously considered to be Proterozoic are in fact Archean (ca. 2740 Ma). Furthermore, inherited zircon ages provide evidence for >2740 Ma crust beneath the Lupa Terrane. Other metamorphic belts surrounding the southern and eastern margins of the Tanzanian Craton (e.g., Mozambique and Usagaran) also contain Archean crust (Muhongo et al., 2001; Kröner et al., 2003; Reddy et al., 2003; Sommer et al., 2003). These studies proposed that large portions of the metamorphic belts enveloping the Tanzanian Craton represent re-worked Archean crust and are consistent with a growing number of deep seismic studies that demonstrate laterally extensive Archean lithosphere underlying many Proterozoic accretionary orogens (Snyder, 2002). Alternatively, the Archean rocks at depth may be unrelated to the Tanzanian Craton and may have been incorporated within these metamorphic belts during accretion (Muhongo et al., 2001).

The SW extent of the Tanzanian cratonic margin is a subject of debate (e.g., Coolen, 1980; Pinna et al., 2008). Manya (2011) proposed a possible location for the Tanzanian cratonic margin based on Sm-Nd isotopic evidence. However, a sample from Manya (2011) was taken from an outcrop in the Lupa Terrane and possessed an Archean Nd model age (2688 Ma). That Archean sample is ca. 150 km away from the newly proposed Tanzanian cratonic margin and Manya (2011) interpreted the anomalous age as either a sliver of tectonically interleaved Archean material or re-melting of Archean crust. Archean foliated granites in the Lupa Terrane are older (ca. 2740 Ma) than Rb-Sr and K-Ar ages for the Tanzanian craton (2.4–2.6 Ga; Cahen et al., 1984), but are in good agreement with re-worked Archean rocks in the Usagaran (ca. 2700 Ma; Reddy et al., 2003) and Mozambique Belts [ca. 2740–2608 (Muhongo et al., 2001); ca. 2970–2500 Ma (Sommer et al., 2003)] and recent U-Pb zircon SIMS ages for the Tanzanian Craton (3.2–2.6 Ga; Kabete et al., 2012).

U-Pb and Lu-Hf isotopic evidence provides petrogenetic evidence that constrains the geologic setting of the Archean granitoids. U-Pb zircon ages from CL098, CL109 and CL1020 record multiple zircon populations that have undergone non-zero Pb-loss, nevertheless interpreted crystallization ages are broadly within analytical uncertainty at ca. 2740 Ma. The $^{176}Hf/^{177}Hf_{initial}$ ratios for interpreted magmatic zircons from all three samples are also largely within analytical uncertainty (2σ) and suggests that all three foliated granitoid samples possess a homogeneous $^{176}Hf/^{177}Hf$ source. Calculated εHf values (-2.2–2.8) plot lower than the depleted mantle (Griffin et al., 2000) and the Neo-Mesoarchean mantle (Shirey et al., 2008) evolution curve (Fig. 2.15c). Juvenile melts (mantle melts) are expected to possess $^{176}Hf/^{177}Hf_{initial}$ compositions that overlap with the $^{176}Hf/^{177}Hf$ composition of the mantle source and our results imply that foliated granitoids are not juvenile mantle melts, but likely formed from melting of >2740 Ma crust (Fig. 2.15c). Melting was likely related to an Archean volcanic-arc that is consistent with

the subduction signature suggested by the Archean granitoids trace element compositions (e.g., LREE enrichment; steeply dipping REE patterns; negative Nb and Ti anomalies; Fig. 2.8e, f).

Crustal residence ages (CR) can be estimated from the calculated $^{176}Hf/^{177}Hf_{initial}$ values and assuming a Lu-Hf composition of the mantle source (e.g., Shirey et al., 2008 and references therein). Our two-stage Lu-Hf model ages are subject to large uncertainties because of ^{176}Lu decay constant uncertainty, the poorly constrained Lu-Hf isotopic composition of the source, uncertainty regarding the $^{207}Pb/^{206}Pb$ crystallization age of the samples and uncertainties on individual Lu-Hf measurements (e.g., Davis et al., 2005). As a result, a range of model ages can be calculated from a single zircon crystal (e.g., Whitehouse and Kemp, 2010). The arithmetic average CR age for samples CL098, CL109 and CL1020 (not including inherited zircons) is 3.1 Ga (± 0.9 Ga 2SD; n = 46). The significance of this age is unclear because of the limitations described above, but depleted mantle ages provide the first evidence for ≥ 3.1 Ga basement underlying the Lupa Terrane. The age of this basement is consistent with Nd model ages (2.8–3.1 Ga) from the Tanzanian Craton, Usagaran Belt and the Mozambique Belt (Maboko, 1995; Maboko and Nakamura, 1996; Möller et al., 1998).

CL1020 includes inherited zircons with $^{207}Pb/^{206}Pb$ ages ca. 100 Myr older than the interpreted crystallization age at ca. 2740 Ma. The $^{176}Hf/^{177}Hf_{initial}$ values for suspected inherited zircons are generally lower (arithmetic average = 0.281010 ± 0.000045 at 2SD, n =26) but possess significant overlap with zircons that are thought to represent crystallization of CL1020 at ca. 2740 Ma (arithmetic average = 0.281032 ± 0.000029 at 2SD, n = 16). Therefore, in addition to older $^{207}Pb/^{206}Pb$ ages the suspected inherited zircons appear to have a different $^{176}Hf/^{177}Hf$ source than the magmatic zircons. Inherited zircons (≥ 2740 Ma) may have been sourced from several protoliths of different ages or a single protolith that crystallized at ca. 2850 Ma and subsequently underwent non-zero Pb-loss to produce a range of $^{207}Pb/^{206}Pb$ ages (Friend and Kinny, 1995). We favour the latter interpretation because the $^{177}Hf/^{176}Hf_{initial}$ ratios of inherited zircons are largely within analytical uncertainty of each other and suggest a common $^{176}Hf/^{177}Hf_{initial}$ source.

Previous workers have suggested that Archean rocks within the Ubendian and Usagaran Belts were tectonically interleaved during accretion (Muhongo et al., 2001; Manya, 2011). This hypothesis seems unlikely in the Lupa Terrane where magmatic contacts are clearly observed between the Archean and Paleoproterozoic granitoids (Fig. 2.4c). Seismic tomography models provide evidence for re-worked Archean crust and upper lithosphere extending SW from the Tanzanian Craton to the Bangweulu Block (see Fig. 2 of Begg et al., 2009). If correct, significant portions of the Ubendian Belt may represent re-worked Archean crust. Our U-Pb and Lu-Hf support this hypothesis and we propose that the Tanzanian cratonic margin is located at least 150 km SW from its currently accepted position (Manya, 2011; Fig. 2.1). Our proposed model implies that Archean granitoids are present between Lake Rukwa and currently known exposures of the Tanzanian Craton near the town of Rungwa but may be difficult to identify in the field as a result of reworking and/or the intrusion of voluminous Paleoproterozoic granitoids.

2.5.2 Paleoproterozoic granitoid and diorite-gabbro petrogenesis

Ratios of highly incompatible elements have been shown to remain unchanged during large degrees of partial melting or crystal fractionation and thus incompatible elements can be used as tracers for magmatic processes (e.g., Pearce and Peate, 1995). One important element for tracing subduction zone processes is Nb, which is preferentially retained in the down-going slab within mineral phases (e.g., rutile; Pearce and Peate, 1995). Nb depletions, such as those exhibited by Lupa intrusive phases, are therefore characteristic of melts generated in volcanic arcs (Fig. 2.8). The diorite-gabbro suite also displays other trace element compositions that are typical of modern day volcanic-arcs. LREE enrichment (Hildreth and Moorbath, 1988), low TiO_2 contents (<2.0 wt. %; Pearce and Cann, 1973), large Ba/Ta and Ba/Nb ratios (>450 and >28, respectively; Gill, 1981), low Y/Cr ratios (Pearce. 1982), high Th/Nb and Ce/Nb ratios (Saunders et al., 1988) all suggest the diorite-gabbro suite are typical of calc-alkaline subduction-related (volcanic-arc) magmas (Fig. 2.10). The diorite-gabbro suite also plots in the island-arc field of La-Sm-Th-Yb-Nb log-transformed discrimination diagrams (Agrawal et al., 2008; Fig. 2.10e, f). Paleoproterozoic granitoids also possess trace element characteristics typical of volcanic arcs (e.g., Nb and Ti depletions, high Hf/Ta ratios range from 2–9; Pearce et al., 1984; Harris et al., 1986). Furthermore, the concave-up pattern of the granodiorite samples (CL0975; CL0911; CL0921; and CL0958) are typical of volcanic-arc granites in which MREE strongly partition into hydrous phases, such as amphibole, during crystallization, whereas the flat REE profile and deep negative Eu anomalies of Ilunga Syenogranite samples are indicative of fractional crystallization (Pearce, 1996b; Fig. 2.8).

Volcanic-arc melts, oceanic or continental, typically originate as a result of partial melting of depleted asthenosphere. Subduction processes (e.g., metasomatism in mantle wedge) and crust-magma interaction (e.g., Melting-Assimilation-Segregation-Homogenization; Hildreth and Moorbath, 1988) can then modify the trace element composition of melt products (e.g., LILE and LREE enrichment). Therefore, distinguishing source characteristics from crust-magma interaction is difficult using only trace element compositions (e.g., Davidson, 2005). Paleoproterozoic granitoids and the diorite-gabbro suite are observed cross cutting Archean granitoids. Field observations and inherited zircons suggest that Paleoproterozoic magmatic phases likely interacted with this evolved Archean crust (e.g., La/Yb_{cn} = 28.8–64.6) during emplacement. Crust-magma interaction is typical of continental arcs and can explain the enriched LREE signature of Lupa Terrane lithologies (REE modelling; Fig. 2.9). Large variations in LILE/HFSE ratios (e.g., Ba/La) between broadly contemporaneous and spatially overlapping magmatic phases are more readily explained by varying degrees of crustal-magma interaction and magmatic processes rather than variability within melt sources (Hildreth and Moorbath, 1998). Therefore, the trace element compositions of Paleoproterozoic magmatic phases are typical of continental arcs that exhibit evidence for crust-magma interaction and the low Ti-Nb-Ta values argue against an intraplate tectonic setting.

2.5.3 Geochronologic constraints on deformation and metamorphism

The U-Pb geochronologic data from the current study constrains the absolute timing of deformation events within the Lupa Terrane. At least three, temporally distinct, deformation events (D1, D2 and D3) are recognized in the field. The first deformation event (D1) is only developed within the Archean granitoids. Undulating chlorite-rich bands separated by bands of K-feldspar, plagioclase and quartz give Archean granitoids a banded appearance. This tectonic fabric varies in intensity from outcrop to outcrop, but is consistently present across the field area. Archean foliated granitoids (2760–2723 Ma) are cross cut by non-foliated Paleoproterozoic granites, granodiorites, diorites and gabbros (1960–1880 Ma). Our U-Pb data broadly constrains the timing of D1 to 2720–1960 Ma. Brittle-ductile mylonititc shear zones (D2) crosscut all of the dated magmatic phases. This deformation event is economically important as these structures are the primary host for Au mineralization (Chapters Three and Four). Our U-Pb data constrains the timing of D2 to <1890 Ma and is consistent with Re-Os dating of syn-deformational pyrite at ca. 1880 Ma (Chapter Four). Greenschist facies metamorphism is characteristic of the Au bearing shear zones and overprints all of the dated igneous phases. The timing of greenschist facies metamorphism is therefore <1890 Ma but likely related to D2 at ca. 1880 Ma. Gold- and pyrite-bearing quartz veins (D2) are locally crosscut by discrete brittle faults (D3). The timing of D3 is not constrained, however the brittle nature of the faults is in contrast to the ductile nature of deformation during D1 and D2 and suggests different geologic conditions during D3. The proposed temporally-distinct deformation events are only those which are readily distinguished in the field and it is expected that Paleoproterozoic structures have been reactivated during tectonism that has continued to the present day (Theunissen et al., 1996).

2.5.4 Proterozoic Geodynamic model

Paleoproterozoic magmatic rocks in the Lupa Terrane possess trace element compositions that are typical of continental volcanic-arcs. Based on the geologic, geochronologic and geochemical evidence presented above we propose that the Lupa Terrane was a continental-arc during the Paleoproterozoic. In our model, the Lupa Terrane represents the continental margin (i.e., the Tanzanian cratonic margin) on to which allochthonous terranes (i.e., other Ubendian Terranes) were accreted. The 1960–1880 Ma magmatic events in the Lupa Terrane are younger than the 2.1–2.0 Ga Ubendian tectonic phase but are in good agreement with the second Ubendian Tectonic phase at 1.9–1.8 Ga. Current geochronologic constraints suggest that the Katuma-Ufipa-Lupa Terranes possess the oldest ages (>1900 Ma) and are separated by the disparately younger Ubende-Mbozi Terrane (<1900 Ma; Boniface, 2009). Our U-Pb crystallization ages (1960–1880 Ma) overlap with ages reported from each of the lithotectonic terranes; however no ages reported in this study are comparable to the ca. 1860 Ma eclogites in the Ubende Terrane (Boniface et al., 2012). The Katuma Terrane (1977–1900 Ma; Boniface, 2009) lies along strike of the northwest trending Lupa Terrane and possess a similar magmatic history that suggests both terranes may have shared a similar tectono-magmatic evolution.

Recent ages constraining the temporal evolution of the Ubendian Belt are incompatible

with the existing tectonic model (Daly, 1988). For example, any geodynamic model must explain the juxtaposition of greenschist facies metamorphism in the Lupa Terrane and contemporaneous amphibolite-granulite facies metamorphism in the other Ubendian Terranes. The existing model of wrench-dominated tectonics would require several 100 kilometres of lateral displacement to explain this juxtaposition (Daly, 1988). Alternatively, subduction-related thrusting could have brought high-grade metamorphic rocks in adjacent Ubendian Terranes to the same structural level as the contemporaneous greenschist facies rocks comprising the Lupa Terrane. Our model would imply that sub-horizontal lineations on the terrane-bounding shear zones may be related to strike-slip reactivation of terrane sutures rather than Paleoproterozoic lateral accretion. The timing of this juxtaposition is unclear as Mesoproterozoic, Neoproterozoic and Tertiary rifting all likely contributed to the current configuration of Ubendian Terranes (Boniface, 2009; Boniface et al., 2012; Boniface and Schenk, 2012). The exact geodynamic evolution of the Ubendian Belt remains enigmatic and requires additional constraints. Nevertheless, our results are consistent with the proposed diachronous and protracted accretion history during the 1.9–1.8 Ga Ubendian tectonic phase (Boniface et al., 2009).

2.6 Summary and conclusions

The Lupa Terrane's magmatic history began in the Archean (ca. 2740 Ma) with the intrusion of evolved, calc-alkaline and arc-type granites. Inherited U-Pb zircon ages and Lu-Hf zircon isotopic evidence imply that these granites are the products of partial melting and incorporation of substantially older crust at depth (ca. 3.1 Ga). Archean granitoids were structurally deformed to produce a weakly developed fabric (D1; 2740–1960 Ma) and were then intruded by non-foliated Paleoproterozoic (1960–1880 Ma) calc-alkaline granitoids (syenogranites, monzogranites and granodiorites) and dioritic-gabbroic intrusions. Paleoproterozoic igneous lithologies are cross cut by Au-bearing and greenschist facies shear zones (D2) that host the orogenic Au deposits of the Lupa Terrane. Based on the U-Pb, Lu-Hf, trace element and field evidence presented above we propose:

- At least a 150km SW extension of the Tanzanian cratonic margin to the Rukwa escarpment. Our results are consistent with seismic tomography studies that provide evidence for Archean upper lithosphere extending SW from the Tanzanian Craton to the Bangweulu Block (Begg et al., 2009).

- That Paleoproterozoic magmatic activity possesses trace element characteristics that are analogous to modern-day continental arcs.

- That the Lupa Terrane acted as the continental margin onto which the other Ubendian Terranes were accreted during the Paleoproterozoic. Inherited zircons, trace elements and REE modelling suggest the diorite-gabbro suite underwent magma-crust interaction that is consistent with a continental arc setting.

- That Paleoproterozoic eclogites with MORB-like chemistry (Boniface et al., 2012) imply subduction and thrusting were important accretion processes in contrast to the wrench-dominated tectonics proposed by Daly (1988). Thrusting could also explain the juxtaposition of contemporaneous greenschist facies metamorphism in the Lupa with amphibolite-granulite facies metamorphism characteristic of the other Ubendian Terranes.

2.7 References

Agrawal, S., Guevara, M., and Verma, S., 2008, Tectonic discrimination of basic and ultrabasic volcanic rocks through log-transformed ratios of immobile trace elements: International Geology Review, v. 50, p. 1057–1079.

Begg, G.C., Griffin, W.L., Natapov, L.M., O'Reilly, S.Y., Grand, S.P., O'Neill, C.J., Hronsky, J.M.A., Poudjom Djomani, Y., Swain, C.J., Deen, T., and Bowden, P., 2009, The lithospheric architecture of Africa: seismic tomography, mantle petrology, and tectonic evolution: Geosphere, v. 5, p. 23–50.

Boniface, N., 2009, Eburnian, Kibaran, and Pan-African metamorphic events in the Ubendian Belt of Tanzania: petrology, zircon and monazite geochronology: Unpublished PhD thesis, Kiel University, Germany, 110 p.

Boniface, N., Schenk, V., and Appel, P., 2012, Paleoproterozoic eclogites of MORB-type chemistry and three Proterozoic orogenic cycles in the Ubendian Belt (Tanzania): evidence from monazite and zircon geochronology, and geochemistry: Precambrian Research, v. 192–195, p. 16–33.

Boniface, N., and Schenk, V., 2012, Neoproterozoic eclogites in the Paleoproterozoic Ubendian Belt of Tanzania: evidence for a Pan-African suture between the Bangweulu Block and the Tanzania Craton: Precambrian Research, v. 208–211, p. 72–89.

Boven, A., Theunissen, K., Skylarov, E., Klerkx, J., Melnikov, A., Mruma, A., and Punzalan, L., 1999, Timing of exhumation of a high-pressure mafic granulite Terrane of the Paleoproterozoic Ubende Belt (west Tanzania): Precambrian Research, v. 93, p. 119–137.

Brock, P.W.G., 1963, The Mbozi syenite-gabbro complex: Unpublished PhD Thesis, University of Leeds, UK, 261 p.

Cahen, L., Snelling, N.J., Delhal, J., and Vail, J., 1984, The geochronology and evolution of Africa, Clarendon Press, Oxford, 512 p.

Chauvel, C., and Blichert-Toft, J., 2001, A hafnium isotope and trace element perspective on melting of the depleted mantle: Earth and Planetary Science Letters, v. 190, p. 137–151.

Collins, A.S., Reddy, S.M., Buchan, C., and Mruma, A., 2004, Temporal constraints on Palaeoproterozoic eclogite formation and exhumation (Usagaran, Orogen, Tanzania): Earth and Planetary Science Letters, v. 224, p. 175–192.

Coolen, J.J.M.M.M., 1980, Chemical petrology of the Furua Granulite Complex, southern Tanzania: Unpublished PhD thesis, 13Vrije University, Amsterdam, GUA pap. Geol., Ser. 1, 258 p.

Crowley, J.L., Schoene, B., and Bowring, S.A., 2007, U-Pb dating of zircon in the Bishop Tuff at the millennial scale: Geology, v. 35, p. 1123–1126.

Daly, M.C., 1988, Crustal shear zones in central Africa a kinematic approach to Proterozoic tectonics: Episodes, v. 11, p. 5–11.

Davidson, J.P., Hora, J.M., Garrison, J.M., and Dungan, M.A., 2005, Crustal forensics in arc magmas: Journal of Volcanology and Geothermal Research, v. 140, p. 157–170.

Davis, D.W., Amelin, Y., Nowell, G.M., and Parrish, R.R., 2005, Hf isotopes in zircon from the western Superior Province, Canada: Implications for Archean crustal development and evolution of the depleted mantle reservoir: Precambrian Research, v. 140, p. 132–156.

Dodson, M.H., Cavanagh, B.J., Thatcher, E.C., and Aftalion, M., 1975, Age limits for the Ubendian metamorphic episode in northern Malawi: Geological Magazine, v. 112, p. 403–410.

Friend, C.R.L., and Kinny, R.D., 1995, New evidence for protolith ages of Lewisian granulites, northwest Scotland: Geology, v. 23, p. 1027–1030.

Floyd, P.A., and Winchester, J.A., 1975, Magma type and tectonic setting discrimination using immobile elements: Earth and Planetary Science Letters, v. 27, p. 211–218.

Gallagher, D.R., 1939, Preliminary account of the geology of a portion of Lupa goldfield: Economic Geology, v. 34, p. 306–323.

Gerdes, A., and Zeh, A., 2009, Zircon formation versus zircon alteration – new insights from the combined U-Pb and Lu-Hf in-situ LA-ICP-MS analyses, and consequences for the interpretation of Archean zircon from the Central Zone of the Limpopo Belt: Chemical Geology, v. 261, p. 230–243.

Gill, J.B., 1981, Orogenic Andesites and Plate Tectonics, Springer-Verlag, Berlin, 390 p.

Grant, J.A., 2005, Isocon analysis: a brief review of the method and applications: Physics and Chemistry of the Earth, Parts A/B/C, 30, p. 997–1004.

Grantham, D.R., 1931, Lupa river goldfield: Mining Magazine, v. 45, p. 265–276.

Grantham, D.R., 1932, Lupa goldfield: Bulletin of the Geological Survey of Tanganyika, v. 3, p. 34 p.

Grantham, D.R., 1933, The eastern extension of Lupa goldfield: Geological Survey of Tanganyika, short paper 11, 9 p.

Green, N.L., 2006, Influence of slab thermal structure on basalt source regions and melting conditions: REE and HFSE constraints from the Garibaldi volcanic Belt, northern Cascadia subduction system: Lithos, v. 87, p. 23–49.

Griffin, W.L., Pearson, N.J., Belousova, E., Jackson, S.E., van Achterbergh, E., O'Reilly, S.Y., Shee, S.R., 2000, The Hf isotope composition of cratonic mantle: LAM-MC-ICPMS analysis of zircon megacrysts in Kimberlites: Geochimica et Cosmochimica Acta, v. 64, p. 133–147.

Hanson, R.E., 2003, Proterozoic geochronology and tectonic evolution of southern Africa, in: Yoshida, M., Windley, B.F., and Dasgupta, S., eds., Proterozoic East Gondwana: Supercontinent Assembly and Breakup, Geological Society, London, Special Publications, v. 206, p. 427–463.

Harris, J.F., 1961, Summary of geology of Tanganyika: Geological Survey of Tanganyika Memoir, v. 1, p. 64–67.

Harris, N.B.W., Pearce, J.A., and Tindle, A.G., 1986, Geochemical characteristics of collision-zone magmatism, *in:* Coward, M.P., and Ries, A.C., eds., Collision Tectonics, Geological Society Special Publications, v. 19, p. 51–81.

Hiess, J., Condon, D. J., McLean, N., and Noble, S. R., 2012, 238U/235U Systematics in Terrestrial Uranium-Bearing Minerals, Science 335 (no. 6076), p. 1610-1614.

Hildreth, W., and Moorbath, S., 1988, Crustal contributions to arc magmatism in the Andes of central Chile: Contributions to Mineralogy and Petrology, v. 98, p. 455–489.

Jackson, S.E., Pearson, N.J., Griffin, W.L., and Belousova, E.A., 2004, The application of laser ablation-inductively coupled plasma-mass spectrometry to in situ U-Pb zircon geochronology: Chemical Geology, v. 211, p. 47–69.

Jaffey, A. H., Flynn, K. F., Glendenin, L. E., Bentley, W. C., and Essling, A. M., 1971, Precision measurement of half-lives and specific of 235U and 238U: Physics Reviews C4, p. 1889-1906.

Kabete, J., McNaughton, N.J., Groves, D.I., and Mruma, A.H., 2008, Reconnaissance SHRIMP U-Pb zircon geochronology of the Tanzanian Craton: evidence for Neoarchean granitoid-greenstone belts in the central Tanzania region and the south east African Orogen: Precambrian Research, v. 216–219, p. 232–266.

Kemp, A.I.S., Foster, G.L., Scherstén, A., Whitehouse, M.J., Darling, J., and Storey, C., 2009, Concurrent Pb-Hf isotope analysis of zircon by laser ablation multi-collector ICP-MS, with implications for the crustal evolution of Greenland and the Himalayas: Chemical Geology, v. 261, p. 244–260.

Kilembe, E.A., and Rosendahl, B.R., 1992, Structure and stratigraphy of the Rukwa rift: Tectonophysics, v. 209, p. 143–158.

Kimambo, R.H.N., 1984, Mining and mineral prospects in Tanzania, Eastern Africa Publications Ltd., Arusha, 250 p.

Kinzler, R.J., 1997, Melting of mantle peridotite at pressures approaching the spinel to garnet transition: applications to mid-ocean ridge basalt petrogenesis: Journal of Geophysical Research, v. 102, p. 853–874.

Kröner, A., Muhongo, S., Hegner, E., and Wingate, M.T.D., 2003, Single-zircon geochronology and Nd isotopic systemtics of Proterozoic high-grade rocks from the Mozambique belt of southern Tanzania (Masasi area): implications for Gondwana assembly: Journal of the Geological Society, v. 160, p. 745–757.

Lawley, C.J.M., Selby, D., Condon, D.J., Horstwood, M.S.A., Crowley, Q.G., Imber, J., and

MacKenzie, C., 2010, Geochronology of Granites and Gold in the Lupa Goldfield, Southwest Tanzania: Applied Earth Science (Trans. Inst. Min. Metall. B) 119, p. 87.

Lawley, C.J.M., Imber, J., Selby, D., and MacKenzie, C., 2011, Transpressional deformation and implications for ore body geometry of orogenic gold deposits: Applied Earth Science (Trans. Inst. Min. Metall. B) 120, p. 69.

LeMaitre, R.W., Streckeisen, A., Zanettin, B., Le Bas, M.J., Bonin, B., and Bateman, P., 2002. Igneous rocks: a classification and glossary of terms: recommendations of the International Union of Geological Sciences Subcommission on the systematics of igneous rocks, Cambridge University Press, Cambridge, 236 p.

Lenoir, J.L., Liégeois, J.P., Theunissen, K., and Klerkx, J., 1994, The Palaeoproterozoic Ubendian shear Belt in Tanzania: geochronology and structure: Journal of African Earth Sciences, v. 19, p. 169–184.

Ludwig, K.A. 2008, User's Manual for Isoplot 3.6, A Geochronological Toolkit for Microsoft Excel: Berkeley Geochronology Center Special Publication No. 4, 77 p.

Maboko, M.A.H., 1995, Neodymium isotopic constraints on the protolith ages of rocks involved in Pan-African tectonism in the Mozambique Belt of Tanzania: Journal of the Geological Society, v. 152, p. 911–916.

Maboko, M.A.H., and Nakamura, E., 1996, Nd and Sr isotopic mapping of the Archaean-Proterozoic boundary in southeastern Tanzania using granites as probes for crustal growth: Precambrian Research, v. 77, p. 105–115.

Manya, S., 2011, Nd-isotope mapping of the Archean-Proterozoic boundary in southwestern Tanzania: implication for the size of the Archean Tanzanian Craton: Gondwana Research, v. 20, p. 325–334.

Marobhe, I., 1989, Interpretation of aerogeophysical anomalies of southwestern Tanzania: Geological Survey of Finland Bulletin, v. 350, 72 p.

Mattinson, J.M., 2005, Zircon U-Pb chemical abrasion ("CA-TIMS") method: combined annealing and multi-step partial dissolution analysis for improved precision and accuracy of zircon ages: Chemical Geology, v. 220, p. 47–66.

McConnell, R.B., 1950, Outline of the geology of Ufipa and Ubende: Geological Survey of Tanganyika Bulletin, v. 19, 62 p.

McKenzie, D., and O'Nions, R.K., 1991, Partial melt distribution from inversion of rare earth element concentrations: Journal of Petrology, v. 32, p. 1021–1091.

Meschede, M., 1986, A method of discriminating between different types of mid-ocean ridge basalts and continental tholeiites with the Nb-Zr-Y diagram: Chemical Geology, v. 56, p. 207–218.

Mnali, S.R., 1999, Palaeoproterozoic felsic magmatism and associated gold-quartz vein mineralization in the western part of the Lupa goldfield, south-western Tanzania: Unpublished PhD thesis, University of Dar es Salaam, Tanzania 198 p.

Mnali, S.R., 2002, Tectonic setting of gabbroic rocks in the western part of the Lupa gold field, south-west Tanzania: Tanzanian Journal of Science, v. 28, p. 99–113.

Möller, A., Appel, P., Mezger, K., and Schenk, V., 1995, Evidence for a 2 Ga subduction zone: eclogites in the Usagaran Belt of Tanzania: Geology, v. 23, p. 1067–1070.

Möller, A., Mezger, K., and Schenk, V., 1998, Crustal age domains and the evolution of the continental crust in the Mozambique Belt of Tanzania: combined Sm-Nd, Rb-Sr, and Pb-Pb isotopic evidence: Journal of Petrology, v. 39, p. 749–783.

Muhongo, S., Tuisku, P., Mnali, S., Temu, E., Appel, P., and Stendal, H., 2001, High-pressure granulite-facies metagabbros in the Ubendian Belt of SW Tanzania: preliminary petrography and P-T estimates: Journal of African Earth Sciences, v. 34, p. 279–285.

Nowell, G.M., and Parrish, R.R., 2001, Simultaneous acquisition of isotope compositions and parent/daughter ratios by non-isotope dilution-mode plasma ionisation multi-collector mass spectrometry (PIMMS), *in*: Holland, G. and Tanner, S.D., eds., Plasma Source Mass Spectrometry: The New Millenium. Royal Chemical Society, Special Publication 267, p. 298–310.

Patchett, P.J., and Tatsumoto, M., 1980, Halfnium isotope variations in oceanic basalts: Geophysical Research Letters, v. 7, p. 1077–1080.

Pearce, J.A., and Cann, J.R., 1973, Tectonic setting of basic volcanic rocks determined using trace element analysis: Earth and Planetary Science Letters, v. 19, p. 290–300.

Pearce, J.A., 1982, Trace element characteristics of lavas from destructive plate boundaries, *in*: Thorpe, R.S., ed., Andesites, Wiley, New York, p. 525–548.

—, 1983, Role of the subcontinental lithosphere in magma genesis at active continental margins, *in*: Hawkesworth, C.J., and Norry, M.J., eds., Continental Basalts and Mantle Xenoliths, Cheshire, UK, Shiva Press Ltd., p. 230–249.

Pearce, J.A., Harris, N.B.W., and Tindle, A.G., 1984, Trace element discrimination diagrams for the tectonic interpretation of granitic rocks: Journal of Petrology, v. 25, p. 956–983.

Pearce, J.A., and Parkinson, I.J., 1993, Trace element models for mantle melting: application to volcanic arc petrogenesis, *in*: Prichard, H.M., Alabaster, T., Harris, N.B.W., and Neary, C.R., eds., Magmatic Processes and Plate Tectonics, Geological Society Special Publication, v. 76, p. 373–403.

Pearce, J.A., and Peate, D.W., 1995, Tectonic implications of the composition of volcanic arc magmas: Annual Review of Earth and Planetary Sciences, v. 23, p. 251–285.

Pearce, J.A., 1996a, A user's guide to basalt discrimination diagrams, *in*: Wyman, D.A., (Ed.), Trace Element Geochemistry of Volcanic Rocks: Applications for Massive Sulphide Exploration. Geological Association of Canada, Short Course Notes 12, p. 79–113.

—, 1996b, Sources and settings of granitic rocks: Episodes, v. 19, p. 120–125.

Pietranik A.B., Hawkesworth C.J., Storey C.D., Kemp A.I.S., Sircombe K.N., Whitehouse M.J., and Bleeker W., 2008, Episodic mafic crust formation from 4.5 to 2.8 Ga: New evidence

from detrital zircons, Slave craton, Canada: Geology, v. 36, p. 875–878.

Pinna, P., Muhongo, S., Mcharo, A., Le Goff, E., Deschamps, Y., Ralay, F., Milesi, J.P., 2008, Geology and mineral map of Tanzania: Geological Survey of Tanzania, Dodoma.

Priem, H.N.A., Boelrijk, N.A.I.M., Hebeda, E.H., Verdurmen, E.A.T., Verschure, R.H., Oen, I.S., and Westra, L., 1979, Isotopic age determinations on granitic and gneissic rocks from the Ubendian-Usagaran system in southern Tanzania: Precambrian Research, v. 9, p. 227–239.

Reddy, S.M., Collins, A.S., and Mruma, A., 2003, Complex high-strain deformation in the Usagaran Orogen, Tanzania: structural setting of Palaeoproterozoic eclogites: Tectonophysics, v. 375, p. 01–123.

Reddy, S.M., and Evans, D.A.D., 2009, Palaoproterozoic supercontinents and global evolution: correlations from core to atmosphere, *in*: Reddy, S.M., Mazumder, R., Evans, D.A.D., and Collins, A.S., eds., Palaeoproterozoic Supercontinents and Global Evolution: Geological Society Special Publications, v. 232, p. 1–26.

Ring, U., 1993, Aspects of the kinematic history and mechanisms of superposition of the Proterozoic mobile Belts of eastern Central Africa (northern Malawi and southern Tanzania): Precambrian Research, v. 62, p. 207–226.

Ring, U., Kröner, A., and Toulkeridis, T., 1997, Palaeoproterozoic granulite-facies metamorphism and granitoid intrusions in the Ubendian-Usagaran Orogen of northern Malawai, east-central Africa: Precambrian Research, v. 85, p. 27–51.

Sango, P.M., 1988, Structural and lithological controls of gold mineralization in the Lupa goldfield, Tanzania, *in*: Ho, S.E., and Groves, D.I., eds., Recent Advances in Understanding Precambrian Gold Deposits. Geology Department and University Extension, The University of Western Australia, Publication No. 12, pp. 99–109.

Saunders, A.D., Norry, M.J., and Tarney, J., 1988, Origin of MORB and chemically-depleted mantle reservoirs: trace element constraints: Journal of Petrology (Special Lithosphere Issue), p. 415–445.

Schandelmeier, H., 1983, The geochronology of post-Ubendian granitoids and dolerites from the Mambwe area, northern province, Zambia: Report Institute Geological Sciences, v. 83, p. 40–46.

Shaw, D.M., 1970, Trace element fractionation during anatexsis: Geochimica Cosmochimica Acta, v. 34, p. 237–243.

Schmitz, M.D., and Schoene, B., 2007, Derivation of isotope ratios, errors, and error correlations for U-Pb geochronology using 205Pb-235U(233U)-spiked isotope dilution thermal ionization mass spectrometric data: Geochemistry, Geophysics, Geosystems, v. 8, 20 p.

Shervais, J.W., 1982, Ti-V plots and the petrogenesis of modern ophiolitic lavas: Earth and Planetary Science Letters, v. 59, p. 101–118.

Shirey, S.B., Kamber, B.S., Whitehouse, M.J., Mueller, P.A., and Basu, A.R., 2008. A review of the isotopic and trace element evidence for mantle and crustal processes in the Hadean and Archaean: implications for the onset of plate tectonic subduction, *in*: Condie, K.C.,

and Pease, V.L., eds., When did Plate Tectonics Start on Earth?, Geological Society of America, Memoir 440, p. 1–29.

Simpson, R., 2012, NI 43-101 mineral resource estimate update for the Saza-Makongolosi Gold Project, Tanzania: Unpublished SRK consulting report, 217 p.

Sláma, J., Košler, J., Condon, D.J., Crowley, J.L., Gerdes, A., Hanchar, J.M., Horstwood, M.S.A., Morris, G.A., Nasdala, L., Norberg, N., Schaltegger, U., Schoene, B., Tubrett, M.N., Whitehouse, M.J., 2008, Plesovice zircon — a new natural reference material for U-Pb and Hf isotopic microanalysis: Chemical Geology, v. 249, p. 1–35.

Smirnov, V., Pentel'kov, V., Tolochko, V., Trifan, M., and Zhukov, S., 1973, Geology and minerals of the central part of the western rift: Report on Geological Mapping, Mineral and Resource Division, Dodoma, Tanzania, 333 p.

Sommer, H., Kröner, A., Hauzenberger, C., Muhongo, S., and Wingate, M.T.D., 2003, Metamorphic petrology and zircon geochronology of high-grade rocks from the central Mozambique Belt of Tanzania: crustal recycling of Archean and Paleoproterozoic material during the Pan-African orogeny: Journal of Metamorphic Geology, v. 21, p. 915–934.

Sommer, H., Kröner, A., Muhongo, S., and Hauzenberger, C., 2005, Ages for post-Usagaran granitoid and rhyolitic rocks, Tanzania: South African Journal of Geology, v. 108, p. 247–256.

Sun, S.S., and McDonough, W.F., 1989, Chemical and isotopic systematics of ocean basalts; implications for mantle composition and processes, *in*: Saunders, A.D., Norry, M.J., eds., Magmatism in Ocean Basins: Geological Society of London Special Publication, v. 42, p. 313–345.

Sutton, J., Watson, J., and James, T.C., 1954, A study of the metamorphic rocks of Karema and Kungwe bay, western Tanganyika: Bulletin of the Geological Survey of Tanganyika, v. 22, 70 p.

Snyder, D.B., 2002, Lithospheric growth at margins of cratons: Tectonophysics, v. 355, p. 7–22.

Teale, E.O., Eades, N.W., Harkin, D.A., Harpum, J.R., and Horne, R.G., 1935, Brief explanation of the geology of Irambo area, quarter degree sheet 245, Geological Survey of Tanganyika, Dodoma.

Theunissen, K., Lenoir, J. L., Liégeois, J-P., Delvaux, D., and Mruma, A., 1992, Empreinte pan-africaine majeure dans la chaine ubendienne de Tanzanie sud-occidentale: geochronologie U-Pb sur zircon et contexte structural: Comptes Rendus de l'Académie des Sciences, v. 314, p. 1355–1362.

Theunissen, K., Klerkx, J., Melnikov, A., and Mruma, A., 1996, Mechanisms of inheritance of rift faulting in the western branch of the east African Rift, Tanzania: Tectonics, v. 15, p. 776–790.

Van Straaten, V.P., 1984, Gold Mineralization in Tanzania – a review, *in*: Foster, R.P., eds., Gold '82: the Geology, Geochemistry and Genesis of Gold Deposits. A.A. Balkema, Rotterdam, p. 673–685.

Vervoort, J.D. and Blichert-Toft, J., 1999, Evolution of the depleted mantle: Hf isotope evidence from juvenile rocks through time: Geochimica et Cosmochimica Acta, v. 63, p. 533–556.

Walter, M.J., 1998, Melting of garnet peridotite and the origin of komatiite and depleted lithosphere: Journal of Petrology, v. 39, p. 29–60.

Whitehouse, M.J., and Kemp, A.I.S., 2010, On the difficulty of assigning crustal residence, magmatic protolith and metamorphic ages to Lewisian granulites: constraints from combined in situ U-Pb and Lu-Hf isotopes, *in*: Law, R.D., Butler, R.W.H., Holdsworth, R.E., Krabbendam, M., and Strachan, R.A., eds., Continental Tectonics and Mountain Building; the Legacy of Peach and Horne: Geological Society Special Publications, v. 335, p. 81–101.

Winchester, J.A., and Floyd, P.A., 1977, Geochemical discrimination of different magma series and their differentiation products using immobile elements: Chemical Geology, v. 20, p. 325–343.

Wiedenbeck, M., Allé, P., Corfu, F., Griffin, W.L., Meier, M., Oberli, F., Von Quadt, A., Roddick, J.C., and Spiegel, W., 1995, Three natural zircon standards for the U-Th-Pb, Lu-Hf, trace element and REE analysis: Geostandards and Geoanalytical Research, v. 19, p. 1–23.

Wood, D.A., 1980, The application of a Th-Hf-Ta diagram to problems of tectonomagmatic classification and to establishing the nature of crustal contamination of basaltic lavas of the British Tertiary volcanic province: Earth and Planetary Sciences Letters, v. 50, p. 11–30.

Zhoa, G., Cawood, P.A., Wilde, S.A., and Sun, M., 2002, Review of global 2.1–1.8 Ga orogens: implications for a pre-Rodinia supercontinent: Earth Science Reviews, v. 59, p. 125–162.

– Chapter Three –

Re-Os Geochronology of Quartz Enclosed Ultrafine Molybdenite: Implications for Ore Geochronology

Chapter Three is published with the journal Economic Geology

Lawley, C.J.M., Selby, D., 2012, Re-Os Geochronology of Quartz Enclosed Ultrafine Molybdenite: Implications for Ore Geochronology, Economic Geology, v. 107, p. 1499–1505.

Collaborator: David Selby[1]

[1]Department of Earth Sciences, Durham University, Durham, DH1 3LE, UK

3.1 Introduction

Molybdenite Re-Os geochronology is a well established geochemical tool in the study of ore deposits (e.g., Stein et al., 1997; Selby and Creaser, 2001). The utility of molybdenite as a geochronometer stems from: 1) its occurrence in a wide variety of ore deposit types (e.g., porphyry, epithermal, skarn, orogenic gold and others); 2) its closed-system behaviour during hydrothermal alteration and regional metamorphism (e.g., Stein et al., 1998; Selby and Creaser, 2001; Bingen and Stein, 2003; Ootes et al., 2007; Bingen et al., 2008); and 3) its geochemical tendency to incorporate ppm levels of Re and exclude Os upon crystallization (e.g., Stein et al., 2001 and references therein; Takahashi et al., 2007). The exclusion of Os during molybdenite precipitation simplifies the dating process as all measured Os is radiogenic ($^{187}Os^{r}$) and results from the in-situ decay of ^{187}Re (cf. Markey et al., 2007 and references therein). As a result, Re-Os molybdenite model ages can be calculated from the following equation: $t = \ln(^{187}Os/^{187}Re + 1)/\lambda$ (where t = model age and $\lambda = {}^{187}Re$ decay constant, 1.666×10^{-11} a^{-1}; Smoliar et al., 1996; and Selby et al., 2007). The advantages of the molybdenite Re-Os geochronometer over more traditional radiogenic systems (e.g., K-Ar and Rb-Sr) has resulted in a proliferation of precise and robust age-determinations that have greatly improved our understanding of ore deposit genesis (e.g., Stein et al., 1997; Ballard et al., 2001; Brown et al., 2002; Selby et al., 2002; Barra et al., 2003; Mao et al., 2008).

The starting point for any molybdenite Re-Os analysis is to acquire a pure molybdenite mineral separate. Molybdenite (MoS_2) is a soft, platy, hexagonal and metallic lustred mineral.

Porphyry molybdenite deposits possess the largest concentrations of molybdenite and are the most important economic source for the element molybdenum. However molybdenite is a common accessory sulfide phase for several other ore deposit types. Pure molybdenite mineral separates can be obtained using conventional mineral separation techniques. Rock samples are typically crushed and milled before passing through a sieve and using a combination of heavy liquids (e.g., methyl iodide), magnetic separation (e.g., Frantz isodynamic magnetic separator) and high-purity water flotation. These time-tested mineral separation techniques have proved to be extremely successful for samples where molybdenite crystals are abundant and coarse grained (commonly >0.5 mm). However, in many situations molybdenite crystals are fine grained and are lost within the clay size-fraction during sieving or remain as composite grains encased by silicate minerals, particularly quartz. As a result, ultrafine molybdenite (i.e., molybdenite crystals with diameters less than <50 μm; Fig. 3.1) samples require a novel approach to mineral separation. Ultrafine molybdenite samples in this study were collected from orogenic Au deposits in the Lupa goldfield, SW Tanzania and similar molybdenite occurrences have been reported for other orogenic Au deposits (e.g., Ispolatov et al., 2008). In addition, very-fine molybdenite has also been reported in porphyry and other deposit types (e.g., Stevenson, 1940). A potential solution for these samples lies in the contrasting solubility of sulfide and silicate minerals in hydrofluoric acid (HF; Neuerburg, 1961). Quartz and other silicates rapidly dissolve in HF, whereas most sulfide minerals (e.g., molybdenite) are known to be resistant to dissolution (Neuerburg, 1961). The effect of HF on the Re-Os isotopic composition of molybdenite has not been previously tested despite the potential applicability to isolating ultrafine molybdenite. We approach this problem by exposing four previously dated molybdenite mineral separates (e.g., NIST RM8599, in-house standards) to concentrated HF and demonstrate that the Re-Os isotopic composition of molybdenite is unaffected by exposure to HF. Further we apply this approach to the study of ultrafine molybdenite examples from the Lupa Goldfield, SW Tanzania.

3.2 Samples

3.2.1 Molybdenite control samples and NIST 8599

We tested the effect of HF exposure on Re-Os molybdenite systematics by comparing the Re-Os molybdenite model ages of four previously dated and well-constrained molybdenite mineral separates before and after exposure. The location and characteristics of each sample are presented in Table 3.1. Two of these samples, National Institute of Standards and Technology (NIST) RM8599 and HLP-5, are previously reported as Reference Materials (cf. Markey et al., 1998; Du et al., 2004; Selby and Creaser, 2004; Markey et al., 2007). Both reference materials have also been analyzed using the facilities at the Northern Centre for Isotopic and Elemental Tracing (NCIET) in the TOTAL Laboratory for Source Rock Geochronology and Geochemistry at Durham University (e.g., Porter and Selby, 2010 and references therein). As a result, the Re-Os molybdenite model ages for these two samples are well constrained and have been reproduced by several laboratories using different analytical protocols. The RM8599 and HLP-5 molybdenite powder samples have been produced by mixing crushed ore-rock with

flotation oils at the Henderson and Huanglongpu deposit mills, respectively. The milling process produces fine-grained (similar to ultra-fine molybdenite grain size) and extremely well mixed samples that are ideally suited for Re-Os analysis (Stein et al., 1998; Selby and Creaser, 2004). However, the Re-Os ages of milled samples represent an average age for ore mineralization and may mask subtle age variations related to the complex evolution of most ore systems (e.g., Selby and Creaser, 2001).

In addition to the reference material molybdenite samples we have also utilized samples from the previously dated MAX (Lawley et al., 2010) and Endako porphyry Mo deposits (Selby and Creaser, 2001). Molybdenite samples from the MAX and Endako deposits represent the potassic and phyllic stage of mineralization, respectively and thus provide the absolute timing of that period of ore mineralization. The mineral separates were prepared using traditional mineral separation methods that included crushing, pulverizing, Frantz isodynamic magnetic separation, heavy liquids (i.e., LST [lithium heteropolytungstates] heavy liquid and methyl iodide) and MilliQ flotation.

3.2.2 Ultrafine molybdenite samples

Molybdenite samples are from the Lupa goldfield, SW Tanzania. The Lupa goldfield

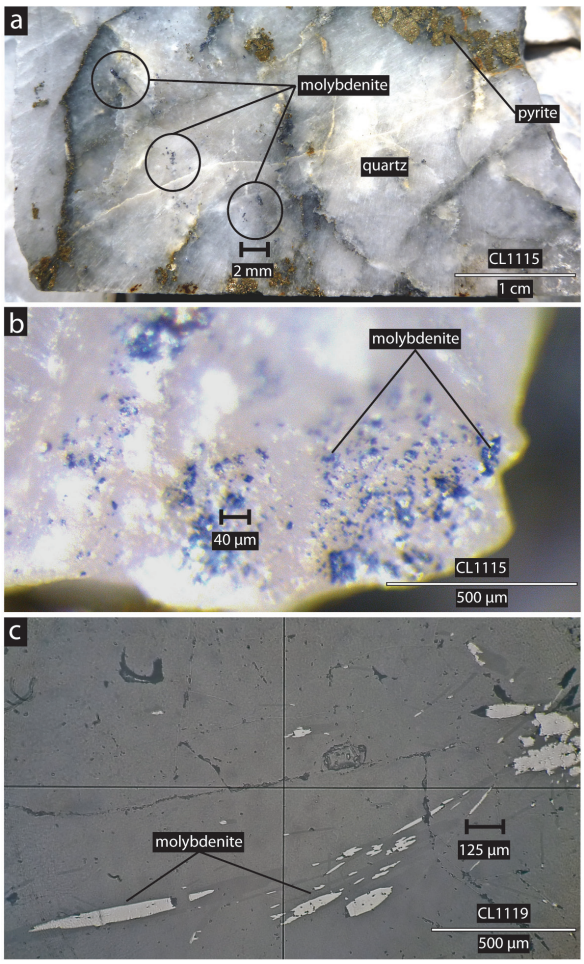

Figure 3.1 – (a) Ultra-fine molybdenite within quartz vein; (b) ultra-fine molybdenite coating and enclosed within quartz grains; and (c) reflected light photomicrograph of molybdenite within and along quartz grain boundaries.

is one of eight litho-tectonic terranes comprising the Paleoproterozoic Ubendian Belt (Daly, 1988). Gold is associated with pyrite, chalcopyrite and trace molybdenite within quartz veins and mylonitic rocks. Sample locations and characteristics are reported in Table 3.1. Molybdenite is present as fracture coatings, mono-mineralic stringer veins and as ultrafine grained disseminations within quartz veins and the granitic host rock (Fig. 3.1). The bulk of the molybdenite from these samples is <50 μm in diameter within quartz crystals and along quartz crystal boundaries (Fig. 3.1c). Samples were crushed, pulverized, sieved and passed through a Frantz magnetic separator before heavy liquid separation. Composite grains (molybdenite encased by quartz) were concentrated in the light fraction of the density separation whereas liberated pyrite and other sulfide grains were concentrated in the heavy fraction of the density separation.

Rhenium-osmium analytical methods utilises sealed borosilicate glass tubes using oxidizing acidic mediums, e.g., *aqua regia* to achieve tracer solution (^{185}Re + isotopically normal Os) and sample Re and Os isotope equilibration. The latter is not capable of digesting quartz and thus any encased molybdenite is also not digested. As a result, ultrafine samples were then chemically separated using the method described below.

3.3 Analytical protocol

3.3.1 Ultrafine molybdenite chemical separation method

Our series of HF tests indicates that approximately 8 mL of 32N HF will dissolve 0.750 g of quartz in 24 hours at room temperature (adapted from Neuerburg, 1961). For each control sample / reference material a known amount of sample was placed into a Savillex Teflon digestion vessel, with 8ml of 32N HF (ROMIL Ltd. UpA high purity HF) and left at room-temperature for 24 hours. After this, the HF was removed by rinsing the molybdenite three times with 10 ml of MilliQ. Finally the molybdenite was rinsed with ethanol and dried at 60°C. High-purity HF (trace element impurities at ppt levels) was used in this study in order to maintain low analytical blanks, however less pure HF could also be used because the majority of HF is removed in the rinsing process and we expect that any Re and Os impurities within the HF are insignificant relative to the ppm and ppb levels of these elements within molybdenite. Sample recovery ranged from 80–90% during the rinsing procedure based on the difference in sample weight before and after rinsing. Sample loss is explained by minor amounts of the sample adhering to the centrifuge tube and within the pipette during rinsing. This was particularly apparent for the two fine-grained mill samples, RM8599 and HLP-5. One of the control samples, "CL100 3 weeks", was exposed to the HF protocol for three weeks prior to analysis in order to assess the longer term affects of HF on the Re-Os systematics.

The same protocol was followed to liberate molybdenite from the quartz-enclosed molybdenite. After the silicate (quartz) digestion, the sample typically contained molybdenite plus trace pyrite. The grain size of these samples precluded hand picking as a means for removing trace amounts of pyrite. However the Re and Os contribution of trace pyrite is insignificant relative to the much larger concentrations of Re and O present within molybdenite. Ultrafine molybdenite samples with more complicated mineralogy (e.g., quartz-feldspar-molybdenite

veins) typically possessed HF insoluble products after digestion. The majority of these HF insoluble products were removed during the following MilliQ rinsing stage. Neuerburg (1961) reported that any remaining HF- and water-insoluble products can be removed by exposing the sample to aluminium chloride; however this was not deemed necessary for the sample suite.

3.3.2 Re-Os isotopic analytical method

The Re and Os abundance and isotope composition determinations for molybdenite mineral separates follow those previously published (e.g., Porter and Selby, 2010). In brief, a weighed aliquant of the molybdenite mineral separate and tracer solution (^{185}Re + isotopically normal Os) were then loaded into a Carius tube with 11N HCl (1 mL) and 15.5N HNO_3 (3 mL), sealed and digested at 220ºC for ~24 hrs. Osmium was purified from the acid medium using solvent extraction ($CHCl_3$) at room temperature and micro-distillation methods. The Re fraction was isolated using standard anion column chromatography. Rhenium and Os were loaded onto coated Ni and Pt filaments, respectively, and their isotopic compositions were measured using negative thermal ionization mass spectrometry (Creaser et al., 1991; Völkening et al., 1991). Analyses were conducted on a Thermo Electron TRITON mass spectrometer with the Re and Os isotopic composition measured using static Faraday collection. Analytical uncertainties are propagated and incorporate uncertainties related to Re and Os mass spectrometer measurements, blank abundances and isotopic compositions, spike calibrations and reproducibility of standard Re and Os isotope values. During the course of this study Re and Os blanks were <4 pg and 1 pg, respectively, with the ^{187}Os/^{188}Os of the blank being 0.25 ± 0.02.

3.4 Results

3.4.1 Re-Os control samples

All Re-Os results are listed in Table 3.1 and presented in Figure 3.2.

RM8599 - Two aliquants of approximately 100 mg of RM8599 were analyzed and provided identical molybdenite Re-Os model ages of 27.6 ± 0.1 Ma. These ages are in excellent agreement with the arithmetic average of this sample 27.7 ± 0.0 Ma (n = 48; Markey et al., 2007) and previously reported analyses 27.6 ± 0.1 Ma and 27.7 ± 0.1 (Porter and Selby, 2010). The ^{187}Re and ^{187}Os concentrations are 7.2 ± 0.0 ppm and 3.3 ± 0.0 ppb, respectively and overlap within uncertainty with previously reported values (Markey et al., 2007; Porter and Selby, 2010).

HLP-5 - One aliquant of approximately 6 mg of HLP-5 was analyzed and provided a molybdenite model age of 220.0 ± 0.9 Ma. This age is in excellent agreement with the accepted weighted average age of 220.5 ± 0.2 Ma (MSWD = 1.3; n =17; Selby and Creaser, 2004) and also the date reported by Porter and Selby (2010; 221.4 ± 0.9 Ma). The ^{187}Re and ^{187}Os concentrations are 201.1 ± 1.5 ppm and 738.3 ± 5.5 ppb, respectively and are significantly higher than the ^{187}Re (~170 ppm) and ^{187}Os (~600 ppb) concentrations previously reported (Selby and Creaser, 2004 and references therein; Porter and Selby, 2010). The potential explanation for this discrepancy is discussed further below.

2706SWB - One aliquant of approximately 15 mg of 2706SWB was analyzed and provided

Table 3.1. Sample locations, characteristics, and Re-Os results

Sample	Sample Location	Brief Sample Description	sample wt. (g)	Re (ppm)	±	^{187}Re (ppm)	±	^{187}Os (ppb)	±	Model Age (Ma)[1]	± (Ma)
Control Samples											
RM8599	Henderson Deposit, USA	Molybdenite powder; Molybdenite Reference Material	0.092	11.39	0.04	7.16	0.02	3.30	0.01	27.6	0.1
			0.103	11.36	0.04	7.14	0.02	3.29	0.01	27.6	0.1
HLP-5	Huanglongpu Deposit, China	~1 m X 500 m calcite-quartz-molybdenite veins	0.006	319.90	2.42	201.06	1.52	738.28	5.46	220.0	0.9
2706SWB	Endako Deposit, Canada	Laminated quartz-molybdenite veins	0.016	32.85	0.14	20.65	0.09	50.19	0.18	145.7	0.6
CL100	MAX Deposit, Canada	Quartz-molybdenite vein from high-grade zone	0.012	54.67	0.26	34.36	0.16	46.07	0.20	80.4	0.3
			0.021	56.26	0.21	35.36	0.13	47.47	0.15	80.5	0.3
CL100 3 weeks			0.021	49.89	0.19	31.36	0.12	42.23	0.14	80.8	0.3
Ultra-fine Molybdenite Samples											
CL1115	Kenge, Lupa Goldfield, Tanzania	Disseminated molybdenite within quartz vein	0.022	7.40	0.03	4.65	0.02	153.65	0.50	1950	8
CL1116	Kenge, Lupa Goldfield, Tanzania	Disseminated molybdenite within quartz vein	0.015	8.55	0.04	5.37	0.02	177.64	0.75	1952	10
CL1117	Kenge, Lupa Goldfield, Tanzania	Disseminated molybdenite within quartz vein	0.023	13.35	0.06	8.39	0.04	278.02	0.85	1957	9
CL1118	Porcupine, Lupa Goldfield, Tanzania	Disseminated molybdenite within quartz-feldspar vein	0.023	1.96	0.01	1.23	0.01	39.26	0.13	1882	9
			0.019	1.72	0.01	1.08	0.01	34.66	0.13	1890	10
CL1119	Porcupine, Lupa Goldfield, Tanzania	Disseminated molybdenite within granite	0.020	3.35	0.02	2.11	0.01	67.65	0.35	1896	13
CL1120	Porcupine, Lupa Goldfield, Tanzania	Disseminated molybdenite within granite	0.020	10.29	0.04	6.47	0.03	206.09	0.68	1882	8

[1] Model age calculated from the simplified isotope equation [$t = \ln(^{187}Os/^{187}Re + 1)/\lambda$; where t = model age, and $\lambda = ^{187}$Re decay constant] and assumes no initial radiogenic Os
Analytical uncertainties are reported at 2σ

a molybdenite model age of 145.7 ± 0.6 Ma. This age is identical within analytical uncertainty with the weighted average age of 145.8 ± 0.4 Ma (MSWD = 2.8; n = 10; Selby and Creaser, 2004). The ^{187}Re and ^{187}Os concentrations are 20.7 ± 0.1 ppm and 50.2 ± 0.2 ppb, respectively and are slightly higher (~19 ppm for ^{187}Re and 45 ppb ^{187}Os) than those reported in Selby and Creaser (2004).

CL100 - Three aliquants of molybdenite from the MAX porphyry deposit provide molybdenite model ages of 80.4 ± 0.3 Ma, 80.5 ± 0.3 Ma; and 80.8 ± 0.3 Ma. All three ages agree within analytical uncertainty with the previously reported Re-Os age for CL100 (80.5 ± 0.4 Ma) and two other Re-Os molybdenite dates from this deposit (80.1 ± 0.4 Ma; and 80.2 ± 0.4 Ma; Lawley et al., 2010). The ^{187}Re and ^{187}Os concentrations for the HF treated CL100 sample are 34.4 ± 0.2 ppm, 35.4 ± 0.1 ppm; 31.4 ± 0.1 ppm and 46.1 ± 0.2 ppb, 47.5 ± 0.2 ppb, 42.2 ± 0.1, respectively. All of these concentrations are slightly higher (^{187}Re = 27.8 ± 0.1 ppm; ^{187}Os = 37.3 ± 0.1 ppb) than those reported in Lawley et al. (2010). One aliquant of sample CL100 was left in HF for three weeks at room temperature (CL100 3 weeks). The Re-Os model age for the latter is within uncertainty to the sample aliquants of CL100 that were only treated for 24 hours. However, the 3 week treated sample gave slightly less Re and Os abundances, which are nonetheless similar to those published for this sample by Lawley et al. (2010). In addition, Re-Os results are also in good agreement with U-Pb and Ar-Ar ages of the host intrusion and associated hydrothermal alteration at MAX (Lawley et al., 2010).

3.4.2 Re-Os ultrafine molybdenite

Ultrafine molybdenite results for the Kenge and Porcupine deposits are listed in Table 3.1 and presented in Figure 3.3. A weighted average Re-Os model molybdenite model age for the three samples from the Kenge deposit is 1953 ± 5 Ma (MSWD = 0.6; n = 3). A weighted average Re-Os molybdenite model age for the three samples and one repeat analyses from the Porcupine deposit is 1886 ± 5 Ma (MSWD = 1.5; n = 4). Total Re concentrations for samples from the Kenge deposit range from 7–13 ppm, whereas total Re concentrations for samples from the Porcupine deposit range from 1–10 ppm. These ranges are comparable with previously reported values from samples prepared using conventional mineral separation techniques (Chapter Four).

3.5 Discussion

3.5.1 HF and Re-Os molybdenite systematics

We tested the effect of HF on Re-Os systematics by exposing previously dated molybdenite mineral separates (i.e., control samples) to HF and compared the molybdenite model age with and without HF exposure. Molybdenite model ages for analyses with and without exposure to HF overlap within analytical uncertainty and are shown graphically in Figure 3.2. In addition, one molybdenite mineral separate (i.e., CL100 3 weeks) was exposed to HF at room temperature for three weeks and possesses a Re-Os molybdenite model age that is indistinguishable to samples prepared using conventional mineral separation techniques. This suggests that HF at room temperature does not affect the Re-Os isotopic composition of

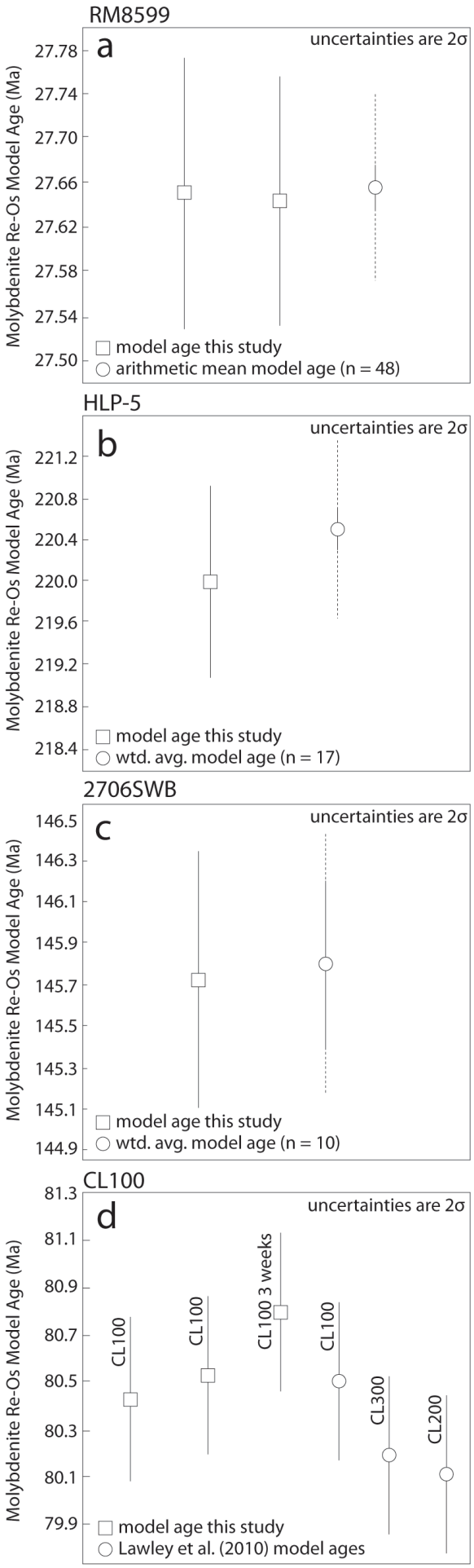

Figure 3.2 – (a) Molybdenite Re-Os model ages of RM8599 after exposure to HF and accepted age from Markey et al. (2007). Dotted error bars on arithmetic mean model age represents the typical uncertainty for an individual analysis; (b) molybdenite Re-Os model age of HLP-5 after exposure to HF and accepted age from Selby and Creaser (2004). Dotted error bars on the weighted average model age represent the typical uncertainty for an individual analysis; (c) molybdenite Re-Os model age of 2706SWB after exposure to HF and accepted age from Selby and Creaser (2004). Dotted error bars on the weighted average model age represents the typical uncertainty for an individual analysis; and (d) molybdenite Re-Os model ages of CL100 after exposure to HF and previously reported ages from Lawley et al. (2010).

molybdenite and that the proposed analytical protocol is suitable for isolating molybdenite from silicate enclosed molybdenite samples for Re-Os geochronology.

With exception to RM8599, the control samples (CL100, 2706SWB and HLP-5) possess ^{187}Re and ^{187}Os concentrations that are either slightly higher or significantly higher than previously reported values. However, any variation in ^{187}Re is coupled with ^{187}Os as all control samples yield Re-Os model ages that are in excellent agreement with previously reported ages. Interestingly, the analyses of sample CL100 reported in this study possess up to 7 ppm more ^{187}Re than the previously published analysis (Lawley et al., 2010), however, the sample left in the HF for 3 weeks gave values very similar to those for CL100 reported by Lawley et al. (2010).

Re and Os concentration variations such as this should be expected from analysing aliquants of natural molybdenite mineral separates and do not necessarily affect molybdenite Re-Os model ages (Selby and Creaser, 2004). HLP-5 is one such example where previous workers have reported a range of total Re (240–290 ppm) whereas molybdenite Re-Os model ages for these analyses all overlap within analytical uncertainty (Markey et al., 1998; Suzuki et al., 2001; Du et al., 2004; Selby and Creaser, 2004). The HLP-5 analysis treated by HF prior to the traditional Re-Os analytical protocol possesses 320 ppm total Re and 738 ppb ^{187}Os, thus possessing ~40 ppm more total Re and ~98 ppb ^{187}Os than reported by previous workers. However, as noted above this difference in Re-Os abundance is coupled as Re-Os model age identical to reported values determined for not only HLP-5, but all control samples. Previously,

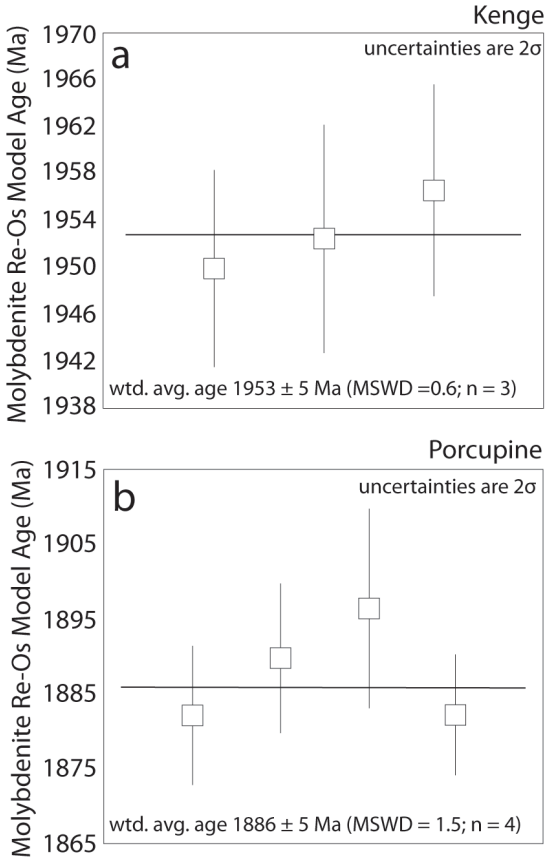

Figure 3.3 – (a) Molybdenite Re-Os model ages of ultra-fine molybdenite samples from the Kenge deposit. All three analyses provide a weighted average molybdenite Re-Os model age of 1953 ± 5 Ma (MSWD = 0.6; n =3); and (b) molybdenite Re-Os model ages of ultra-fine molybdenite samples from the Porcupine deposit. All four analyses provide a weighted average molybdenite Re-Os model age of 1886 ± 5 Ma (MSWD = 1.5; n = 4).

variations in Re and ^{187}Os abundance with repeat analysis was suggested to relate to the non-homogeneous nature of Re and ^{187}Os in molybdenite (Selby and Creaser, 2004). Alternatively, the variability of Re and Os abundances could relate to sample impurities within HLP-5. Atomic absorption inductively couple plasma-mass spectrometry (AA-ICP-MS) and inductively coupled-atomic emission spectrometry (ICP-AES) analyses suggest HLP-5 contains significant (>1% m/m) Ca, Pb, Fe and Al which are unexpected in a pure MoS_2 (molybdenite) mineral separate (Markey et al., 1998; Du et al., 2004). These additional elements could be present as mineral inclusions within molybdenite crystals or as free mineral phases that were incorporated into the molybdenite mineral separate during froth flotation. We consider the HF technique may have leached the sample and thus HLP-5 may contain higher Re and Os abundances than previously reported. This is supported by ICP-MS analyses of the HF used in the HF treatment of HLP-5, completed as part of this study, which measured approximately 10 ppm Ca, 10 ppm Pb, 6 ppm Fe, 5 ppm Al and 3 ppm K within the HF leachate. Our results suggest that HF dissolution removes HF soluble mineral phases within HLP-5 or incorporated with the mineral separate and that the proposed method is a better approximation to the true Re content of HLP-5.

3.5.2 Ultrafine molybdenite

Molybdenite from the Lupa goldfield is present as molybdenite coated fractures, mono-mineralic stringer veins and as ultrafine disseminations within quartz veins and the host granite. Conventional mineral separation techniques were unable to separate sufficient quantities of molybdenite due to the ultrafine grained nature of some molybdenite samples. The chemical separation technique developed here provided sufficient quantities (20–60 mg) of ultrafine molybdenite for Re-Os analysis. Three Re-Os molybdenite model ages from the Kenge deposit all overlap within uncertainty as exemplified from the low MSWD of the weighted average calculation (i.e., 1953 ± 5 Ma; MSWD = 0.6). The four Re-Os molybdenite model ages from the Porcupine deposit also overlap within error of each other but possess slightly more scatter resulting in a slightly higher MSWD (i.e., 1886 ± 5 Ma; MSWD = 1.5). Both ages are supported by Re-Os pyrite and U-Pb dating reported in and Chapters Two and Four.

3.5.3 Advantages of chemical mineral separation

Improved sample recovery is the greatest advantage of chemical mineral separation over conventional mineral separation techniques. High sample recovery is especially important for samples with low modal abundances of molybdenite and/or for small volume samples. In the case of ultrafine molybdenite, chemical mineral separation maintains high sample recovery regardless of crystal size. Neuerberg (1961) measured that sulfide abundance is two to three times greater for mineral separates prepared using chemical mineral separation techniques when compared to mineral separates prepared by heavy media methods. The proposed method would likely generate higher sample recoveries than Neuerberg (1961) because it requires less sample handling which is where the majority of fine grained sample material is lost.

Whole rock samples can also be digested, but typically require more time to digest and, depending on sample size, may require repeated applications of HF. The advantage of this approach is that molybdenite crystals are relatively undamaged when compared to mineral separates prepared using conventional techniques. Undamaged crystals are especially important for Re-Os molybdenite geochronology as Re and Os are susceptible to intra-grain decoupling (Stein et al., 2003). Selby and Creaser (2004) overcame Re-Os decoupling by increasing the analytical sample size utilised for Re-Os geochronology from a mineral separate. Larger sample sizes homogenize the sample and mask the decoupling in order to produce accurate and reproducible ages. Molybdenite mineral separates produced by chemical mineral separation provides another possible solution to Re-Os decoupling by preserving the original crystal morphology.

Another advantage of chemical mineral separation over conventional methods is the minimal time requirement. Once the samples are loaded with HF, no supervision is required during sample digestion. This differs from conventional techniques where constant supervision is required through the mineral separation process. Additional time savings are gained by the ability to digest multiple samples at the same time. As a result, the number of samples that can be prepared at one time with chemical mineral separation is only limited by the number of digestion vessels.

3.6 Conclusions

Conventional mineral separation techniques are not ideally suited for samples possessing fine grained molybdenite (< 50 μm) and thus hamper the application of Re-Os geochronology for such samples. In this contribution we have demonstrated:

- The Re and Os isotopic composition of molybdenite is unaffected by exposure to HF at room temperature and is thus capable of isolating ultrafine molybdenite for Re-Os geochronology.

- The chemical mineral separation protocol described above is advantageous for samples with low modal abundances of molybdenite and/or samples containing ultrafine molybdenite (e.g., <50μm).

- The proposed chemical mineral separation technique has produced six reproducible Re-Os molybdenite model ages from samples that were unsuitable for Re-Os analysis using traditional mineral separation techniques.

3.7 References

Ballard, J.R., Palin, J.M., Williams, I.S., Campbell, I.H., and Faunes, A., 2001, Two ages of porphyry intrusion resolved for the super-giant Chuquicamata copper deposit of northern Chile by ELA-ICP-MS and SHRIMP: Geology, v. 29, p. 383–386.

Barra, F., Ruiz, J., Mathur, R., and Titley, S., 2003, A Re-Os study of sulphide minerals from the Bagdad porphyry Cu-Mo deposit, northern Arizona, USA: Mineralium Deposita, v. 38, p. 585–596.

Bingen, B., and Stein, H., 2003, Molybdenite Re-Os dating of biotite dehydration melting in the Rogaland high-temperature granulites, S. Norway: Earth and Planetary Science Letters, v. 208, p. 181–195.

Bingen, B., Davis, W.J., Hamilton, M.A., Engvik, A.K., Stein, H.J., Skar, O., and Nordgulen, O., 2008, Geochronology of high-grade metamorphism in the Sveconorwegian nelt, S. Norway; U-Pb, Th-Pb, and Re-Os data: Norwegian Journal of Geology, v. 88, p. 12–42.

Brown, S.M., Fletcher, I.R., Stein, H.J., Snee, L.W., and Groves, D.I., 2002, Geochronological constraints on pre-, syn-, and postmineralization events at the world-class Cleo gold deposit, Eastern Goldfields Province, western Australia: Economic Geology, v. 97, p. 541–559.

Creaser, R.A., Papanastassiou, D.A., and Wasserburg, G.J., 1991, Negative thermal ion mass spectrometry of osmium, rhenium, and iridium: Geochimica et Cosmochimica Acta, v. 55, p. 396–401.

Daly, M.C., 1988, Crustal shear zone in central Africa; a kinematic approach to Proterozoic tectonics: Episodes, v. 11, p. 5–11.

Du, A., Wu, S., Sun, D., Wang, S., Qu, W., Markey, R., Stein, H., Morgan, J., and Malinovskiy, D., 2004, Preparation and certification of Re-Os dating reference materials; molybdenites HLP and JDC: Geostandards and Geoanalytical Research, v. 28, p. 41–52.

Ispolatov, V., Lafrance, B., Dubé, B., Creaser, R., and Hamilton, M., 2008, Geologic and structural setting of gold mineralization in the Kirkland Lake-Larder Lake gold belt, Ontario: Economic Geology, v. 103, p. 1309–1340.

Lawley, C.J.M., Richards, J.P., Andersen, R.G., Creaser, R.A., and Heaman, L.M., 2010, Geochronology and geochemistry of the MAX porphyry Mo deposit and its relationship to Pb-Zn-Ag mineralization, Kootenay Arc, southeastern British Columbia, Canada: Economic Geology, v. 105, p. 1113–1142.

Markey, R., Stein, H., and Morgan, J., 1998, Highly precise Re-Os dating for molybdenite using alkaline fusion and NTIMS: Talanta, v. 45, p. 935–946.

Markey, R., Stein, H.J., Hannah, J.L., Zimmerman, A., Selby, D., and Creaser, R.A., 2007, Standardizing Re-Os geochronology; A new molybdenite reference material (Hendersen, USA) and the stoichiometry of Os salts: Chemical Geology, v. 244, p. 74–87.

Mao, J.W., Xie, G.Q., Bierlin, F., Qu, W.J., Du, A.D., Ye, H.S., Pirajino, F., Li, H.M., Guo, B.J., Li, Y.F., and Yang, Z.Q., 2008, Tectonic implications from Re-Os dating of Mesozoic molybdenum deposits in the east Qinling-Dabie orogenic belt: Geochimica et Cosmochimica Acta, v. 72, p. 4607–4626.

Neuerburg, G.J., 1961, A method of mineral separation using hydrofluoric acid: The American Mineralogist, v. 46, p. 1498–1501.

Ootes, L., Lentz, D.R., Creaser, R.A., Ketchum, J.W.F., and Falck, H., 2007, Re-Os molybdenite

ages from the Archean Yellowknife greenstone belt comparison to U-Pb ages and evidence for metal introduction at similar to 2675 Ma: Economic Geology, v. 102, p. 511–518.

Porter, S.J., and Selby, D., 2010, Rhenium-Osmium (Re-Os) molybdenite systematics and geochronology of the Cruchan Granite skarn mineralization, Etive Complex; implications for emplacement chronology: Scottish Journal of Geology, v. 46, p. 17–21.

Selby, D., and Creaser, R.A., 2001, Re-Os geochronology and systematics in molybdenite from the Endako porphyry molybdenum deposit, British Columbia, Canada: Economic Geology, v. 96, p. 196–204.

Selby, D., Creaser, R.A., Hart, C.J.R., Rombach, C.S., Thompson, J.F.H., Smith, M.T., Bakke, A.A., Goldfarb, R.J., 2002, Absolute timing of sulfide and gold mineralization; a comparison of Re-Os molybdenite and Ar-Ar mica methods from the Tintina Gold Belt, Alaska: Geology, v. 30, p. 791–794.

Selby, D., and Creaser, R.A., 2004, Macroscale NTIMS and microscale LA-MC-ICP-MS Re-Os isotopic analysis of molybdenite; Testing spatial restrictions for reliable Re-Os age determinations, and implications for the decoupling of Re and Os within molybdenite: Geochimica et Cosmochimica Acta, v. 68, p. 3897–3908.

Selby, D., Creaser, R.A., Stein, H.J., Markey, R.J., and Hannah, J.L., 2007, Assessment of the ^{187}Re decay constant by cross calibration of Re-Os molybdenite and U-Pb zircon chronometers in magmatic ore systems: Geochimica et Cosmochimica Acta, v. 71, p. 1999–2013.

Smoliar, M.I., Walker, R.J., and Morgan, J.W., 1996, Re-Os ages of group IIA, IIIA, IVA, and IVB iron meterorites: Science, v. 271, p. 1099–1102.

Stein, H.J., Markey, R.J., Morgan, J.W., Du, A., and Sun, Y., 1997, Highly precise and accurate Re-Os ages for molybdenite from the East Qinlin molybdenum belt, Shaanxi Province, China: Economic Geology, v. 92, p. 827–835.

Stein, H.J., Sundbland, K., Markey, R.J., Morgan, J.W., and Motuza, G., 1998; Re-Os ages for Archean molybdenite and pyrite, Kuittila-Kivisuo, Finland and Proterozoic molybdenite, Kabeliai, Lithuania; testing the chronometer in a metamorphic and metasomatic setting: Mineralium Deposita, v. 33, p. 329–345.

Stein, H.J., Markey, R.J., Morgan, J.W., Hannah, J.L., and Acherstén, A., 2001, The remarkable Re-Os chronometer in molybdenite; how and why it works: Terra Nova, v. 13, p. 479–486.

Stein, H., Schersten, A., Hannah, J., Markey, R., 2003, Subgrain-scale decoupling of Re and Os-187 and assessment of laser ablation ICP-MS spot dating in molybdenite: Geochimica et Cosmochimica Acta, v. 67, p. 3673–3686.

Stevenson, J.S., 1940, Molybdenum deposits of British Columbia: Bulletin of the British Columbia Department of Mines, v. 9, 96 p.

Suzuki, K., Feely, M., and O'Reilly, 2001, Disturbance of the Re-Os chronometer of molybdenites from the late-Caledonian Galway granite, Ireland, by hydrothermal fluid circulation: Geochemical Journal, v. 35, p. 29–35.

Takahashi, Y., Uruga, T., Suzuki, K., Tanida, H., Terada, Y., and Hattori, K.H., 2007, An atomic

level study of rhenium and radiogenic osmium in molybdenite: v. 71, p. 5180–5190.

Völkening, J., Walczyk, T., and Heumann, K.G., 1991, Osmium isotope ratio determinations by negative thermal ionization mass spectrometry: International Journal of Mass Spectrometry and Ion Processes, v. 105, p. 147–159.

– Chapter Four –

Re-Os Molybdenite, Pyrite and Chalcopyrite Geochronology, Lupa Goldfield, SW Tanzania: Tracing Hydrothermal Fluid System Connectivity and Metallogenic Time Scales at Mid-Crustal Shear Zones Hosting Orogenic Au Deposits

Chapter Four is submitted to the journal Economic Geology

Collaborators: David Selby[1] and Jonathan Imber[1]
[1]Department of Earth Sciences, Durham University, Durham, DH1 3LE, UK

4.1 Introduction

The dearth of geochronologic constraints on the absolute timing of Au mineralization is a limiting factor in our understanding of the orogenic Au deposit model (Groves et al., 2003). Constraining the absolute age(s) of Au mineralization is especially important in ancient poly-deformed metamorphic belts that host the largest examples of this deposit type (Groves et al., 1998; Goldfarb et al., 2001). In these complex geologic settings, spatially overprinting tectono-thermal events are characteristic and identifying the causal relationship between Au mineralization and other geologic processes is generally equivocal in the absence of precise geochronologic constraints. The scarcity of suitable minerals required for traditional geochronologic methods at most orogenic Au deposits has led previous studies to constrain the timing of Au mineralization using U-Pb zircon dating of cross cutting dikes (e.g., Kerrich and Cassidy, 1994). Re-Os geochronology provides a possible alternative to this approach by directly dating sulfide minerals present within the Au-bearing veins and shear zones. Most previous Re-Os studies utilize molybdenite and/or arsenopyrite geochronometers, which are now well-established geochronologic tools that are known to provide robust age determinations up to amphibolite facies metamorphic conditions (e.g., Stein et al., 1998; Bingen and Stein, 2003; Morelli et al., 2010). The utility of Re-Os pyrite and chalcopyrite geochronology have also been tested at a variety of epigenetic deposits and are shown to provide robust age determinations up to upper greenschist facies metamorphism (e.g., Du et al., 1993; Stein et al., 2000; Barra et al., 2003; Morelli et al., 2005; Feng et al., 2009; Selby et al., 2009; Scherstén et al., 2012). In contrast, very few Re-Os pyrite and chalcopyrite studies have investigated the timing of mineralization at orogenic Au deposits despite the abundance of these minerals and their inferred co-genetic relationship with Au at this deposit type (for exceptions see Arne et al., 2001; Bjerkgard et al.,

2009; Ootes et al., 2011).

Orogenic Au deposits are hosted by networks of greenschist facies brittle-ductile mylonitic shear zones and provide an excellent opportunity to study mid-crustal hydrothermal plumbing systems (Groves et al., 1993). The architecture of hydrothermal systems is poorly understood at most orogenic Au deposits and has important implications for mineral exploration efforts for this deposit type (Groves et al., 2003). In this study, we investigate sulfides from distinct paragenetic vein sets at five ore bodies hosted by shear zones of disparate geometry and strike lengths in order to investigate the connectivity of the shear zone-related hydrothermal system (Oliver, 2001). Understanding fluid connectivity in the mid-crust is important because the steeply dipping attitude and long strike length of the Au-bearing structures suggests that shear zones possess a considerable vertical extent (10s of km; Hammer et al., 2010) and may play a key role in transporting hydrothermal fluids from deep crustal levels to the upper crust where other economic ore deposits may develop (e.g., Hronsky, 2012). The time scale(s) of hydrothermal processes at crustal-scale faults also have important implications for the rheology and long-term weakening of crustal-scale faults (e.g., Jeffries et al., 2006).

Here we present a detailed Re-Os molybdenite, pyrite and chalcopyrite geochronologic study that places new constraints on the timing and time scale(s) of Au mineralization at orogenic Au-type mineral systems from the Lupa goldfield, SW Tanzania. Our Re-Os results demonstrate that mineralization and brittle-ductile deformation occurred contemporaneously within analytical uncertainty, but episodically over ca. 70 Myr and that second- and third-order Au-bearing structures (second order shear zones possess strike lengths ≥ 10 km, whereas third order structures possess strike lengths < 10 km) formed a connected hydrothermal fluid system in the crust during the Paleoproterozoic.

4.2 Geologic setting

4.2.1 Ubendian geology

The Paleoproterozoic Ubendian Belt is a granulite-greenschist facies metamorphic belt that mantles the western margin of the Tanzanian Craton (Grantham 1931, 1932, 1932; Teale et al., 1935; Harris, 1961; Fig. 4.1). Current tectonic models divide the Ubendian Belt into eight litho-tectonic terranes (Ubende, Wakole, Katuma, Ufipa, Mbozi, Lupa, Upangwa and Nyika), which resulted from a series of tectono-thermal events spanning ca. 300 Myr (Daly, 1988). The earliest Ubendian tectonic phase (2.1–2.0 Ga) culminated in eclogite-granulite facies metamorphism and the development of an east-west trending tectonic fabric (Lenoir et al., 1994). The 2.1–2.0 Ga tectonic phase is overprinted by the 1.9–1.8 Ga Ubendian tectonic phase, which produced northwest-southeast trending terrane-bounding shear zones, amphibolite facies metamorphism and preserved ca. 1.9 Ga eclogites with MORB-like chemistry (Lenoir et al., 1994; Theunissen et al., 1996; Boniface et al., 2012). The latter represent Paleoproterozoic suture zones and record some of Earth's earliest evidence for high pressure and low temperature metamorphism that is analogous to metamorphic conditions at modern-day subduction zones (Boniface et al., 2012). Paleoproterozoic metamorphism has been overprinted by Meso- and Neoproterozoic

metamorphic events that are correlated to the Kibaran (1.4–1.0 Ga) and Pan-African (650–450 Ma) orogenic cycles, respectively (Hanson, 2003; Boniface, 2009; Boniface et al., 2012; Boniface ad Schenk, 2012). The trend of the western branch of the East African Rift System parallels the trend of the Ubendian basement and suggests periodic reactivation of Ubendian structures has occurred from the Paleoproterozoic until the present day (Kilembe and Rosendahl, 1992; Theunissen et al., 1996).

4.2.2 Lupa goldfield geology

The Lupa goldfield is a triangular shaped block bound by the Rukwa Escarpment to the west, the Usangu Escarpment to the east and the Mkondo magnetic lineament to the north (Kilembe and Rosendahl, 1992; Marobhe, 1989). The field area for the current study is located in the western portion of the Lupa and corresponds with the mineral licenses currently controlled by Helio Resources Corp. (Fig. 4.2). All rocks within the field area have undergone hydrothermal alteration and greenschist facies metamorphism. Thus, all rock names are metamorphic and for the remaining discussion all igneous rock names should have the prefix "meta-". Archean foliated granites (ca. 2750 Ma) are intruded by non-foliated and voluminous Paleoproterozoic (ca. 1960–1920 Ma) granitoids and dioritic-gabbroic intrusions (Chapter Two). U-Pb ages constrain three, temporally distinct, deformation events that have been defined on the basis of observed field relationships (D1, D2 and D3; the characteristics of each are summarized in Table 4.1).

4.2.3 Au occurrence geology

The geology and mineral exploration history of the Lupa goldfield is described by Gallagher (1939, 1941), Van Straaten, (1984), Sango (1988) and Kuehn et al. (1990). Gold was

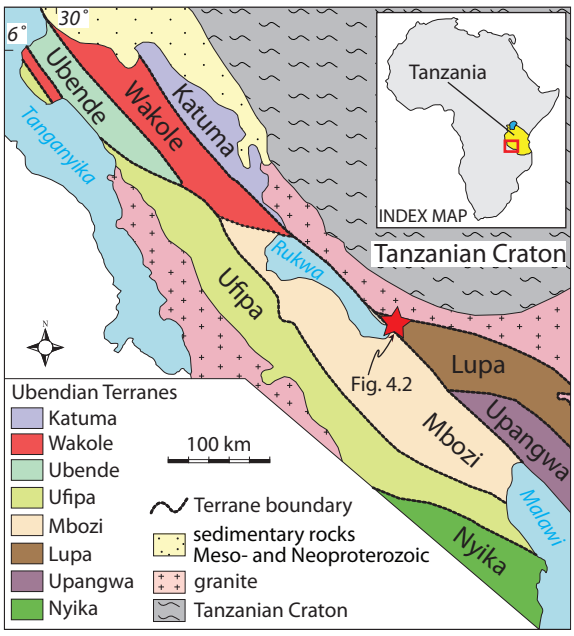

Figure 4.1 – Regional geology map of SW Tanzania showing Ubendian Terranes and the field area for the current study (modified from Daly, 1988).

first discovered in 1922 and led to the development of commercial mine workings along the Saza shear zone and near what are formerly known as Razorback and Saza mines (Chapter Five; Gallagher 1939). Production declined after the 1950s once an estimated 25,000 kg of Au had been extracted (Kuehn et al., 1990). Lupa goldfield production figures are likely an underestimate of total Au production as artisanal workers continue to extract small quantities of Au in alluvial and lode-workings (Fig. 4.2). The geology and Au occurrences of the Lupa goldfield are currently the subject of renewed interest due to mineral exploration success in the western portion of the goldfield by Helio Resource Corp. (Simpson, 2012). Five mineral exploration targets were investigated as part of this study for Re-Os sulfide geochronology: Kenge, Mbenge, Konokono, Porcupine and Dubwana. These Au occurrences are representative of the geology observed at a large number of artisanal workings (Fig. 4.2).

Kenge and Mbenge - Kenge is hosted by a ca. 2 km long and ca. 20 m wide (up to 40 m wide), northwest-southeast trending (120º; Right Hand Rule; RHR), steeply-dipping (70º) and left-stepping shear zone. The Mbenge ore body is located adjacent to the Kenge shear zone and is hosted by an E-W trending (089º; RHR) and S dipping (70º) shear zone that shares many geologic similarities with Kenge. A NI-43-101 compliant resource (National Instrument 43-101 is the mineral resource classification scheme used by companies listed on a Canadian stock exchange) of Kenge, Mbenge and other nearby exploration targets includes a measured and indicated resource of 370,000 oz of contained Au (8.7 Mt at 1.33 g/t Au using a 0.5 g/t Au cut-off; Simpson, 2012). Foliated Archean granite (ca. 2740 Ma) is the dominant hangingwall lithology and a non-foliated dioritic-gabbroic intrusion/dike(?) is the dominant footwall lithology (suspected to be Paleoproterozoic based on U-Pb zircon dating of a cross cutting granodiorite dike CL0911; Chapter Two). Proximal to the shear zone boundary, hangingwall and

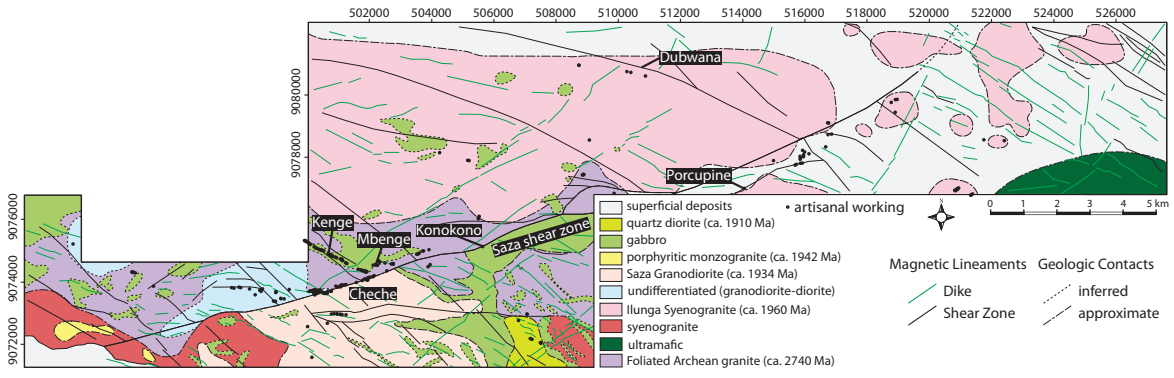

Figure 4.2 – Simplified local geology map showing the location of Kenge, Mbenge, Konokono, Porcupine and Dubwana exploration targets. Artisanal workings visited during field seasons in 2010 and 2011 are also shown (closed circles) and do not include alluvial workings, which are present in the majority of rivers in the field area. Eastings and northings are reported as UTM coordinates (WGS84, Zone 36S). Approximate lithologic contacts are based on a series of river traverses by the first author. Inferred lithologic contacts are based on unpublished aeromagnetic and radiometric surveys acquired from Helio Resource Corp. Shear zone locations are based, in part, on mapping and correspond to negative magnetic anomalies, whereas dikes are buried and interpreted from linear magnetic highs.

footwall rocks become veined (quartz ± calcite ± chlorite ± pyrite veins), intensely chloritized (± epidote) and possess a fracture cleavage that is oriented sub-parallel to the shear zone margins. However, the majority of strain, hydrothermal alteration and Au-mineralization are confined to the Kenge shear zone. Hydrothermal alteration related to mylonitization (chlorite ± muscovite ± calcite ± epidote ± quartz ± pyrite) overprints feldspar sericitization and silicification of the Archean granite, which in turn overprints a hematite-magnetite alteration assemblage. Thus, Kenge host rocks are suspected to have undergone a series of hydrothermal alteration events that may have played a role in rheologically weakening the wall rock by replacement of feldspar with structurally weaker phyllosilicates, which in turn localized strain and triggered crystal plastic and fluid-assisted diffusion deformation processes (Chapter Five). The Kenge mylonitic shear zone is partially filled with a thick (locally 10 m wide), laminated, deformed and Au-bearing quartz vein (fault-fill quartz vein; Robert and Poulsen, 2001). Fragments of mylonititzed granite are observed within the fault-fill veins and undulating pyrite ± molybdenite veins (stylolite-like veins) locally gives the fault-fill veins a laminated appearance. The saw-tooth pattern of the sulfide veins is generally oriented sub-parallel to the steeply-dipping fault-fill vein margins and suggests stress-induced solution transfer may have been an important mineralizing process during sub-horizontal shortening (see below). Fault-fill veins also possess quartz slickensides on vein-mylonite contacts and complex fracture patterns. All of the observed fault-fill vein fabrics are indicative of a complex vein history and are typical of the fault-fill vein type (Robert and Poulsen, 2001). Kinematic indictors at Kenge and Mbenge (asymmetric porphyroclasts and S/C fabrics) are consistent with transpressional deformation and record reverse oblique movement (south-side up; Chapter Five). The ore zone is inferred to have been subsequently offset by a northwest-trending and moderately dipping reverse fault. The timing of this later deformation is currently unconstrained (Table 4.1).

Porcupine - Porcupine is hosted by a 300 m long and 50 m (up to 90 m) wide band of hydrothermally altered, veined and locally strained Paleoproterozoic Ilunga Syenogranite (ca. 1960 Ma; Chapter Five). A NI-43-101 compliant resource of the currently explored Porcupine

Table 4.1 - Structural framework

Event	Timing	Characteristics
D1	2740 to 1960 Ma[1]	Foliated Archean granitoids; foliation varies in development at the outcrop scale; generally E-W to WNW-ESE trending and steeply dipping; chlorite-rich bands alternate with quartzofeldspathic bands; no high-grade minerals; crystal plastically deformed quartz; greenschist facies metamorphism suspected based on metamorphic mineral assemblage and temperature-pressure limits of quartz plasticity
D2	ca. 1885 Ma[2]	Brittle-ductile and greenschist facies mylonitic shear zones cross cut all magmatic phases; main ore event; generally NW-SE and E-W trending and steeply dipping; all rocks in the field area have undergone greenschist facies metamorphism; replacement of Fe-Mg minerals with chlorite ± muscovite ± epidote ± calcite ± titanite
D3	1885 Ma to present[3]	Brittle fault offsets Kenge ore body; brittle faults offset mineralized veins; unconsolidated fault gouge

[1]Chapter Two
[2]this study
[3]Theunissen et al., 1996; this study

and peripheral ore bodies includes a measured and indicated resource of 650,000 oz of contained Au (15.4 Mt at 1.31 g/t Au; Simpson, 2012). Whilst the vast majority of hydrothermal alteration and strain is restricted to mylonitic shear zones (059º / 64º; RHR), significant Au-mineralization is also associated with hydrothermally altered but unstrained Ilunga Syenogranite proximal to the shear zones and associated quartz veins. These quartz veins possess variable strikes, are moderately to shallowly dipping and are interpreted as oblique-extension veins (Robert and Poulsen, 2001). The flat orientation and the relatively undeformed nature of the veins are in contrast with the sheared and sub-vertical attitude of fault-fill veins (Robert and Poulsen, 2001). The Ilunga Syenogranite has been overprinted by a quartz ± muscovite ± calcite ± pyrite alteration assemblage that forms at the margins of Au-bearing quartz veins and overprints an earlier hematite ± magnetite alteration assemblage. Both hydrothermal alteration mineral assemblages are in turn overprinted by hydrothermal alteration related to the greenschist-facies mylonitic shear zones (chlorite ± muscovite ± calcite ± epidote ± pyrite). Kinematic indicators (asymmetric porphyroclasts and S/C fabrics) suggest reverse oblique movement along the shear zones hosting the Porcupine ore body (Chapter Five).

Konokono and Dubwana – Konokono and Dubwana are the least understood of the five exploration targets. The main Au-bearing shear zone at Konokono parallels the Saza shear zone, trends ENE-WSW (075º; RHR) and dips steeply to the SE (70º). Archean granite is the dominant host rock and is cross cut by Au-bearing greenschist facies mylonitic shear zones. Quartz veins are another important host for Au at Konokono and possess a similar appearance and flat geometry to oblique-extension veins described at Porcupine. Dubwana is hosted by a major NW-SE trending shear zone cross cutting the Ilunga Syenogranite. Very little information is currently available for this exploration target other than five diamond drill holes that intersected hydrothermally altered and veined Ilunga Syenogranite hosting significant Au grade (e.g., 1 meter at 66 g/t Au) and located adjacent to a major NW-SE trending shear zone (strike length > 20 km). The currently understood geologic history of Konokono and Dubwana possess many similarities with the Kenge, Porcupine and a large number of Au occurrences across the field area.

4.2.3 Sulfiide and Au paragenesis

The sulfide mineralogy at Au occurrences in the Lupa goldfield is relatively simple and consists of pyrite with accessory chalcopyrite, molybdenite, galena, covellite, chalcocite and sphalerite (Gallagher, 1941; Simpson, 2012; this study). Pyrite is intergrown with chalcopyrite and molybdenite at Kenge and Porcupine and suggest that all three minerals may have been deposited during the same mineralization event. However, the genetic significance of sulfide intergrowths is tentative, as auriferous veins locally possess complex cross cutting relationships that imply multiple hydrothermal and metallogenic events. Fault-fill veins at Kenge and Porcupine record exceptionally complex vein histories characterized by repeated crack-seal textures, poly-modal vein fractures and cross cutting fluid inclusion trails. Complex relationships between fault-fill vein development and deformation is also inferred from mylonitized wall rock

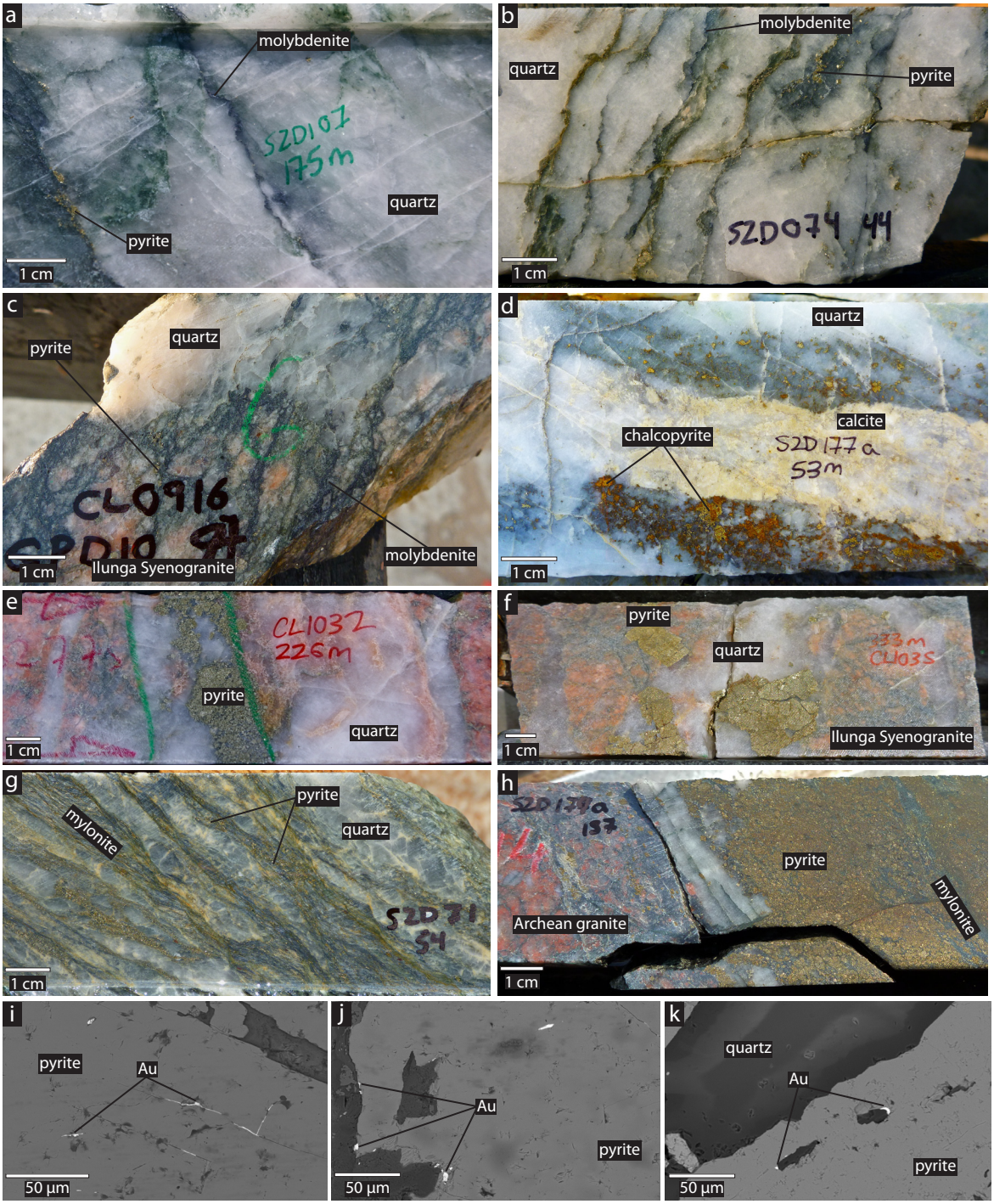

Figure 4.3 – (a) molybdenite stylolite-like vein hosted by fault-fill vein at Mbenge; (b) pyrite and molybdenite stylolite-like veins within fault-fill veins at Mbenge; (c) molybdenite hosted by sheared Ilunga Syenogranite at Porcupine; (d) complex vein relationships at Konokono showing chalcopyrite-bearing quartz vein (with vein margins not shown) cross cut by unmineralized quartz-calcite vein. Narrow quartz-calcite veins are observed extending from the wider quartz-calcite vein at high-angles; (e) pyrite hosted by quartz veins in hydrothermally altered Ilunga Syenogranite at Porcupine; (f) pyrite hosted by quartz vein in hydrothermally altered Ilunga Syenogranite that is paragenetically similar to Fig. 4.2e, but records anomalously younger ages; (g) pyrite hosted by sulfidized mylonitic shear zone at Kenge; (h) pyrite hosted by sulfidized mylonitic shear zone, quartz vein, and Archean granite wall rock at Konokono; (i) scanning electron microscope (SEM) images of Au observed as pyrite inclusions and fracture fills (SZD23 at 107 m); (j) scanning electron microscope (SEM) images of Au observed on the margins and as inclusions within pyrite (SZD23 at 107 m); (k) scanning electron microscope (SEM) images of Au observed as pyrite inclusions (SZD71 at 53 m).

fragments intercalated with fault-fill veins (Fig. 4.3g) and slickensides on fault-fill vein contacts. The geologic and metallogenic history of fault-fill veins is thus expected to be complex, but the absolute time scale(s) of fault-fill vein development are poorly understood. Oblique-extension veins at Porcupine and Konokono are expected to possess comparatively simple geologic histories inferred from the absence of complex vein textures (Fig. 4.3f). Quartz veining, hydrothermal alteration and deformation are interpreted as broadly contemporaneous at most orogenic Au deposits based on mutually cross-cutting field relationships, whereas the absolute temporal relationships between different vein styles have not been addressed (Hodgson, 1989; Robert and Poulsen, 2001). Distinguishing superficially similar sulfide generations in veins with complex hydrothermal histories is a continuing challenge at many orogenic Au deposits. Here we attempt to address this problem and quantify the time scale(s) of hydrothermal events by sampling a variety of sulfide minerals from different vein types at five Au occurrences.

Gold is present as native Au, Au-bearing tellurides and electrum (Simpson, 2012). The majority of Au-bearing minerals observed in thin sections prepared for this study occur as pyrite inclusions, pyrite fracture-fills and free Au. Our results are also consistent with previous petrographic studies (Simpson, 2012). Native Au inclusions within pyrite points to a co-genetic relationship between the two minerals, whereas the association of Au in pyrite fracture fills and pyrite grain boundaries may suggest Au at least locally post-dates pyrite deposition (Fig. 4.3i–k). The micro-scale association of Au and pyrite is partly supported by Helio Resources Corp.'s assay results, which suggest that the highest Au grades are associated with sulfidized mylonitic shear zones and quartz veins. As a result, pyrite and Au are considered to be at least locally co-genetic and Re-Os pyrite ages thus represent the best possible proxy to constrain the timing of Au deposition (the paragenetic relationship between Au and Re-Os geochronometers is discussed further below).

4.3 Sampling

4.3.1 Kenge and Mbenge

Molybdenite at the Kenge ore body is present as ultrafine (<50 μm) disseminations, undulating molybdenite veins (stylolite-like veins) hosted by fault-fill veins (Figs. 4.3a, b) and molybdenite coated fracture surfaces. The latter are interpreted as molybdenite veins that were reactivated as slip surfaces during later deformation. Three samples of ultrafine disseminated molybdenite and six samples of molybdenite from stylolite-like veins were analyzed. None of the thin sections prepared for molybdenite-bearing veins contained Au and the genetic relationship between Au and molybdenite remains unclear. However, the molybenite-rich zone at Kenge corresponds with high Au grades and implies at least a spatial association between the two minerals. Pyrite is present as disseminations within mylonitic shear zones, stylolite-like veins within fault fill veins and disseminations within the hangingwall and footwall rocks. Six samples of pyrite from mylonitic shear zones and six samples of pyrite from fault-fill veins were analyzed. Pyrite hosted by mylonitic shear zones occurs as fine to medium grained (<250–5000 μm) disseminations and are generally finer grained than pyrite samples hosted by fault-fill veins

(0.5–10 mm; Fig. 4.3f). Fine-grained native Au inclusions (<10–100 μm) hosted by pyrite grains from mylonite samples signifies a co-genetic relationship between the two minerals for this sample set. Furthermore, the highest Au grades are associated with mineralized stylolite-like veins hosted by fault-fill veins and suggest Re-Os pyrite geochronology provides the timing of Au mineralization in stylolite-like veins at Kenge.

4.3.2 Porcupine

Molybdenite at the Porcupine ore body is present as stringer veins within the sheared Ilunga Syenogranite, as ultrafine disseminations (<50 μm) within quartz veins and as coatings on fracture surfaces. The latter are interpreted as molybdenite vein surfaces that may have been reactivated during subsequent deformation. Molybdenite and Au were not observed in the same thin section, but the highest Au grades at Porcupine are also associated with molybdenite-rich zones and suggest that Au mineralization was accompanied with molybdenite deposition. Pyrite is present as disseminations within mylonitic shear zones, stylolite-like veins within fault fill veins and disseminations within hydrothermally altered Ilunga Syenogranite. Four pyrite samples hosted by oblique-extension veins were analyzed from Porcupine. Pyrite crystals from these samples occur as fine to medium grained (<250–1000 μm) disseminations forming aggregates and coarse-grained cubic disseminations (1–30 mm; Fig. 4.3d, e). Oblique-extension veins are associated with high-Au grades and act to significantly widen the mineralized zone at Porcupine. The association between Au grade and sulphidized quartz veins indicates pyrite is a suitable proxy to constrain the timing of Au mineralization at Porcupine.

4.3.3 Konokono and Dubwana

No molybdenite was observed in the exploration drill core at Konokono or Dubwana. Pyrite is present as disseminations within quartz veins, mylonitic shear zones and within the hydrothermally altered wall rocks. At Konokono, one pyrite sample and one sample of chalcopyrite were collected from quartz veins, plus three pyrite samples were collected from the mylonitic shear zone and hydrothermally altered Archean granite. Grain size for all five samples ranged from <250–10,000 μm and pyrite samples are considered the best possible proxy to constrain the timing of Au at Konokono. The Dubwana pyrite sample was collected from a 3 cm wide pyrite aggregate hosted by hydrothermally altered Ilunga Syenogranite. The relationship between Au and pyrite is unclear at Dubwana due to limited drilling at this early-stage exploration target and the absence of Au in the thin section prepared for this sample. The geology is very similar to the other shear-hosted deposits in the field area and pyrite is expected to represent a suitable proxy for the timing of Au.

4.4 Re-Os methodology

Re-Os analyses were conducted at the TOTAL laboratory for source rock geochronology and chemistry in the Northern Centre for Isotope and Element Tracing (NCIET) at Durham University. Re-Os pyrite and chalcopyrite analyses followed the analytical protocol of Selby

et al., (2009), whereas Re-Os molybdenite analyses followed the analytical protocol of Porter and Selby (2010). Molybdenite, pyrite and chalcopyrite samples (with exception of ultrafine molybdenite samples) were prepared via traditional mineral separation methods (crushing, pulverizing in a ceramic disc mill, Frantz isodynamic separator, heavy liquids and hand-picking). Ultrafine molybdenite samples (CL1115–CL1120) were separated using a novel HF acid chemical separation technique (Chapter Three). HF was used to dissolve silicate minerals encasing the ultrafine molybdenite at room temperature and is demonstrated not to affect the Re-Os molybdenite systematics (Chapter Three).

Mineral separates were weighed, spiked with a Re-Os tracer solution and loaded into Carius tubes (Shirey and Walker, 1995). The Re-Os tracer solution used for molybdenite samples contains a known ^{185}Re and isotopically normal Os composition and abundance. The majority of pyrite and chalcopyrite samples were equilibrated with a different Re-Os tracer solution that contains a known ^{185}Re and ^{190}Os composition and abundance. Selected pyrite samples that contain insignificant common Os were also analyzed with the ^{185}Re and isotopically normal Os tracer solution in order to test the suitability of Re-Os pyrite model ages (discussed further below). Samples and tracer solution were digested in 11N HCl (1 mL for molybdenite; 3 mL for pyrite and chalcopyrite) and 15.5N HNO_3 (3mL for molybdenite; 8 mL for pyrite and chalcopyrite) in a sealed Carius tube at 220°C for 24 hours. Osmium was purified from the acid medium using solvent extraction ($CHCl_3$) at room temperature and micro-distillation methods. The rhenium fraction was isolated using standard anion column chromatography. For pyrite and chalcopyrite samples, the rhenium fraction was further purified by single-bead chromatography. Rhenium and osmium were then loaded onto nickel and platinum filaments, respectively. Analyses were conducted on a Thermo Electron TRITON mass spectrometer with the Re isotopic composition measured using static Faraday collection mode. Osmium isotopic compositions of molybdenite samples were also measured in static Faraday collection, whereas osmium isotopic compositions of pyrite and chalcopyrite samples were measured in peak-hoping mode using the secondary electron multiplier.

Analytical uncertainties are propagated and incorporate uncertainties related to Re and Os mass spectrometer measurements, isotopic composition and abundance of the blank, spike calibrations, reproducibility of standard Re and Os isotope values, decay constant uncertainty (1.666×10^{-11} year^{-1}; Smoliar et al., 1996) and are reported at the 2σ level. During the course of this study Re and Os blanks were <4 and 1 pg, respectively, with the blank ^{187}Os/^{188}Os ratio measured at 0.25 ± 0.02 (n = 4). Standard solutions of Re and Os were analyzed during each analytical session in order to monitor long-term mass spectrometry reproducibility. The Re standard comprises 99.999% zone-refined Re ribbon, whereas the Os standard used in this study was the Durham Romil Osmium Standard (DROsS). The Os standard measurements recorded in this study (e.g., ^{187}Os/^{188}Os = 0.16102 ± 0.00039 2SD; n = 15) are identical to the long-term average ^{187}Os/^{188}Os = 0.16095 (± 0.00097 2SD; n = 172). The Re standard measurements recorded in this study (e.g., ^{185}Re/^{187}Re = 0.59697 ± 0.00216 2SD; n = 19) are similar with uncertainty to the long-term Re standard average ^{185}Re/^{187}Re = 0.59811 (± 0.00296 2SD; n =

256). Furthermore, Re-Os model ages of molybdenite reference materials (NIST RM8599 = 27.6 ± 0.1 and 27.6 ± 0.1 Ma; HLP-5 = 220.0 ± 0.9 Ma) analyzed during the course of this study are in good agreement with their accepted values (Porter and Selby 2010 and references therein). All isochron and weighted average model ages were calculated using Isoplot v. 4.15 (Ludwig, 2008).

4.5 Re-Os results

4.5.1 Re-Os molybdenite results

Kenge molybdenite - Ten analyses of nine samples from Kenge are reported in Table 4.2 and Fig. 4.4. We note that the Re-Os data for the ultrafine molybdenite have previous been reported (Chapter Three); however their geological significance has not been discussed. All molybdenite samples possess a range of ^{187}Re and ^{187}Os abundances of 4,653–58,018 and 154–1,896 ppb, respectively. Calculated Re-Os molybdenite model ages range from 1957–1937 Ma with the oldest and youngest ages corresponding to ultrafine disseminated and stylolite-like vein molybdenite samples, respectively. Individual analytical uncertainties on Re-Os model ages range from 10–14 Ma (including decay constant uncertainty; Smoliar et al., 1996; Selby et al., 2007) and thus the oldest and youngest ages partially overlap within analytical uncertainty. Ultrafine disseminated molybdenite yields a weighted average Re-Os molybdenite model age of 1953 ± 6 Ma (MSWD = 0.4; n = 3; Fig. 4.4a) that is in good agreement with a three-point ^{187}Re vs. ^{187}Os Model 1 York regression isochron age for the same sample set at 1965 ± 25 Ma (± 27 including the uncertainty in λ; initial ^{187}Os = -1.2 ± 2.4 ppb; MSWD = 0.01; n = 3; Fig. 4.4b). Molybdenite samples hosted by stylolite-like veins possess slightly younger ages and yield a weighted average

Table 4.2 - Re-Os Molybdenite Data

Sample	Target	DH / Depth (m)	Paragenesis	sample wt. (g)	Re (ppm)	±	^{187}Re (ppb)	±	^{187}Os (ppb)	±	Model Age (Ma)[1]	± (Ma)
CL091	Kenge	Kenge pit	stylolite	0.008	92.31	0.57	58018	359	1896.11	11.06	1930	10
CL0920	Kenge	SZD71 / 65	stylolite	0.014	30.22	0.13	18994	84	623.41	2.49	1938	10
SZMO1	Kenge	SZD23 / 110	stylolite	0.005	10.16	0.09	6384	59	209.24	1.90	1936	14
SZMO2 F1	Kenge	SZD24 / 150	stylolite	0.022	46.39	0.18	29160	111	956.82	2.96	1938	10
SZMO2 F2				0.031	30.33	0.10	19063	66	625.28	1.76	1937	10
SZMO2b	Kenge	SZD24 / 151	stylolite	0.020	82.07	0.31	51581	193	1693.22	5.39	1939	10
SZMO2-drill	Kenge	SZD24 / 150	stylolite	0.030	31.22	0.11	19624	69	643.87	1.82	1938	10
CL1115	Kenge	SZD71 / 66	ultrafine	0.022	7.40	0.03	4653	18	153.65	0.50	1950	10
CL1116	Kenge	SZD71 / 65	ultrafine	0.015	8.55	0.04	5373	25	177.64	0.75	1952	12
CL1117	Kenge	Kenge pit	ultrafine	0.023	13.35	0.06	8391	36	278.02	0.85	1957	11
CL0916	Porcupine	GPD18a / 140	sheared granite	0.018	7.56	0.03	4753	20	150.91	0.52	1876	10
CL103	Porcupine	GPD1 / 54	sheared granite	0.102	0.48	0.00	303	2	9.60	0.04	1870	14
CL1038 F1	Porcupine	GPD18a / 154	stylolite	0.021	1.92	0.01	1205	6	38.13	0.13	1870	12
CL1038 F2				0.018	1.73	0.01	1088	8	34.49	0.23	1874	18
CL1039	Porcupine	GPD18a / 162	stylolite	0.021	3.37	0.01	2119	9	67.32	0.23	1877	11
CL1042	Porcupine	GPD10 / 99	altered granite	0.021	10.79	0.04	6780	26	214.41	0.69	1869	10
CL1118 F1	Porcupine	GPD18a / 141	ultrafine	0.023	1.96	0.01	1232	5	39.26	0.13	1882	11
CL1118 F2				0.019	1.72	0.01	1084	5	34.66	0.13	1890	12
CL1119	Porcupine	GPD18a / 163	ultrafine	0.020	3.35	0.02	2108	12	67.65	0.35	1896	15
CL1120	Porcupine	GPD10 / 100	ultrafine	0.020	10.29	0.04	6469	25	206.09	0.68	1882	10

[1] Model age calculated from the simplified isotope equation [$t = \ln(^{187}Os/^{187}Re + 1)/\lambda$; where t = model age, and $\lambda = ^{187}$Re decay constant] and assumes no initial radiogenic Os

N.B. uncertainties are reported at the 2σ level

Re-Os molybdenite model age at 1937 ± 4 Ma (MSWD = 0.3; n = 7; Fig. 4.4a). This weighted average age is in good agreement with a ^{187}Re vs. ^{187}Os Model 1 York regression isochron age for the same sample set at 1937 ± 8 Ma (± 11 including the uncertainty in λ; initial ^{187}Os = 0.1 ± 2.9 ppb; MSWD = 0.2; n = 7; Fig. 4.4c).

Porcupine molybdenite - Ten analyses from eight samples of the Porcupine deposit are reported in Table 4.2 and Fig. 4.4. We note that the Re-Os data for the ultrafine molybdenite of the Porcupine deposit have previous been reported (Chapter Three); however their geological significant has not been discussed. Samples possess ^{187}Re and ^{187}Os abundances that range from 303–6,780 and 10–214 ppb, respectively and are significantly less than those for molybdenite

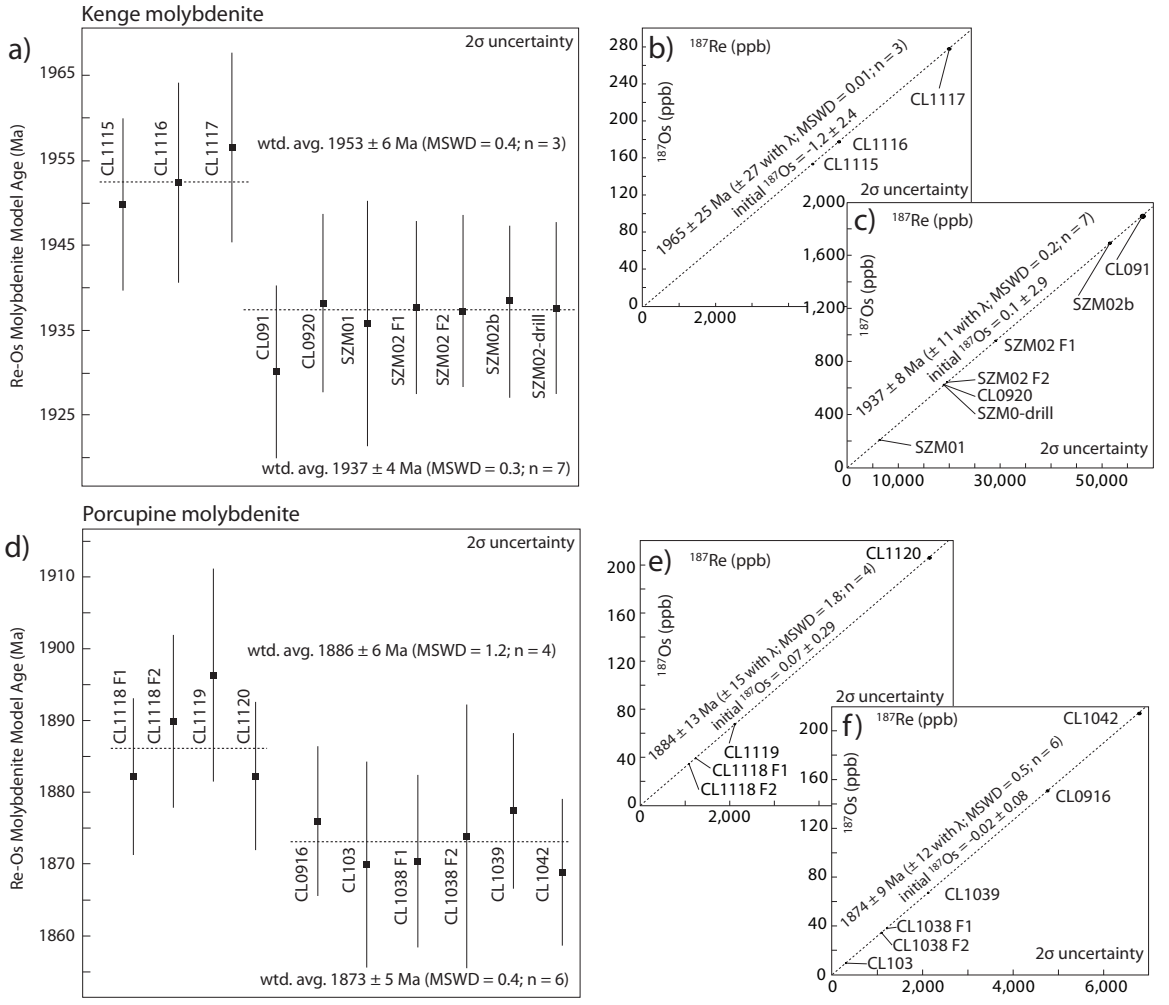

Figure 4.4 – (a) Re-Os molybdenite models age from ultrafine molybdenite samples (Chapter Three) and molybdenite from stylolite-like veins at Kenge. Weighted average (wtd. avg.) Re-Os molybdenite model age are reported for both sample sets; (b) Model 1 York regression ^{187}Re vs. ^{187}Os isochron from ultrafine molybdenite samples at Kenge; (c) Model 1 York regression ^{187}Re vs. ^{187}Os isochron of molybdenite from stylolite like veins at Kenge; (d) Re-Os molybdenite model age from ultrafine molybdenite samples (Chapter Three) and molybdenite from sheared granite samples at Porcupine. Weighted average (wtd. avg.) Re-Os molybdenite model age are reported for both sample sets; (e) Model 1 York regression ^{187}Re vs. ^{187}Os isochron of molybdenite from ultrafine molybdenite samples at Porcupine; (f) Model 1 York regression ^{187}Re vs. ^{187}Os isochron of molybdenite from sheared granite samples at Porcupine.

from the Kenge deposit. Calculated Re-Os model ages range from 1869–1896 Ma and provide evidence for two age populations that partially overlap within uncertainty at the 2σ level (individual analytical uncertainties on Re-Os model ages range from 10–18 Ma and include decay constant uncertainty). Finely disseminated molybdenite samples from quartz veins and hydrothermally altered, but unstrained Ilunga Syenogranite, possess the oldest ages and yield a weighted average Re-Os molybdenite model age at 1886 ± 6 Ma (MSWD = 1.2; n = 4; Fig. 4.4d) that is in good agreement with a ^{187}Re vs. ^{187}Os Model 1 York regression isochron age of the same sample set at 1884 ± 13 Ma (± 15 Ma including the uncertainty in λ; initial ^{187}Os = 0.1 ± 0.3; MSWD = 1.8; n = 4; Fig. 4.4e). Molybdenite from stylolite-like veins and sheared Ilunga Syenogranite samples yield a slightly younger, but partially overlapping within uncertainty at the 2σ level, weighted average Re-Os molybdenite model age at 1873 ± 5 Ma (MSWD = 0.4; n = 6; Fig. 4.4c). The latter is in good agreement with a ^{187}Re vs. ^{187}Os Model 1 York regression isochron age for the same sample set at 1874 ± 9 Ma (± 12 Ma including the uncertainty in λ; initial ^{187}Os = -0.02 ± 0.08; MSWD = 0.5; n = 6; Fig. 4.4f).

4.5.2 Re-Os pyrite and chalcopyrite results summary

Pyrite and chalcopyrite analyses possess a wide range of ^{187}Re (347–86,887 ppt) and ^{187}Os (11–2,863 ppt) concentrations with no systematic difference observed between ore bodies and/or vein types (Table 4.3). Nearly all of the measured Os is radiogenic ^{187}Os (>99% radiogenic ^{187}Os) and, where coupled with high ^{187}Re/^{188}Os ratios (386–2,745,328), suggests that sulfide samples are typical of Low-Level Highly Radiogenic (LLHR) sulfides (Stein et al., 2000). Large and correlated analytical uncertainties (rho ~1; Ludwig, 2008) are associated with the highest ^{187}Re/^{188}Os and ^{187}Os/^{188}Os ratios due to the near absence of common Os and the propagated blank uncertainties. Radiogenic Os concentrations (^{187}Os^{r}) were calculated using the ^{187}Os/^{188}Os$_{initial}$ ratio and its uncertainty based on the regression of the ^{187}Re/^{188}Os vs. ^{187}Os/^{188}Os data. The relative abundance of ^{187}Os^{r} permits Re-Os model ages to be calculated from ^{187}Re and ^{187}Os^{r} concentrations and the isotope equation $t = \ln(^{187}Os^{r}/^{187}Re + 1)/\lambda$; where t = model age and $\lambda = 1.666 \times 10^{-11}$ (Smoliar et al., 1996; Selby et al., 2007). Calculated Re-Os pyrite and chalcopyrite model ages are analogous to Re-Os molybdenite model ages and represent the preferred method of age determination for LLHR samples (Stein et al., 2000; Selby et al., 2009; Ootes et al., 2011). Isochron ages (^{187}Re vs. ^{187}Os^{r} and ^{187}Re/^{188}Os vs. ^{187}Os/^{188}Os) were also calculated and can provide meaningful age determinations despite large and correlated analytical uncertainties for highly radiogenic samples (Stein et al., 2000; Morelli et al., 2005, 2007, 2010; Selby et al., 2009; Kerr and Selby, 2012). Several samples (CL095, CL0918b, CL0919, CL0927b, CL0969 and CL0951) possess exceptionally high ^{187}Re/^{188}Os ratios. The latter were re-analyzed with ^{185}Re and isotopically normal Os tracer solution (i.e., the method for Re-Os molybdenite geochronology, see above). These samples possess Re-Os model ages that are in broad agreement with Re-Os model ages calculated for samples that were spiked with ^{185}Re and ^{190}Os and suggest Re-Os model age calculations are appropriate for our LLHR sample set.

4.5.3 Re-Os pyrite and chalcopyrite results

Kenge and Mbenge mylonite pyrite - Eleven analyses from five pyrite bearing mylonite samples from Kenge and two analyses from one pyrite (± Au) bearing mylonite sample (CL092) from Mbenge were analyzed and are reported in Table 4.3 and Figure 4.5. The ^{187}Re and $^{187}Os^{r}$ concentrations range from 347–31,798 and 11–1,040 ppt, respectively (Fig. 4.5b). Almost all of the measured Os is radiogenic ^{187}Os (>99% radiogenic $^{187}Os^{r}$) and $^{187}Re/^{188}Os$ ratios range from 386–369,409. Analyses with the highest $^{187}Re/^{188}Os$ ratios are associated with large analytical

Table 4.3 - Re-Os pyrite and chalcopyrite results

Sample	Deposit	Location Drill Hole / Meter	Min.	Paragenesis	wt. (g)	Total Re and Os				^{187}Re vs. $^{187}Os^{r}$ Isochron[2]			
						Re ppb	±	Os ppt	±	^{187}Re ppt	±	$^{187}Os^{r}$ ppt	±
CL092 F1	Mbenge	SZD74 / 44	Py	mylonite	0.20041	4.19	0.20	93.26	22.16	2635.7	122.6	85.3	0.3
CL092 F2					0.30376	3.35	0.05	73.28	16.54	2107.8	28.7	67.7	0.2
CL0927 F1					0.30171	1.15	0.01	23.28	49.17	724.3	8.8	22.6	0.3
CL0927 F2[1]	Kenge	SZD7 / 31	Py	mylonite	0.45651	17.66	0.36	-	-	11100.7	225.0	348.6	7.0
CL0927 F3					0.30464	1.19	0.01	25.80	15.33	747.3	8.9	23.7	0.1
CL0945	Kenge	SZD7 / 46	Py	mylonite	0.41452	0.86	0.01	27.96	1.67	541.9	6.4	17.3	0.3
CL0966 F1					0.30697	1.25	0.01	30.90	5.88	787.0	8.7	25.1	0.2
CL0966 F2	Kenge	SZD57 /52	Py	mylonite	0.40057	0.55	0.01	17.05	1.91	347.0	6.4	11.0	0.2
CL0966 F3					0.30319	1.41	0.01	38.61	3.69	888.2	9.1	28.1	0.3
CL0968	Kenge	SZD59 / 58	Py	mylonite	0.40453	1.93	0.02	43.00	8.87	1215.4	11.9	38.5	0.9
CL0969 F1					0.40567	7.06	0.03	142.76	58.75	4434.4	17.6	140.3	2.4
CL0969 F2	Kenge	SZD60 / 150	Py	mylonite	0.10728	7.10	0.33	146.24	6139.27	4464.9	208.0	146.1	0.6
CL0969 F3[1]					0.40139	50.59	0.44	-	-	31798.2	274.9	1039.9	8.8
CL0901	Kenge	mine dump	Py	fault-fill vein	0.30319	1.41	0.01	38.61	3.69	888.2	9.1	28.0	0.2
CL095 F1[1]	Kenge	SZD23 / 106	Cpy	fault-fill vein	0.50402	7.23	0.07	-	-	4541.8	44.1	143.4	1.2
CL095 F2[1]					0.56275	9.25	0.09	-	-	5812.7	53.6	184.4	1.6
CL0918	Kenge	SZD71 / 60	Py	fault-fill vein	0.50762	27.86	0.10	560.34	9429.59	17509.7	64.1	560.3	11.1
CL0918b F1[1]	Kenge	SZD71 / 66	Py	fault-fill vein	0.42679	37.88	0.40	-	-	23807.7	250.5	796.5	8.3
CL0918b F2[1]					0.40509	34.77	0.37	-	-	21852.6	230.2	730.9	7.6
CL0919[1]	Kenge	SZD71 / 65	Py	fault-fill vein	0.44385	138.24	0.54	-	-	86887.4	339.3	2863.4	9.8
CL0927b	Kenge	SZD7 / 31	Py	fault-fill vein	0.30464	1.19	0.01	25.80	15.33	747.3	8.9	23.7	0.1
CL0955 F1					0.40666	1.41	0.02	27.93	3.01	887.1	13.0	20.7	0.2
CL0955 F2	Konokono	SZD177a / 53	Cpy	fault-fill vein	0.47723	1.22	0.01	25.80	2.22	767.3	6.0	18.4	0.2
CL0955 F3					0.47174	1.33	0.01	27.31	1.89	837.2	6.1	18.5	0.2
CL1023 F1	Konokono	SZD175 / 19	Py	altered granite	0.21201	10.84	0.04	116.33	45.93	6812.3	27.4	111.5	0.5
CL1023 F2					0.30090	8.30	0.11	90.34	25.29	5219.1	67.5	85.6	0.2
CL1025 F1	Konokono	SZD177a / 79	Py	quartz vein	0.53766	4.26	0.02	137.61	1.26	2678.3	10.8	82.6	1.2
CL1025 F2					0.43526	3.81	0.02	139.88	1.23	2391.7	10.5	74.4	1.4
CL1026 F1					0.40070	3.19	0.02	89.02	2.59	2005.3	9.6	62.9	0.6
CL1026 F2	Konokono	SZD177a / 104	Py	quartz vein	0.50681	3.06	0.01	91.82	1.76	1925.2	8.6	61.4	0.7
CL1026 F3					0.42341	3.28	0.02	100.16	2.04	2063.9	9.6	66.5	0.8
CL1028 F1					0.32010	10.12	0.04	218.67	16.63	6360.2	24.4	202.7	0.7
CL1028 F2	Konokono	SZD177a / 137	Py	altered granite	0.21447	7.58	0.03	158.81	44.98	4761.9	20.9	152.2	0.7
CL1028 F3					0.53970	9.28	0.03	212.45	5.75	5830.2	21.7	186.3	1.1
CL1028 F4					0.60501	8.87	0.03	192.63	8.44	5574.6	20.7	177.4	1.6
CL0939 F1	Porcupine	GPD15 / 193	Py	quartz vein	0.54287	2.70	0.01	27.55	9.48	1697.9	8.0	25.5	0.3
CL0939 F2					0.47170	3.31	0.01	34.70	12.85	2080.3	9.3	32.5	0.1
CL1032	Porcupine	GPD50 / 22	Py	quartz vein	1.03121	32.48	0.12	663.02	43.44	20411.9	74.1	654.7	19.4
CL1035 F1					0.30176	10.13	0.13	116.76	367.02	6365.8	82.1	116.3	0.6
CL1035 F2	Porcupine	GPD52 / 333	Py	quartz vein	0.30143	10.21	0.13	114.61	192.43	6417.2	82.7	113.8	0.5
CL1035 F3					0.47704	9.94	0.04	109.60	436.34	6247.7	23.3	109.4	1.1
CL1036	Porcupine	GPD48 / 268	Py	quartz vein	1.04500	1.10	0.01	27.67	2.07	691.9	3.5	22.2	0.9
CL0951 F1[1]	Dubwana	MND02 / 348	Py	altered granite	0.44729	9.12	0.13	-	-	5731.9	79.8	185.4	2.5
CL0951 F2[1]					0.47234	13.48	0.19	-	-	8469.6	116.9	272.4	3.7

[1]analyses conducted using a mixed tracer solution of ^{185}Re and isotopically normal Os (see text for discussion)
[2]calculated using initial $^{187}Os/^{188}Os$ value plus its uncertainty from $^{187}Re/^{188}Os$ vs. $^{187}Os/^{188}Os$ regression (see text for discussion)
[3]model age calculated from the isotope equation [$t = \ln(^{187}Os^{r}/^{187}Re + 1)/\lambda$
where t = model age, and λ = 187Re decay constant; 1.666 x 10-11 a-1; Smoliar et al., 1996]
N.B. uncertainties are reported at the 2σ level; all data are blank corrected; blanks for Re and Os were 3.5 ± 2.0 and 0.7 ± 0.15 pg

Table 4.3 – cont'd

$^{187}Re/^{188}Os$ vs. $^{187}Os/^{188}Os$ Isochron					Model age[3]		
$^{187}Re/^{188}Os$	±	$^{187}Os/^{188}Os$	±	rho	Ma	±	% $^{187}Os^{r}$
2512	475	81	15	0.97	1912	91	100
2865	496	92	16	1.00	1898	28	100
8703	13350	272	418	1.00	1848	34	100
-	-	-	-	-	1856	54	-
2696	1231	86	39	1.00	1874	25	100
386	26	12	1	0.98	1887	37	99
1031	170	33	5	1.00	1885	25	100
432	53	14	2	0.99	1867	47	99
640	59	20	2	0.99	1868	27	99
2041	330	65	11	0.99	1871	49	100
13770	4072	436	129	1.00	1870	34	100
369409	10972615	12092	359163	1.00	1933	92	100
-	-	-	-	-	1932	25	-
640	59	20	2	0.99	1862	26	99
-	-	-	-	-	1866	25	-
-	-	-	-	-	1874	25	-
2745328	32670332	87848	1045427	1.00	1891	39	100
-	-	-	-	-	1975	30	-
-	-	-	-	-	1975	30	-
-	-	-	-	-	1946	12	-
2696	1231	86	39	1.00	1872	25	100
945	96	22	2	0.99	1387	24	99
795	67	19	2	0.99	1423	18	99
724	51	16	1	0.99	1309	17	99
10898	3168	179	52	1.00	975	6	100
8498	1775	140	29	1.00	977	13	100
373	4	12	0	0.90	1824	28	99
280	3	9	0	0.88	1840	36	99
587	17	19	1	0.98	1853	21	99
485	10	16	0	0.95	1885	24	99
469	10	15	0	0.96	1902	24	99
3050	177	97	6	1.00	1883	11	100
5529	1154	177	37	1.00	1889	14	100
1704	37	55	1	0.96	1888	15	100
2809	93	90	3	0.96	1881	20	100
6267	1644	94	25	1.00	894	12	100
7113	1987	111	31	1.00	929	7	100
18722	789	601	31	0.81	1895	58	100
111241	248162	2033	4535	1.00	1087	16	100
60029	71766	1065	1273	1.00	1055	15	100
218200	615442	3820	10775	1.00	1042	12	100
953	57	31	2	0.83	1892	77	100
-	-	-	-	-	1911	37	-
-	-	-	-	-	1900	37	-

uncertainties and near-perfectly correlated errors (expressed by the parameter rho ~ 1). As a result, our samples are typical of LLHR sample sets (Stein et al., 2000). Eleven analyses yield a $^{187}Re/^{188}Os$ vs. $^{187}Os/^{188}Os$ Model 1 York regression isochron age of 1880 ± 15 Ma (± 17 Ma including the uncertainty in λ; $^{187}Os/^{188}Os_{initial}$ = 0.04 ± 0.18; MSWD = 0.8; n = 11; Fig. 4.5a). The large correlated uncertainties on $^{187}Re/^{188}Os$ vs. $^{187}Os/^{188}Os$ plots are related to the difficulty in measuring small concentrations of ^{188}Os that are close to the concentration of the analytical blank (Stein et al., 2000; Selby et al., 2009; Morelli et al., 2010). To calculate model ages, the $^{187}Os^{r}$ is determined using the $^{187}Os/^{188}Os_{initial}$ and its associated uncertainty from the $^{187}Re/^{188}Os$ vs. $^{187}Os/^{188}Os$ isochron. Although the calculated $^{187}Os/^{188}Os_{initial}$ (0.04 ± 0.18) is

lower than the $^{187}Os/^{188}Os$ composition of the primordial solar system, the relatively large uncertainty on the calculated $^{187}Os/^{188}Os_{initial}$ overlaps within uncertainty with mantle values and was used for the calculation of model age and $^{187}Os^{r}$ concentrations for mylonite samples (Shirey and Walker, 1998). Direct regression of $^{187}Os^{r}$ against ^{187}Re is appropriate for LLHR samples, but a Model 1 York regression cannot be fitted to our results (probability of fit = 0) because of data-point scatter that is not accounted for by the assigned analytical uncertainties. A Model 2 York regression (a Model 2 York regression weighs all analyses equally) yields a ^{187}Re vs. $^{187}Os^{r}$ isochron age of 1928 ± 17 Ma (± 19 Ma including the uncertainty in λ; $^{187}Os_{initial}$ = -1.7 ± 2.8; MSWD = 1.8; n = 13). This age is outside of analytical uncertainty of the $^{187}Re/^{188}Os$ vs. $^{187}Os/^{188}Os$ Model 1 York regression due to the inclusion of the disparately older "CL0969 F3" analysis (1932 ± 25 Ma). If this analysis is excluded, the remaining analyses yield a ^{187}Re vs. $^{187}Os^{r}$ Model 2 York regression isochron age of 1884 ± 19 Ma (± 21 Ma including the uncertainty in λ; $^{187}Os_{initial}$ = -0.11 ± 0.26; MSWD = 1.0; n = 12; Fig. 4.5b). The low $^{187}Os_{initial}$ is consistent with our sample set containing insignificant common Os and warrants the calculation of Re-Os model ages for individual analyses. Individual Re-Os pyrite model ages range from 1933–1848 Ma (analytical uncertainty at the 2σ level on individual analyses range from 25–91 Myr and include λ uncertainty; including CL0963 F3) and are in broad agreement with isochron age determinations. Because of the virtual absence of common Os, our preferred age for pyrite (± Au) mineralization hosted by mylonites at Kenge and Mbenge is the weighted average Re-Os pyrite model age of all analyses at 1876 ± 10 Ma (MSWD = 0.86; n = 12 excluding CL0969 F3; Fig. 4.5c).

Kenge fault-fill vein pyrite and chalcopyrite – Eight analyses from five pyrite samples and one chalcopyrite sample (CL095) hosted by fault-fill veins at Kenge were analyzed (Table 4.3; Fig. 4.6). Samples possess ^{187}Re and $^{187}Os^{r}$ concentrations that range from 747–86,887 and 24–2,863 ppt, respectively. Almost all of the measured Os is radiogenic (>99% radiogenic ^{187}Os) and $^{187}Re/^{188}Os$ ratios range from 640–2,745,328. Three samples (CL0901, CL0918 and CL0927b) were analyzed with the ^{185}Re and ^{190}Os tracer solution. These analyses yield a $^{187}Re/^{188}Os$ vs. $^{187}Os/^{188}Os$ Model 1 York regression isochron age of 1875 ± 30 Ma (± 32 Ma including the uncertainty in λ; $^{187}Os/^{188}Os_{initial}$ = -0.03 ± 0.43; MSWD = 0.03; n = 3; Fig. 4.6a). The negative lower intercept ($^{187}Os/^{188}Os_{initial}$) is spurious and is caused by the difficulty in measuring common Os concentrations that are close to the analytical blank. We evaluated the effect of the assumed $^{187}Os/^{188}Os_{initial}$ on model ages by varying the $^{187}Os/^{188}Os_{initial}$ between 0.1–1 and found that calculated model ages for samples CL1018 and CL0927 ranged from 1891–1890 Ma and 1872–1853 Ma, respectively. Sample CL0901 is relatively more sensitive to the assumed $^{187}Os/^{188}Os_{initial}$ and model ages for this sample ranged from 1862–1781 Ma. The greater sensitivity of CL101 to the assumed $^{187}Os/^{188}Os_{initial}$ is due to the greater concentration of common Os in this sample compared to the more radiogenic samples (CL0918 and CL0927b). Nevertheless, we expect a mantle-like $^{187}Os/^{188}Os_{initial}$ is appropriate for this sample set (mantle = 0.115 ± 0.16 at 2.0 Ga; Shirey and Walker, 1998) because of the relatively unradiogenic $^{187}Os/^{188}Os_{initial}$ calculated

from the $^{187}Re/^{188}Os$ vs. $^{187}Os/^{188}Os$ isochron regression and the low $^{187}Os/^{188}Os_{initial}$ of the mylonite pyrite sample set. Re-Os pyrite and chalcopyrite model ages provide evidence for two disparately aged sample populations from fault-fill veins at Kenge that are indistinguishable paragenetically and/or visually. Samples CL0918 and CL0918b are particularly noteworthy as they were collected from different parts of the same fault-fill vein and yield disparate model ages (discussed further below). The oldest three samples yield a ^{187}Re vs. $^{187}Os^r$ Model 2 York regression isochron age of 1936 ± 15 Ma (± 17 Ma including the uncertainty in λ; $^{187}Os_{initial}$ =

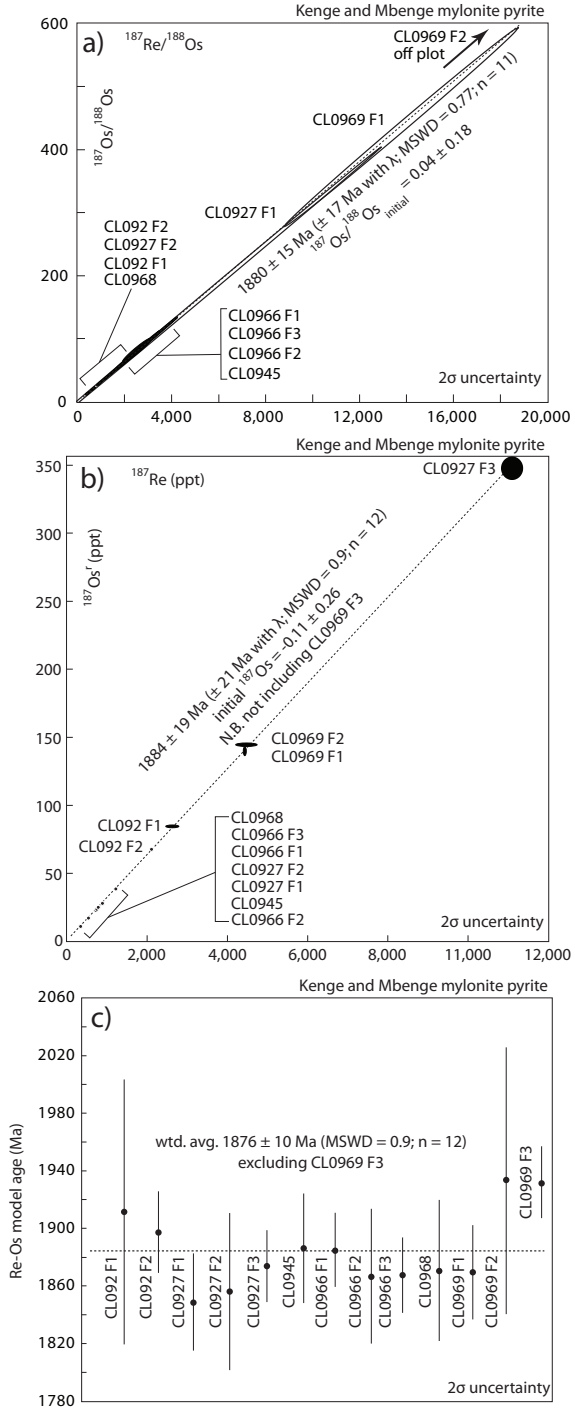

Figure 4.5 – (a) Model 1 York regression $^{187}Re/^{188}Os$ vs. $^{187}Os/^{188}Os$ isochron of pyrite samples from mylonitic shear zones at Kenge (CL0945, CL0927, CL0966, CL0968 and CL0969) and Mbenge (CL092). Analyses with exceptionally high $^{187}Re/^{188}Os$ ratios possess large correlated uncertainties and are typical of LLHR samples; (b) Model 2 York regression ^{187}Re vs. $^{187}Os^r$ isochron of pyrite samples from mylonitic shear zones at Kenge; (c) Re-Os pyrite model ages for samples from mylonitic shear zones at Kenge with weighted average Re-Os pyrite model age.

15 ± 12; MSWD = 0.04; n = 3; Fig. 4.6b). This age contrasts with a ^{187}Re vs. $^{187}Os^{r}$ Model 2 York regression isochron age of the four younger samples at 1874 ± 17 Ma (± 19 Ma including the uncertainty in λ; $^{187}Os_{initial}$ = -0.1 ± 0.4; MSWD = 0.5; n = 5; Fig. 4.6b). Because of the near absence of common Os our preferred age for both sample sets are the weighted average Re-Os model ages at 1953 ± 37 Ma (MSWD = 2.8; n = 3; includes uncertainty with λ) and 1871 ± 12 Ma (MSWD = 0.4; n = 5; includes uncertainty with λ), respectively (Fig. 4.6c).

Konokono pyrite and chalcopyrite – Thirteen analyses from four pyrite samples and one

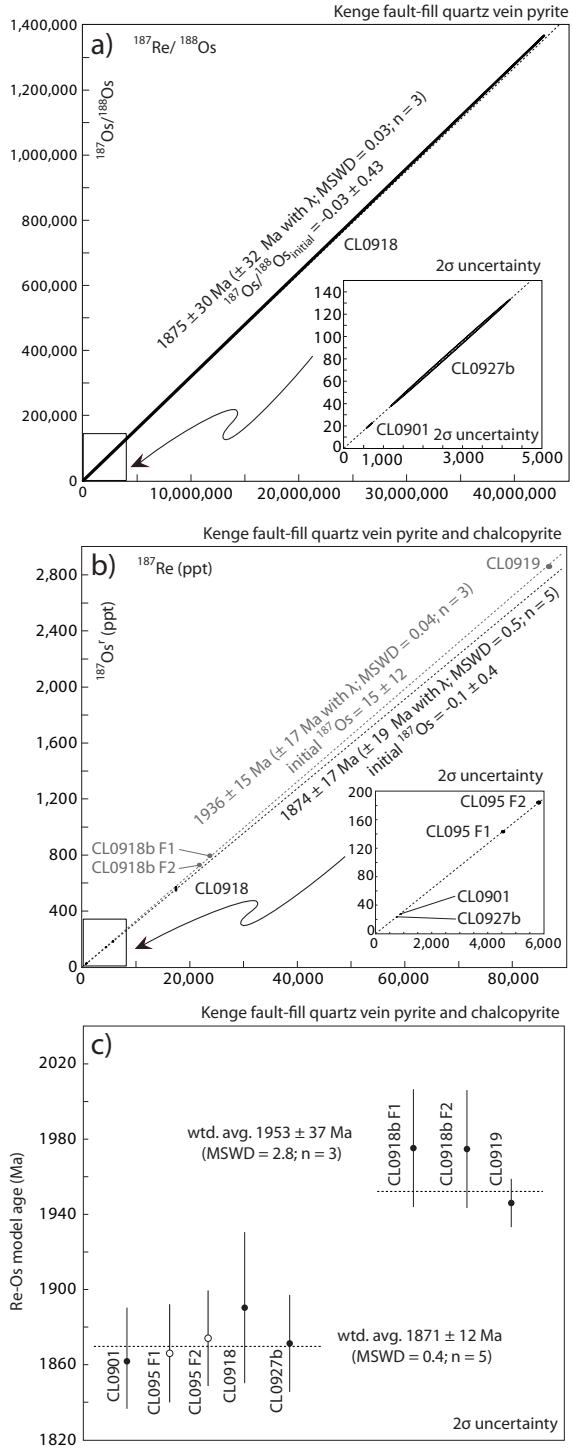

Figure 4.6 – (a) Model 1 York regression $^{187}Re/^{188}Os$ vs. $^{187}Os/^{188}Os$ isochron of pyrite samples from fault-fill veins at Kenge; (b) Model 2 York regression ^{187}Re vs. $^{187}Os^{r}$ isochron of pyrite and chalcopyrite samples from fault-fill veins at Kenge; (c) Re-Os pyrite (CL0918a, CL0918b, CL0919, CL0966b; closed circles) and chalcopyrite (CL095; open circles) model ages hosted by fault-fill veins at Kenge.

chalcopyrite sample were analyzed from Konokono (Table 4.3; Fig. 4.7). Pyrite and chalcopyrite samples were collected from hydrothermally altered wall rock and fault-fill veins. Pyrite sample ^{187}Re and $^{187}Os^{r}$ concentrations range from 1,925–6360 and 62–203 ppt, respectively. These concentrations are greater than those possessed by the chalcopyrite sample (CL0955; ^{187}Re = 767–887 and ^{187}Os = 19–21); however all samples are dominated by radiogenic Os (>99% radiogenic ^{187}Os) and possess $^{187}Re/^{188}Os$ ratios from 485–10,898. Two samples (CL0955 and CL1023) possess anomalously young Re-Os model "ages" and plot significantly below the $^{187}Re/^{188}Os$ vs. $^{187}Os/^{188}Os$ isochron regression defined by the other analyses and are not included

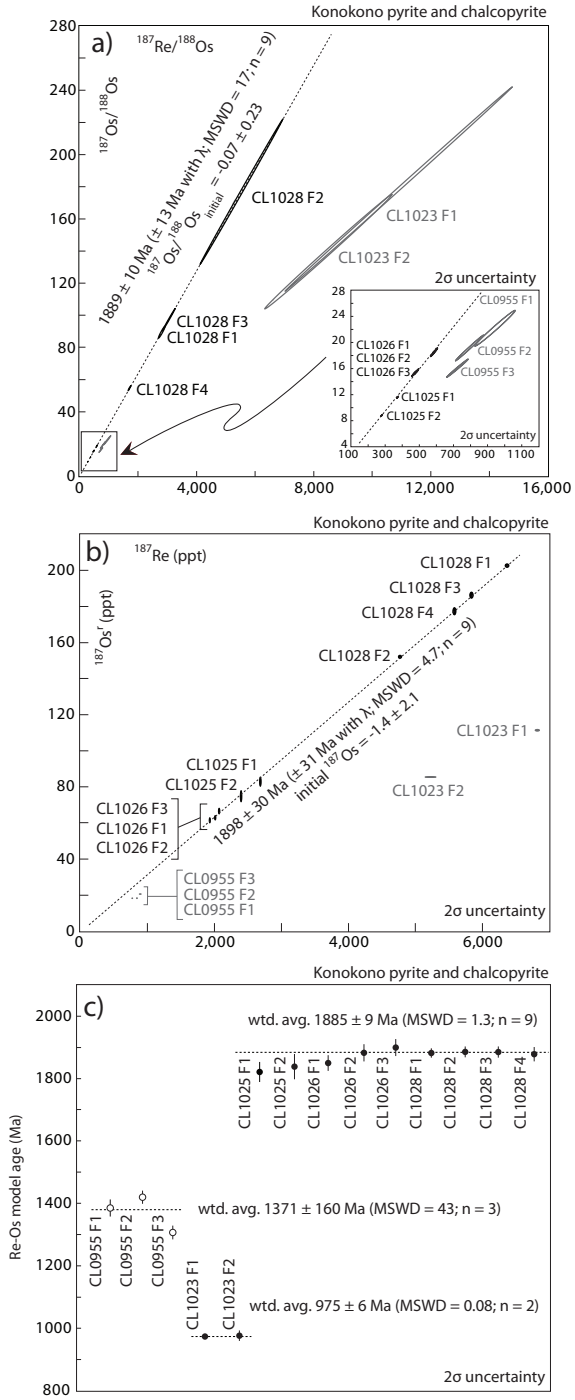

Figure 4.7 – (a) Model-3 York regression $^{187}Re/^{188}Os$ vs. $^{187}Os/^{188}Os$ isochron of pyrite samples (CL1023, CL1025, CL1026 and CL1028) and one chalcopyrite sample from Konokono. Two samples (CL1023 and CL0955) plot significantly off the regression defined by the other analyses and are not included in the isochron regression calculation (plotted in grey); (b) Model-2 York regression ^{187}Re vs. $^{187}Os^{r}$ isochron of pyrite and chalcopyrite samples from Konokono. Two samples (CL1023 and CL0955) plot significantly off the regression defined by the other analyses and are not included in the isochron regression calculation (plotted in grey); (c) Re-Os pyrite and chalcopyrite model ages for samples from Konokono. Weighted average Re-Os model ages are calculated for each of the interpreted sample sets.

in the isochron age calculations. Both of these samples are visually and paragenetically similar to the other Konokono samples and the significance of these ages is discussed further below. The remaining analyses cannot be fitted with a Model 1 York regression (probability of fit = 0) because of geologic scatter that is not accounted for by our assigned analytical uncertainties. The data were fitted with a Model 3 York regression (Model 3 York regression assumes scatter about the linear regression is a combination of assigned uncertainties, including an unknown initial $^{187}Os/^{188}Os$ ratio variation) and yield a $^{187}Re/^{188}Os$ vs. $^{187}Os/^{188}Os$ isochron age at 1889 ± 10 Ma (± 13 Ma including the uncertainty in λ; $^{187}Os/^{188}Os_{initial}$ = -0.07 ± 0.23; MSWD = 17; n = 9; Fig. 4.7a). The negative $^{187}Os/^{188}Os_{initial}$ is obviously spurious but overlaps within analytical uncertainty with mantle-like values. We tested the effect of the assumed $^{187}Os/^{188}Os_{initial}$ on model ages by varying the value from 0.1–1 and found that model ages for samples CL1023 and CL1028 were relatively insensitive to the assumed $^{187}Os/^{188}Os_{initial}$ and ranged from 974–970 Ma and 1888–1866 Ma, respectively. Samples with relatively more common Os (e.g., CL0955, CL1025 and CL1026) are more sensitive to the assumed initial Os composition and varying the $^{187}Os/^{188}Os_{initial}$ from 0.1–1 for these samples results in model ages ranging by up to 190 Myr. However, we expect a mantle-like $^{187}Os/^{188}Os_{initial}$ (mantle = 0.115 ± 0.16 at 2.0 Ga; Shirey and Walker, 1998) is appropriate for our sample set based on the unradiogenic $^{187}Os/^{188}Os_{initial}$ calculated from the $^{187}Re/^{188}Os$ vs. $^{187}Os/^{188}Os$ isochron regression and the low $^{187}Os/^{188}Os_{initial}$ calculated for the mylonite sample set. Furthermore, all of the calculated values reported in Table 4.3 include uncertainty in the assumed $^{187}Os/^{188}Os_{initial}$. The ^{187}Re vs. $^{187}Os^{r}$ regression is more appropriate for LLHR sample sets and a Model 2 York regression of Konokono pyrite analyses yield an isochron age of 1898 ± 30 Ma (± 31 Ma including the uncertainty in λ; MSWD = 4.7; n =9; Fig. 4.7b). Individual Re-Os pyrite model ages for samples CL1025, CL1026 and CL1028 range from 1902–1824 Ma (analytical uncertainty at the 2σ level on individual analyses range from 6–36 Myr and include uncertainty in λ), which are in excellent agreement with both isochron ages. Because of the effective absence of common Os, our preferred age determination for these samples is a weighted average Re-Os pyrite model age at 1885 ± 9 Ma (MSWD = 1.3; n = 9; 6c). This weighted average age differs from Re-Os pyrite model ages of 975 ± 6 and 977 ± 13 from replicate analyses of CL1023 and Re-Os chalcopyrite ages of 1387 ± 24, 1423 ± 18 and 1309 ± 17 Ma from replicate analyses of CL0955. The significance of these younger ages is unclear and is discussed further below.

Porcupine pyrite – Seven analyses from four pyrite samples hosted by oblique-extension veins at the Porcupine were analyzed (Table 4.3; Fig. 4.8). Samples possess ^{187}Re and $^{187}Os^{r}$ concentrations that range from 692–20,412 and 22–655 ppt, respectively. Almost all of the measured Os is present as the radiogenic daughter product of ^{187}Re (>99% radiogenic ^{187}Os) and $^{187}Re/^{188}Os$ ratios range from 953–218,200. The two oldest samples yield a $^{187}Re/^{188}Os$ vs. $^{187}Os/^{188}Os$ Model 1 York regression isochron age of 1895 ± 58 Ma (± 59 Ma including the uncertainty in λ; $^{187}Os/^{188}Os_{initial}$ = 0.0 ± 1.6; n = 2; Fig. 4.8a), whereas the five youngest analyses yield a $^{187}Re/^{188}Os$ vs. $^{187}Os/^{188}Os$ Model 1 York regression isochron age of 1096 ± 23 Ma (± 24 Ma including uncertainty with λ; $^{187}Os/^{188}Os_{initial}$ = -20.8 ± 4.9; MSWD = 0.4; n = 5; Fig.

4.8a). Both of the calculated $^{187}Os/^{188}Os_{initial}$ values are spurious and possess large uncertainties that are related to the difficulty in measuring common Os concentrations that are similar to analytical blank. Calculated model ages for Porcupine samples are relatively insensitive (varying the assumed $^{187}Os/^{188}Os_{initial}$ from 0.1–1 resulted in all of the calculated model ages overlapping within analytical uncertainty at 2σ and ranging by up to 58 Myr) to the assumed $^{187}Os/^{188}Os_{initial}$ and so we assumed mantle-like $^{187}Os/^{188}Os_{initial}$ value (mantle = 0.115 ± 0.16 at 2.0 Ga; Shirey and Walker, 1998) in order to calculate model ages and $^{187}Os^{r}$ concentrations. The model ages and

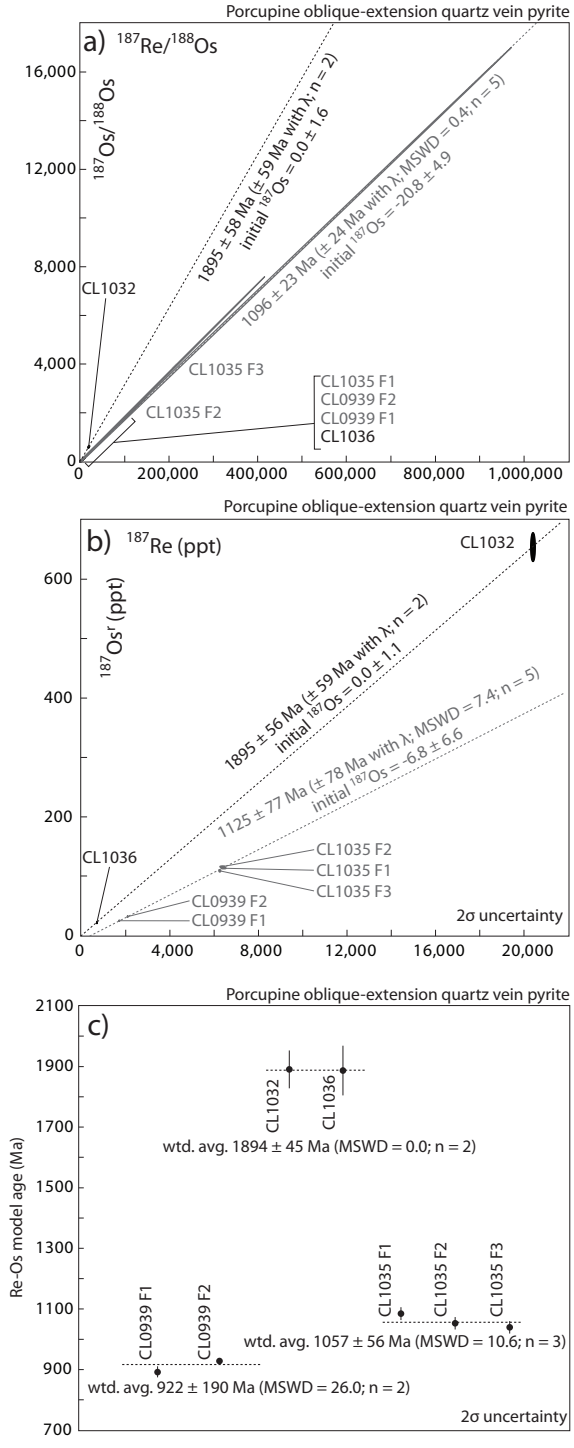

Figure 4.8 – (a) Model 1 York regression $^{187}Re/^{188}Os$ vs. $^{187}Os/^{188}Os$ isochron plot of pyrite samples from oblique-extension veins at Porcupine. Two samples (CL1032 and CL1036) yield an isochron age that is in good agreement with ages reported for Kenge, Mbenge and Konokono, whereas two samples (CL0939 and CL1035) plot significantly below the regression defined by the other two samples and yield a younger isochron age (plotted in grey); (b) Model-2 York regression ^{187}Re vs. $^{187}Os^{r}$ isochron plot of pyrite from oblique-extension veins at Porcupine. Two samples define a Mesoproterozoic isocron age (CL0939 and CL1035; plotted in grey) that contrast with the Paleoproterozoic age of the other two samples (CL1032 and CL1036); (c) Re-Os pyrite model ages hosted by oblique-extension veins at Porcupine. Weighted average Re-Os pyrite model ages are calculated for each of the interpreted sample sets.

$^{187}Os^{r}$ concentrations reported in Table 4.3 include uncertainty in the assumed $^{187}Os/^{188}Os_{initial}$ value. A ^{187}Re vs. $^{187}Os^{r}$ Model 2 York regression isochron age of the oldest and youngest sample sets are 1895 ± 56 Ma (± 59 Ma including the uncertainty in λ; $^{187}Os_{initial}$ = -0.1 ± 1.1; n = 2) and 1125 ± 77 Ma (± 78 Ma including the uncertainty in λ; initial ^{187}Os = -6.8 ± 6.6; MSWD = 7.2; n = 5), respectively (Fig. 4.8b). Our preferred ages for these samples are the more precise weighted average Re-Os model age at 1894 ± 45, 1057 ± 56 and 922 ± 190 Ma (Fig. 4.8c).

Dubwana pyrite – Two replicate analyses of one pyrite sample were analyzed from Dubwana (Table 4.3). Each replicate possesses similar ^{187}Re (5,732 and 8,470 ppt) and ^{187}Os (185 and 272 ppt) concentrations. The ^{185}Re and isotopically normal Os tracer was used for both analyses due to the near absence of common Os. As a result, the calculated Re-Os pyrite analyses are analogous to molybdenite model ages and overlap within analytical uncertainty at 1910 ± 38 Ma and 1900 ± 38 Ma.

4.6 Discussion

4.6.1 Timing of sulfidation (Au) at Kenge, Porcupine, Konokono and Dubwana

Here, we provide the first Re-Os molybdenite, pyrite and chalcopyrite age constraints in SW Tanzania and provide evidence for a protracted metallogenic history at five shear zones that host orogenic Au deposits from the Lupa goldfield (Fig. 4.9). The oldest Re-Os ages correspond to ultrafine disseminated molybdenite samples at Kenge and yield a weighted average Re-Os molybdenite model age at 1953 ± 6 Ma, whereas molybdenite from stylolite-like veins at the same ore body possess nominally younger Re-Os weighted average age at 1937 ± 4 Ma. In broad agreement with these Re-Os molybdenite ages are three pyrite ages from fault-fill veins at Kenge that yield a weighted average Re-Os pyrite model age at 1953 ± 10 Ma. All pyrite and chalcopyrite samples were carefully selected to avoid molybdenite intergrowths and mineral separates were checked for molybdenite under stereoscopic microscope. As a result, the broad agreement between Re-Os molybdenite and pyrite ages suggests molybdenite deposition was at least locally contemporaneous with pyrite deposition. Re-Os molybdenite and pyrite ages at ca. 1950 Ma and 1940 are 60–80 Myr older than Re-Os pyrite ages from veins and shear zones at the same deposit (Fig. 4.9). Disseminated pyrite hosted by mylonitic shear zones at Kenge and Mbenge yield a weighted average Re-Os pyrite model age at 1876 ± 10 Ma that overlaps within analytical uncertainty at the 2σ level with a weighted average Re-Os pyrite and chalcopyrite model age of fault-fill veins from Kenge at 1873 ± 12 Ma. These younger fault-fill vein samples are visually indistinguishable from the ca. 1940 and 1950 Ma fault-fill veins samples and imply a complex history characterized by at least two mineralizing events at ca. 1940 and 1885 Ma. The complex metallogenic history at Kenge is particularly apparent for samples CL0918 and CL0918b that record both mineralizing events from different parts of the same fault-fill vein. The disparately older CL0918b sample (ca. 1950 Ma) was collected from towards the middle of the fault-fill vein, whereas the younger CL0918 (ca. 1885 Ma) was collected towards the fault-fill vein margin and possess a Re-Os model that is indistinguishable from the mylonite samples. The close proximity to the mylonite contact may have played a role in permitting the ingress

of hydrothermal fluids related to mylonitization and precipitating sulfides. These samples are visually identical and suggest that fault-fill veins possess protracted histories that are consistent with complex fluid inclusions trails and vein textures at the micro-scale (e.g., Hodgson, 1989; Robert and Poulsen, 2001). Disseminated pyrite samples hosted by Kenge and Mbenge shear zones are interpreted as syn-deformational (pyrite lozenges are concordant with and wrapped by chlorite ± muscovite comprising the mylonitic fabric) and are interpreted to record the timing of sulfidation and mylonitization at ca. 1880 Ma. Mylonite-hosted pyrite samples also possess native Au inclusions and Re-Os ages from this sample set are considered the best proxy for Au mineralization at Kenge and Mbenge (Fig. 4.3). The relationship between Au and the ca. 1950 and 1940 Ma molybdenite and pyrite deposition event is less clear due to the absence of Au in thin sections prepared for this same set. Nevertheless, the association between the highest Au grades and fault-fill veins suggests Au mineralization is linked with both of the recognized metallogenic events.

Ultrafine disseminated molybdenite samples at Porcupine yield a weighted average Re-Os molybdenite model age of 1886 ± 6 Ma that is slightly outside of analytical uncertainty with weighted average Re-Os molybdenite model age for disseminated molybdenite hosted by stylolite-like veins and sheared granite samples at 1873 ± 5 Ma. Re-Os molybdenite model ages at Porcupine are broadly contemporaneous with a weighted average of two Re-Os pyrite

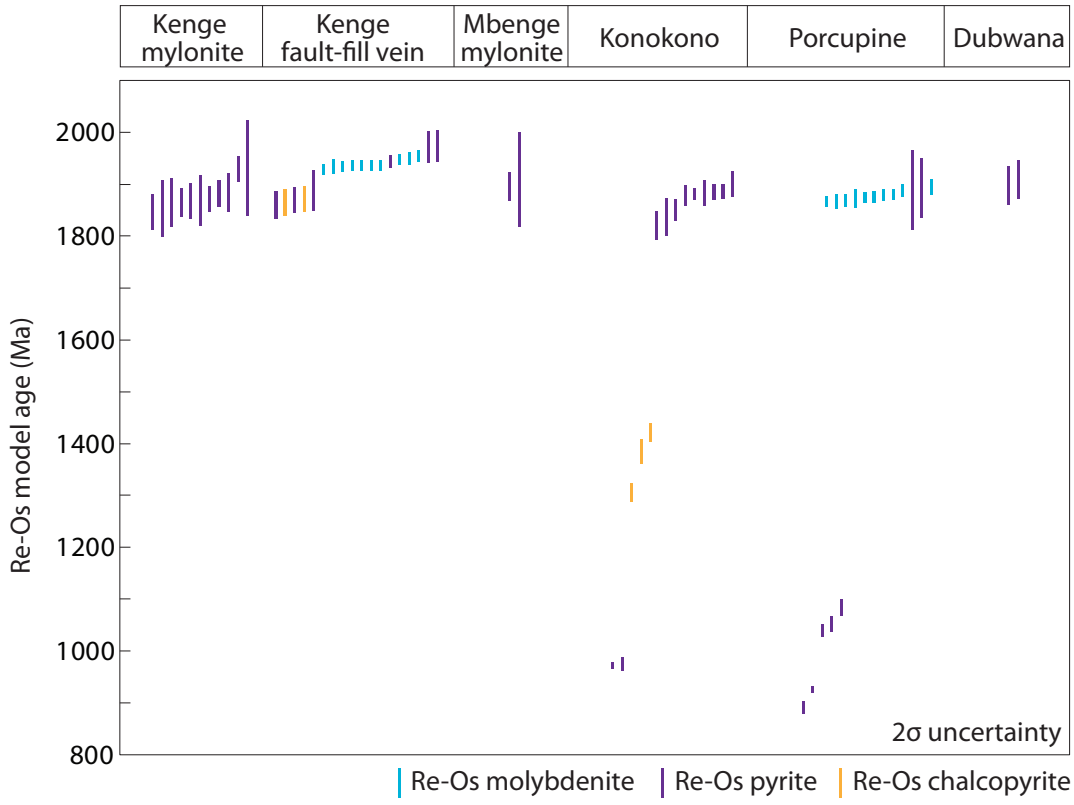

Figure 4.9 – Summary diagram showing all Re-Os model ages at 2σ uncertainty level (Re-Os molybdenite model ages are in blue; Re-Os chalcopyrite ages in yellow; Re-Os pyrite ages in purple).

model ages at 1892 ± 46 Ma from oblique-extension veins, but are significantly older than weighted average Re-Os pyrite model ages for samples CL0939 (922 ± 190 Ma) and CL1035 (1057 ± 56 Ma), respectively. The ca. 1885 Ma molybdenite and pyrite ages at Porcupine are indistinguishable from the ca. 1885 Ma pyrite ages at Kenge and Mbenge and provide evidence for broadly contemporaneous mineralization at all three ore bodies (Fig. 4.9). The strong association between pyrite-bearing quartz veins and Au grade strongly suggests that Re-Os molybdenite and pyrite ages are a suitable proxy for constraining the timing of Au mineralization at Porcupine. The significance of Meso- and Neoproterozoic ages are discussed further below.

Re-Os pyrite ages at Konokono yield a weighted average Re-Os pyrite age at 1885 ± 9 Ma that is in consistent with the ca. 1885 Ma metallogenic event identified at Kenge, Mbenge and Porcupine (Fig. 4.9). However, two samples (CL1023 and CL0955) from the same sample suite possess Meso- and Neoproterozoic ages (1423–975 Ma) that are similar to Re-Os pyrite model ages reported from oblique-extension veins at Porcupine. Finally, the ca. 1885 Ma age recorded at Kenge, Mbenge, Porcupine and Konokono overlaps within analytical uncertainty at the 2σ level with replicate analyses from one pyrite sample collected from the Dubwana exploration target (1910 ± 38 Ma and 1900 ± 38 Ma). Our Re-Os results provide evidence for at least two mineralizing events at ca. 1940 and 1885 Ma with the latter mineralizing event more widely distributed and recorded at all five of the dated shear zones (Kenge, Mbenge, Konokono, Porcupine and Dubwana).

4.6.2 Paleoproterozoic correlations

The Paleoproterozoic 2.1–1.8 Ga is one of several periods of Earth's history important for the formation of orogenic Au deposits (Goldfarb et al., 2001). Examples of this deposit type can be found in a number of Paleoproterozoic metamorphic belts and include several world-class deposits (e.g., Ashanti, Ghana; Oberthür et al., 1998). The Re-Os ages reported in this study are consistent with this globally correlated metallogenic event, but are significantly younger than the 2.1–2.0 Ga Eburnean orogenic Au deposits in West Africa (Oberthür et al., 1998; McFarlane et al., 2011) and Archean orogenic Au deposits typical of northern Tanzania (Kuehn et al., 1990; Foster and Piper, 1993). The Mpanda goldfield, Tanzania, lies along strike of the Lupa goldfield and is suggested to be considerably younger than Re-Os ages reported in this study based on a Pb isochron age of whole-rock and mineral separates (galena, pyrite, chalcopyrite, hematite and siderite) at 719 ± 38 Ma (Stendal et al., 2004). The significance of this ca. 720 Ma date is unclear given widespread evidence for Pb remobilization during the Pan-African Orogeny and conflicting Pb model ages from galena mineral separates (1400 ± 150 Ma; Coomer and Robertson, 1974; Möller et al., 1998). Poorly constrained Pb model ages are also reported for galena mineral separates from the Lupa goldfield (2400 ± 150 Ma; Coomer and Robertson, 1974) and, in light of the Re-Os results presented as part of this study, we suggest that the significance of Pb model ages should be interpreted with care (Robertson, 1973; Möller et al., 1998).

The Re-Os ages here are in good agreement with the 1.9–1.8 Ga Ubendian tectonic phase

that is recorded by Rb-Sr whole-rock and U-Pb zircon dating of gneisses and granitoids in other litho-tectonic terranes comprising the Ubendian Belt (e.g., Cahen et al., 1984; Lenoir et al., 1994; Boniface et al., 2012). In particular, eclogites with MORB-like chemistry dated at 1890–1860 Ma suggest high-grade metamorphism and subduction of ocean crust in the Ubende Terrane was concomitant with greenschist-facies metamorphism, deformation and Au mineralization in the Lupa goldfield (Boniface, 2009; Boniface et al., 2012). The juxtaposition of contemporaneous high- and low-grade metamorphic rocks implies significant displacement along the terrane-bounding shear zones and also provides a temporal link between Au mineralization and subduction zone processes (Şener et al., 2005). The timing of this juxtaposition is unclear due to overprinting Meso- and Neoproterozoic orogenic cycles coupled with Tertiary rifting, which all likely contributed to the current configuration of the Ubendian Terranes (Theunissen et al., 1996).

U-Pb zircon ID-TIMS and LA-MC-ICP-MS ages of felsic-mafic intrusions and dikes of the Lupa goldfield constrain magmatic episodes ranging in age from 1960–1880 Ma and provide evidence for magmatic activity concomitant with sulfidation (Chapter Two). High-precision U-Pb zircon ID-TIMS ages for the Saza granodiorite (weighted average $^{207}Pb/^{206}Pb$ age of concordant zircons at 1934.5 ± 1.0; MSWD = 1.7; n = 5; Chapter Two) are in excellent agreement with Re-Os molybdenite ages from stylolite-like veins at Kenge (weighted average Re-Os molybdenite model age 1937 ± 4 Ma) and provide unequivocal evidence for sulfidation at least locally associated with magmatism at the Myr time scale. The timing of the Ilunga Syenogranite (weighted average $^{207}Pb/^{206}Pb$ age of concordant zircons at 1959.6 ± 1.1; MSWD = 1.4; n = 5; Chapter Two) is also concurrent with the weighted average Re-Os age of ultrafine molybdenite samples (1953 ± 6 Ma) and pyrite samples (1953 ± 37 Ma) at Kenge. Furthermore, the ca. 1885 metallogenic event identified in this study is also compatible with two poorly defined U-Pb zircon LA-MC-ICP-MS ages of a quartz diorite intrusion and gabbroic dike at 1891 ± 17 Ma and 1880 ± 17 Ma, respectively (Chapter Two). The close spatial relationship and contemporaneity between magmatic activity and Au has also been satisfactorily demonstrated at a number of Au deposits globally and has led to the so-called "intrusion-related" deposit type (Sillitoe and Thompson, 1988; Groves et al., 1998; Groves et al., 2003). The genetic significance of this temporal overlap at the Lupa goldfield is less clear because of the contrasting time scales of magmatic auriferous hydrothermal systems and the observed Re-Os model age range presented in this study. Theoretical and empirical studies of magmatic hydrothermal systems suggest hydrothermal circulation of metallogenic fluids is typically sustained for ≤1 Myr (Cathles et al., 1997; Ronacher et al., 2002; von Quadt et al., 2011). As a result, none of the dated intrusions can explain all of the observed Re-Os sulfide ages and we propose that the protracted metallogenic history developed here argues against a genetic link between mineralization and hydrothermal fluids exsolved purely from any individual magmatic phase. Further, all magmatic phases are cross cut by mylonitic shear zones dated at ca. 1880 Ma (Re-Os pyrite ages, this study) and thus the regional metallogenic event occurred relatively late in the magmatic history of the Lupa goldfield. The ca. 1950 and 1940 Ma molybdenite and pyrite

ages at Kenge are distinctly older than mylonitization at the same deposit and provide evidence for hydrothermal processes prior to mylonitization (D2; Table 4.1). Ingress of hydrothermal fluids along pre-D2 fractures (Chapters Two and Five) resulted in replacement of feldspar with rheologically weaker and finer grained phyllosilicates. Grain size reduction likely created the ideal conditions for strain localization and, locally, may have led to the onset of crystal plastic deformation and fluid-assisted diffusion processes (Handy, 1990; Wintsch, et al., 1995; Imber et al., 2001; Chapter Five). The ca. 1950 and 1940 Ma metallogenic events appear to possess a restricted distribution (Kenge) compared to the interpreted regional metallogenic event at ca. 1885 Ma (Kenge, Mbenge, Konokono, Porcupine and Dubwana).

4.6.3 Time scales of metallogenesis at orogenic Au deposits

The mylonitic shear zones that host orogenic Au deposits are considered to be permeable fluid conduits that are critical in focusing auriferous fluids from some source(s) at depth (e.g., upper mantle) to crustal levels (10 ± 5 km) where the majority of deposits of this type form (Groves, 1993). The spatial relationship between shear zones, of varying dimensions, and ore deposits is well documented and is an important mineral exploration criterion (e.g., Weinberg et al., 2004; Micklethwaite et al., 2010). Shear zone intersections, step-overs and dilational jogs along second and third-order shear zones have been implicated as particularly important sites for the focusing of fluids despite a dearth of constraints on the timing of these disparate shear zone segments (e.g., Sibson, 1989; Micklethwaite and Cox, 2004). The prospectivity of second- and third-order structures (second order shear zones possess strike lengths ≥ 10 km, whereas third order structures possess strike lengths < 10 km) is in contrast to crustal-scale (i.e., first-order) shear zones that are typically devoid of Au mineralization despite their regional significance and potential importance in transporting hydrothermal fluids from some source(s) to 10 ± 5 km depth (e.g., Neumayr et al., 2000). In the absence of precise ages, discrete shear zone segments may have developed over a broad geologic history and may not have been connected at the time of Au deposition (Neumayr and Hagemann, 2002).

Our Re-Os results allow us to address these uncertainties by comparing the ages of sulfidation at five shear zones in the Lupa goldfield. The sampled shear zones range in strike length from 2 to >30 km and are of contrasting geometry. The ca. 1885 Ma sulfide ages reported at all five mineral systems imply that all five shear zones were connected to the same fluid source at the time of Au deposition and that second- and third-order shear zones formed an interconnected network of relatively permeable fluid conduits during the Paleoproterozoic. The broad connectivity of shear zones is further supported by the distribution of artisanal workings, recorded as part of the current study, suggesting that Au mineralization is semi-continuous between the dated ore bodies (Fig. 4.2). As a result, intersections between the third-order shear zones (e.g., Saza shear zone) and second order structures (e.g., Mbenge shear zone) are considered to be attractive mineral exploration targets. The contemporaneity of shear zones also has important implications for structural models and suggests that shear zones were kinematically linked during transpressional deformation (Chapter Five).

The protracted and episodic mineralization history identified at Kenge places new constraints on the time scale(s) of orogenic Au deposit formation. Re-Os results provide evidence for at least two temporally distinct mineralizing events at ca. 1940 and 1885 Ma with a potential third Kenge metallogenic event at ca. 1950 Ma. Replicate analyses typically exhibit less scatter than the data-point scatter observed between samples and suggests subtle age differences between samples that partially overlap within analytical uncertainty at the 2σ level. Therefore, the weighted average calculations that define the three broadly identified sulfidation events likely include multiple mineralizing events of slightly different age. Multiple hydrothermal events are also implied from the complex vein histories observed at all Au-bearing shear zones and artisanal workings. Orogenic Au deposits in the Lupa goldfield thus appear to have formed at multiple time scales with temporally distinct metallogenic events identified at ca. 1950, 1940 and 1880 Ma, albeit represented in detail by a series of veins that formed at a time scale less than the assigned analytical uncertainty at the 2σ level. The resolution of our Re-Os data is unable to differentiate these individual vein histories to within several Myr. The association between Au and pyrite for each of the identified metallogenic events remains tentative, but Au and pyrite are expected to be co-genetic for the mylonite sample set dated at ca. 1880 Ma. Three metallogenic events within a ca. 70 Myr history is consistent with the 100 Myr tectono-thermal history observed at other paleo-convergent margins associated with orogenic Au deposits (e.g., Yilgarn Craton; Groves et al., 2000).

4.6.4 Source of metals

The source(s) of metal at orogenic Au deposits is uncertain despite extensive efforts and the integration of multiple geochemical techniques (Groves et al., 2003). The lack of consensus is largely related to a dearth of diagnostic isotopic tracers and the inevitable fluid-rock interaction that masks the chemical composition of the source. Re-Os studies play a pivotal role in this debate and have provided evidence, based largely on $^{187}Os/^{188}Os_{initial}$ values, for two possible metal sources and mixtures thereof (e.g., crustal source vs. mantle source). Radiogenic $^{187}Os/^{188}Os_{initial}$ values (i.e., >>0.1) greater than chondritic values are typically cited as evidence for some crustal-like source (e.g., Arne et al., 2001; Ootes et al., 2011; Sherstén et al., 2012), whereas chondrite-like $^{187}Os/^{188}Os_{initial}$ values (i.e., ~ 0.1) are typically cited as evidence for a mantle source (e.g., Morelli et al., 2007; Bjerkgard et al., 2009). The calculated $^{187}Os/^{188}Os_{initial}$ ratios reported in this study possess large uncertainties due to the difficulty in measuring such small concentrations of common Os. The most precise and statistically robust $^{187}Os/^{188}Os_{initial}$ is calculated for pyrite samples from mylonitic shear zones at Kenge and Mbenge (0.04 ± 0.18). The relatively large uncertainty on the $^{187}Os/^{188}Os_{initial}$ for Kenge and Mbenge pyrite samples is consistent with an $^{187}Os/^{188}Os$ source as radiogenic as 0.22 and thus overlaps with the mantle value of ca. 0.115 at 2.0 Ga (Shirey and Walker, 1998). The large uncertainty on all of the calculated $^{187}Os/^{188}Os_{initial}$ ratios makes the source(s) of metals in the Lupa goldfield equivocal, but a significant radiogenic source (e.g., crustal contribution) of Os to the hydrothermal system is inconsistent with our results.

4.6.5 Geologic significance of Meso- and Neoproterozoic Re-Os ages

Two samples from Konokono (CL1023 and CL0955) and two samples from Porcupine (CL0939 and CL1035) possess Meso- and Neoproterozoic Re-Os ages that are anomalously young compared to the interpreted Paleoproterozoic ages of the ore bodies. All four samples are visually indistinguishable and are present within paragenetically similar vein types as pyrite samples dated at ca. 1940 and 1885 Ma (Fig. 4.3). The younger ages are particularly interesting as the sampled oblique-extension veins lack complex vein textures and were expected to possess relatively simple histories. Replicate analyses of anomalous samples suggest the younger ages are not an analytical artifact and the relatively low analytical uncertainty on all ten analyses are definitively outside of analytical uncertainty of the ca. 1940 and 1885 Ma samples. The cause of these younger ages is unclear but could be related to several possible scenarios: 1) the ages record open-system behavior with anomalously young ages representing Re gain and/or Os loss. This scenario requires that open system behavior is relatively localized since most pyrite analyses overlap with Re-Os molybdenite ages at the assigned 2σ uncertainty level; 2) the younger ages may record mixing of different pyrite generations; and 3) the ages are geologically meaningful and record a Mesoproterozoic metallogenic event(s). The latter is supported by the broad overlap between five of the apparently younger analyses at Porcupine (CL0939 and CL1035), which define a ^{187}Re vs. $^{187}Os^{r}$ isochron age at 1125 ± 77 Ma (Fig. 4.7b). This isochron age is in good agreement with a U-Pb zircon ID-TIMS lower intercept age of a granodiorite dike at 1126 ± 150 Ma that likely records a Mesoproterozoic Pb-loss event (Chapter Two). Mesoproterozoic Re-Os and U-Pb ages in the Lupa goldfield are both poorly constrained but are consistent with metamorphic U-Pb ages of meta-pelites at 1091 ± 9 and 1175 ± 10 Ma from other Ubendian Terranes. Kibaran (1.4–1.1 Ga; Cahen et al., 1984) and Irumide (1.05–1.00 Ga; de Waele et al., 2006) metamorphic ages have been reported elsewhere in the Ubendian Belt, but hitherto have not been reported for the Lupa goldfield (Lenoir, 2009). Our Re-Os ages may provide evidence for previously unidentified Mesoprotoerzoic tectono-thermal event in the Lupa goldfield. Furthermore, Meso- and Neoproterozoic aged sulfides were sampled from the main ore zone at Konokono and Porcupine, which may suggest ore grade in the Lupa goldfield benefitted from repeated metallogenic events related to two disparate orogenic cycles. Our results also imply that mid-crustal mylonitic shear zones represent long-lived zones of structural weakness that act as permeable fluid conduits over a broad geologic history. Reactivation of the mylonitic shear zones was likely favored over the development of new shear zones because of the phyllosilicate rich nature of the fault rocks (e.g., Jefferies et al., 2006).

4.6.6 Utility of Re-Os pyrite and chalcopyrite geochronology

The Re-Os pyrite and chalcopyrite results reported in this study add to a growing number of relatively high-precision LLHR data sets (Stein et al., 2000; Arne et al., 2001; Morelli et al., 2005; 2007; 2010; Selby et al., 2009; Liu et al., 2012; Kerr and Selby, 2012). However many questions regarding the effects of overprinting hydrothermal alteration, metamorphism and metallogenic histories on Re-Os pyrite and chalcopyrite systematics remain (e.g., Stein et al.,

1998; Mathur et al., 1999). The closure temperature of the Re-Os arsenopyrite geochronometer is conservatively estimated at 400ºC and likely extends up to amphibolite facies metamorphic conditions based on robust age determinations for arsenopyrite samples from the Homestake Au deposit following peak metamorphism at 500ºC and 2–4.5 kbar (Morelli et al., 2010). Molybdenite Re-Os systematics are also demonstrated to be extraordinarily robust at amphibolite facies metamorphic pressure/temperature conditions and can be used as an independent check on pyrite and chalcopyrite closure temperatures in the absence of U-Pb geochronologic constraints (Stein et al., 1998; Stein et al., 2001). Our Re-Os molybdenite ages from Porcupine and Kenge overlap with Re-Os pyrite and chalcopyrite ages at the same deposits and imply that pyrite and chalcopyrite Re-Os systematics are unaffected by greenschist facies metamorphic conditions. The upper temperature limit of metamorphic conditions in the Lupa goldfield are based on the assumed limits of quartz plasticity (300–450ºC; Scholz, 1988; Tullis 2002) and are consistent with fluid inclusion microthermometry results from Au-bearing quartz veins (H_2O-CO_2 ± NaCL inclusions from Kenge, interpreted to best reflect the mineralizing fluid, possess a range of homogenization temperatures from 259–419°C; Shaw, 2009). The inferred closure temperature of pyrite and chalcopyrite are therefore similar to arsenopyrite and conservatively estimated at >400ºC (Selby et al., 2009; Kerr and Selby 2012). The three anomalously young Re-Os pyrite and chalcopyrite samples may exhibit localized open system behavior, but are equally likely to record previously unidentified Meso and Neoproterozoic metallogenic events (see above). Additional dating is required in order to assess the distribution of these Meso and Neoproterozoic ages. The Re-Os results presented here record temporally distinct metallogenic events despite complex vein histories and multiple sulfide generations (Kerr and Selby, 2012). The latter requires careful sample selection and mineral separation techniques to avoid mixing superficially similar, but disparately aged samples (Chapter Three). Our results also highlight the need for detailed geochronologic studies that include multiple samples rather than replicate analyses of a single sample.

4.7 Conclusions

Gold occurrences in the Lupa goldfield possess many similarities with the orogenic Au deposit type and are hosted by a number of greenschist facies brittle-ductile mylonitic shear zones. We have investigated molybdenite, pyrite and chalcopyrite from five Au occurrences hosted by five different shear zones in order to determine the time scale(s) of orogenic Au deposit formation and to trace the connectivity of hydrothermal conduits in the mid-crust. Contemporaneous Re-Os sulfide ages at ca. 1885 Ma from all five shear zones across the field area provide evidence for an interconnected network of relatively permeable shear zones during the Paleoproterozoic. The goldfield wide sulfide event at ca. 1885 Ma is pre-dated by ca. 1950 and 1940 Ma metallogenic events exclusively recorded at Kenge. Complex micro- and meso-scale vein textures observed at all of the Au occurrences and subtle age variations between samples suggests that all three metallogenic events are represented in detail by hydrothermal activity that occurred at a time scale less than the resolution of the Re-Os method. The overlap

in Re-Os pyrite ages of quartz veins (oblique-extension and fault-fill veins) and Re-Os ages of syn-deformational pyrite hosted by mylonitic shear zones provide new evidence for broadly contemporaneous brittle and ductile deformation processes at orogenic Au deposits that is akin to conclusions based on mutually cross-cutting relationships (Robert and Poulsen, 2001).

The Re-Os age range reported in this study (1950–1880 Ma) are in good agreement with a global Paleoproterozoic metallogenic event (2.1–1.8 Ga), the 1.9–1.8 Ga Ubendian tectonic phase and U-Pb zircon ages for felsic-mafic intrusions in the Lupa goldfield (1960–1880 Ma). Specifically, Re-Os molybdenite ages at 1937 ± 4 Ma from Kenge overlap with a high-precision $^{207}Pb/^{206}Pb$ zircon age of the Saza Granodiorite at 1934 ± 1 Ma (Chapter Two). The genetic significance of this temporal overlap remains tenuous due to the contrasting time scales of magmatically derived hydrothermal systems and the Re-Os age range reported in this study. We suggest none of the dated intrusions can explain all of the observed Re-Os sulfide ages and propose the protracted metallogenic history is inconsistent with the "intrusion-related" deposit model for Au occurrences in the Lupa goldfield.

Replicate analyses of four anomalously young Re-Os pyrite and chalcopyrite samples may record Meso- and Neoproterozoic metallogenic events. The Re-Os pyrite isochron age at 1125 ± 77 Ma is in good agreement an inferred Pb-loss event at 1126 ± 150 Ma (based on a ID-TIMS zircon U-Pb lower intercept age; Chapter Two) and U-Pb metamorphic ages from other Ubendian Terranes correlated to the Kibaran/Irumide Orogeny (Boniface, 2009). If correct, ore grade in the Lupa goldfield may have benefitted from repeated metallogenic events spanning at least two orogenic cycles (Ubendian and Kibaran Orogenies). An alternative explanation for these apparently younger ages may lie in Re-Os open system behavior, however the agreement between Re-Os molybdenite model ages and Re-Os pyrite and chalcopyrite model ages implies that any open system behavior must be relatively localized. As a result, we maintain that LLHR samples can provide robust age determinations and remain unaffected by greenschist facies metamorphic conditions (259–420 °C; 3.5–7.5 kbar).

4.8 References

Arne, D.C., Bierlein, F.P., Morgan, J.W., and Stein H.J., 2001, Re-Os dating of sulfides associated with gold mineralization in central Victoria, Australia: Economic Geology, v. 96, p. 1455–1459.

Barra, F., Ruiz, J., Mathur, R., and Titley, S., 2003, A Re-Os study of sulfide minerals from the Bagdad porphyry Cu-Mo deposit, northern Arizona, USA: Mineralium Deposita, v. 38, p. 585–496.

Bingen, B., and Stein, H., 2003, Molybdenite Re-Os dating of biotite dehydration melting in the Rogaland high-temperature granulites, S Norway: Earth and Planetary Science Letters, v. 208, p. 181–195.

Bjerkgard, R., Stein, H.J., Bingen, B., Henderson, I.H.C., Sandstad, J.C., and Moniz, A., 2009, The Niassa Gold Belt, northern Mozambique – a segment of a continental-scale Pan-African gold-bearing structure?: Journal of African Earth Sciences, v. 53, p. 45–58.

Boniface, N., 2009, Eburnian, Kibaran, and Pan-African metamorphic events in the Ubendian Belt of Tanzania; petrology, zircon and monazite geochronology: Unpublished PhD thesis, Kiel, Germany, Kiel University, 110 p.

Boniface, N., Schenk, V., and Appel, P., 2012, Paleoproterozoic eclogites of MORB-type chemistry and three Proterozoic orogenic cycles in the Ubendian Belt (Tanzania): evidence from monazite and zircon geochronology, and geochemistry: Precambrian Research, v. 192–195, p. 16–33.

Boniface, N., and Schenk, V., 2012, Neoproterozoic eclogites in the Paleoproterozoic Ubendian Belt of Tanzania: evidence for a Pan-African suture between the Bangweulu Block and the Tanzania Craton: Precambrian Research, v. 208–211, p. 72–89.

Cahen, L., Snelling, N.J., Delhal, J., and Vail, J., 1984, The geochronology and evolution of Africa, Clarendon Press, Oxford, 512 p.

Cathles, L.M., Erendi, A.H., and Barrie, T., 1997, How long can a hydrothermal system be sustained by a single intrusive event?: Economic Geology, v. 92, p. 766–771.

Commer, P.G., and Robertson, D.K., 1974, A lead isotope study of Archaean mineralized areas in Tanzania: Journal of the Geological Society, v. 130, p. 449–460.

Daly, M.C., 1988, Crustal shear zones in central Africa: a kinematic approach to Proterozoic tectonics: Episodes, v. 11, p. 5–11.

de Waele, B., Kampunzu, A.B., Mapani, B.S.E., and Tembo, F., 2006, The Mesoproterozoic Irumide belt of Zambia: Journal of African Earth Sciences, v. 46, p. 36–70.

Du, A.D., He, H.L., Yin, N.W., Zou, X.Q., Sun, Y.L., Sun, D.Z., Chen, S.Z., and Qu, W.J., 1993, Direct dating of molybdenites using the Re-Os geochronometer: Chinese Science Bulletin, v. 38, p. 1319–1320.

Feng, C., Qu, W., Zhang, D., Dang, X., Du, A., Li, D., and She, H., 2009, Re-Os dating of pyrite from the Tuolugou stratabound Co(Au) deposit, eastern Kunlun Orogenic Belt, northwestern China: Ore Geology Reviews, v. 36, p. 213–220.

Foster, R.P., and Piper, D.P., 1993, Archaean lode gold deposits in Africa; crustal setting, metallogenesis and cratonization: Ore Geology Reviews, v. 8, p. 303–347.

Grantham, D.R., 1931, Lupa river goldfield: Min. Mag., v. 45, p. 265–276.

Grantham, D.R., 1932, Lupa goldfield: Bulletin of the Geological Survey of Tanganyika, v. 3, 34 p.

Grantham, D.R., 1933, The eastern extension of Lupa goldfield: Geological Survey of Tanganyika, short paper 11, 9 p.

Gallagher, D.R., 1939, Preliminary account of the geology of a portion of Lupa goldfield: Economic Geology, v. 34, p. 306–323.

Gallagher, D.R., 1941, A microscopic study of some ores of the Lupa goldfield, Tanganyika

Territory, East Africa: Economic Geology, v. 36, p. 306–323.

Goldfarb, R.J., Groves, D.I., and Gardoll, S., 2001, Orogenic gold and geologic time: a global synthesis: Ore Geology Reviews, v. 18, p. 1–75.

Groves, D.I., 1993, The crustal continuum model for late-Archaean lode-gold deposits of the Yilgarn Block, Western Australia: Mineralium Deposita, v. 28, p. 366–374.

Groves, D.I., Goldfarb, R.J., Gebre-Mariam, M., Hagemann, S.G., and Robert, F., 1998, Orogenic gold deposits: a proposed classification in the context of their crustal distribution and relationships to other gold deposit types: Ore Geology Reviews, v. 13, p. 7–27.

Groves, D.I., Goldfarb, R.J., Knox-Robinson, C.M., Ojala, J., Gardoll, S., Yun, G.Y., and Holyland, P., 2000, Late-kinematic timing of orogenic gold deposits and significance for computer-based exploration techniques with emphasis on the Yilgarn Block, Western Australia: Ore Geology Reviews, v. 17, p. 1–38.

Groves, D.I., Goldfarb, R.J., Robert, F., and Hart, C.J.R., 2003, Gold deposits in metamorphic belts: overview of current understanding, outstanding problems, future research and exploration strategies: Economic Geology, v. 98, p. 1–29.

Hammer, P.T.C., Clowes, R.M., Cook, F.A., van der Velden, A.J. and Vasudevan, K., 2010, The Lithoprobe trans-continental lithospheric cross sections: imaging the internal structure of the North American continent: Canadian Journal of Earth Sciences, v. 47, p. 821–857.

Handy, M.R., 1990, The solid-state flow of polymineralic rocks: Journal of Geophysical Research, v. 96 (B6), p. 8647–8661.

Hanson, R.E., 2003, Proterozoic geochronology and tectonic evolution of southern Africa, *in*: Yoshida, M., Windley, B.F., and Dasgupta, S., eds., Proterozoic East Gondwana: Supercontinent Assembly and Breakup, Geological Society, London, Special Publications, v. 206, p. 427–463.

Harris, J.F., 1961, Summary of geology of Tanganyika: Geological Survey of Tanganyika Memoir, v. 1, p. 64–67.

Hodgson, C.J., 1989, The structure of shear-related, vein-type gold deposits: a review: Ore Geology Reviews, v. 4, p. 231–273.

Hronsky, J.M.A., Groves, D.I., Loucks, R.R., and Begg, G.C., 2012, A unified model for gold mineralisation in accretionary orogens and implications for regional-scale exploration targeting methods: Mineralium Deposita, v. 47, p. 339–358.

Imber, J., Holdsworth, R.E., Butler, C.A., and Strachan, R.A., 2001, A reappraisal of the Sibson-Scholz fault zone model: the nature of the frictional to viscous ("brittle-ductile") transition along a long-lived, crustal-scale fault, Outer Hebrides, Scotland: Tectonics, v. 20, p. 601–624.

Jeffries, S.P., Holdsworth, R.E., Wibberley, C.A.J., Shimamoto, T., Spiers, C.J., Niemeijer, A.R., and Lloyd, G.E., 2006, The nature and importance of phyllonite development in crustal-scale fault cores: an example from the Median Tectonic Line, Japan: Journal of Structural Geology, v. 28, p. 220–235.

Kerr, A., and Selby, D., 2012, The timing of epigenetic gold mineralization on the Baie Verte Peninsula, Newfoundland, Canada: new evidence from Re-Os pyrite geochronology: Mineralium Deposita, v. 47, p. 325–337.

Kerrich, R., and Cassidy, K.F., 1994, Temporal relationships of lode Au mineralization to accretion, magmatism, metamorphism and deformation – Archean to present: a review: Ore Geology Reviews, v. 9, p. 263–310.

Kilembe, E.A., and Rosendahl, B.R., 1992, Structure and stratigraphy of the Rukwa rift: Tectonophysics, v. 209, p. 143–158.

Kuehn, S., Ogola, J., and Sango, P., 1990, Regional setting and nature of gold mineralization in Tanzania and southeast Kenya: Precambrian Research, v. 46, p. 71–82.

Lenoir, J.L., Liégeois, J.P., Theunissen, K., and Klerkx, J., 1994, The Palaeoproterozoic Ubendian shear Belt in Tanzania: geochronology and structure: Journal of African Earth Sciences, v. 19, p. 169–184.

Liu, J., Wu, G., Li, Y., Zhu, M., and Zhong., 2012, Re-Os sulfide (chalcopyrite, pyrite and molybdenite) systematics and fluid inclusion study of the Duobaoshan porphyry Cu (Mo) deposit, Heilongjiang Province, China: Journal of Asian Earth Sciences, v. 49, p. 300–312.

Ludwig, K.A. 2008, User's Manual for Isoplot 3.6, A Geochronological Toolkit for Microsoft Excel. Berkeley Geochronology Center Special Publication No. 4, 77 p.

Marobhe, I., 1989, Interpretation of aerogeophysical anomalies of southwestern Tanzania: Geological Survey of Finland Bulletin, v. 350, 72 p.

Mathur, R., Ruiz, J., and Tornos, F., 1999, Age and source of the ore at Tharsis and Rio Tinto, Iberian pyrite belt, from Re-Os isotopes: Mineralium Deposita, v. 34, p. 790–793.

McFarlane, C.R.M., Mavrogenes, J., Lentz, D., King, K., Allibone, A., Holcombe, R., 2011, Geology and intrusion-related affinity of the Morila Gold Mine, southeast Mali: Economic Geology, v. 106, p. 727–750.

Micklethwaite, S., and Cox, S.F., 2004, Fault-segment rupture, aftershock-zone fluid flow, and mineralization: Geology, v. 32, p. 813–816

Micklethwaite, S., Sheldon, H.A., and Baker, T., 2010, Active fault and shear processes and their implications for mineral deposit formation and discovery: Journal of Structural Geology, v. 32, p. 151–165.

Möller, A., Mezger, K., and Schenk, V., 1998, Crustal age domains and the evolution of the continental crust in the Mozambique Belt of Tanzania; combined Sm-Nd, Rb-Sr, and Pb-Pb isotopic evidence: Journal of Petrology, v. 39, p. 749–783.

Morelli, R.M., Creaser, R., Selby, D., Kontak, D.J., and Horne, R.J., 2005, Rhenium-osmium geochronology of arsenopyrite in Meguma group gold deposits, Meguma terrane, Nova Scotia, Canada: evidence for multiple gold-mineralizing events: Economic Geology, v. 100, p. 1229–1242.

Morelli, R., Creaser, R.A., Seltmann, R., Stuart, F.M., Selby, D., and Graupner, T., 2007, Age constraints for the giant Muruntau gold deposit, Uzbekistan, from coupled Re-Os-He isotopes in arsenopyrite: Geology, v. 35, p. 795–798.

Morelli, R.M., Bell, C.C., Creaser, R.A., ands Simonetti, A., 2010, Constraints on the genesis of gold mineralization at the Homestake gold deposit, Black Hills, South Dakota from rhenium-osmium sulfide geochronology: Mineralium Deposita, v. 45, p. 461–480.

Neumayr, P., Hagemann, S.G., and Couture, J.-F., 2000, Structural setting, textures, and timing of hydrothermal vein systems in the Val d'Or camp, Abitibi, Canada: implications for the evolution of transcrustal, second- and third-order fault zones and gold mineralization: Canadian Journal of Earth Sciences, v. 37, p. 95–114.

Neumayr, P., and Hagemann, S.G., 2002, Hydrothermal fluid evolution within the Cadillac Tectonic Zone, Abitibi Greenstone Belt, Canada: relationship to auriferous fluids in adjacent second- and third-order shear zones: Economic Geology, v. 97, p. 1203–1225.

Oberthür, T., Vetter, U., Davis, D.W., and Amanor, J.A., 1998, Age constraints on gold mineralization and Paleoproterozoic crustal evolution in the Ashanti belt of southern Ghana: Precambrian Research, v. 89, p. 129–143.

Oliver, N.H.S., 2001, Linking of regional and local hydrothermal systems in the mid-crust by shearing and faulting: Tectonophysics, v. 335, p. 147–161.

Ootes, L., Morelli, R.M., Creaser, R.A., Lentz, D.R., Falck, H., and Davis, W.J., 2011, The timing of Yellowknife gold mineralization: a temporal relationship with crustal anatexis?: Economic Geology, v. 106, p. 713–720.

Porter, S.J., and Selby, D., 2010, Rhenium-osmium (Re-Os) molybdenite systematics and geochronology of the Cruchan Granite skarn mineralization, Etive Complex: implications for emplacement chronology: Scottish Journal of Geology, v. 46, p. 17–21.

Robert, F., and Poulsen, K.H., 2001, Vein formation and deformation in greenstone gold deposits, *in* Richards, J.P., and Tosdal, R.M., eds, Structural controls on ore genesis, Society of Economic Geology Reviews, v. 14, p. 111–155.

Robertson, D.K., 1973, A model discussing the early history of the Earth based on a study of lead isotope ratios from veins in Archean cratons of Africa: Geochimica et Cosmochimica Acta, v. 37, p. 2099–2124.

Ronacher, E., Richards, J.P., Villeneuve, M.E., and Johnston, M.D., 2002, Short life-span of the ore-forming system at Porgera gold deposits, Papua New Guinea: laser $^{40}Ar/^{39}Ar$ dates for roscoelite, biotite, and hornblende: Mineralium Deposita, v. 37, p. 75–86.

Sango, P.M., 1988, Structural and lithological controls of gold mineralization in the Lupa goldfield, Tanzania, *in* Ho, S.E., and Groves, D.I., Recent advances in understanding Precambrian gold deposits, Geology Department and University Extension, The University of Western Australia, Publication No. 12, p. 99–109.

Şener, K.A., Young, C., Groves, D.I., Krapež, B., and Fletcher, I.R., 2005, Major orogenic gold episode associated with Cordilleran-style tectonics related to the assembly of Paleoproterozoic Australia: Geology, v. 33, p. 225–228.

Scherstén, A., Szilas, K., Creaser, R.A., Næraa, T., van Gool, J.A.M., and Østergaard, C., 2012, Re-Os and U-Pb constraints on gold mineralisation events in the Meso- to Neoarchaean Storø greenstone belt, Storø, southern West Greenland: Precambrian Research, v. 200–203, p. 149–162.

Scholz, C.H., 1988, The brittle-plastic transition and the depth of seismic faulting: Geologische Rundschau, v. 77, p. 319–328.

Selby, D., Creaser, R.A., Stein, H.J., Markey, R.J., and Hannah, J.L., 2007, Assessment of the ^{187}Re decay constant by cross calibration of Re-Os molybdenite and U-Pb zircon chronometers in magmatic ore systems: Geochimica et Cosmochimica Acta, v. 71, p. 1999–2013.

Selby, D., Kelley, K.D., Hitzman, M.W., and Zieg, J., 2009, Re-Os sulfide (bornite, chalcopyrite, and pyrite) systematics of the carbonate-hosted copper deposits at Ruby Creek, southern Brooks Range, Alaska: Economic Geology, v. 104, p. 437–444.

Shaw, E., 2009, Fluid evolution in the Lupa goldfield, SW Tanzania: Unpublished MGeol Thesis, Leicester, UK, University of Leicester, 54 p.

Shirey, S.B., and Walker, R.J., 1995, Carius tube digestion for low-blank rhenium-osmium analysis: Analytical Chemistry, v. 67, p. 2136–2141.

Shirey, S.B., and Walker, R.J., 1998, The Re-Os isotope system in cosmochemistry and high-temperature geochemistry: Annual Review Earth and Planetary Sciences, v. 26, p. 423–500.

Sibson, R.H., 1989, Earthquake faulting as a structural process: Journal of Structural Geology, v. 11, p. 1–14

Sillitoe, R.H., and Thompson, J.F.H., 1998, Intrusion-related vein gold deposits: types, tectono-magmatic settings and difficulties of distinction from orogenic gold deposits: Resource Geology, v. 48, p. 237–250.

Simpson, R., 2012, NI 43-101 mineral resource estimate update for the Saza-Makongolosi gold project, Tanzania: Unpublished company report, SRK consulting, 217 p.

Smoliar, M.I., Walker, R.J., and Morgan, J.W., 1996, Re-Os constraints on the age of Group IIA, IIIA, IVA, and IVB iron meteorites: Science, v. 271, p. 1099–1102.

Stein, H.J., Sundblad, K., Markey, R.J., Morgan, J.W., and Matuza, G., 1998, Re-Os ages for Archean molybdenite and pyrite, Kuittilia-Kivisuo, Finland, and Proterozoic molybdenite, Kabeiai, Lithuania: testing the chronometer in a metamorphic and metasomatic setting: Mineralium Deposita, v. 433, p. 329–345.

Stein, H.J., Morgan, J.W., and Scherstén, A., 2000, Re-Os dating of low-level highly radiogenic (LLHR) sulphides: the Harnäs gold deposit, southwest Sweden, records continental scale tectonic events: Economic Geology, v. 95, p. 1657–1671.

Stendal, H., Frei, R., Muhongo, S., Ramussen, T.M., Mnali, S., Petro, F., and Temu, E.B., 2004, Gold potential of the Mpanda Mineral Field, SW Tanzania: evaluation based on geological, lead isotopic and aeromagnetic data: Journal of African Earth Sciences, v. 38, p. 437–447.

Teale, E.O., Eades, N.W., Harkin, D.A., Harpum, J.R., and Horne, R.G., 1935, Brief explanation of the geology of Irambo area, quarter degree sheet 245, Geological Survey of Tanganyika, Dodoma.

Theunissen, K., Klerkx, J., Melnikov, A., and Mruma, A., 1996, Mechanisms of inheritance of rift faulting in the western branch of the east African Rift, Tanzania: Tectonics, v. 15, p. 776–790.

Tullis, J., 2002, Deformation of granitic rocks: experimental studies and natural examples: Reviews in Mineralogy and Geochemistry: v. 51, p. 51–95.

van Straaten, V.P., 1984, Gold Mineralization in Tanzania – a review, *in* Foster, R.P., eds., Gold '82; the geology, geochemistry and genesis of gold deposits, A.A. Balkema, Rotterdam, p. 673–685.

von Quadt, A., Erni, M., Martinek, K., Moll, M., Peytcheva, I., Heinrich, C.A., 2011, Zircon crystallization and the lifetimes of ore-forming magmatic-hydrothermal systems: Geology, v. 39, p. 731–734.

Weinberg, R.F., Hodkiewicz, P.F., and Groves, D.I., 2004, What controls gold distribution in Archean terranes?: Geology, v. 32, p. 545–548.

Wintsch, R.P., Christofferson, R., and Kronenberg, A.K., 1995, Fluid-rock reaction weakening of fault zones: Journal of Geophysical Research, v. 100, p. 13,021–13,032.

– Chapter Five –

Fluid-Rock Interaction and Shear Zone Development in a Transpressional Setting: An example from the Lupa Goldfield, SW Tanzania

Chapter Five is submitted to the journal Economic Geology

Collaborators: David Selby[1] , Jonathan Imber[1] and David Holwell[2]
[1]Department of Earth Sciences, Durham University, Durham, DH1 3LE, UK
[2]Department of Geology, University of Leicester, University Road, Leicester, LE1 7RH, UK

5.1 Introduction

Orogenic Au deposits are temporally associated with periods of Earth's history dominated by convergent tectonics and spatially associated with plate boundaries, terrane-scale mid-crustal shear zones and related subsidiary structures (e.g., Groves et al., 1998; Goldfarb et al., 2001). The first-order control on orogenic Au deposits is at a lithospheric scale related to subduction zone processes and potentially a fertile upper-mantle/lower-crust (Kerrich and Wyman, 1990; Bierlein et al., 2009; Hronsky et al., 2012). Transpressional deformation (strike-slip deformation with a component of shortening orthogonal to the deformation zone; Dewey et al., 1998) is expected at convergent plate margins as a consequence of oblique plate convergence and/or irregular plate boundaries (Harland, 1971). The significance of transpressional deformation at the ore deposit-scale is less clear as strain partitioning, facilitated by structurally anisotropic rocks, is predicted to compartmentalize transpressional strain into pure and simple shear-dominated deformation domains (Jones and Tanner, 1995; Jiang et al., 2001; Fig. 5.1). As a result, the deformation path of individual Au-bearing shear zones may conform to pure and/or simple shear models despite transpressional deformation at the regional scale. Strain partitioning could explain the applicability of simple shear models in correctly predicting the geometry of vein and shear structures at a number of orogenic Au deposits associated with oblique convergent margins (e.g., Sigma Mine; Robert and Poulsen, 2001; Daigneault et al., 2002). Whilst strain partitioning is observed at grain- to continent-scales, complete transpressional strain partitioning is unlikely given the widespread field evidence for oblique slip on shear zones of varying dimensions (Fitch, 1972; Molnar, 1992; Teyssier et al., 1995; Jones et al., 1997; Jiang et al., 2001).

The aims of the current study are to characterize the geometry, mineralogy, micro-structure and geochemistry of Au-bearing structures that host orogenic Au ore bodies in the Lupa goldfield, SW Tanzania. We propose that the characteristics and geometry of geologic fabrics/structures within the Au-bearing shear zones are indicative of transpressional and non-

coaxial strain of triclinic, or lower, symmetry and are inconsistent with simple-shear deformation models (Jiang and Williams, 1998). The Lupa goldfield ore bodies, and their host shear zones, therefore provide a case study to examine the effects of transpressional deformation on the development of orogenic Au deposits at the meso- and micro-scales.

Following this introduction, the paper is divided into four sections. The first section outlines the regional and local geologic setting of the Lupa goldfield and describes each of the methods used in the subsequent sections. The second section summaries the fault rock characteristics at the meso- and micro-scales, investigates the lithogeochemical changes related to mylonitization and discusses shear zone kinematics. Section three outlines the geology of the Au occurrences by describing vein and alteration characteristics and synthesizes new structural data collected from artisanal workings and oriented drill core. The final section integrates the results of the previous three sections by discussing the evidence for strain partitioning and evaluating the role of fluid-rock interaction with regards to deformation processes and shear zone development.

5.2 Regional Geology

The Paleoproterozoic Ubendian Belt circumscribes the western edge of the Tanzanian Craton and is divided into eight litho-tectonic terranes: Ubende, Wakole, Katuma, Ufipa, Mbozi, Lupa, Upangwa and Nyika (McConnell, 1950; Sutton et al., 1954; Daly, 1988; Lenoir et al., 1994; Theunissen et al., 1996; Boniface et al., 2009; Fig. 5.2). Amphibolite- to granulite-facies meta-igneous and meta-sedimentary rocks are the dominant lithologies and have been

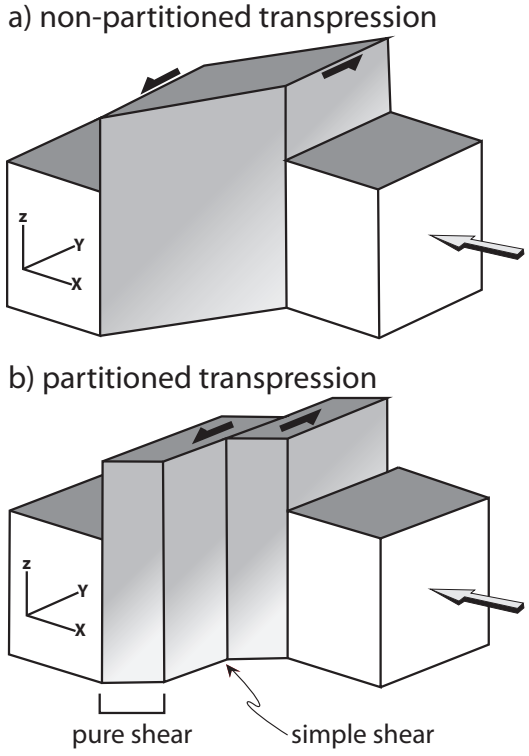

Figure 5.1 – (a) Schematic block model of homogeneous, or non-partitioned transpression; (b) schematic block mode of partitioned transpression where the wrench component of the transpressional strain is compartmentalized into a discrete strike-slip fault (modified from Dewey et al., 1998).

intruded by voluminous Paleoproterozoic granitoids (Cahen et al., 1984; Lenoir et al., 1994). Each Ubendian Terrane is bound by steeply-dipping shear zones with sub-horizontal mineral stretching lineations, which led to the current tectonic model invoking lateral accretion (dextral; Lenoir et al., 1994) of Ubendian Terranes along the western margin of the Tanzanian Craton (Daly, 1988; Lenoir et al., 1994). Lateral accretion in the Ubendian Belt is suspected to have occurred concomitant with thrusting and accretion of the geologically equivalent Usagaran Belt, which lies to the east of the current field area (Daly, 1988).

Ubendian tectonism and metamorphism occurred diachronously with 2.1–2.0 Ga granulite facies metamorphism overprinted by 1.9–1.8 Ga amphibolite facies metamorphism (Lenoir et al., 1994). Paleoproterozoic metamorphism in the Ubendian belt is overprinted by Meso- and Neoproterozoic tectono-thermal events that are correlated to the Kibaran and Pan-African orogenic episodes, respectively (Cahen et al., 1984; Boniface, 2009; Boniface et al., 2012; Boniface and Schenk, 2012). The current study is located adjacent to the Rukwa Rift, which is interpreted as a strike- to oblique-slip half-graben associated with the western branch of the East Africa Rift system (Kilembe and Rosendahl, 1992). The trend of the western branch of the East African Rift System parallels the trend of the Ubendian basement and suggests reactivation of Ubendian structures has occurred from the Paleoproterozoic until the present day (Kilembe and Rosendahl, 1992; Theunissen et al., 1996).

5.3 Local Geology

5.3.1 Lupa Terrane lithologies

The field area for the current study is located in the western portion of the Lupa goldfield and corresponds to the mineral exploration licenses of Helio Resource Corp. (Fig. 5.3). All rocks within the field area have undergone hydrothermal alteration and greenschist

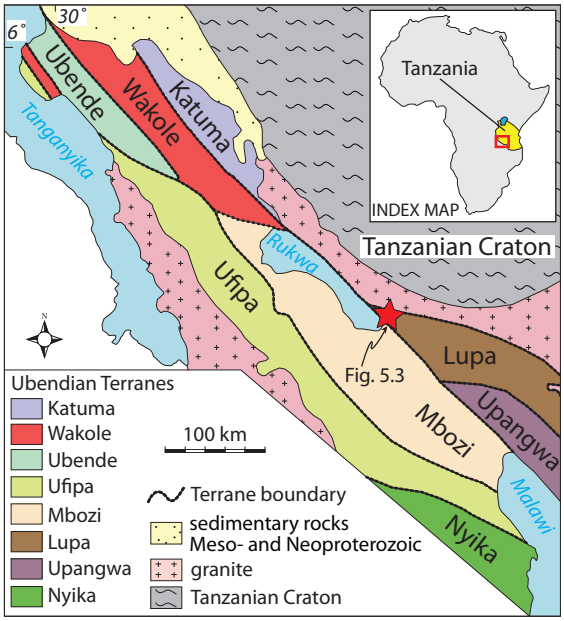

Figure 5.2 – Regional geologic map showing Ubendian Terranes and Tanzanian Craton. The star shows the location of the field area for the current study (modified from Daly, 1988).

facies metamorphism. Thus, all rock names are metamorphic and for the remaining discussion all igneous rock names should have the prefix "meta-". Archean granitoids (ca. 2750 Ma) are the earliest magmatic phase observed in the field area and alternating quartzofeldspathic and chlorite bands give the rock its characteristic banded appearance (Chapter Two; Fig. 5.4). This compositional banding is steeply dipping, generally trends E-W to WNW-ESE and varies in development from outcrop to outcrop, but is consistently present across the field area. Flattened quartz crystals, undulose extinction and cuspate/lobate quartz crystal grain boundaries are indicative of pressure solution and intracrystalline plastic deformation of quartz, which coupled with syntectonic metamorphic reactions (chlorite ± epidote ± calcite ± titanite replacement of primary Fe-Mg minerals), are the dominant deformation mechanisms (Figs. 5.4e, f). Crystal plastic deformation microstructures in quartz and the absence of similar structures in feldspar crystals suggest that deformation occurred at greenschist facies pressure-temperature conditions (Scholz, 1988). Greenschist facies metamorphism is also consistent with the chlorite ± epidote ± calcite metamorphic mineral assemblage (Fig. 5.4f), the absence of higher grade metamorphic minerals, and contrasts with the amphibolite–granulite facies rocks that characterize the other Ubendian Terranes (Lenoir et al., 1994). Non-foliated equigranular to porphyritic granitoids (e.g., monzogranite, syenogranite and granodiorite) and a dioritic–gabbroic suite of plutons and dikes intruded the Archean granitoids during the Paleoproterozoic (1960–1880 Ma; Chapter Two; Fig. 5.3).

5.3.2 Deformation events in the Lupa Terrane

Chapter Two provided U-Pb ages that constrain three, temporally distinct, deformation events (D1, D2, D3) recognized in the field. The first deformation event (D1) is restricted to foliated Archean granitoids, which are cross cut by non-foliated Paleoproterozoic granitoids, diorites and gabbroic rocks that broadly constrain the timing of D1 to 2750–1960 Ma (Chapter Two). Brittle-ductile mylonititc shear zones (D2) cross cut all of the dated magmatic phases, are the primary host for Au mineralization and are the main focus of the current study. Re-Os dating of syn-deformational pyrite suggest mylonitzation (D2) occurred at ca. 1880 Ma (Chapter Four). Pyrite (± Au) bearing quartz veins (D2) are locally cross cut by discrete brittle faults (D3). The timing of D3 is not constrained, however the brittle nature of the faults is in contrast to the crystal plastic deformation processes characteristic of deformation during D1 and D2 and suggests different geologic conditions during D3. The proposed temporally distinct deformation events are only those that are readily distinguished in the field and it is expected that structures have been periodically reactivated from the Paleoproterozoic to the present day (Kilembe and Rosendahl, 1992; Theunissen et al., 1996; Boniface and Schenk, 2012).

5.4 Methods

5.4.1 Lithogeochemistry

Two samples of Saza Granodiorite (Fig. 5.3) and two samples of a mylonitic shear zone cross cutting the Saza Granodiorite were analyzed for major and trace elements using

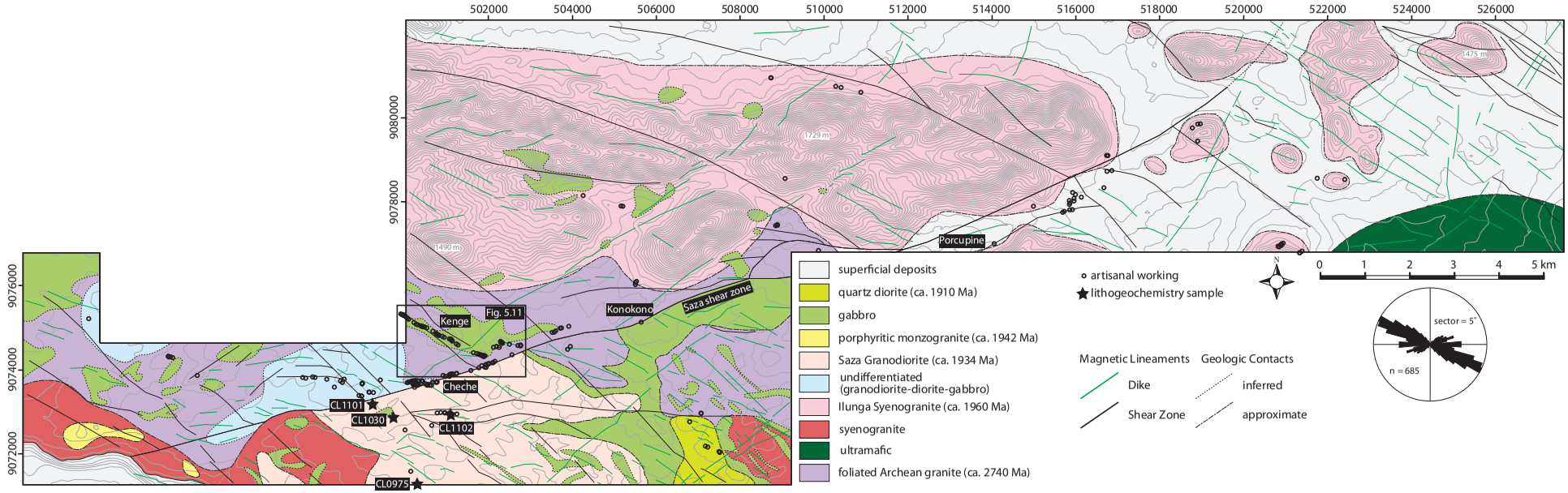

Figure 5.3 – Simplified local geology map showing the location of Kenge, Konokono, Porcupine and Cheche ore bodies. Artisanal workings visited during field seasons in 2010 and 2011 are also shown (open circles) and do not include alluvial workings, which are present in the majority of rivers in the field area. Eastings and northings are reported as UTM coordinates (WGS84, Zone 36S). Approximate lithologic contacts are based on a series of river traverses by the first author. Inferred lithologic contacts are based on unpublished aeromagnetic and radiometric surveys acquired from Helio Resource Corp. Shear zone locations are based, in part, on mapping and correspond to negative magnetic anomalies, whereas dikes are buried and interpreted from linear magnetic highs. The rose diagram shows the trend of magnetic lineaments picked at a 1:50,000 scale from the unpublished first vertical derivative aeromagnetic map. Contour lines are based on an unpublished digital elevation model by Helio Resource Corp. and are shown at 20 m intervals.

a combination of inductively coupled plasma-mass spectrometry (ICP-MS) and instrumental neutron activation analysis (INAA) by Actlabs (Ancaster, Ontario; method 4E-Research). Sample aliquants for ICP-MS analysis were first mixed with a lithium metaborate-tetraborate flux and fused in order to ensure complete digestion of refractory minerals (e.g., zircon). Detection limits for this assay package are in the low ppm and ppb range for most trace elements. These analyses were completed as part of larger geochemical study that included standards and duplicates as a means of quality control. The results for the two samples of un-altered Saza Granodiorite were previously reported in Chapter Two.

5.4.2 Oriented core

Oriented diamond drill holes from Kenge SE, Mbenge and Porcupine were surveyed using a Reflex™ digital down-hole survey tool and diamond drill core intervals were oriented using a combination of Ezy-Mark™ (of 2iC Australia™) and Reflex Act™ (of Reflex™) tools. Ezy-Mark™ and Reflex Act™ orientation tools are highly accurate; however the majority of orientation error can occur during the aligning and "locking" of oriented drill core sections

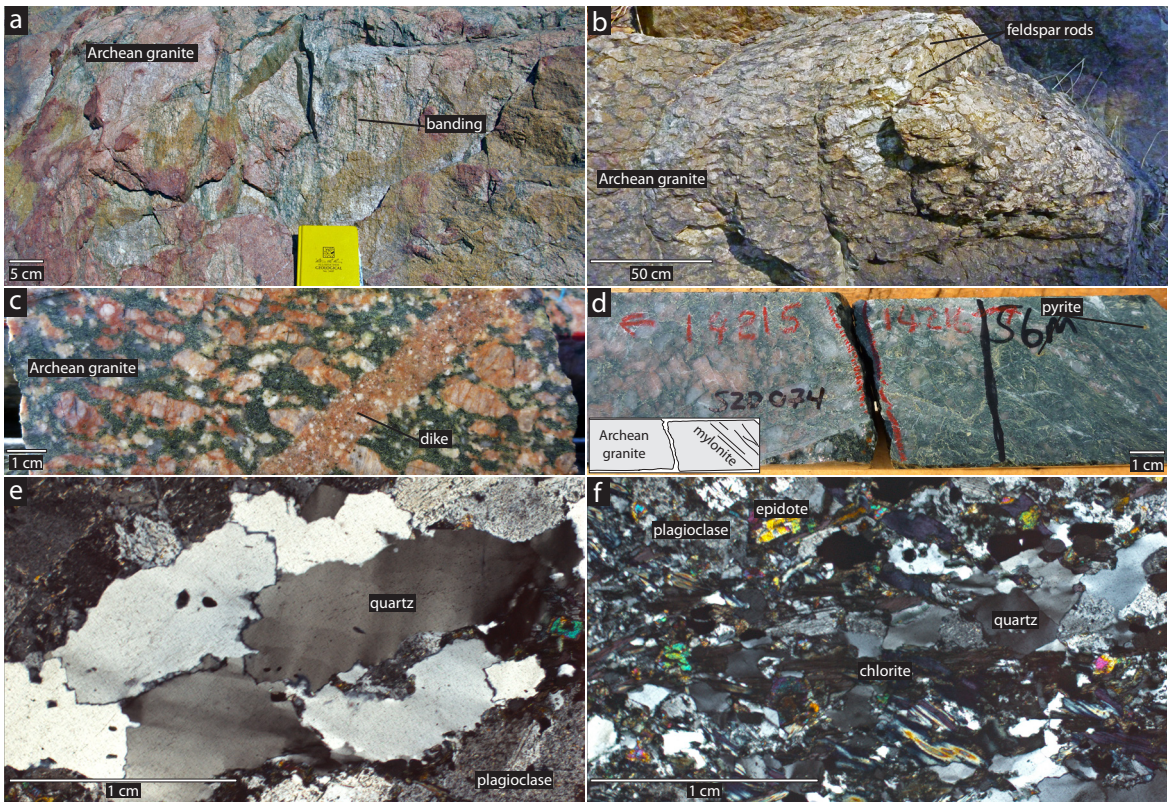

Figure 5.4 – (a–b) field photos of Archean granite highlighting the variability in structure and grain size of the lithologic unit; (c–d) core photos of the Archean granite cross cut by a non-foliated porphyritic dikes and mylonitic fault rocks (D2) cross cutting pre-existing foliation (D1); (e) crossed nicols photomicrograph of Archean granite showing undulatory extinction and cuspate-lobate quartz crystal boundaries; (f) crossed nicols photomicrograph of Archean granite showing alignment of chlorite and undulatory extinction in quartz. The alignment of quartz, K feldspar, and chlorite gives the rock a banded appearance in the field.

down- and up-drill hole (e.g., Blenkinsop and Doyle, 2010). These errors were minimized by selecting intervals of core where the orientation line at the beginning and end of the drill hole interval were within 10º of each other and avoiding intervals of bad ground. Planar and linear measurements were obtained following the method of Holcombe (2008). For planar measurements this involves measuring two angles (alpha and beta angle) relative to the core axis and the orientation line (the core bottom): 1) the alpha angle represents the angle between the core axis and the long axis of the elliptical cross section of the planar feature; and 2) the beta angle represents the angle between the long axis of the elliptical cross section of the planar feature extended down hole and measured clockwise from the orientation line. Alpha and beta measurements were converted to strike/dip (right-hand rule; RHR) and plunge/trend for planar and linear measurements, respectively using GeoCalculator©.

5.4.3 X-Ray Computed Tomography Scanning

Three-dimensional mineralogy analysis was completed on an oriented 1/4 core sample (SZD107 at 176 meters; drill hole azimuth = 360; dip = -49º) from the main ore zone at the Mbenge ore body. The sample is a greenschist facies mylonitic fault rock and is typical of other Au-bearing shear zones within the Lupa goldfield and globally. X-ray Computed Tomography (CT) was completed using a XT225 Metris (Nikon) scanner at the University of Leicester following the approach of Holwell et al. (2012). CT scanning produces a high resolution 3D computer model of the scanned sample that can be further processed to distinguish minerals based on their respective densities. The greater density of pyrite relative to the other mineral constituents comprising the sample matrix (chlorite, muscovite and quartz) allowed us to isolate the 3D shape and distribution of pyrite within the scanned sample. The latter provides valuable insight into grain-scale hydrothermal processes (discussed further below).

5.5 Structural Framework

5.5.1 Fault rock characteristics

Mylonitic fault rocks - Au-bearing mylonitic rocks, which developed during the D2 deformation event in the Lupa goldfield possess a range of matrix-porphyroclast modal proportions/grain sizes and represent the complete spectrum of mylonitic fault rock types (Snoke and Tullis, 1998; Figs. 5.5–5.8). Mylonite and protomylonite fault rock types are dominant and subordinate respectively, with rare ultramylonite observed as narrow <10 cm bands within mylonitic shear zones (Snoke and Tullis, 1998). The main mylonitic foliation is defined by millimetre-scale (locally centimetre-scale) bands of alternating phyllosilicate-rich and quartzofeldspathic micro-lithons. Shear band cleavages (C- and C'- types; Berthé et al., 1979) are locally observed and are characterized by a finer grain size and increased abundance of phyllosilicates compared to the dominant mylonitic foliation (Figs. 5.5e, 5.6b, 5.6c, 5.7c and 5.7h). Multiple C' planes observed at outcrop scale suggest either: 1) overprinting structural deformation produced temporally distinct shear band cleavages; and/or 2) ineffective flow partitioning during a single, but progressive, deformation event (Jiang and White, 1995). The latter is supported by a lack of clear cross

cutting relationships between mylonitic shear zones (Fig. 5.3). The grain size and phyllosilicate-rich nature of the Au-bearing mylonitic fault rocks are comparable to fault rocks previously described as phyllonites (e.g., Jefferies et al., 2006a). Quartz and plagioclase porphyroclasts are wrapped by phyllosilicates, possess oblate shapes (as determined by qualitative shape comparison on serially sliced oriented samples on the interpreted XZ and YZ finite strain planes; Figs. 5.5, 6, 7 and 8) and are consistent with flattening of what are interpreted to be originally equant quartz crystal shapes in the Paleoproterozoic granite protolith. Foliated Archean granitoids possessed flattened quartz crystals (Fig. 5.4e) prior to mylonitization and thus were not used to infer flattening strain. Linear shape fabrics are variably developed, but are subordinate to planar shape fabrics in all observed Au-bearing mylonitic shear zones. Lineations, where present, consist of quartz rods on fault-fill vein (discussed further below) and shear zone contacts, as ridges/grooves on the mylonitic foliation plane and as chlorite slickensides on chlorite vein surfaces and mylonitic foliation planes (Fig. 5.5c). The timing of lineation development is unclear and could represent reactivation of foliation surfaces during subsequent deformation and/or may have developed contemporaneously with the planar shape fabrics (Theunissen et al., 1996). The latter is supported by common mineral assemblage between linear and planar fabrics.

All observed shear zones possess a similar fault rock mineral assemblage (muscovite ± quartz ± chlorite ± calcite ± epidote ± pyrite ± graphite ± gold) that is consistent with metamorphism under greenschist facies pressure-temperature conditions (Figs. 5.7 and 5.8; discussed further below). Muscovite crystals (<0.01–5 mm) locally exhibit sweeping extinction, comprise the mylonite matrix and occur as fine-grained crystals (<10 μm) altering feldspar (plagioclase and K feldspar) porphyroclasts. Chlorite overprints muscovite, wraps quartz and feldspar porphyroclasts and gives a large proportion of mylonitic fault rocks a green appearance (Figs. 5.7c and 5.7f). Quartz exhibits sweeping extinction and occurs as mantled porphyroclasts (σ- type; Passchier and Simpson, 1986), aggregates of polygonal grains, quartz ribbons, pressures shadows and/or fringes, and veins (Fig. 5.8c). Feldspars (plagioclase and K feldspar) exhibit bent twin planes, are present as mantled porphyroclasts (σ- type), are associated with quartz within micro-lithons and are typically absent in high-strain shear zones (completely replaced by phyllosilicates; Fig. 5.8d).

Non-foliated fault rocks - Non-foliated fault rocks observed in the current study represent the complete spectrum of fault rocks classified by Snoke and Tullis (1998; Fig. 5.9). Unaltered cataclasites are locally observed becoming increasingly altered towards mylonite contacts and implies an early phase of brittle deformation that pre-dates hydrothermal alteration related to mylonitization (D2). Pre-D2 brittle deformation is also suggested by vein-mylonite cross cutting relationships and Re-Os sulfide dating, which suggests quartz veins locally pre-date mylonitization by ca. 70 Myr (Fig. 5.9b; Chapter Four). Quartz vein and mylonite clasts observed within cataclasites cross cutting Au-bearing shear zones imply cataclasis also occurred after the D2 event (Fig. 5.9d) and is consistent with discrete brittle faults offsetting mineralized veins. Therefore, the temporal relationship between brittle and ductile deformation is complex, locally interpreted as contemporaneous and is consistent with progressive deformation at the level of

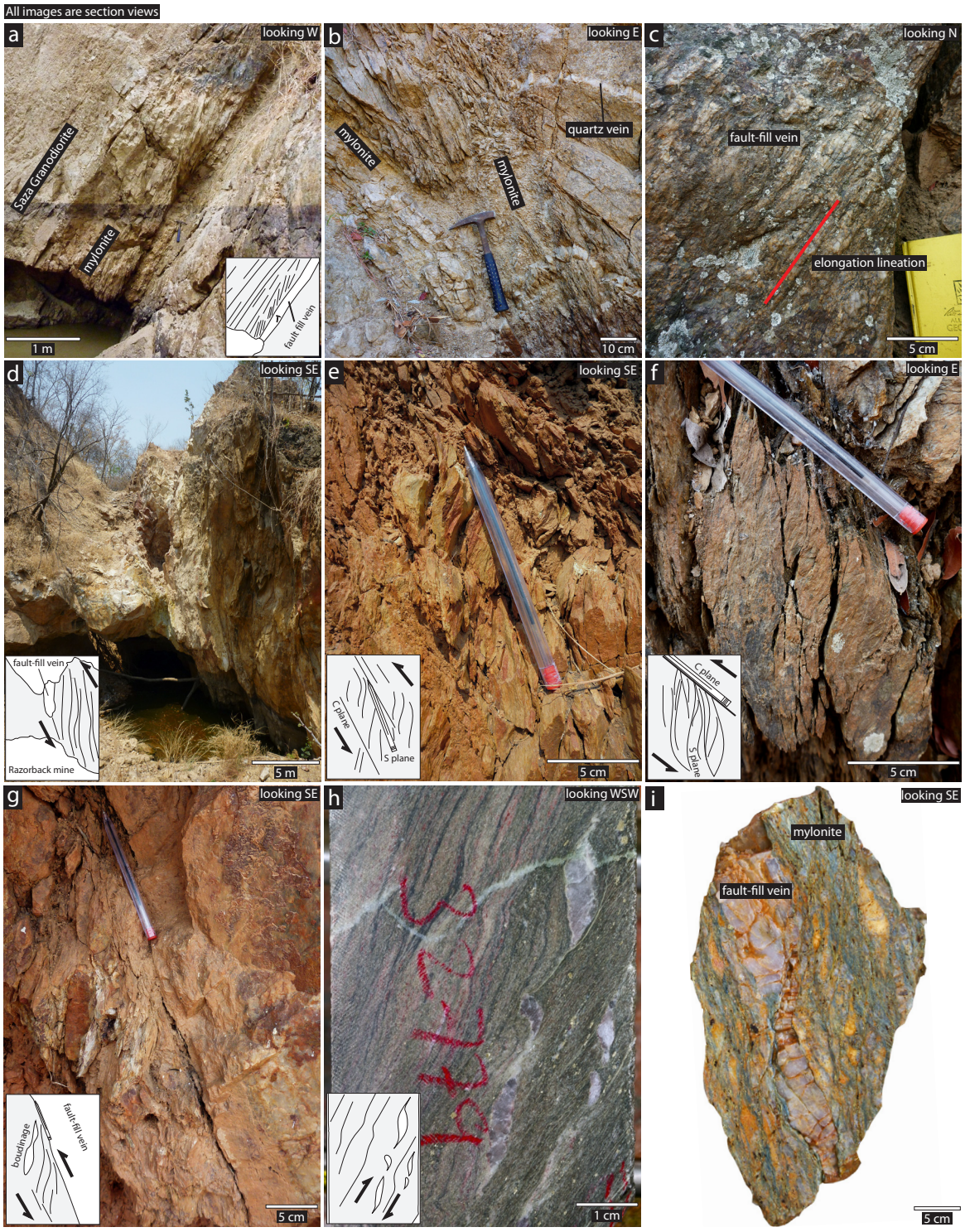

Figure 5.5 – (a) Photo of E-W trending shear zone from artisanal working. The complete transition from hydrothermally altered Saza granodiorite to mylonitic shear zone is exposed; (b) photo of quartz veins pre-dating E-W trending shear zone at artisanal working; (c) quartz rods on fault-fill vein and mylonitic shear zone contact; (d) photo from the Kenge ore body looking SE (standing in what was formerly known as Razorback mine). The mylonitic foliation possesses a steeper dip relative to the shear zone boundary (ca. 70º; not shown); (e) photo from artisanal working at the Kenge SE zone showing S/C fabrics indicative of south-side up movement; (f) photo from E-W trending artisanal working showing S/C fabrics indicative of south-side up movement; (g) photo from artisanal working at the Kenge main zone showing S/C fabrics indicative of south-side up movement; (h) photo of partially oriented core from Porcupine showing asymmetric porphyroclasts and the mylonitic foliation wrapping quartz-feldspar micro-lithons; (i) oriented sample from NW trending shear zone showing deformed fault-fill vein.

the brittle-ductile transition zone. Pseudotachylite fault rocks are also observed cross cutting Archean granites (Fig. 5.9a). These fault rocks possess a black fine grained matrix, angular granite clasts, offset quartz veins and are associated with injection veins. Devitrification structures and spherulites were not observed in pseudotachylite veins and mutually cross cutting relationships between pseudotachylite fault rocks and quartz (± calcite) may indicate that these fault rocks are in fact veins or cataclasites filled with dark minerals (suspected pseudotachylite veins are locally magnetic and could be in-filled with fine-grained magnetite). Unconsolidated gouge has also been observed at Kenge and is suspected to be related to near surface faulting in response to the Tertiary East African Rift System (Theunissen et al., 1996; Kilembe and Rosendahl, 1992). The temporal relationships between disparate non-foliated fault rock types remain unclear. Nevertheless the field evidence presented above and age dating supports periodic reactivation of structures from the Paleoproterozoic to the present day (Boniface et al., 2012).

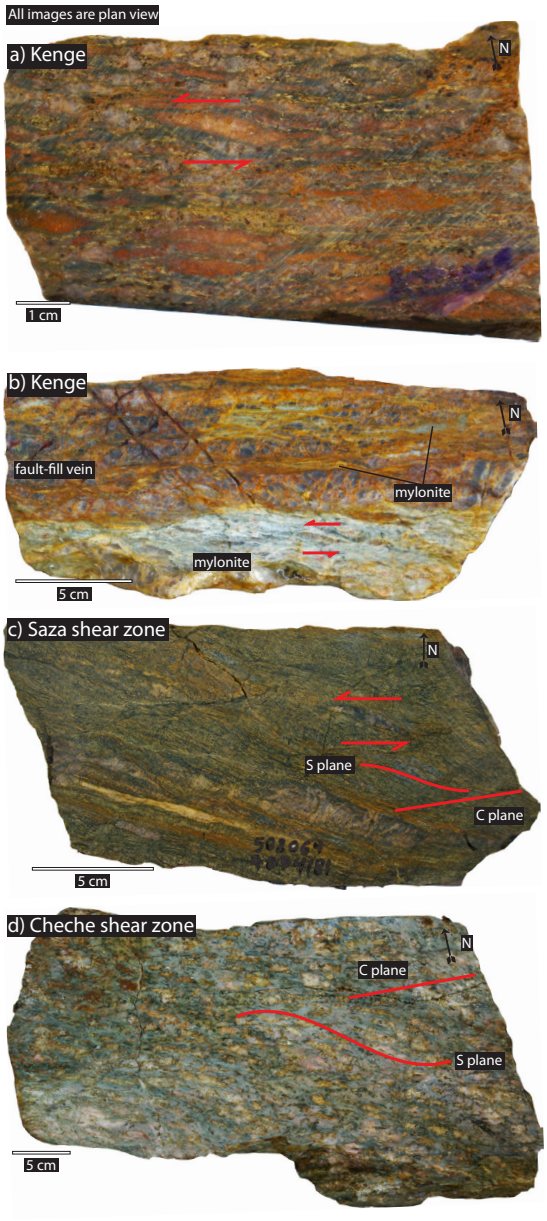

Figure 5.6 – (a) Oriented sample from Kenge ore body showing asymmetric porphyroclasts in plan view suggesting sinistral movement; (b) oriented sample from the Saza shear zone showing asymmetric porphyroclasts and S/C fabrics in plan view suggesting sinistral movement; (c) oriented sample from the Kenge shear zone showing asymmetric porphyroclasts in mylonitic foliation and fault-fill vein. Note slivers of mylonite and complex fracture patterns within the fault-fill vein; (d) oriented sample from Cheche shear zone showing asymmetric porphyroclasts and discontinuous S/C fabrics in plan view again consistent with sinistral shear.

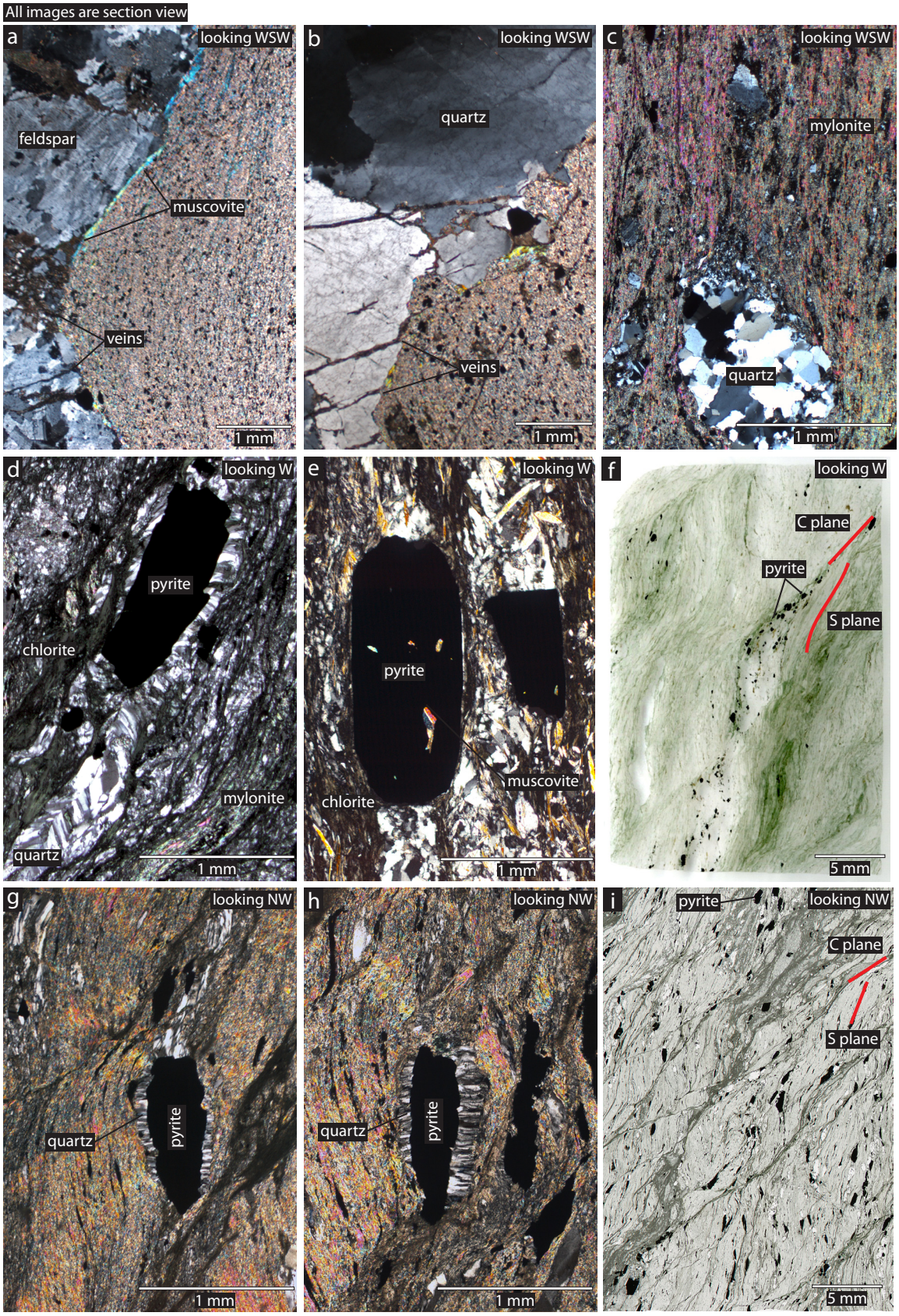

Figure 5.7 – Section view photomicrographs of Porcupine (a–c), Mbenge (d–f), and Kenge (g–i): (a) crossed nicols photomicrograph of sharp and undulating mylonite-granite contact cross cutting muscovite ± calcite ± chlorite veins (GPD44 at 211m); (b) crossed nicols photomicrographs of sharp and undulating fault-fill vein-mylonite contact cross cutting muscovite ± calcite ± chlorite veins (GPD44 at 212m); (c) crossed nicols photomicrograph of quartz porphyroclasts (GPD44 211 m); (d) pyrite wirh quartz strain fringes (SZD74 at 58m); (e) crossed nicols photomicrograph of muscovite included within a pyrite crystal that is concordant with mylonitic foliation

CONT'D... (SZD174 at 48m); (f) plane polarised light photomicrograph of S/C fabrics consistent with reverse movement (south-side up; SZD74 at 58m); (g–h) crossed nicols photomicrographs of pyrite with quartz strain fringes orthogonal to mylonitic foliation (SZD71 at 53m); (i) plane polarised light photomicrograph of S/C fabrics consistent with reverse movement (south-side up; SZD71 at 53m)

5.5.2 Shear zone geochemistry

Two samples of mylonitic shear zones cross cutting the Saza granodiorite were analyzed for major and trace elements (see Table 5.1; Fig. 5.10) to compare against the chemical composition of unaltered Saza Granodiorite (previously reported in Chapter Two) akin to the isocon analysis approach (Grant, 1986). Isocon analysis involves plotting the composition of altered samples against unaltered equivalent samples in order to distinguish mobile and immobile elements during hydrothermal alteration related to mylonitization (Grant, 2005 and references therein). The approach is a graphical solution to Gresens's (1967) zero concentration change equations and predicts that immobile elements will plot as a straight line extending from the origin, whereas mobile elements will plot off this line. Our results show that many of the elements considered to be immobile (e.g., TiO_2, Al_2O_3, light rare earth elements, high-field strength elements and transition elements) plot on or near the unit slope, whereas mobile elements (e.g., MnO and Sr) plot significantly off the unit slope (Fig. 5.10). The significance of those elements that plot slightly above or below the unit slope is unclear since compositional heterogeneity between samples, especially for our small sample set, likely causes some immobile elements to plot off the unit slope (Fig. 5.10a). Nevertheless, the majority of elements plot on or near the unit slope and implies significant volume loss and elemental differentiation were not associated with mylonitization.

Several elements plot significantly below the unit slope, for example MnO and Sr, and imply that these elements were lost during hydrothermal alteration. The loss of Sr is consistent with albite replacement during mylonitization and is supported by slight depletion and enrichment of Na_2O (plots slightly below the unit slope) and K_2O (plots slightly above the unit slope), respectively (Fig. 5.10b). Other elements, for example Sb and Cr, plot considerably above the others and suggest that these elements were gained during hydrothermal alteration related to mylonitization. The dominant source of Cr in the Lupa goldfield is present within gabbroic intrusions/dikes and we propose that fluids migrating through shear zones may have scavenged Cr from intermediate-mafic rocks and deposited them within mylonitized Saza Granodiorite. The enrichment of Sb and As is typical of many epigenetic Au deposits, however in this case Sb is not accompanied with any noticeable enrichment of As and suggests these two elements were de-coupled during hydrothermal alteration associated with mylonitization (Craw et al., 2002).

5.5.3 Shear Zone Kinematics

Shear zone kinematics were interpreted from inspection of rock exposures within artisanal shafts and trenches, oriented drill core and serially sliced oriented hand samples (Figs. 5.5, 5.6,

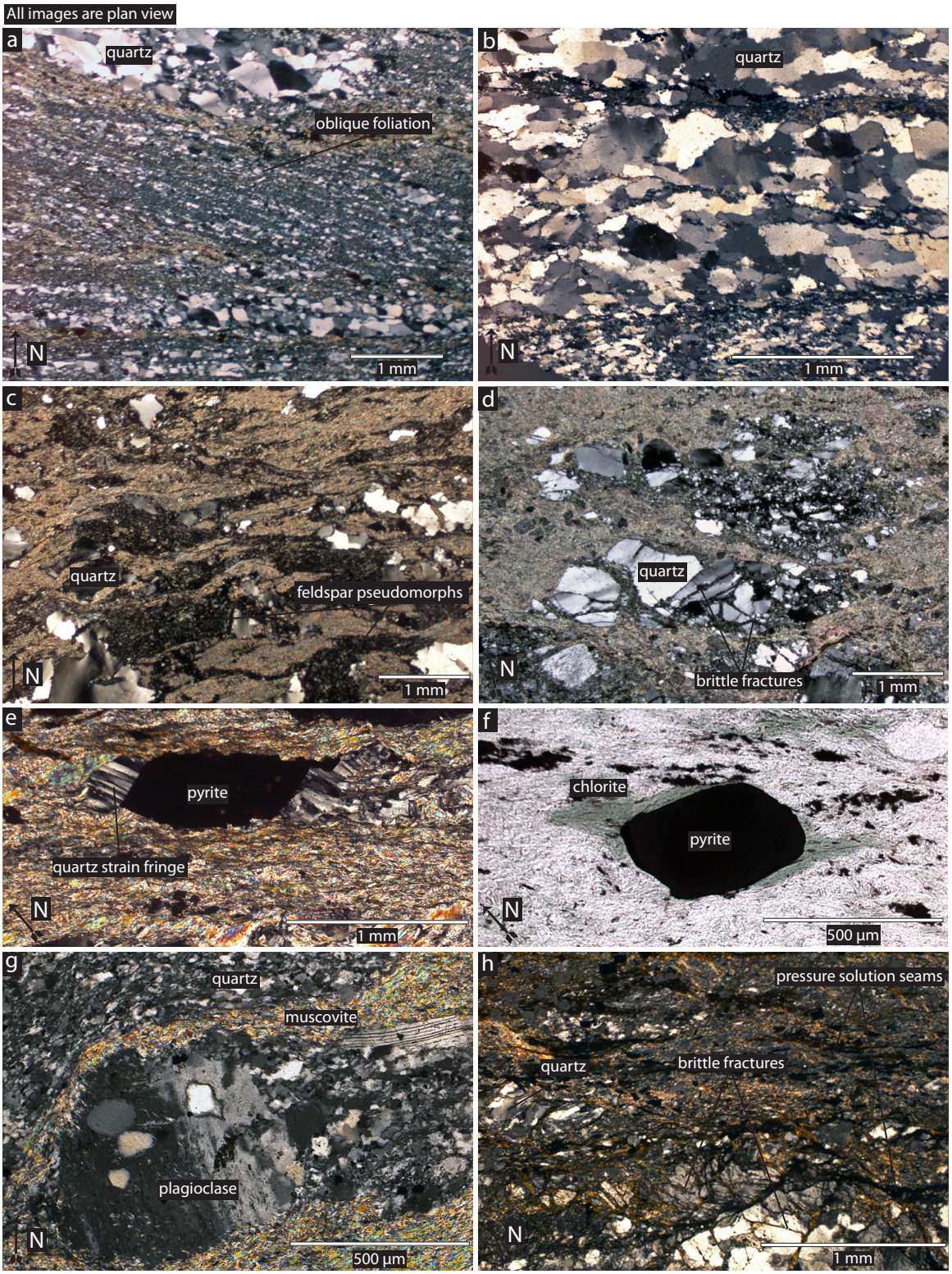

Figure 5.8 – Plan view photomicrographs: (a) crossed nicols photomicrograph of oblique foliation development in plan view (518905, 9079993); (b) crossed nicols photomicrograph showing undulatory extinction, dynamic recrystallization and sub-grain rotation in quartz (518905, 9079993); (c) crossed nicols photomicrograph of feldspar pseudomorphs and strained quartz (498933, 9073405); (d) crossed nicols photomicrograph of quartz ribbons, undulatory extinction and dynamic recrystallization in quartz (499282, 9073258); (e) crossed nicols photomicrograph of pyrite with quartz strain fringe (501850, 9074362); (f) plane polarized light photomicrograph of asymmetric pyrite porphyroclast (501850, 9074362); (g) crossed nicols photomicrograph of plagioclase porphyroclasts wrapped by mylonitic fabric. Note dynamic recrystallization of quartz and neocrystallization of feldspar at porphyroclasts margin (501137, 9072969); (h) crossed nicols photomicrograph of brittle fractured

CONT'D... feldspars and quartz within the mylonitic matrix. Note dark brown, undulating pressure solution seams concordant with mylonitic foliation (502064, 9074181).

5.7 and 5.8). The mylonitic foliation is considered here to approximately record the XY plane of the finite strain ellipsoid (Jones et al., 2004). As a result, sub-horizontal and sub-vertical planes perpendicular to the mylonitic foliation are interpreted as the YZ and XZ planes of the finite strain ellipsoid, respectively. Most of the observed shear zones are south-dipping structures that possess multiple kinematic indicators on the sub-vertical plane perpendicular to the mylonitic foliation (section view; XZ plane). Asymmetric porphyroclasts (σ-type; Hanmer and Passchier, 1991), asymmetric pressure shadows, asymmetric boudins, and S/C textures are all indicative of reverse movement (south-side up). Kinematic indicators are also observed, but less abundant, on the sub-horizontal plane perpendicular to the mylonitic foliation (plan view; YZ plane). Asymmetric porphyroclasts, asymmetric boudins and S/C textures in plan view, where observed, are indicative of sinistral movement. Together the observed kinematic indicators imply a finite oblique reverse slip displacement vector on northwest-southeast and east-west striking and south-dipping shear zones (Figs. 5.5 and 5.6). Mineral stretching lineations are variably oriented at outcrop scale despite the consistent kinematics inferred from kinematic indicators (Fig. 5.11). This is particularly apparent for the regionally significant Saza shear zone which is interpreted to have undergone reverse oblique slip despite possessing generally steep, but variably plunging, mineral stretching lineations (Fig. 5.11). The presence of kinematic indictors on both planes perpendicular to the mylonitic foliation implies non-coaxiality of both strike-slip and dip-slip strain components and are typical of shear zones exhibiting triclinic, or lower, symmetry (Jiang and Williams, 1998; Jones and Holdsworth, 1998; Lin et al., 1998; Jones et al., 2004). Mineral stretching lineation orientations in transpressional shear zones can vary continuously from horizontal to sub-vertical and thus generally cannot be used to infer movement direction (Lin and Jiang, 2001). Furthermore, strain partitioning can further complicate the interpretation of mineral stretching lineation orientations in transpressional settings where pure- and strike-slip deformation components may vary across the shear zone (discussed further below).

5.6 Mineral system and vein characteristics

Inspection of artisanal workings and oriented core reveals a remarkable variability of Au-bearing structures in the Lupa goldfield. Most of the exposed Au occurrences are hosted by steeply dipping quartz veins and mylonitic shear zones and are typical of the Kenge and Mbenge ore bodies (Figs. 5.3, 5.11, and 5.12). Hydrothermal alteration, strain and mineralization at these Au occurrences are largely restricted to the host shear zone (Fig. 5.13). Recent drilling by Helio Resource Corp. has identified a second, geologically distinct, mineral system type (e.g., Porcupine) that comprises a network of narrow and discontinuous mylonitic shear zones separated by non-foliated but hydrothermally altered and veined granite (Fig. 5.14). The highest

Au grades at Porcupine are associated with shallow dipping quartz veins and intervals of sericitized, silicified and non-foliated Ilunga syenogranite (Fig. 5.14). Auriferous and shallow dipping quartz veins occur adjacent to the mylonitic shear zones, which significantly widen the mineralized zone at Porcupine, are notably absent at the Kenge and Mbenge ore bodies. Detailed geologic characteristics for Kenge, Mbenge and Porcupine are discussed further below.

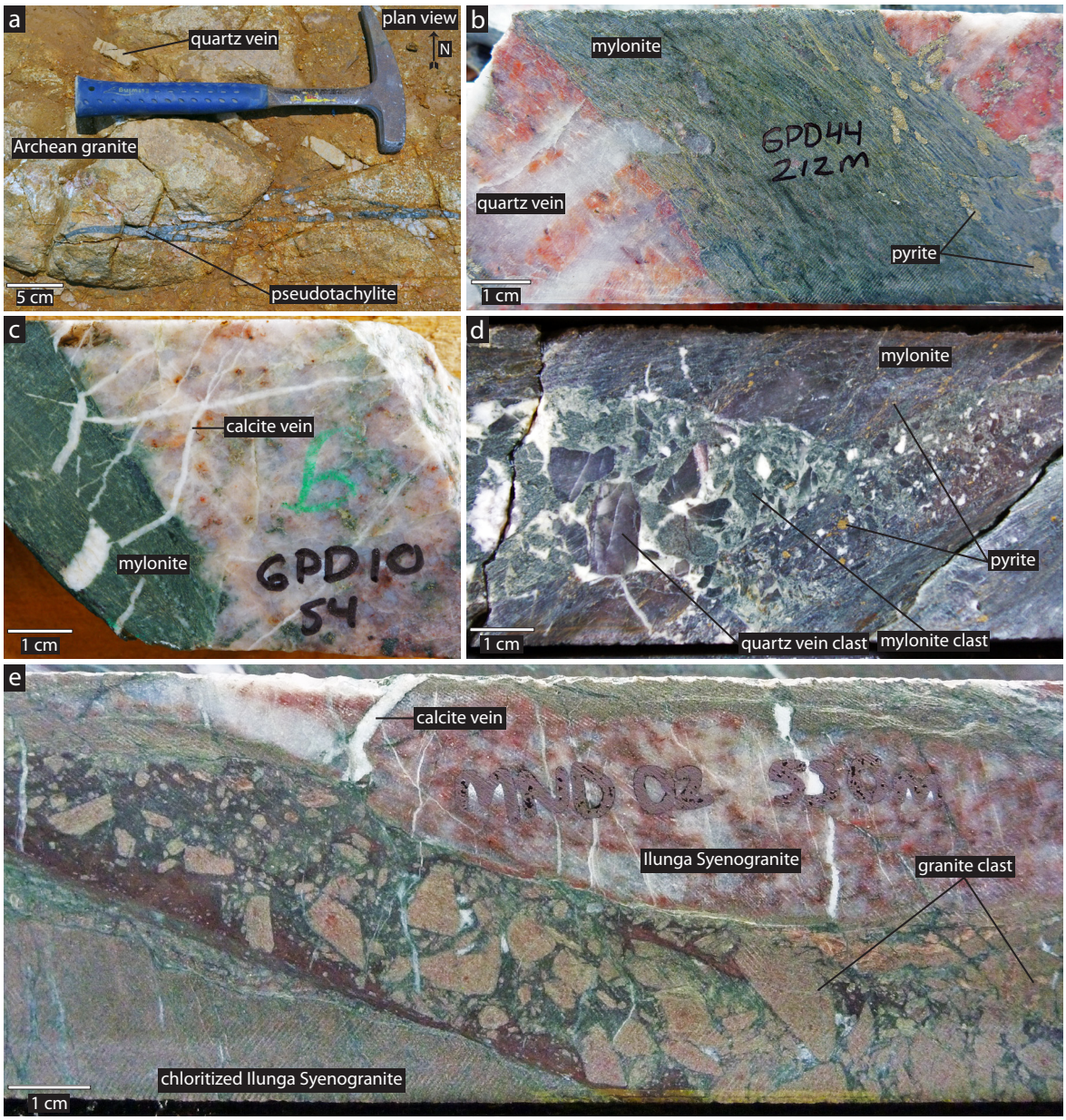

Figure 5.9 – (a) Plan view photo of suspected pseudotachylite fault rock offsetting quartz veins and cross cutting Archean foliated granite; (b) quartz veins cross cutting Ilunga syenogranite and becoming transposed sub-parallel to the mylonitic foliation; (c) calcite veins cross cutting Ilunga Syenogranite and mylonite. Calcite veins are in turn offset by later movement parallel to mylonitic foliation; (d) cataclasites cross cutting mineralized mylonite; (e) cataclasites cross cutting and containing angular to sub-rounded clasts of Ilunga Syenogranite. Note complex calcite veining.

5.6.1 Kenge and Mbenge

The Kenge and Mbenge ore bodies contain a measured and indicated resource of 370,000 oz (8.7 Mt at 1.33 g/t Au using a 0.5 g/t Au cut-off; Simpson, 2012) and include what was known as Razorback mine (Figs. 5.11; van Straaten, 1984; Sango, 1988; Kuhen et al., 1990). The Kenge ore body is associated with NW–SE striking (ca. 120º), SW dipping (ca. 70º) and left-stepping shear zones. Each NW–SE trending shear zone segment is connected to a more WNW trending shear zone segment and gives the ca. 2 km long ore body en-echelon geometry (Fig. 5.11). The mineralization at Kenge is discontinuous down-dip and Helio Resource Corp., has hypothesized a NW–SE trending reverse fault offsetting the main mineralized zone (Fig. 5.13). The dominant NW–SE trend of the Kenge ore body changes towards the SE and becomes more WNW trending (ca. 103º) and this segment is known as the "Kenge SE" zone (Harrison, 2011).

Examination of diamond drill core has established that the Kenge shear zone occurs at the igneous contact between the Archean granitoid (hangingwall) and Paleoproterozoic diorite-gabbro intrusion (footwall; Fig. 5.13). Therefore, igneous contacts appear to have acted as zones of pre-existing weakness and/or stress risers during deformation (Dubé et al., 1989; Lin and Corfu, 2002). Au is found as free grains and is also associated with pyrite hosted by mylonitic fault rocks and fault-fill veins (Robert and Poulsen, 2001 and references therein). The mylonitic foliation at Kenge and Mbenge varies in development and orientation, but is typically

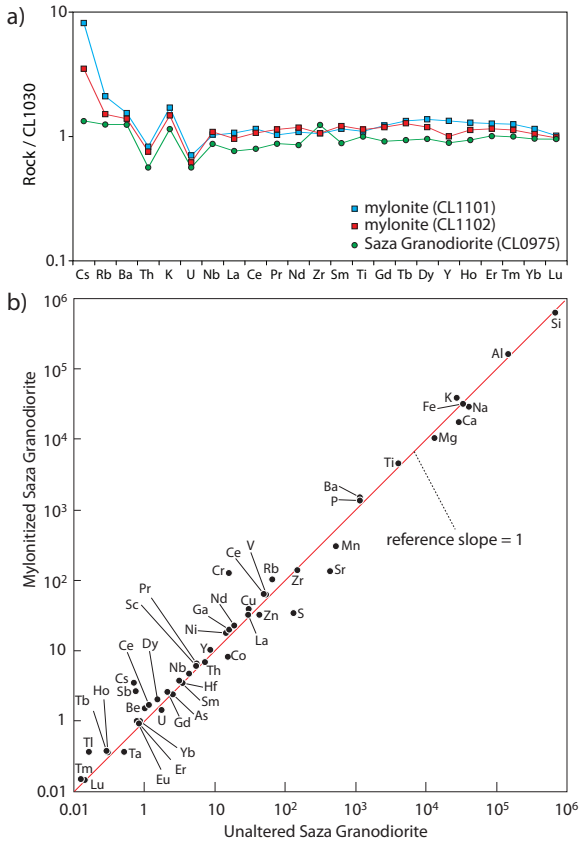

Figure 5.10 – (a) Trace element plot normalized to unaltered Saza Granodiorite sample CL1030. Note trace element homogeneity between all 4 samples except for large ion lithophile elements (e.g., Cs, Rb, Ba); (b) Diagram comparing the concentrations of elements in mylonitized Saza granodiorite and unaltered Saza Granodiorite. Elements concentrations are average values based on 2 samples of mylonitized and unaltered Saza Granodiorite. Major element oxide analyses were converted to elemental parts per million. Solid line represents the unit slope (slope = 1) and defines constant composition.

Table 5.1 - Lithogeochemistry Results

				CL1101	CL1102
Analyte	Analysis Method[1]	Unit[2]	D.L.	499282 / 9073258[3]	501137 / 9072969[3]
SiO2	FUS-ICP	%	0.01	67.44	62.77
Al2O3	FUS-ICP	%	0.01	15.94	17.19
Fe2O3(T)	FUS-ICP	%	0.01	3.7	2.83
MnO	FUS-ICP	%	0.001	0.032	0.028
MgO	FUS-ICP	%	0.01	1.38	0.73
CaO	FUS-ICP	%	0.01	0.46	3.09
Na2O	FUS-ICP	%	0.01	1.83	4.06
K2O	FUS-ICP	%	0.01	4.32	3.73
TiO2	FUS-ICP	%	0.001	0.445	0.46
P2O5	FUS-ICP	%	0.01	0.13	0.14
LOI	FUS-ICP	%		3.06	4.13
Total	FUS-ICP	%	0.01	98.74	99.14
Au	INAA	ppb	1	< 1	40
Ag	TD-ICP	ppm	0.5	< 0.5	< 0.5
As	INAA	ppm	1	2	3
Ba	FUS-ICP	ppm	1	1553	1399
Be	FUS-ICP	ppm	1	1	2
Bi	FUS-MS	ppm	0.1	0.1	0.3
Br	INAA	ppm	0.5	< 0.5	< 0.5
Cd	TD-ICP	ppm	0.5	< 0.5	< 0.5
Co	INAA	ppm	0.1	7.7	9.4
Cr	INAA	ppm	0.5	128	118
Cs	FUS-MS	ppm	0.1	4.9	2.1
Cu	TD-ICP	ppm	1	32	47
Ga	FUS-MS	ppm	1	19	20
Ge	FUS-MS	ppm	0.5	1.7	1.7
Hf	FUS-MS	ppm	0.1	3.5	3.4
Hg	INAA	ppm	1	< 1	< 1
In	FUS-MS	ppm	0.1	< 0.1	< 0.1
Ir	INAA	ppb	1	< 1	< 1
Mo	FUS-MS	ppm	2	< 2	< 2
Nb	FUS-MS	ppm	0.2	4.7	5
Ni	TD-ICP	ppm	1	23	13
Pb	TD-ICP	ppm	5	< 5	11
Rb	FUS-MS	ppm	1	120	86
S	TD-ICP	%	0.001	0.003	0.004
Sb	INAA	ppm	0.1	2.7	2.6
Sc	INAA	ppm	0.01	5.78	6.37
Se	INAA	ppm	0.5	< 0.5	< 0.5
Sn	FUS-MS	ppm	1	1	< 1
Sr	FUS-ICP	ppm	2	94	178
Ta	FUS-MS	ppm	0.01	0.36	0.39
Th	FUS-MS	ppm	0.05	7.52	6.84
U	FUS-MS	ppm	0.01	1.56	1.37
V	FUS-ICP	ppm	5	60	74
W	INAA	ppm	1	3	9
Y	FUS-ICP	ppm	1	12	9
Zn	TD-ICP	ppm	1	34	30
Zr	FUS-MS	ppm	1	139	140
La	FUS-MS	ppm	0.05	35.2	31.7
Ce	FUS-MS	ppm	0.05	68.1	63.1
Pr	FUS-MS	ppm	0.01	6.15	6.81
Nd	FUS-MS	ppm	0.05	21.8	23.8
Sm	FUS-MS	ppm	0.01	3.73	3.94
Eu	FUS-MS	ppm	0.005	0.994	1.01
Gd	FUS-MS	ppm	0.01	2.73	2.65
Tb	FUS-MS	ppm	0.01	0.4	0.38
Dy	FUS-MS	ppm	0.01	2.18	1.89
Ho	FUS-MS	ppm	0.01	0.4	0.35
Er	FUS-MS	ppm	0.01	1.08	0.98
Tl	FUS-MS	ppm	0.05	0.42	0.32
Tm	FUS-MS	ppm	0.005	0.158	0.142
Yb	FUS-MS	ppm	0.01	1	0.91
Lu	FUS-MS	ppm	0.002	0.148	0.142

[1]Analysis method abbreviations: FUS-ICP = Fusion Inductively Coupled Plasma Mass Spectrometry; INAA = Instrumental Neutron Activation Analysis; TD-ICP = Total Dissolution Inductively Coupled Plasma Mass Spectrometry; MULT INAA = Multi-element Instrumental Neutron Activation Analysis

[2]Detection Limit

[3]eastings and northings are reported as UTM coordinates (WGS84, Zone 36S)

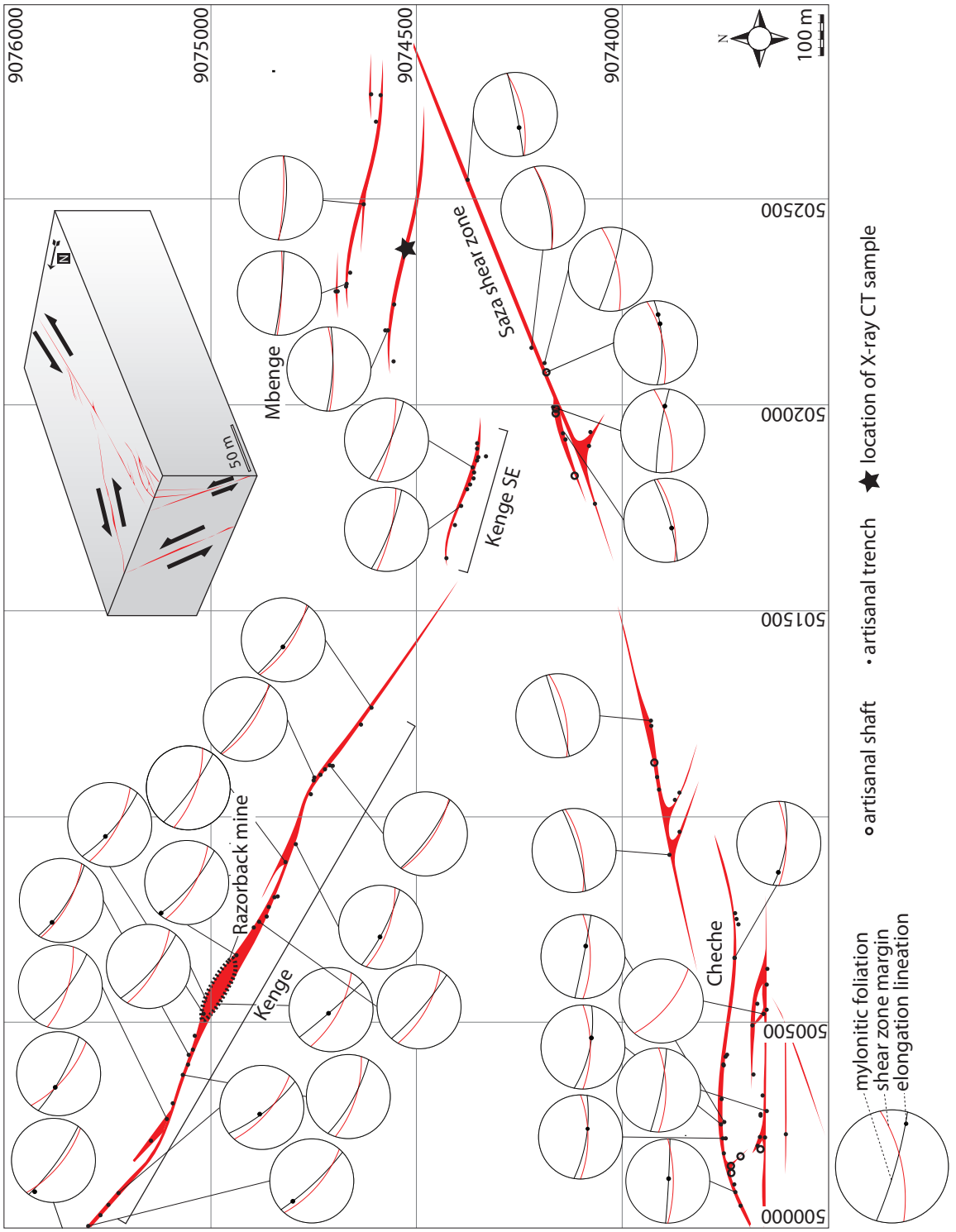

Figure 5.11 – Map of the Kenge and Mbenge shear zones showing the orientation of individual mylonitic foliation measurements, shear zone boundaries and individual mineral stretching lineation measurements. The locations of artisanal trenches/shafts are shown and were used to interpret the continuity of the mineralized shear zones (red polygons). The mylonitic foliation is generally more steeply inclined and oriented clockwise relative to the shear zone boundaries and suggests reverse (south-side up) and sinistral kinematics. Interpreted kinematics and shear zone orientations are summarized in the schematic block model.

more steeply dipping and oriented clockwise relative to the shear zone boundary. The reverse and sinistral kinematics suggested by the obliquity between the mylonitic foliation and shear zone boundary are consistent with kinematics inferred from asymmetric porphyroclasts and shear band cleavage fabrics observed on both planes perpendicular to the mylonitic foliation regardless of mineral stretching lineation orientation (Figs. 5.5 and 5.6). The observed kinematic indictors thus consistently imply a transpressional structural setting for the shear zones that is further supported by flattening strain inferred from quartz veins boudinaged in plane and section views, oblate-shaped quartz/feldspar porphyroclasts and variably plunging mineral stretching lineations (Jones et al., 2004).

Pyrite (± Au) crystals are locally observed concentrated in low-strain sites within the Kenge and Mbenge shear zones (e.g., quartz vein boudin necks) and also possess quartz strain fringes

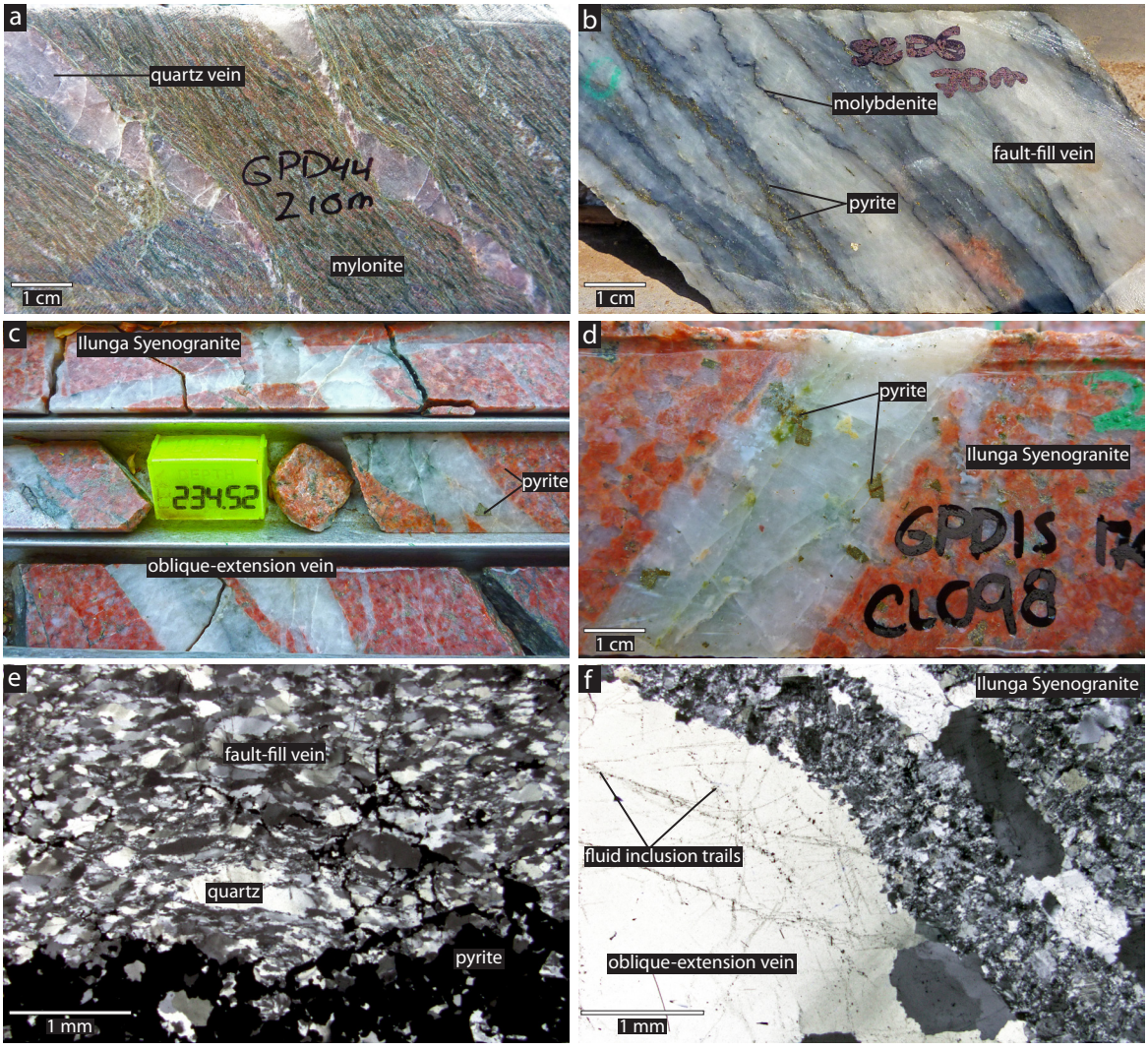

Figure 5.12 – Quartz vein photos from non-oriented core: (a) boudinaged and potentially transposed quartz veins hosted by mylonitic shear zone at Porcupine; (b) fault-fill vein at Saza shear zone showing stylolite-like sulfide stringer veins; (c) oblique-extension veins at Porcupine; (d) oblique-extension vein at Porcupine; (e) crossed nicols photomicrogrpah of fault-fill quartz vein. Note flattening and sub-grain rotation (SZD23 at 107m); (f) oblique extension vein at Porcupine. Not less deformed nature of quartz compared to fault-fill veins (GPD1 at 54m).

that provide evidence for complex temporal relationships between sulphidation, greenschist facies metamorphism, pressure solution processes and deformation. For example, apparently unmodified quartz strain fringe fibres are observed in the same hand samples as transposed quartz strain fringe fibres and likely records strain fringe development during progressive deformation. The orientation of apparently unmodified quartz strain fringe fibres perpendicular to the mylonitic foliation represents a paradox as previous studies have demonstrated that the long axis of straight strain fringe fibres record the X axis of the instantaneous strain ellipsoid (e.g., Durney and Ramsay, 1973; Köhn et al., 2003). If the mylonitic foliation is assumed to

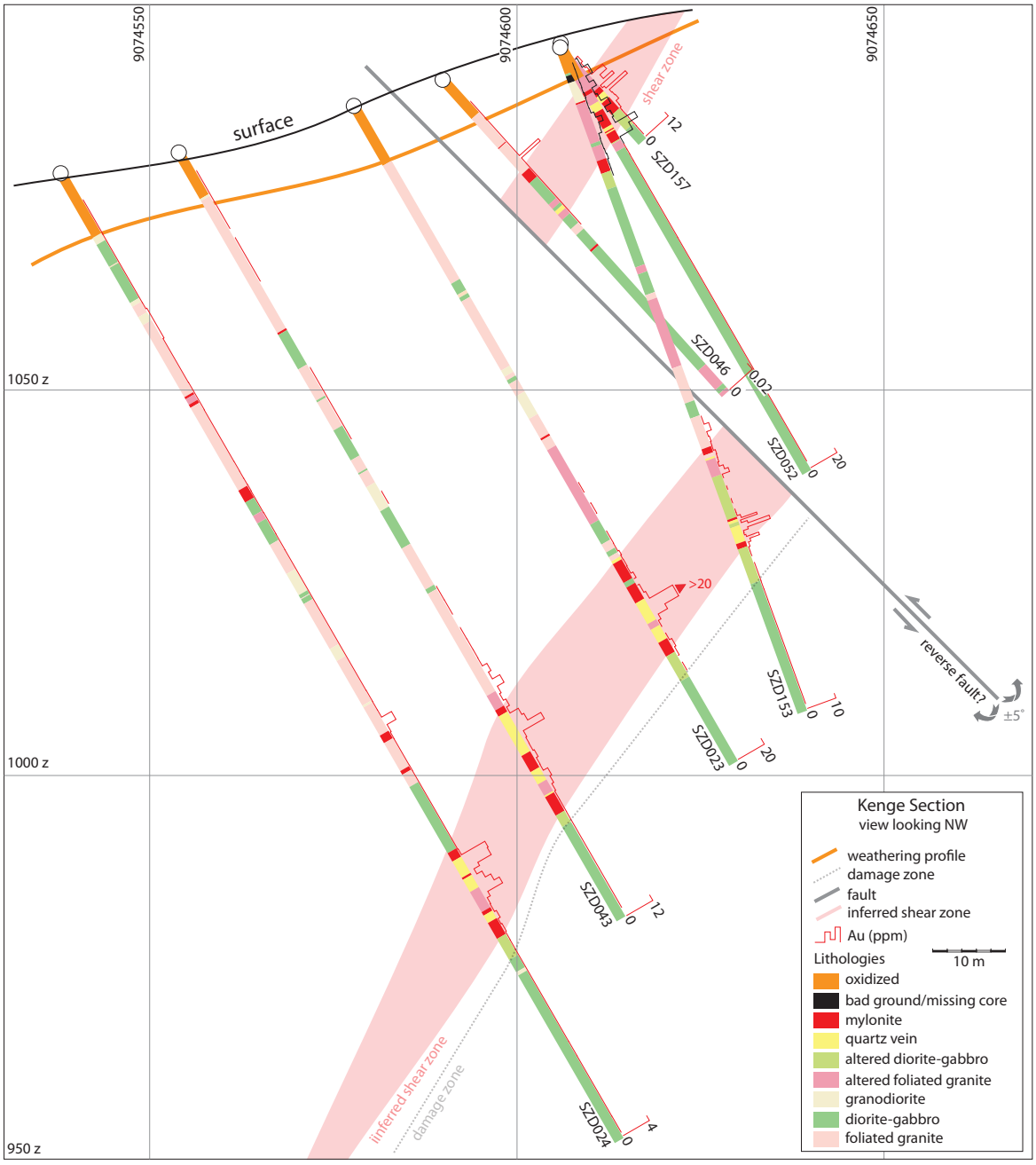

Figure 5.13 – Cross section of Kenge with lithology logs parallel to diamond drill hole traces. Note inferred reverse fault offsetting the interpreted mylonitic shear zone.

approximate the XY plane of the finite strain ellipsoid, then quartz fringe fibres perpendicular to the foliation are oriented roughly parallel to the Z axis of the finite strain ellipsoid (Figs. 5.7h and 5.7i). In the Lupa goldfield, quartz fibre growth on pyrite crystals potentially record the orientation of the instantaneous strain ellipsoid at the time of mineralization and thus provide valuable insight mineralizing processes and also shed light on the emplacement mechanisms of economically important fault-fill veins (discussed further below).

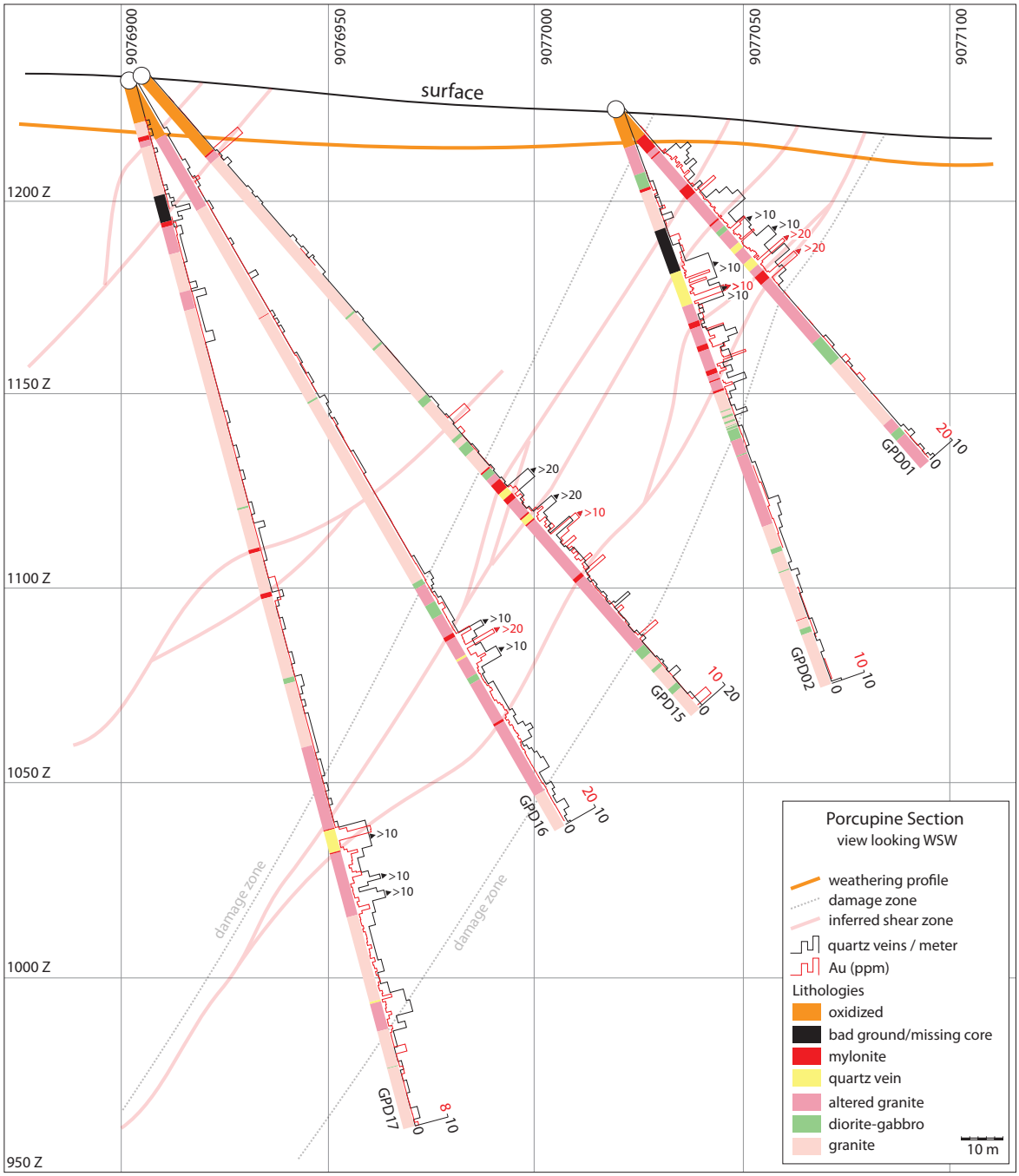

Figure 5.14 – Cross section of Porcupine with lithology logs parallel to diamond drill hole traces. Note correlation between quartz vein intensity (measured as quartz veins / meter) and Au grade. The extent of the damage zone is inferred from the increase in quartz vein density near the interpreted shear zone boundaries.

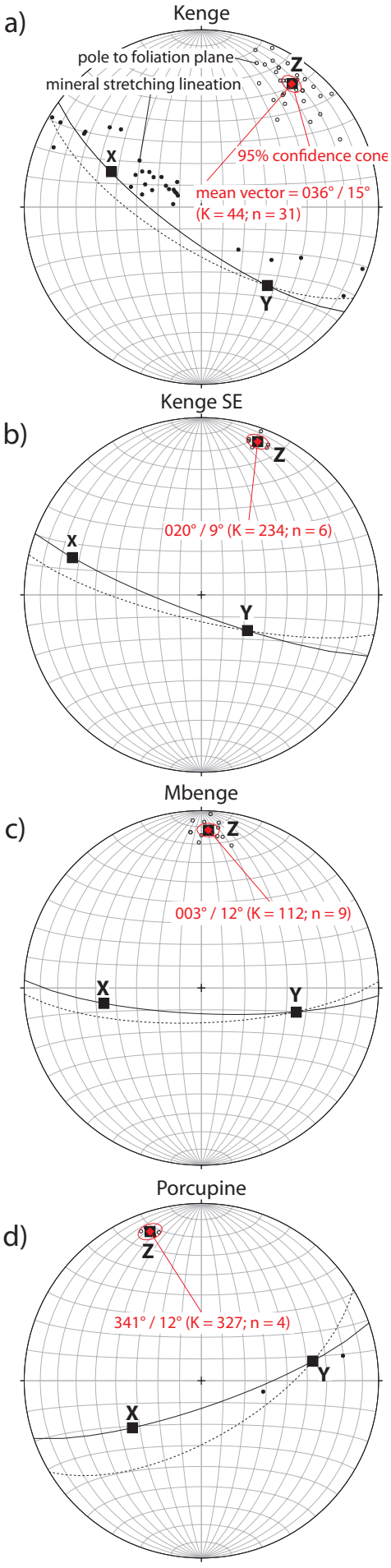

Figure 5.15 – (a–d) Lower-hemisphere equal-area stereonets of the Kenge, Kenge SE, Mbenge and Porcupine ore body geometry, respectively. The orientations of the finite strain ellipsoid axes (X ³ Y ³ Z; closed squares) are based on the finite strain approach (Robert and Poulsen, 2001) where the intersection of the average mylonitic foliation (black solid line) and the average shear zone boundary (black dotted line) represents the Y axis. The X axis of the finite strain ellipsoid is assumed to lie 90° away from the Y axis and along the mylonitic foliation whereas the Z axis is fixed by the location of the other finite strain axes (see text for further discussion). Structural measurements are from surface exposures (closed circles = mineral stretching lineations; open circles = mylonitic foliation poles to planes; mean mylonitic foliation pole to plane = red diamond; 95% confidence interval of mean = red ellipse). K values are a measure of the tendency of linear data to fit a girdle or a cluster (K values approaching zero represent girdles, whereas K values approaching infinity represent clusters) following the approach of Woodcock and Naylor (1983).

Steeply-dipping fault-fill veins are present throughout the Kenge and Mbenge shear zones and range in thickness from a few cm to over 10 m (Figs. 5.12a and 5.13). The mechanical coniditions requried to epxlain the development of thick fault-fill veins are discussed further below. Stylolite veins comprising molybdenite and pyrite oriented parallel to fault-fill vein margins are consistent with a sub-horizontal compression setting and suggest stress induced solution transfer may have been an important mineralizing process (Fig. 5.12b). Slivers of mylonitized and hydrothermally altered wall rock, sheared vein margins, poly-modal fracturing/ fluid inclusion trails, and quartz rods on mylonite-vein contacts are all features which record complex feedback between hydrothermal fluids and deformation that is typical of the fault-fill vein type at other orogenic Au deposits (Robert and Poulsen, 2001 and references therein). Fault-fill veins intersect the mylonitic foliation and the shear zone boundaries at low angles and possess steeply dipping and NW–SE trending geometries (Figs. 5.5 and 5.6). Prominent quartz rods are also present on fault-fill vein surfaces in contact with the mylonitic foliation and, similar to shear zone mineral stretching lineations, are variably oriented (Figs. 5.5c and 5.11). The highly-strained nature of the fault-fill veins makes the structural significance of the current vein orientation relative to the original vein geometry unclear. Furthermore, narrow quartz veins (less than 10 cm thick) with orientations at high angles to shear zone boundaries are locally observed becoming transposed sub-parallel to the mylonitic fabric within the shear zone (Figs. 5.5b and 5.9b). Vein transposition is likely an important process at Au occurrences across the Lupa goldfield and is to be expected in structural settings characterized by progressive deformation. However, narrow transposed quartz veins are distinct from the up to 10 m thick quartz veins characterized by crack-seal textures, stylolite-like surfaces and containing slivers of mylonitized and hydrothermally altered wall rock. The absence of veins with the characteristics of the latter outside of shear zones suggests that main auriferous quartz veins at Kenge and Mbenge represent fault-fill veins (s.s. Robert and Poulsen, 2001). The mechanical conditions required for the development of thick fault fill veins are discussed below.

Narrow (1–5 cm) calcite and chlorite (± epidote) veins occur at the margins of the shear zone and possess complex cross cutting relationships with the mylonitic fabric (Figs. 5.7a and 7b). The majority of calcite veins occur in the dioritic-gabbroic footwall of the ore body and form a ca. 10 m wide damage zone (Fig. 5.13). The timing of calcite veins is unclear, however they are suspected to be related to mylonitization as they are spatially related to the shear zone and are observed cross cutting and are in turn cross cut by the mylonitic shear zone. Similarly, chlorite veins are also present in the hangingwall and footwall of the ore body and also exhibit mutually cross cutting relationships to the mylonitic shear zone. In the Kenge SE zone, chlorite and calcite veins possess variable dips but are generally NW trending and approximately parallel to the Kenge trend. Many of the vein surfaces possess slickensides and suggest vein surfaces were reactivated as fault-slip surfaces during subsequent deformation. Chlorite slickensides are variably oriented at Kenge SE and may indicate mylonitic shear zones were reactivated as variably oriented oblique-slip brittle faults. Structural geometries observed at Kenge are summarized in Figure 5.16a.

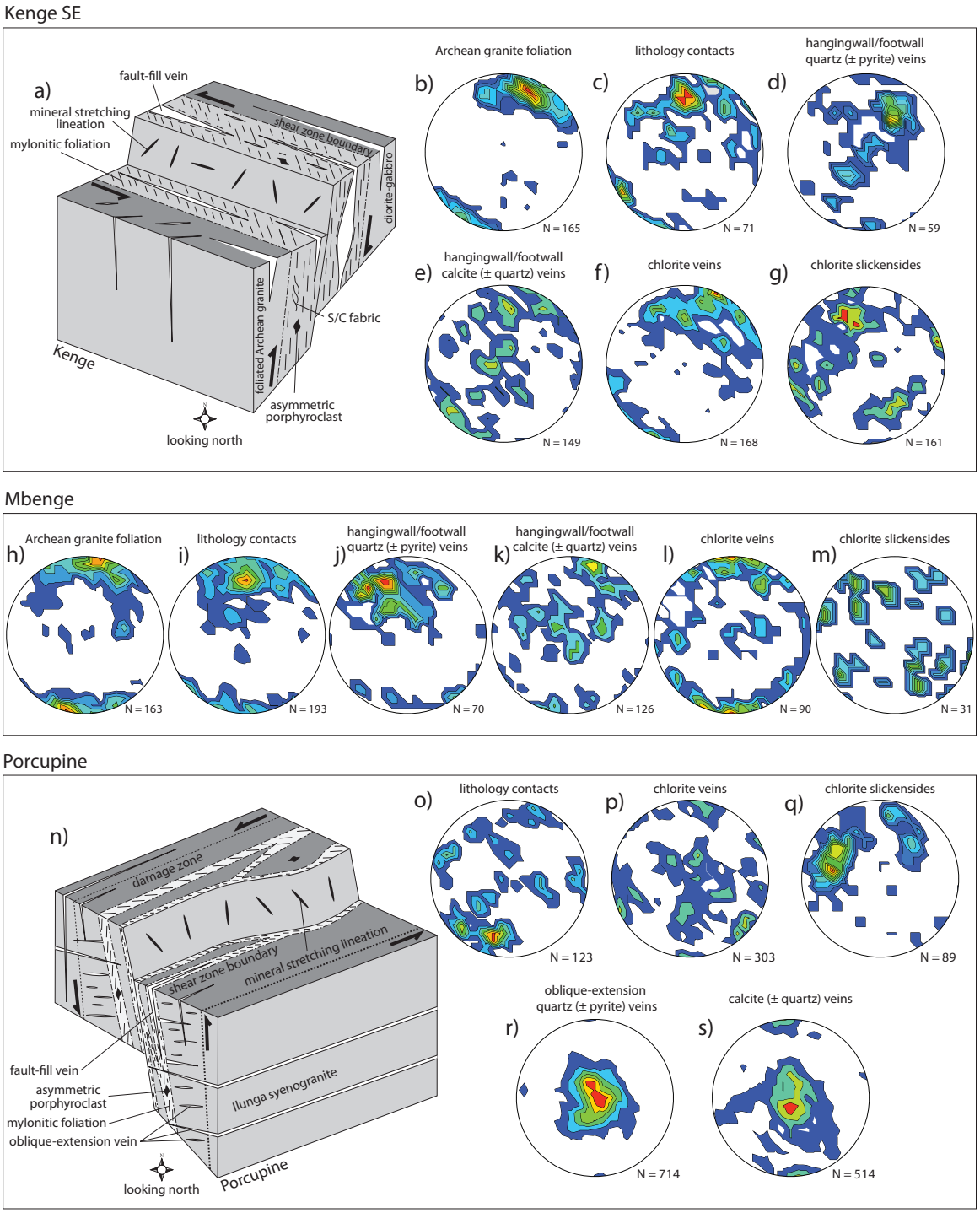

Figure 5.16 – (a) Schematic block model of Kenge summarizing structural fabrics; (b–g) lower hemisphere equal area contoured stereonets of planar and linear fabrics measured from oriented core at Kenge SE; (h–m) lower hemisphere equal area contoured stereonets of planar and linear fabrics measured from oriented core at the Mbenge; (n) schematic block model of Porcupine summarizing structural fabrics; (o–s) lower hemisphere equal area contoured stereonets of planar and linear fabrics measured from oriented core at Porcupine. All contours are plotted following the 1% area method using OSX Stereonet (v 1.4; contour intervals set at 1).

The Mbenge ore body is hosted by E-W trending (ca. 089º) and SW dipping (ca. 70º) mylonitic shear zones and fault-fill veins that share geologic similarities with the Au-bearing shear zone at Kenge. Kinematic indictors in the Au-bearing mylonitic shear zone, similar to those described above, imply reverse and sinistral movement (south-side up). The Mbenge ore body is poorly exposed at surface in several shallow artisanal workings and ore body characteristics are largely based on examination of diamond drill core. Archean granitoids and Paleoproterozoic granodiorite-diorite-gabbro are the dominant wall rocks and are cross cut by calcite ± chlorite ± epidote veins. Veins cross cut and are in turn cross cut by the mylonitic shear zone, possess variable orientations and increase in density towards the shear zone boundaries. The temporal relationship between calcite ± chlorite ± epidote veining and mylonitization remains tenuous despite the close spatial relationship due the potential for shear zone reactivation during subsequent deformation. As a result, chlorite slickenlines on chlorite vein surfaces likely record shear zone reactivation as oblique slip faults (Fig. 5.16m).

The three dimensional distribution of pyrite was investigated by X-ray CT scanning a sample of the Au-bearing shear zone hosting the Mbenge ore body (SZD107 at 176m; drill hole azimuth = 360; dip = -49º; Figs. 5.11 and 5.17). Examination of the three-dimensional distribution of pyrite provides an opportunity trace paleo-fluid pathways in three dimensions and shows that pyrite (± Au) crystals are concentrated along the main mylonitic foliation and the associated shear band cleavage. The latter is oblique to the main mylonitic foliation in section and plan views and implies a transpressional deformation setting at the Mbenge shear zone. The obliquity of the shear band cleavage with the mylonitic foliation also provides a three-dimensional network of relatively permeable fluid conduits that led to the disseminated style of mineralization at Mbenge and potentially other shear zones in the Lupa goldfield.

5.6.2 Porcupine

The Porcupine ore body contains a NI 43-101 compliant measured and indicated resource of 650,000 oz (15.4 Mt at 1.31 g/t Au using a 0.5 g/t Au cut-off; Simpson, 2012). The majority of mineralization is hosted by an ENE–WSW trending (ca. 59°) and south-dipping (ca. 64°) band of hydrothermally altered, veined and locally sheared Paleoproterozoic Ilunga Syenogranite (ca. 1960 Ma; Chapter Two). On surface, the Porcupine main zone is exposed in two artisanal workings and so the following ore body characteristics are largely based on observations from diamond drill core.

Two types of quartz veins are present at the Porcupine Main zone: 1) fault-fill veins with similar characteristics to those observed at the Kenge, Mbenge and artisanal workings (Fig. 5.12a); and 2) shallowly dipping extension/oblique-extension veins (Robert and Poulsen, 2001; Figs. 5.12c). Both vein types are Au-bearing but the oblique-extension veins are economically important as they act to significantly widen the mineralized zone. Oblique-extension veins are shallowly dipping structures (mean vein strike / dip = 285º/02º; n = 714), possess parallel and planar vein margins, are composed of massive quartz (bull quartz) and lack textural evidence to identify their opening vector (Fig. 5.12d). The latter makes it difficult to distinguish whether

quartz veins at Porcupine represent "true" extensional veins with opening vectors perpendicular to the vein margin or oblique-extension veins. Nevertheless, the massive and unstrained nature of the veins coupled with the shallow dipping orientation makes quartz veins at Porcupine distinct from fault-fill veins at Kenge and Mbenge.

5.7 Discussion

5.7.1 Strain Partitioning

Kinematic indicators from auriferous shear zones in the Lupa goldfield record evidence for transpressional deformation. The asymmetry of kinematic indicators in plan and section views imply non-coaxility of the strike- and dip-slip components of deformation and are at odds with theoretical partitioned transpressional shear zones where transpressional strain is compartmentalized into pure and simple shear-dominated deformation domains (Dewey et al., 1998). Complete strain partitioning into strike- and dip-slip components appears to be uncommon in natural shear zones and the scale(s) at which partitioning occurs remains poorly understood (Jones and Tanner, 1995). Evidence for deposit-scale strain partitioning at Kenge is potentially recorded by the orientation of mineral stretching lineations, which vary from horizontal to vertical but display a weak and moderately NW plunging cluster (Fig. 5.15a). Mineral stretching lineations along strike of the Saza shear zone show a similar range of plunges but are more

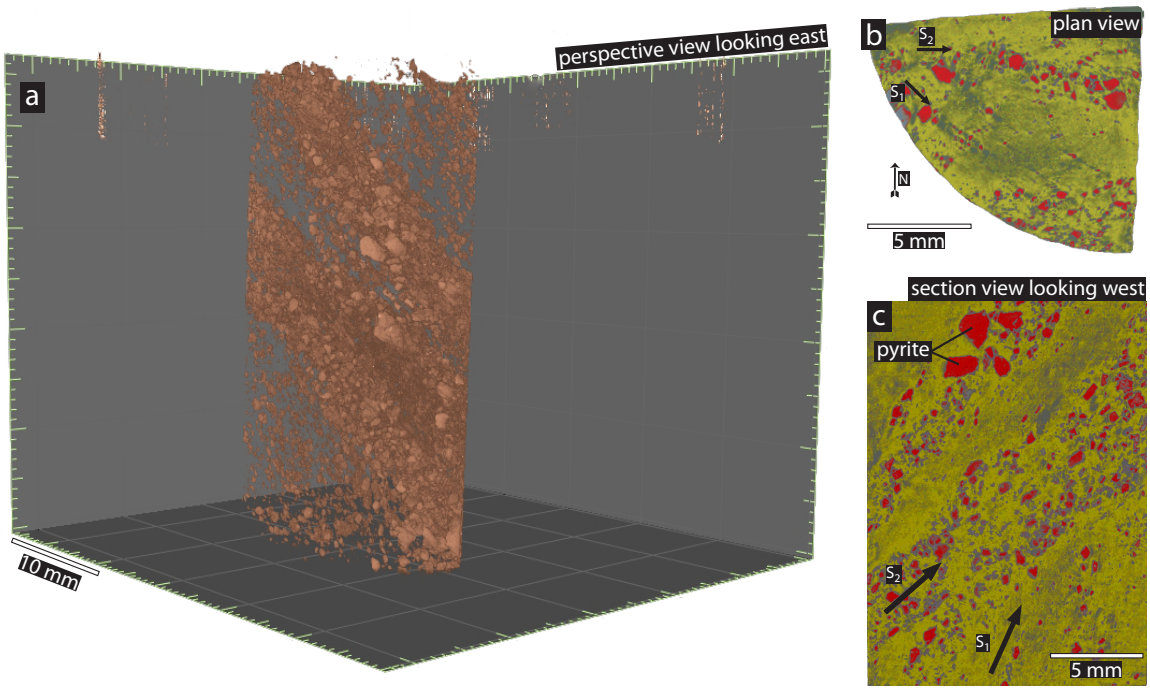

Figure 5.17 – (a) Perspective view of a 3-D X-ray CT model of a Au-bearing mylonite ¼ core sample from Mbenge. Pyrite is isolated based on density and shows the distribution closely follows the mylonitic foliation and associated shear band cleavage; (b) plan view of the same CT model with colors based on relative mineral density (yellow and grey are low density minerals and correspond to muscovite, chlorite, quartz and calcite; whereas red represents high density phases and corresponds to pyrite ± Au); (c) section view of the same CT model with colors based on relative density (same as previous).

generally steeply dipping (Fig. 5.11). The cause of this variability is possibly explained by strain partitioning along strike and/or across the shear zones. In this model, shear zone segments with sub-horizontal mineral stretching lineation would reflect wrench-dominated finite strain, whereas shear zone segments with down-dip lineations would reflect a greater component of pure-shear. However, variably oriented mineral stretching lineations are also a hallmark of theoretical and natural examples of non-partitioned shear zones (Jiang and White, 1995, Jiang and Williams, 1998; Lin et al., 1998; Jones et al., 2004). Shear zones following these types of deformation paths can exhibit mineral stretching lineation orientations that vary continuously from horizontal to vertical due to complex rotation of the instantaneous strain axis during deformation and variations in the intensity of finite strain along and/or across the shear zone (Lin and Jiang, 2001). No clear relationship between the intensity of finite strain and mineral stretching lineation orientation was observed in the study area and the dearth of constraints on the shear zone boundary conditions make assessing the extent of strain partitioning at the deposit scale equivocal. Nevertheless, the observed obliquity of the mylonitic foliation and kinematic indictors in plan and section view coupled with oblique mineral stretching lineations suggest transpressional deformation was incompletely partitioned at the outcrop scale. The subtle cluster of mineral stretching lineations less than 90° away from the intersection of the mylonitic foliation and shear zone boundary and Kenge is also typical of shear zones with exhibiting triclinic symmetry and may suggest transpressional strain was incompletely partitioned at the deposit scale (Fig. 5.15a; Jones et al., 2004).

The significance of strain partitioning to mineral explorationists also remains unclear since shear zones are mineralized regardless of mineral stretching lineations orientation and/or variations observed in finite strain intensity (e.g., the obliquity of the mylonitic fabric relative to the shear zone boundary). At Kenge, the thickest mineralized zone (i.e., Razorback mine) corresponds with a shear zone step-over, whereas shear zone intersections and splays appear to be important mineral controls along the Saza shear zone (Fig. 5.11). Dilational jogs and shear zone step overs/intersections are well documented sites of increased permeability and fluid focusing and are suggested here to be important controls for gold mineralization in the Lupa goldfield despite the complex structural setting of mineralization (Cox et al., 2001).

5.7.2 Relationships between Au, hydrothermal alteration and deformation

Recent studies have demonstrated that phyllosilicate-rich mylonites (phyllonites) are weak relative to the granitic wall rocks and may give rise to long-term weakening and reactivation of fault zones (e.g., Stewart et al., 2000; Collettini and Holdsworth, 2004; Jefferies et al., 2006b). Mylonites in the Lupa goldfield are typical of these "weak" shear zones and shear zone weakening may explain the periodic reactivation of structures (Figs. 5.9c and 5.9d). The mineralogy and grain size of the observed auriferous mylonites thus appears to have played a key role in strain weakening and promoting brittle reactivation of ductile structures. However, brittle deformation is also observed pre-dating mylonitic shear zones and hydrothermal alteration, coupled with cataclasis in these pre-D2 structures, resulted in grain size reduction

and feldspar (plagioclase and K-feldspar) replacement with intrinsically weaker phyllosilicates (Fig. 5.8c). The finer grain size and mineralogy of hydrothermally altered granitic host rocks (grain size reduction was also accomplished through dynamic recrystallization of quartz and neo-crystallization of quartz and feldspar) creates the ideal conditions for strain localization and, locally, may have led to the onset of crystal plastic deformation and fluid-assisted diffusion processes (Fig. 5.8; Handy, 1990; Wintsch, et al., 1995; Imber et al., 2001). In this model, pre-D2 cataclasis produced dilatancy, enhanced permeability and focused fluids (Reches and Lockner, 1994; McCaig, 1997; Cox, 2005; Jefferies 2006b). Three samples of Ilunga Syenogranite that exhibit varying degrees of hydrothermal alteration and strain illustrate the proposed model in Fig. 5.18. Continued feedback between fluid, rock and deformation generated interconnected networks of weak mylonitic shear zones that are prone to reactivation (e.g., Imber et al., 1997). The phyllosilicate rich nature of the fault rocks may have also promoted deformation under conditions of low differential stress and the implications of low differential stress for Au mineralization are discussed further below.

The geochemical evidence presented as part of this study records the breakdown of plagioclase to phyllosilicates by the depletion of Sr and minor depletion and enirhcment of

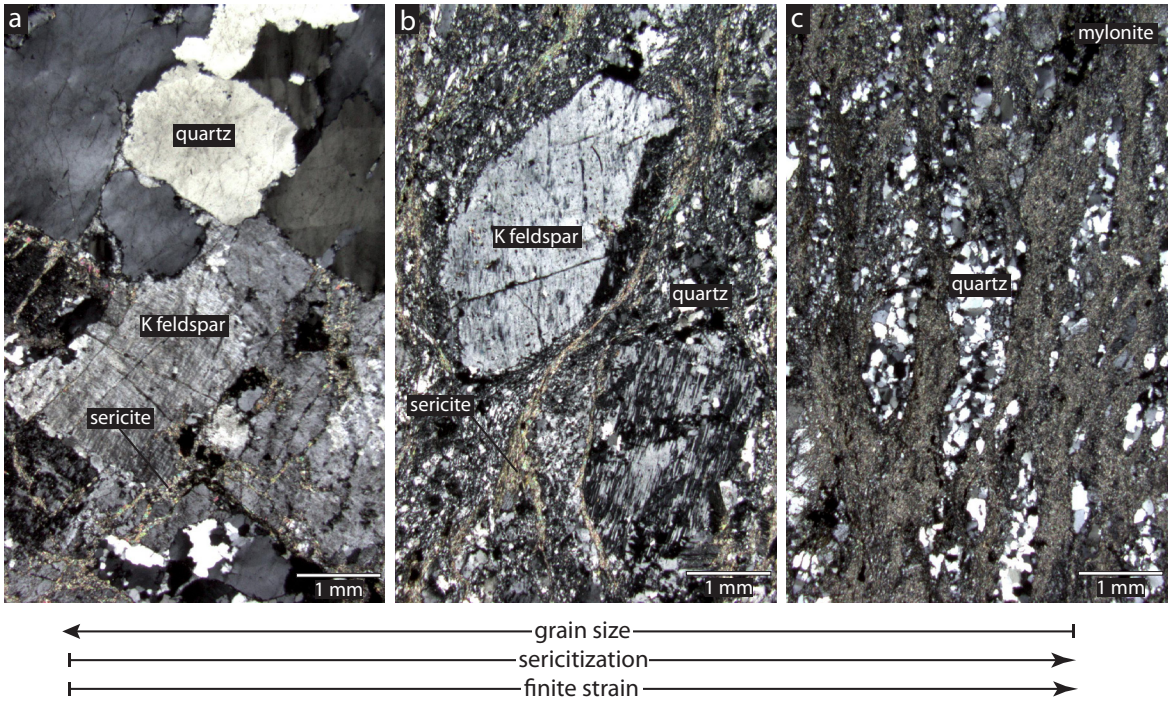

Figure 5.18 – (a–c) Crossed nicols photomicrographs of three Ilunga Syenogranite samples exhibiting various degrees of hydrothermal alteration and finite strain. Our proposed model for shear zone development would place these three samples into a progressive sequence from left to right. (a) Coarse grained, non-foliated and relatively unaltered granite becomes hydrothermally altered, potentially due to pre-D2 brittle fracturing, and results in the replacement of feldspars with intrinsically weaker phyllosilicates (GPD44 at 251m); (b) continued hydrothermal promotes strain localization within the altered granite and leads to increasing finite strain and mylonitization (505500, 9081129); (c) complete replacement of feldspars with further grain size reduction producing a quartz-phyllosilicate mylonite (508512, 9080975)

Na_2O and K_2O, respectively. However, the general trend of most elements plotting on or near the unit slope suggests mylonitization was relatively isochemical. The latter is at odds with the geochemical signature of mylonites reported in other studies, which typically exhibit evidence for significant volume change associated with mylonitization. The unusual geochemical signature of mylonites in the Lupa goldfield likely reflects, in part, high fluid rock ratios that effectively homogenized the geochemical composition of the mylonites and the granitic wall rocks. The Miyamae shear zone provides a comparable example of phyllonitic shear zones that are geochemically indistinguishable from their respective granitic wall rocks (Jefferies, 2006a). If correct, the isochemical signature of the auriferous mylonites represents homogenization of the geochemical signature and may mask any volumetric changes related to mylonitization.

5.7.3 *Micro-scale deformation processes and micro-structural/mineralogic constraints on P-T conditions of deformation and metamorphism during mineralization*

Microstructural examination suggests a variety of deformation mechanisms are responsible for the development of mylonitic shear zones (e.g., Schmid 1983; Knipe, 1989; Williams et al., 1994). Stylolitic veins and fibrous quartz in pressure shadows/fringes are indicative of dissolution and precipitation, respectively (Figs. 5.7 and 5.8). Furthermore, stress-induced solution transfer appears to have occurred concomitant with brittle-failure and quartz vein formation. Undulose extinction, deformation lamellae, sub-grain rotation and grain boundary migration observed in quartz are indicative of crystal plastic deformation mechanisms (Figs. 5.8b). Crystal plastic deformation is also suggested to be an important deformation mechanism for muscovite crystals (e.g., muscovite exhibits sweeping extinction, kinking and folding), whereas feldspar crystals exhibit comparatively little evidence for strain except for rare kinking and brittle fractures (Figs. 5.8g and 5.8h).

The disparate microstructures and deformation mechanisms observed between quartz, muscovite and feldspar provide first-order constraints on the P-T conditions of deformation (Tullis and Yund, 1985). The onset of quartz plasticity, as observed in Au-bearing shear zones, is expected to occur at 300ºC, whereas feldspar plasticity is expected to initiate at 450ºC (Scholz, 1988). These temperatures are consistent with the Au-bearing shear zone mineral assemblage (muscovite ± quartz ± chlorite ± calcite ± epidote) that is typical of other greenschist facies mylonitic shear zones (Goldfarb et al., 2001; Groves et al., 2003; Elmer et al., 2006). Fluid inclusion microthermometry from Au-bearing quartz veins implies a comparable temperature range for hydrothermal fluids (H_2O-CO_2 ± NaCL inclusions from Kenge interpreted to best reflect the mineralizing fluid possess a range of homogenization temperatures from 259–419°C; Shaw, 2009). The depth at which the brittle-ductile transition occurs in average quartz-feldspathic crust provides a first-order estimate of the depth at which deformation occurred (ca. 10 ± 5 km; Sibson, 1983; Scholz, 1988). However, geothermal gradients, strain rates, pore-fluid pressures, and fault rock composition all influence the temperature and pressure range of the brittle-ductile transition zone (Sibson, 1983; Tullis and Yund, 1980; White et al., 1986, Handy, 1990; Imber et al., 2001). Fluid-rock interaction is a particularly important factor that has been demonstrated

to significantly shallow the brittle-ductile transition zone (ca. 5 km; e.g., Imber et al., 2001) and lower the temperature required for ductile deformation processes (e.g., hydrolytic weakening; Liu et al., 2002). A shallow brittle-ductile transition zone may have important implications for orogenic Au deposit models where brittle-ductile deformation is characteristic and is typically cited as evidence for deposit formation at mid-crustal levels (ca. 10 ± 5 km; Sibson, 1983). In this contribution we have emphasized that feedback between hydrothermal alteration and deformation may have, at least locally, led to the onset of crystal plastic deformation processes for auriferous shear zones in the Lupa goldfield. The depth of ore deposit formation in the Lupa goldfield remains equivocal and requires additional study but the deformation processes that characterize auriferous mylonites are suggested to be compatible with shallower crustal levels than previously expected.

5.7.4 Fluid pressure and dilation mechanisms

Experimental and field-based studies emphasise the importance of fracturing — at a variety of scales — in generating permeable fluid conduits in brittle-ductile shear zones (e.g., Kolb et al., 2004; Zhang et al., 2008). The opening of these fractures and the development of meso-scale veins at Au occurrences in the Lupa goldfield requires specific conditions of differential stress, fluid pressure and fracture orientation (presented here as a schematic Mohr circle diagram; Fig. 5.19). In compressional settings, shallow-dipping extensional veins form when fluid pressure (P_f) exceeds the sum of the wall rock tensile strength ($T_{granite}$) and the near-vertical least compressive stress (σ_3). Oblique-extension veins, forming at angles less than 30º to the near-horizontal maximum compressive stress (σ_1), develop during conditions of high fluid pressure and differential stress that is greater than required for the development of extension veins, but lower than the differential stress required for shear failure (Cox et al., 2001; Fig. 5.19). The opening of sub-vertical fault-fill veins sub-parallel to the maximum compressive stress represents a paradox in compressional deformation settings and requires special conditions (Kerrich and Allison, 1978; Vearncombe, 1998). The tensile strength of phyllosilicate-rich mylonitic fault rocks ($T_{mylonite}$) is lower than granitic wall rocks and, where coupled with low differential stress, can result in fluid pressures exceeding the normal stress (σ_n) on the shear

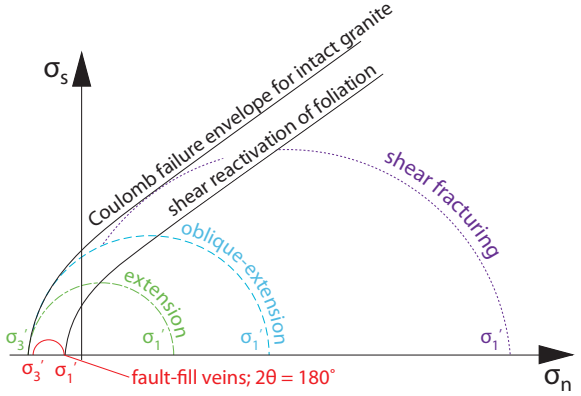

Figure 5.19 – Schematic Mohr diagram showing the geomechanics of the three main vein types at orogenic Au deposits (modified after Vearncombe, 1998). Fault-fill veins that form parallel to the mylonitic foliation requires negative effective σ_1' and σ_3', low differential stress and high fluid pressure (σ_n = normal stress; σ_s = shear stress; σ_1' = maximum effective compressive stress; σ_3' = minimum effective compressive stress).

zone (Cox et al., 1995; Fig 5.19). The development of sub-vertical fault-fill veins thus requires the following conditions:

$$(\sigma_3 + T_{granite}) \geq P_f \geq (\sigma_n + T_{mylonite}) \qquad \text{Equation 1 (Cox et al., 1995)}$$

The presence of oblique-extension and fault-fill veins at Porcupine provides valuable insight into the transient fluid pressure conditions at Au occurrences in the Lupa goldfield. During oblique-extension vein formation, fluid pressures are inferred to have exceeded the sum of the tensile strength of the granitic wall rock and the least compressive stress ($P_f \geq \sigma_3 + T_{granite}$); whereas fluid pressures during fault-fill vein formation must have been lower, but nevertheless sufficient to exceed the sum of the tensile strength of the fault and the normal stress acting on the shear zone (Equation 1). Mutually cross cutting relationships between both auriferous vein types demonstrates mineralization occurred concomitant with these episodic fluid pressures fluctuations. The absence of oblique-extension veins at Kenge implies fluid pressures at this Au occurrence were lower and suggests the Kenge shear zone may have been more favourably oriented for shear failure, which prevented fluid pressure build-up (Sibson et al., 1988; Sibson, 1990, 2004).

Meso-scale veins and micro-fractures provide clear evidence for the importance of brittle fractures as fluid pathways at Au occurrences in the Lupa goldfield, however intergranular flow within phyllosilicate-dominated mylonite fault-rock matrix is also expected (Cox and Etheridge, 1989; Knipe and McCaig, 1994). X-ray CT scanning of an auriferous shear zone sample from Mbenge demonstrates the three-dimensional distribution of pyrite is clearly concentrated parallel to the main mylonitic foliation and associated shear band cleavages at the grain scale (Fig. 5.17). The mylonitic fabrics therefore represent a three dimensional network of relatively permeable fluid conduits that led to the disseminated style of pyrite in Au-bearing shear zones. Dilation normal to the shear zone (during fault-fill vein formation) likely facilitated intergranular flow of hydrothermal fluids as suggested by the paradoxical orientation of quartz strain fringes and the ubiquitous association of disseminated pyrite concordant with mylonitic fabrics (Fig. 5.17). Intergranular flow and micro-fractures are thought to be relatively ineffective at distributing large fluid fluxes and likely resulted in the fluid pressure necessary for the development of oblique-extension veins (Kolb et al., 2004).

5.8 Conclusions

Examination of rocks within Lupa goldfield artisanal workings and oriented core reveals a remarkable variability of Au-bearing structures. Auriferous mylonitic shear zones and fault-fill veins characterize Kenge, Mbenge and the majority of artisanal mines, whereas the highest Au grades at Porcupine are hosted by hydrothermally altered and veined but non-foliated granite. Widespread evidence for hydrothermal alteration is suggested to be the commonality between disparate Au-bearing structures and micro- to meso-scale observations imply feedback between hydrothermal alteration, deformation and mineralization. In particular, hydrothermal alteration led to the replacement of strong, load bearing feldspars (plagioclase and K feldspar) with weak phyllosilicates locally producing the ideal conditions for strain localization, mylonitization and

further fluid flow. Pre-existing structural weaknesses (e.g., D1 foliation, lithologic contacts, and/or pre-D2 brittle deformation) likely played a key role during the initial localization of hydrothermal fluids and strain.

Asymmetric fabrics in plan and section views imply non-coaxility of the strike- and dip-slip components of strain and a transpressional deformation setting (reverse oblique movement vector) along the examined shear zones that is consistent with the flattening strain inferred from oblate porphyroclasts and the prevalence of S-type tectonites. Variably oriented mineral stretching lineations may record strain partitioning along and across the examined shear zones, however kinematic indicators in plan and section view suggest strain was incompletely partitioned at the outcrop and deposit scales.

The occurrence of fault-fill and oblique-extension veins at Porcupine suggests fluid pressure fluctuations occurred concomitant with mineralization. Thick fault-fill veins with crack-seal textures suggest fluid pressures may have locally exceeded the sum of the tensile strength of the fault and the normal stress acting on the shear zone. Shear zone normal dilation caused by these excess fluid pressures likely promoted intergranular flow and led to the disseminated style of mineralization observed in auriferous mylonites.

5.9 References

Berthé, D., Choukroune, P., and Jegouzo, P., 1979, Orthogneiss, mylonite and non-coxial deformation of granites: the example of the South Armoricain shear zone: Journal of Structural Geology, v. 1, p. 31–42.

Bierlein, F.P., Groves, D.I., and Cawood, P.A., 2009, Metallogeny of accretionary orogens – the connection between lithospheric processes and metal endowment: Ore Geology Reviews, v. 36, p. 282–292.

Blenkinsop, T.G., and Doyle, M.G., 2010, A method for measuring the orientations of planar structures in cut core: Journal of Structural Geology, v. 32, p. 741–745.

Boniface, N., 2009, Eburnian, Kibaran, and Pan-African metamorphic events in the Ubendian Belt of Tanzania: petrology, zircon and monazite geochronology: Unpublished PhD thesis, Kiel, Germany, Kiel University, 110 p.

Boniface, N., Schenk, V., and Appel, P., 2012, Paleoproterozoic eclogites of MORB-type chemistry and three Proterozoic orogenic cycles in the Ubendian Belt (Tanzania): evidence from monazite and zircon geochronology, and geochemistry: Precambrian Research, v. 192–195, p. 16–33.

Boniface, N., and Schenk, 2012, Neoproterozoic eclogites in the Paleoproterozoic Ubendian Belt of Tanzania: evidence for a Pan-African suture between the Bangweulu Block and the Tanzania Craton: Precambrian Research, v. 208–211, p. 72–89.

Cahen, L., Snelling, N.J., Delhal, J., and Vail, J., 1984, The geochronology and evolution of Africa, Clarendon Press, Oxford, 512 p.

Collettini, C., and Holdsworth, R.E., 2004, Fault zone weakening and character of slip along low-angle normal faults: insights from the Zuccale Fault, Elba, Italy: Journal of the Geological Society, London, v. 161, p. 1039–1051.

Cox, S.F., 1995, Faulting processes at high fluid pressures: an example of fault-valve behaviour from the Wattle Gully Fault, Victoria, Australia: Journal of Geophysical Research, v. 100, p. 12,841–12,860.

Cox, S.F., and Etheridge, M.A., 1989, Coupled grain-scale dilatancy and mass transfer during deformation at high fluid pressures: examples from Mount Lyell, Tasmania: Journal of Structural Geology, v. 11, p. 147–162.

Cox, S.F., Knackstedt, M.A., and Braun, J., 2001, Principles of structural control on permeability and fluid flow in hydrothermal systems, *in* Richards, J.P., and Tosdal, R.M., eds, Structural controls on ore genesis, Society of Economic Geology Reviews, v. 14, p. 1–24.

Cox, S.F., 2005, Coupling between deformation, fluid pressures and fluid flow in ore-producing hydrothermal systems at depth in the crust, *in* Hedenquist, J.W., et al., eds., Economic Geology 100th Anniversary Volume, Denver, Colorado, Society of Economic Geologists, p. 39–75.

Craw, D., 2002, Geochemistry of late metamorphic hydrothermal alteration and graphitisation of host rock, Macres gold mine, Otago Schist, New Zealand: Chemical Geology, v. 191, p. 257–275.

Daigneault, R., Mueller, W.U., and Chown, E.H., 2002, Oblique Archean subduction: accretion and exhumation of an oceanic arc during dextral transpression, Southern volcanic zone, Abitibi subprovince, Canada: Precambrian Research, v. 115, p. 261–290.

Daly, M.C., 1988, Crustal shear zones in central Africa; a kinematic approach to Proterozoic tectonics: Episodes, v. 11, p. 5–11.

Dewey, J.F., Holdsworth, R.E., and Strachan, R.A., 1998, Transpression and transtension zones, *in* Holdsworth, R.E., Strachan, R.A., and Dewey, J.F., eds., Continental Transpressional and Transtensional Tectonics: Geological Society, London, Special Publications, v. 135, p. 1–14.

Dubé, B., Poulsen, K.H., and Guha, J., 1989, The effects of layer anisotropy on auriferous shear zones: the Norbeau Mine, Quebec: Economic Geology, v. 84, p. 871–878.

Durney, D.W., and Ramsay, J.G., 1973, Incremental strains measured by syn-tectonic crystal growths, *in* DeJong, K.A., and Sholten, R., eds., Gravity and Tectonics, Wiley, New York, p. 67–95.

Elmer, F.L., White, R.W. and Powell, R., 2006, Devolatilization of metabasic rocks during greenschist–amphibolite facies metamorphism: Journal of Metamorphic Geology, v. 24, p. 497–513.

Fitch, T.J., 1972, Plate convergence, transcurrent faults, and internal deformation adjacent to southeast Asia and the western Pacific: Journal of Geophysical Research, v. 77, p. 4432–4460.

Goldfarb, R.J., Groves, D.I., and Gardoll, S., 2001, Orogenic gold and geologic time: A global synthesis: Ore Geology Reviews, v. 18, p. 1–75.

Grant, J.A., 1986, The Isocon diagram — a simple solution to Gresens' equation for metasomatic alteration: Economic Geology, v. 81, p. 1976–1982.

—, 2005, Isocon analysis: a brief review of the method and applications: Physics and Chemistry of the Earth, v. 30, p. 997–1004.

Gresens, R.L., 1967, Composition-volume relationships of metasomatism: Chemical Geology, v. 2, p. 47–55.

Groves, D.I., Goldfarb, R.J., Gebre-Mariam, M., Hagemann, S.G., and Robert, F., 1998, Orogenic gold deposits: a proposed classification in the context of their crustal distribution and relationships to other gold deposit types: Ore Geology Reviews, v. 13, p. 7–27.

Groves, D.I., Goldfarb, R.J., Robert, F., and Hart, C.J., 2003, Gold deposits in metamorphic belts: overview of current understanding, outstanding problems, future research, and exploration significance: Economic Geology, v. 98, p. 1–29.

Handy, M.R., 1990, The solid-state flow of polymineralic rocks: Journal of Geophysical Research, v. 96 (B6), p. 8647–8661.

Hanmer, S., and Passchier, C., 1991, Shear sense indictors: a review: Geological Survey of Canada, Paper 90-17, 72 p.

Harland, W.B., 1971, Tectonic transpression in Caledonian Spitzbergen: Geological Magazine, v. 108, p. 27–42.

Harrison, A., 2011, Mineral resource estimate of the Saza Makongolosi project for Helio Resource Corporation: Unpublished Golder Associates NI 43-101 Technical Report, 201 p.

Holcombe, R., 2008. Oriented drillcore: measurement and calculation procedures for structural and exploration geologists (http://www.holcombecoughlin.com/HCA_downloads.htm). Last accessed 22/11/2012.

Holwell, D.A., Abraham-Jones, T., Keays, R.R., and Boyce, A.J., 2012, The nature and genesis of marginal Cu-PGE-Au sulphide mineralisation in Paleogene Macrodykes of the Kangerlussuaq region, East Greenland: Mineralium Deposita, v. 47, p. 3–21.

Hronsky, J.M.A., Groves, D.I., Loucks, R.R., and Begg, G.C., 2012, A unified model for gold mineralisation in accretionary orogens and implications for regional-scale exploration targeting methods: Mineralium Deposita, v. 47, p. 339–358.

Imber, J., Holdsworth, R.E., Butler, C.A., and Lloyd, G.E., 1997, Fault-zone weakening processes along the reactivated Outer Hebrides Fault Zone, Scotland: Journal of the Geological Society, v. 154, p. 105–109.

Imber, J., Holdsworth, R.E., Butler, C.A., and Strachan, R.A., 2001, A reappraisal of the Sibson-Scholz fault zone model: the nature of the frictional to viscous ("brittle-ductile")

transition along a long-lived, crustal-scale fault, Outer Hebrides, Scotland: Tectonics, v. 20, p. 601–624.

Jefferies, S.P., 2006, Microstructural and geochemical processes in long-lived reactivated crustal-scale fault zones: a case study from the Median Tectonic Line, SW Japan: Unpublished PhD Thesis, Durham University, Durham, UK, 232 p.

Jefferies, S.P., Holdsworth, R.E., Wibberley, C.A.J., Shimamoto, T., Spiers, C.J., Niemeijer, A.R., and Lloyd, G.E., 2006, The nature and importance of phyllonite development in crustal-scale fault cores: an example from the Median Tectonic Line, Japan: Journal of Structural Geology, v. 28, p. 220–235.

Jiang, D., and White, J.C., 1995, Kinematics of rock flow and the interpretation of geological structures, with particular reference to shear zones: Journal of Structural Geology, v. 17, p. 1249–1265.

Jiang, D., and Williams, P.F., 1998, High-strain zones: a unified model: Journal of Structural Geology, v. 20, p. 1105–1120.

Jiang, D., Lin, S., and Williams, P.F., 2001, Deformation path in high-strain zones, with reference to slip partitioning in transpressional plate-boundary regions: Journal of Structural Geology, v. 23, p. 991–1005.

Jones, R.R., and Tanner, P.W.G., 1995, Strain partitioning in transpression zones: Journal of Structural Geology, v. 17, p. 793–802.

Jones, R.R., Holdsworth, R.E., and Baily, W., 1997, Lateral extrusion in transpressional zones: Journal of Structural Geology, v. 19, p. 1201–1217.

Jones, R.R., and Holdsworth, R.E., 1998, Oblique simple shear in transpression zones, *in* Holdsworth, R.E., Strachan, R.A., and Dewey, J.F., eds., Continental Transpressional and Transtensional Tectonics, Geological Society, London, Special Publication, v. 135, p. 35–40.

Jones, R.R., Holdsworth, R.E., Clegg, P., McCaffrey, K., and Tavarnelli, E., 2004, Inclined transpression: Journal of Structural Geology, v. 26, p. 1531–1548.

Kilembe, E.A., and Rosendahl, B.R., 1992, Structure and stratigraphy of the Rukwa rift: Tectonophysics, v. 209, p. 143–158.

Kerrich, R., and Allison, I., 1978, Vein geometry and hydrostatics during Yellowknife mineralization: Canadian Journal of Earth Sciences, v. 15, p. 1653–1660.

Kerrich, R., and Wyman, D., 1990, Geodynamic setting of mesothermal gold deposits: an association with accretionary tectonic regimes: Geology, v. 18, p. 882–885.

Köhn, D., Bons, P.D., Hilgers, C., and Passchier, C.W., 2003, Development of antitaxial strain fringes during non-coaxial deformation: an experimental study: Journal of Structural Geology, v. 25, p. 263–275.

Kolb, J., Rogers, A., Meyer, M.F., and Vennemann, T.W., 2004, Development of fluid conduits in the auriferous shear zones of the Hutti Gold Mine, India: evidence for spatially and

temporally heterogeneous fluid flow: Tectonophysics, v. 378, p. 65–84.

Knipe, R.J., 1989, Deformation mechanisms — recognition from natural tectonites: Journal of Structural Geology, v. 11, p. 127–146.

Knipe, R.J., and McCaig, A.M., 1994, Microstructural and microchemical consequences of fluid flow in deforming rocks, *in* Parnell, J., ed., Geofluids: origin, migration, and evolution of fluids in sedimentary basins, Geological Society, Special Publication, v. 78, pp. 99–111.

Kuehn, S., Ogola, J., and Sango, P., 1990, Regional setting and nature of gold mineralization in Tanzania and southwest Kenya: Precambrian Research, v. 46, p. 71–82.

Lenoir, J.L., Liégeois, J.P., Theunissen, K., and Klerkx, J., 1994, The Palaeoproterozoic Ubendian shear Belt in Tanzania: geochronology and structure: Journal of African Earth Sciences, v. 19, p. 169–184.

Lin, S., Jiang, D., and Williams, P.F., 1998, Transpression (or transtension) zones of triclinic symmetry: natural example and theoretical modelling, *in* Holdsworth, R.E., Strachan, R.A., and Dewey, J.F., eds., Continental Transpressional and Transtensional Tectonics, Geological Society, London, Special Publication, v. 135, p. 41–57.

Lin, S., and Corfu, F., 2002, Structural setting and geochronology of auriferous quartz veins at the High Rock Island gold deposit, northwestern Superior Province, Manitoba, Canada: Economic Geology, v. 97, p. 43–57.

Lin, S., and Jiang, D., 2001, Using along-strike variation in strain and kinematics to define the movement direction of curved transpressional shear zones: an example from northwestern Superior Province, Manitoba: Geology, v. 29, p. 767–770.

Liu, J., Walter, J.M., and Weber, K., 2002, Fluid-enhanced low-temperature plasticity of calcite marble: microstructures and mechanisms: Geology, v. 30, p. 787–790.

Molnar, P., 1992, Brace-Goetze strength profiles, the partitioning of strike-slip and thrust faulting at zones of oblique convergence, and the stress-heat flow paradox of the San Andreas fault, *in* Evans, B., Wong, T., eds., Fault Mechanics and Transport Properties of Rocks, Academic Press, San Diego, p. 435–459.

McConnell, R.B., 1950, Outline of the geology of Ufipa and Ubende: Geological Survey of Tanganyika Bulletin, v. 19, 62 p.

McCaig, A., 1987, Deformation and fluid-rock interaction in metasomatic dilatant shear bands: Tectonophysics, v. 135, p. 121–132.

Passchier, C.W., and Simpson, C., 1986, Porphyroclast systems as kinematic indicators: Journal of Structural Geology, v. 8, p. 831–843.

Reches, Z., and Lockner, D.A., 1994, Nucleation and growth of faults in brittle rocks: Journal of Geophysical Research-Solid Earth, v. 99, p. 18159–18173.

Robert, F., and Poulsen, K.H., 2001, Vein formation and deformation in greenstone gold deposits, *in* Richards, J.P., and Tosdal, R.M., eds., Structural controls on ore genesis, Society of Economic Geology Reviews, v. 14, p. 111–155.

Sango, P.M., 1988, Structural and lithological controls of gold mineralization in the Lupa goldfield, Tanzania, *in* Ho, S.E., and Groves, D.I. eds., Recent advances in understanding Precambrian gold deposits, Geology Department and University Extension, The University of Western Australia, Publication No. 12, p. 99–109.

Schmid, S.M., 1983, Microfabric studies as indictors of deformation mechanisms and flow laws operative in mountain building, *in* Hsü, K.J., ed., Mountain Building Processes, New York, Academic Press, p. 95–110.

Scholz, C.H., 1988, The brittle-plastic transition and the depth of seismic faulting: Geologische Rundschau, v. 77, p. 319–328.

Shaw, E., 2009, Fluid evolution in the Lupa goldfield, southwest Tanzania: Unpublished MGeol Thesis, Leicester, University of Leicester, 54 p.

Sibson, R.H., 1983, Continental fault structure and shallow earthquake source: Journal of the Geological Society, London, v. 140, p. 741–767.

Sibson, R.H., Robert, F., and Poulsen, H., 1988, High-angle reverse faults, fluid-pressure cycling, and mesothermal gold-quartz deposits: Geology, v. 16, p. 551–555.

Sibson, R.H., 1990, Conditions for fault-valve behaviour, *in* Knipe, R.J., and Rutter, E.H., eds., Deformation Mechanisms, Rheology and Tectonics, Geological Society Special Publication, London, v. 54, p. 15–28.

Sibson, R.H., 2004, Controls on maximum fluid overpressure defining conditions for mesozonal mineralisation: Journal of Structural Geology, v. 26, p. 1127–1136.

Simpson, R., 2012, NI 43-101 mineral resource estimate update for the Saza-Makongolosi gold project, Tanzania: Unpublished company report, SRK consulting, 217 p.

Snoke, A.W., and Tullis, J., 1998, An overview of fault rocks, *in* Snoke, A.W., Tullis, J., and Todd, V.R., eds., Fault-related Rocks; a photographic atlas, Princeton, New Jersey, Princeton University Press, p. 3–18.

Stewart, M., Holdsworth, R.E., Strachan, R.E., 2000, Deformation processes and weakening mechanisms within the frictional-viscous transition zone of major crustal-scale faults: insights from the Great Glen Fault Zone, Scotland: Journal of Structural Geology, v. 22, p. 543–560.

Sutton, J., Watson, J., and James, T.C., 1954, A study of the metamorphic rocks of Karema and Kungwe bay, western Tanganyika: Bulletin of the Geological Survey of Tanganyika, v. 22, 70 p.

Teyssier, C.B., Tikoff, B., and Markley, M., 1995, Oblique plate motion and continental tectonics: Geology, v. 23, p. 447–450.

Theunissen, K., Klerkx, J., Melnikov, A., and Mruma, A., 1996, Mechanisms of inheritance of rift faulting in the western branch of the east African Rift, Tanzania: Tectonics, v. 15, p. 776–790.

Tullis, J., and Yund, R.A., 1980, Hydrolytic weakening of experimentally deformed Westerly granite and Hale albite rock: Journal of Structural Geology, v. 2, p. 439–451.

Tullis, J., and Yund, R.A., 1985, Dynamic recrystallization of feldspar: a mechanism for ductile shear zone formation: Geology, v. 13, p. 238–241.

White, S.H., Bretan, P.G., and Rutter, E.H., 1986, Fault-zone reactivation: kinematics and mechanisms, Philosophical Transactions of the Royal Society, London, series A317, p. 81–97.

Williams, P.F., Goodwin, L.B., and Raiser, S., 1994, Ductile deformation processes, *in* Hancock, P.L., ed., Continental Deformation, Oxford, Pergamon Press, p. 1–27.

Wintsch, R.P., Christofferson, R., and Kronenberg, A.K., 1995, Fluid-rock reaction weakening of fault zones: Journal of Geophysical Research, v. 100, p. 13,021–13,032.

Woodcock, N.H., and Naylor, M.A., 1983, Randomness testing in three-dimensional orientation data: Journal of Structural Geology, v. 5, p. 539–548.

Van Straaten, V.P., 1984, Gold Mineralization in Tanzania – a review, *in* Foster, R.P., eds., Gold '82; the geology, geochemistry and genesis of gold deposits, A.A. Balkema, Rotterdam, p. 673–685.

Vearncombe, J.R., 1998, Shear zones, fault networks, and Archean gold: Geology, v. 26, p. 855–858.

Zhang, Y., Schaubs, P.M., Zhao, C., Ord, A., Hobbs, B.E., and Barnicoat, A.C., 2008, Fault-related dilation, permeability enhancement, fluid flow and mineral precipitation patterns: numerical models, *in* The internal Structure of Fault Zones: Implications for Mechanical and Fluid-Flow Properties, Wibberley, C.A.J., Kurz, W., Imber, J., Holdsworth, R.E., and Collettini, C., eds., Geological Society Special Publications, v. 299, p. 239–255.

– Chapter Six –

U-Pb Titanite Geochronology: Implications for the orogenic Au deposit model from the Lupa goldfield, SW Tanzania

Chapter Six is to be submitted to a peer-reviewed journal

Collaborators: David Selby[1], Daniel Condon[2] and Jonathan Imber[1]
[1]Department of Earth Sciences, Durham University, Science Labs, Durham, DH1 3LE, UK
[2]Natural Environment Research Council Isotope Geosciences Laboratory, British Geological Survey, Keyworth, Nottingham, NG12 5GG, UK

6.1 Introduction

Deciphering the superimposed tectono-thermal histories of orogenic belts is a continuing challenge due to the difficulty in extracting the timing of the different stages of this thermal evolution from the rock record. The Lupa goldfield, SW Tanzania records evidence for at least three orogenic cycles spanning ca. 2 Byr and thus correlating deformation, magmatism and mineralization to a particular orogenic cycle is equivocal in the absence of precise geochronologic constraints (Boniface et al., 2012; Boniface and Schenk, 2012; Chapter Two). The U-Pb titanite geochronometer is a valuable tool in these complex geologic settings because of its occurrence in a wide variety of rock types, the incorporation of significant U (ppm levels) into its structure during crystallization and its relatively high closure temperature (550–650ºC; Frost et al., 2000). The latter makes U-Pb titanite geochronology particularly effective for dating igneous and prograde metamorphic events despite overprinting greenschist to amphibolite facies metamorphism (e.g., Lucassen and Becchio, 2003). Titanite is also highly reactive in metamorphic environments due to its chemical composition ($CaTiSiO_5$) and is therefore locally observed as a mineral constituent of metamorphic mineral assemblages and/or deformation fabrics. Thus, U-Pb titanite ages can record the timing of metamorphism and/or deformation and provide insights into the tectono-thermal evolution of a poly-orogenic setting.

Here we present new U-Pb titanite ID-TIMS geochronology which, coupled with previously reported U-Pb zircon and Re-Os sulfide ages, establishes absolute ages for metamorphism, magmatism and metallogenesis at orogenic Au deposits in the Lupa Goldfield, SW Tanzania. In particular, comparing U-Pb titanite ages with U-Pb zircon ages for the same samples proves to be a powerful tool in constraining the metamorphic and structural evolution of the goldfield. The absolute ages presented here quantify the time scale(s) of tectonic, magmatic and metallogenic

events in the Lupa goldfield and contribute to a better understanding of the tectono-thermal evolution of East Africa. The results are further applied to address many of the uncertainties related to the orogenic Au deposit models that are a consequence of a dearth of geochronologic constraints.

6.2 The chronology of orogenic Au deposits

Determining the absolute age(s) of magmatism, metamorphism and orogenic Au deposits is the subject of concentrated study and continuing controversy (e.g., Groves et al., 2003). Establishing the timing of mineralization is particularly challenging due the dearth of suitable minerals for traditional geochronologic methods. Recent Re-Os studies utilizing sulfide geochronometers co-genetic with Au provide unequivocal examples of Au mineralization concomitant with magmatic intrusions at the Myr time scale (e.g., Morelli et al., 2007; Ootes et al., 2011; Chapter Four). These studies add to an expanding global database of geochronologic ages that demonstrate broad contemporaneity between the absolute timing of Au and magmatism at most world-class goldfields (e.g., Kerrich and Cassidy, 1994; Kerrich and Kyser, 1994; Oberthur et al., 1998; Arne et al., 2001; Davis and Lin, 2003; Bucci et al., 2004; Dziggel et al., 2010; McFarlane et al., 2011). The temporal relationship between magmatism and Au mineralization has led to the "intrusion-related" deposit model and is cited as evidence for the importance of magmatically derived hydrothermal fluids in the formation of epigenetic Au deposits hosted by metamorphic belts (Groves et al., 1998; Sillitoe and Thompson, 1998; Groves et al., 2003). The inference of magmatic and thus locally derived hydrothermal fluids is at odds with orogenic gold deposits, which are hosted in similar geologic settings, but form as a result of distal hydrothermal fluids of probable metamorphic origin (e.g., Phillips and Powell, 2010). Whilst the genetic relationship between magmatic fluids and Au is satisfactorily demonstrated at several deposits (e.g., Hemlo; Davis and Lin, 2003), the exact role of magmatism in the formation of orogenic Au remains uncertain at most orogenic Au deposits (e.g., Charter Towers; Kreuzer, 2005).

Constraining the timing of greenschist to amphibolite facies metamorphism is typically more problematic with pre-, post- and syn-metamorphic deposits all represented in the literature (e.g., Kerrich and Cassidy, 1994). Whilst all three relative-age scenarios are plausible, there is a general consensus that most Au deposits occur relatively late in the tectono-thermal evolution of accretionary orogens (e.g., Kerrich and Wyman, 1990; Witt and Vanderhor, 1998; Groves et al., 2000). Au occurrences in the Lupa goldfield occur in Paleoproterozoic magmatic arc at the Tanzanian cratonic margin and thus share a close spatial and temporal relationship with granitic intrusions (Chapters Two and Four), whereas the timing of metamorphism has not been previously constrained.

6.3 Lupa goldfield geology

6.3.1 Regional and local geologic setting

The Lupa Terrane represents one of eight litho-tectonic terranes comprising the

Paleoproterozoic Ubendian Belt (Daly, 1988; Fig. 6.1). The 2.1–2.0 Ga Paleoproterozoic Ubendian tectonic phase is characterized by rare granulite facies tectonites and is overprinted by a 1.9–1.8 Ga tectonic phase that resulted in the characteristic amphibolite facies metamorphism and NW-SE trending terrane-bounding shear zones (Lenoir et al., 1994). The Paleoproterozoic tectono-thermal event is overprinted by Meso- and Neoproterozoic orogenic cycles and later rifting associated with the western branch of the East African Rift system, which all contributed to the current configuration of the Ubendian Belt litho-tectonic terranes (Theunissen et al., 1996; Boniface et al., 2012; Boniface and Schenk, 2012).

The field area for the current study is located in the western portion of the Lupa goldfield, SW Tanzania (Fig. 6.1). Foliated Archean granitoids (ca. 2740 Ma) are intruded by non-foliated Paleoproterozoic granitoids (1960–1880 Ma; Chapter 2). The temperature and pressure conditions of foliation development (D1; 2740–1960 Ma) occurred at greenschist facies metamorphic conditions based on crystal plasticity of quartz and the chlorite ± muscovite ± epidote ± calcite metamorphic mineral assemblage (300–450°C; 1–3 kbar; Scholz, 1988). All magmatic phases have experienced greenschist facies metamorphism and are cross cut by mylonitic shear zones (D2; Chapters Four and Five). The latter occurred concomitant with a goldfield-wide sulphidation event dated by Re-Os syn-deformational pyrite geochronology at ca. 1885 Ma (Chapter 4). Individual Re-Os molybdenite, pyrite and chalcopyrite model ages range from 1950–1880 Ma and are thus broadly contemporaneous with the entire magmatic history (1960–1880 Ma).

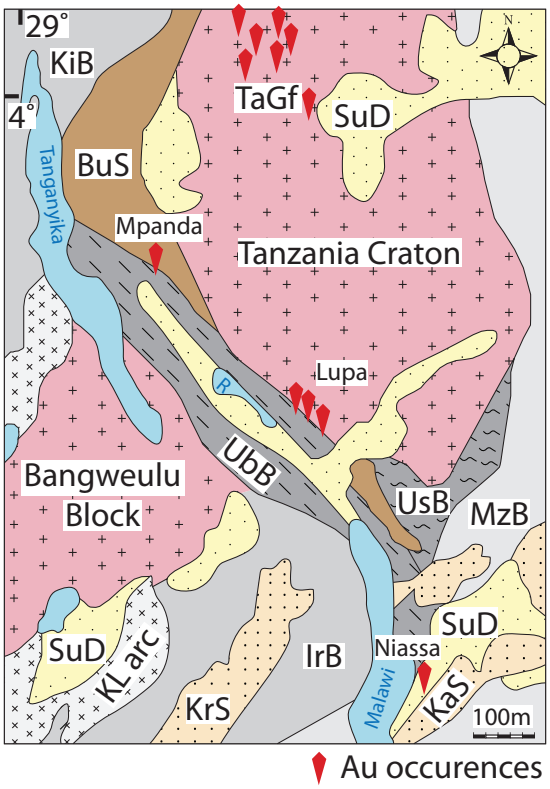

Figure 6.1 – Simplified regional geology map showing the location of goldfields in East Africa relative to Archean Cratons and Proterozoic mobile Belts (modified from CCGM/CGMW, 2002; UbB = Ubendian Belt; UsB = Usagaran Belt; KiB = Kibaran Belt; IrB = Irumide Belt; MzB = Mozambique Belt; KL arc = Katangan-Lufilian Arc; KaS = Karoo sedimentary rocks; BuS = Bukoban sedimentary rocks; SuD = surficial deposits; R = Lake Rukwa).

6.3.2 Titanite paragenesis

Foliated Archean granitoids (2757 ± 10 Ma; sample CL109; Chapter 2) are characterized by alternating quartzofeldspathic and chlorite-rich bands produced during greenschist facies metamorphism (D1). The minimum age of D1 is constrained by the U-Pb zircon ages of non-foliated cross cutting dikes (e.g., 1960 ± 1 Ma; sample CL0911; Chapter 2). Titanite crystals are concentrated within the D1 chlorite-rich bands and the greenschist facies metamorphic assemblage of chlorite ± epidote ± calcite ± titanite ± opaques overprinting the protlith's Fe-Mg minrals (Fig. 6.2a). The petrographic association of titanite with the tectonic fabric and metamorphic mineral assemblage are consistent with titanite neo-crystallization during greenschist facies metamorphism (e.g., Frost et al., 2000). The nature of this metamorphic phase transition is unclear, but could be related to the breakdown of primary clinopyroxene and/or amphibole by the hydration reaction clinopyroxene + ilmenite + quartz + H_2O = amphibole + titanite and/or the oxidation reaction amphibole + ilmenite + O_2 = titanite + magnetite + quartz + H_2O (Harlov et al., 2006).

Primary Fe-Mg minerals of the Paleoproterozoic Saza Granodiorite (U-Pb zircon ID-TIMS weighted average $^{207}Pb/^{206}Pb$ age at 1934.5 ± 1.0; sample CL1035; Chapter Two) are also replaced to a greenschist facies metamorphic mineral assemblage of chlorite ± epidote ± calcite ± titanite ± opaques. The association of titanite with the metamorphic mineral assemblage is consistent with titanite neo-crystallization during greenschist facies metamorphism, however euhedral titanite crystals isolated from the metamorphic mineral assemblage may represent relict magmatic titanite (Fig. 6.2b). Multiple titanite populations are characteristic of metamorphosed lithologies and are typically distinguished through a combination of optical/chemical characteristics and/or comparison of titanite ages with independent estimates for the

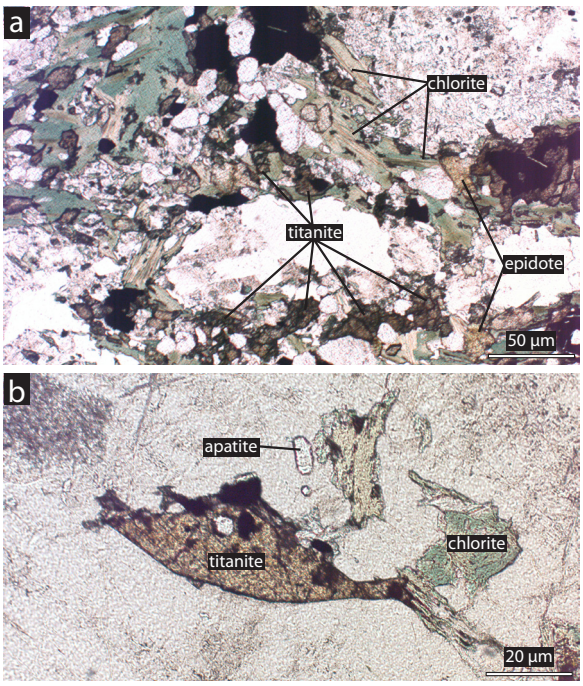

Figure 6.2 – Plane polarized light photomicrographs: (a) photomicrograph of titanite associated with greenschist facies metamorphic mineral assemblage and tectonic fabric (SZD23 at 32m); (b) euhedral titanite crystal from CL0975 (500237 / 9071994).

crystallization age of the sample (Jung and Hellebrand, 2007).

The titanite crystals present within the bulk mineral separate from sample CL109 and CL1035 are translucent, range in colour from brown to clear and are present as broken fragments and fine-grained wedge-shaped crystals in the bulk mineral separate. For samples CL109 and CL1035 translucent and clear titanite crystals devoid of inclusions were selected for U-Pb ID-TIMS analysis.

6.5 U-Pb titanite ID-TIMS Methodology

All of the analysed titanite crystals were ultrasonically cleaned for an hour before being placed on a hot plate for 30 minutes, photographed in transmitted light and rinsed in ultrapure acetone. After rinsing, titanite fractions were transferred to 300 μl Teflon FEP microcapsules and spiked with a mixed ^{233}U–^{235}U–^{205}Pb tracer. Titanite was dissolved in ~120 μl of 29 M HF with a trace amount of 30% HNO_3 within microcapsules, placed in Parr vessels at ~220°C for 48 hours, dried to fluorides and then converted to chlorides at ~180°C overnight. U and Pb for all titanite fractions were separated using standard HBr and HNO_3-based anion-exchange chromatographic procedures. Isotope ratios were measured at the NERC Isotope Geosciences Laboratory (NIGL), UK, using a Thermo-Electron Triton Thermal Ionisation Mass-Spectrometer (TIMS). Pb and U were loaded separately on a single Re filaments in a silica-gel/phosphoric acid mixture. Pb was measured by peak-hopping on a single SEM detector. U isotopic measurements were made in static Faraday mode. Age calculations and uncertainty estimation (including U/Th disequilibrium) was based upon the algorithms of Schmitz and Schoene (2007) and using the updated consensus value of $^{238}U/^{235}U = 137.818 \pm 0.045$ (Hiess et al., 2012)

6.6 U-Pb titanite ID-TIMS results

The analytical protocol and U-Pb data are reported in Table 6.1 and Fig. 6.3. For the foliated Archean granitoid (sample CL109), the three analyzed titanite fractions yield $^{238}U/^{204}Pb$ and $^{206}Pb/^{204}Pb$ ratios ranging from 112–555 and 39–172, respectively. The latter is indicative of a significant contribution of common Pb that was corrected for by using the model Pb composition at 1.9 Ga (Stacey and Kramers, 1975). All three fractions are discordant, but define a three-point Model 1 York regression with an upper concordia intercept age at 1947 ± 14 Ma and lower concordia intercept age at 475 ± 110 Ma (MSWD = 1.4; n =3; Fig. 6.3a). The analyzed titanite fractions contain significant common Pb that makes calculated ages highly dependent on the choice of the initial Pb isotopic composition (Frost et al., 2000). We tested the effect of the assumed initial Pb composition on titanite ages by varying the Stacey and Kramer (1975) model age composition from 2.0–1.8 Ga and found that calculated $^{207}Pb/^{206}Pb$ titanite ages changed from 4–31 Myr. Titanite fraction S1 was the least sensitive to the assumed initial Pb composition, whereas titanite fractions S3 and S4 were considerably more sensitive. However, the upper intercept age at 1947 ± 14 Ma is in good agreement with the onset of Paleoproterozoic magmatism (1960–1880 Ma; Chapter Two) and suggests that titanite neocrystallization occurred

Table 6.1 – U-Pb-Th titanite ID-TIMS results

		Compositional Parameters								Radiogenic Isotope Ratios								Isotopic Ages					
Sample	Wt. mg	U ppm	$\frac{Th}{U}$	Pb ppm	$^{206}Pb^*$ x10^{-13} mol	mol % $\frac{^{206}Pb^*}{^{206}Pb^*}$	$\frac{Pb^*}{Pb_c}$	Pb_c (pg)	$\frac{^{206}Pb}{^{204}Pb}$	$\frac{^{208}Pb}{^{206}Pb}$	$\frac{^{207}Pb}{^{206}Pb}$	% err	$\frac{^{207}Pb}{^{235}U}$	% err	$\frac{^{206}Pb}{^{238}U}$	% err	corr. coef.	$\frac{^{207}Pb}{^{206}Pb}$	±	$\frac{^{207}Pb}{^{235}U}$	±	$\frac{^{206}Pb}{^{238}U}$	±
(a)	(b)	(c)	(d)	(c)	(e)	(e)	(e)	(e)	(f)	(g)	(g)	(h)	(g)	(h)	(g)	(h)		(i)	(h)	(i)	(h)	(i)	(h)
CL0975																							
s1	1.0	0.9	7.101	1.0	12.6005	86.95%	5	169.8	118	2.041	0.118251	0.507	5.751013	0.543	0.352884	0.272	0.380	1929.28	9.08	1939.07	4.70	1948.25	4.58
s2	1.0	0.4	7.024	0.4	5.5666	87.75%	5	69.62	126	1.988	0.118536	0.462	5.944301	0.505	0.363870	0.251	0.411	1933.57	8.27	1967.73	4.39	2000.39	4.32
s3	1.0	1	6.545	0.6	8.6624	95.07%	13	40.14	315	1.774	0.117771	0.214	6.364791	0.292	0.392138	0.141	0.716	1921.95	3.84	2027.43	2.56	2132.65	2.57
s4	1.0	0	7.634	0.2	2.3294	93.04%	10	15.47	226	2.200	0.118160	0.289	5.711312	0.379	0.350718	0.178	0.684	1927.92	5.17	1933.08	3.28	1937.90	2.98
s5	1.0	0	6.950	0.2	3.5224	94.50%	13	18.24	285	2.013	0.118414	0.248	5.685637	0.373	0.348394	0.223	0.765	1931.74	4.44	1929.19	3.22	1926.82	3.71
CL109																							
s1	1.0	0	8.692	0.2	1.8601	90.05%	8	17.55	172	2.651	0.117158	0.381	5.047031	0.456	0.312438	0.223	0.556	1913.51	6.83	1827.25	3.87	1752.53	3.42
s3	1.0	0	5.655	0.1	0.8898	63.26%	1	44.26	46	2.104	0.105822	5.900	2.660328	6.444	0.182329	1.263	0.510	1728.87	108.30	1317.51	47.55	1079.57	12.55
s4	1.0	0	8.915	0.1	0.3829	55.99%	1	25.74	39	3.132	0.106000	3.392	3.051459	3.553	0.208785	1.481	0.315	1732.10	62.24	1420.60	27.18	1222.12	16.49

(a) s1, s2 etc. are labels for fractions composed of single titanite grains or fragments; all fractions annealed and chemically abraded after Mattinson (2005).
(b) Nominal fraction weights estimated from photomicrographic grain dimensions, adjusted for partial dissolution during chemical abrasion.
(c) Nominal U and total Pb concentrations subject to uncertainty in photomicrographic estimation of weight and partial dissolution during chemical abrasion.
(d) Model Th/U ratio calculated from radiogenic $^{208}Pb/^{206}Pb$ ratio and $^{207}Pb/^{235}U$ age.
(e) Pb* and Pbc represent radiogenic and common Pb, respectively; mol % $^{206}Pb^*$ with respect to radiogenic, blank and initial common Pb.
(f) Measured ratio corrected for spike and fractionation only.
Daly analyses, based on analysis of NBS-981 and NBS-982.
(g) Corrected for fractionation, spike, and common Pb; up to 1 pg of common Pb was assumed to be procedural blank: $^{206}Pb/^{204}Pb = 18.60 \pm 0.80\%$; $^{207}Pb/^{204}Pb = 15.69 \pm 0.32\%$; $^{208}Pb/^{204}Pb = 38.51 \pm 0.74\%$ (all uncertainties 1-sigma). Excess over blank was assigned to initial common Pb.
(h) Errors are 2-sigma, propagated using the algorithms of Schmitz and Schoene (2007) and Crowley et al. (2007).
(i) Calculations are based on the decay constants of Jaffey et al. (1971). $^{206}Pb/^{238}U$ and $^{207}Pb/^{206}Pb$ ages corrected for initial disequilibrium in $^{230}Th/^{238}U$ using Th/U [magma] = 3.
(j) Corrected for fractionation, spike, and blank Pb only.

during the Paleoproterozoic (discussed further below).

For the Saza granodiorite, five titanite fractions (sample CL0975) possess a range of $^{238}U/^{204}Pb$ and $^{206}Pb/^{204}Pb$ from 294–859 and 118–315, respectively. These ratios imply that titanite crystals from CL0975 are more U rich and possess less common Pb than titanite analyses from CL109. As result, the choice of the initial Pb isotopic composition using the model Pb composition at 1.9 Ga (Stacey and Kramers, 1975) has a smaller effect on the calculated ages (for example changing the model age Pb composition from 2.0–1.8 Ga results in $^{207}Pb/^{206}Pb$ titanite ages changing by 2–6 Myr). Three titanite fractions overlap with the Concordia curve, whereas two titanite analyses are 3–11% reversely discordant (Fig. 6.3b). The cause of reverse discordance is unclear and could be related to U loss and/or represent an analytical effect. A weighted average $^{207}Pb/^{206}Pb$ age of the three concordant titanite fractions at 1930 ± 3 (MSWD = 0.6; n = 3) is slightly younger, including uncertainty at the 2σ, than the weighted average $^{207}Pb/^{206}Pb$ age of concordant zircons from the same sample at 1935 ± 1 Ma (Chapter Two).

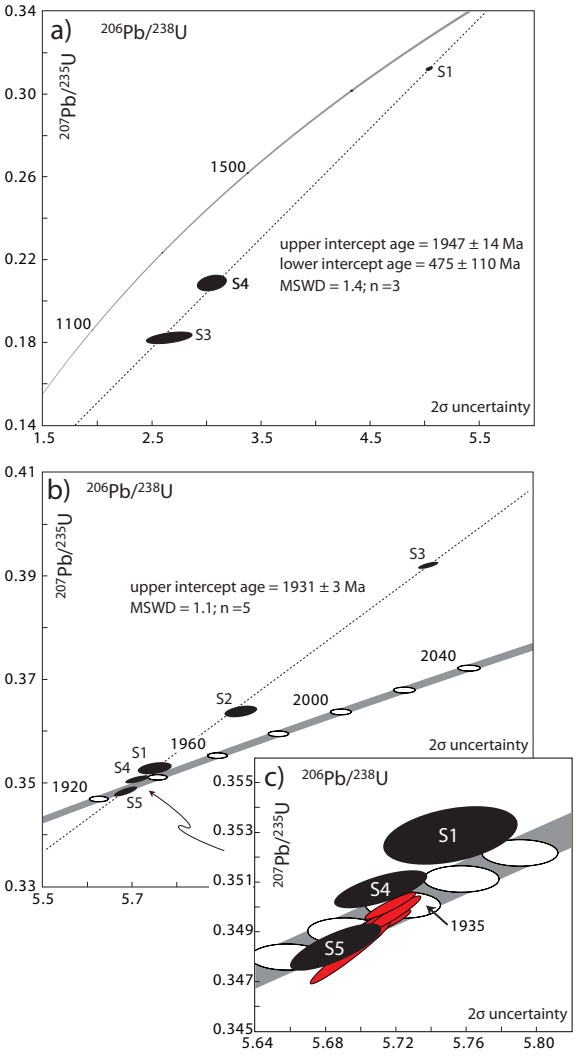

Figure 6.3 – (a) Concordia plot showing U-Pb titanite analyses and upper/lower intercept ages for sample CL109; (b) Concordia plots showing U-Pb titanite analyses (black ellipses) and upper intercept age for sample CL0975. Inset diagram shows concordant U-Pb titanite analyses and U-Pb zircon analyses (red ellipses) for CL0975 (Chapter Two).

6.7 Discussion

6.7.1 Geologic significance of U-Pb titanite ages

Titanite crystals from the foliated Archean granite sample (CL109) are spatially associated with the metamorphic fabric/mineral assemblage and provide clear evidence for titanite neo-crystallization during greenschist facies metamorphism and deformation. The absence of unambiguous magmatic titanite, which is expected given the chemical composition of CL109, suggests all primary titanite crystals were recrystallized during subsequent metamorphism. The high common Pb and low $^{238}U/^{204}Pb$ ratios of the analyzed titanite fractions support this interpretation and are consistent with the compositional characteristics of metamorphic titanite reported in previous studies (e.g., Jung and Hellebrand, 2007). The three point Model 1 York regression upper concordia intercept age at 1947 ± 14 Ma is also significantly younger than the U-Pb zircon age for the same sample at 2757 ± 10 Ma (Chapter Two). Therefore, we interpret the U-Pb titanite age as a metamorphic age that provides a first-order constraint on the onset of greenschist facies metamorphism and the timing of deformation (D1). Foliated Archean granites are cross cut by ca. 1960 Ma non-foliated granitoids and imply that deformation preceded the intrusion of these magmatic phases (Chapter Two). Our U-Pb titanite age partially overlaps with this upper temporal constraint and, if the U-Pb titanite age is presumed to represent a geologically meaningful age, suggests either: 1) deformation and the development of the metamorphic fabric exhibited by Archean granites samples occurred immediately prior to ca. 1960 Ma magmatism; or 2) deformation and the development of the metamorphic fabric exhibited by Archean granite samples occurred significantly prior to ca. 1960 Ma and the U-Pb titanite age records the most recent metamorphic overprint during the Paleoproterozoic. The latter is consistent with pre-1960 Ma tectono-thermal events recorded in other Ubendian Terranes (Lenoir et al., 1994), however given the small number of analyses and the large common Pb correction the precise age of metamorphic titanite remains tentative.

Titanite from the non-foliated Saza granodiorite (sample CL0975) are locally associated with the greenschist facies mineral assemblage overprinting the Saza Granodiorite and are thus similar to titanite crystals observed in the foliated Archean granitoid (sample CL109). However, euhedral titanite crystals isolated from the Saza Granodiorite provide evidence for a magmatic titanite population. The higher $^{206}Pb/^{238}U$ ratios and lower common Pb within the analyzed titanite fractions from the Saza granodiorite are distinct from titanite fractions from the foliated Archean granitoid and are more consistent with the composition of magmatic titanite (e.g., Jung and Hellebrand, 2007). The weighted average $^{207}Pb/^{206}Pb$ titanite age of the three concordant titanite analyses (1930 ± 3 Ma) are slightly outside of analytical uncertainty of the weighted average $^{207}Pb/^{206}Pb$ zircon age (1935 ± 1 Ma) of concordant zircons for the same sample and support a magmatic origin for the analyzed titanite fractions. The slight discrepancy between the interpreted crystallization age and U-Pb titanite ages could be related to minor Pb-loss in the analyzed titanite fractions, later closure during cooling and/or sub-solidus recrystallization (Frost et al., 2000). If the nominally younger ages represent cooling ages, our results would imply that the Saza Granodiorite cooled relatively quickly since U-Pb titanite and zircon ages are

only <1 Myr outside of analytical uncertainty at 2σ level. Establishing the cooling history of the Saza Granodiorite is particularly important for ore deposit models that invoke the importance of magmatically derived hydrothermal fluids (discussed further below).

6.7.2 Timing of granites, Au and metamorphism in the Lupa goldfield

Here we integrate the new U-Pb titanite ages with previously reported U-Pb and Re-Os ages to address some of the outstanding uncertainties regarding Au occurences within the Lupa goldfield and explore the implications of our results for other examples of the orogenic Au deposit type globally. At least two metallogenic events at ca. 1940 and 1885 Ma have been identified in the Lupa goldfield (Chapter Four). Each of these broad metallogenic events are represented in detail by complex vein histories that imply mineralization occurred at a time scale that is less than the resolution of the Re-Os method. This episodic, but protracted mineralizing history (1950–1880 Ma) overlaps with the magmatic history of the goldfield as determined by U-Pb zircon dating of felsic-mafic intrusions/dikes (1960–1880 Ma; Chapter Two). Furthermore, high-precision U-Pb zircon ID-TIMS ages for the Saza Granodiorite overlap with Re-Os molybdenite ages and provide unequivocal evidence for sulphidation that is concomitant with magmatism at the Myr time scale. The genetic significance of this temporal overlap is less clear since Re-Os model ages pre- and post-date individual magmatic phases and metallogenesis appears to occur at a time scale that is far greater than the expected duration of magmatically derived hydrothermal fluid circulation (e.g., <1 Myr; von Quadt et al., 2011). Therefore, hydrothermal fluids exsolving from any of the dated magmatic phases are unable to explain the entire range of Re-Os sulfide model ages. The U-Pb titanite ages from the foliated Archean granitoid, suggests that greenschist facies metamorphism initiated at ca. 1950 Ma. All of the rocks observed in the field area have undergone greenschist facies metamorphism and implies that greenschist facies pressure and temperature conditions either persisted until at least 1880 Ma or require a second metamorphic event at <1880 Ma. Pyrite crystals wrapped by the greenschist facies mylonitic fabric and, dated at ca. 1880 Ma, constrain the timing of mylonitization and also likely record the timing of this younger metamorphic event. The broad temporal overlap between metallogenic (1950–1880 Ma), magmatic (1960–1880 Ma) and metamorphic (1950–1880 Ma) events in the Lupa goldfield are also well correlated to tectono-thermal events in other Ubendian terranes. Specifically, the Paleoproteorzoic MORB-like chemistry eclogites (ca. 1890 and 1860 Ma; Boniface et al., 2012) in the Ubende Terrane demonstrates that high-grade metamorphism related to subduction of oceanic crust occurred simultaneously with metallogenesis in the Lupa goldfield. Paleoproterozoic eclogitic rocks in the Ubende Terrane are amongst the oldest eclogites on Earth (Boniface et al., 2012). As a result, the orogenic Au deposits in the Lupa goldfield represent one of the earliest analogs for Phanerozoic orogenic Au deposits. A holistic understanding of Ubendian tectonics requires additional study, but the link between subduction processes and orogenic Au in the Lupa goldfield is implied.

6.7.3 Implications for the orogenic Au deposit model

Modern convergent margins are associated with protracted histories of broadly contemporaneous metamorphism, deformation and magmatism. The temporal framework developed here suggests an analogous geologic setting for orogenic Au deposits in the Lupa goldfield. Our results preclude individual intrusions as the source of Au at orogenic gold deposits in the Lupa goldfield, but also highlight the need to integrate geochronologic studies with other geochemical tools in order to identify the source(s) of metalliferous fluids. Temporal relationships are generally not sufficient to determine genetic relationships between metamorphism, magmatism and metallogenesis as all three are intrinsically linked at accretionary orogens where orogenic Au deposits develop (Bierlein et al., 2009).

Whilst the source of metals remains uncertain, there is a growing consensus that a Au-enriched upper-mantle is likely a first order control on orogenic Au deposit formation (e.g., Hronsky et al., 2012). A mantle source is also consistent with $^{187}Os/^{188}Os_{initial}$ values of pyrite co-genetic with Au reported in the Lupa goldfield and other orogenic Au deposits (e.g., Morelli et al., 2007; Chapter Four). The enrichment of the upper mantle is likely related to subduction zone processes and concentration of incompatible elements during mantle melting (Richards, 2009). The locus of the Lupa goldfield at the Tanzanian cratonic margin may have had an important role in allowing upper-mantle fertilization over a protracted period and through multiple orogenic cycles. The latter is supported by Meso- and Neoproterozoic Re-Os model ages and lower intercept U-Pb ages recorded in the Lupa Goldfield that can be correlated with the Kibaran/Irumide and Pan African orogenic cycles (Chapter 2). Furthermore, Neoproterozoic and Paleozoic orogenic Au deposits are recorded to the NW and to the SE of the Lupa goldfield and along strike of the Ubendian Belt (e.g., Mpanda goldfield, Stendal et al., 2004; Niassa goldfield, Bjerkgard et al., 2009; Fig. 6.1). The cratonic margins bordering the Ubendian Belt are therefore highly prospective for orogenic Au deposits that may have developed during at least three discrete orogenic cycles and over a period of at least 1.5 Byr. Our results affirm previous suggestions that the association of orogenic Au deposits and cratonic margins may be related to Au-enriched upper mantle source that is long-lived and can be repeatedly tapped during temporally distinct orogenic cycles (Hronsky et al., 2012). The high permeability of mid-crustal shear zones relative to the wall rock likely transported hydrothermal fluids from some source(s) at depth during each orogenic cycle and led to overprinting sulphidation and potentially upgraded Au grade at pre-existing deposits.

6.8 Conclusions

Titanite U-Pb geochronology for a foliated Archean granitoid at 1947 ± 14 Ma provides a first order constraint on the onset of greenschist facies metamorphism and deformation during the Paleoproterozoic. In contrast, U-Pb titanite ages for the non-foliated Saza Granodiorite at 1930 ± 3 Ma are only nominally younger than the U-Pb zircon age (1935 ± 1 Ma) for the same sample. These U-Pb titanite ages, combined with previously reported U-Pb zircon and Re-Os sulfide geochronology, constrain the timing of magmatism (1960–1880 Ma), metallogenesis

(1950–1880 Ma) and metamorphism (1947–1880 Ma) in the Lupa goldfield. The tectono-magmatic-metallogenic evolution of the Lupa goldfield occurred concurrently with amphibolite to eclogite facies metamorphism and subduction of oceanic crust in other Ubendian Terranes. The Paleoproterozoic metallogenic events in the Lupa goldfield represent the earliest episode of orogenic Au deposit formation and are superseded by younger orogenic Au-type mineralization related to three discrete orogenic cycles. Cratonic margins bordering the Ubendian Belt are therefore highly prospective for orogenic Au deposits that may have formed during its 2.7 Byr tectono-thermal history.

6.9 References

Arne, D.C., Bierlein, F.P., Morgan, W., and Stein, H.J., 2001, Re-Os dating of sulfides associated with gold mineralization in central Victoria, Australia: Economic Geology, v. 96, p. 1455–1459.

Bierlein, F.P., Groves, D.I., and Cawood, P.A., 2009, Metallogeny of accretionary orogens – the connection between lithospheric processes and metal endowment: Ore Geology Reviews, v. 36, p. 282–292.

Bjerkgard, R., Stein, H.J., Bingen, B., Henderson, I.H.C., Sandstad, J.C., and Moniz, A., 2009, The Niassa Gold Belt, northern Mozambique – a segment of a continental-scale Pan-African gold-bearing structure?: Journal of African Earth Sciences, v. 53, p. 45–58.

Boniface, N., Schenk, V., and Appel, P., 2012, Paleoproterozoic eclogites of MORB-type chemistry and three Proterozoic orogenic cycles in the Ubendian Belt (Tanzania): evidence from monazite and zircon geochronology, and geochemistry: Precambrian Research, v. 192–195, p. 16–33.

Boniface, N., and Schenk, V., 2012, Neoproterozoic eclogites in the Paleoproterozoic Ubendian Belt of Tanzania: evidence for a Pan-African suture between the Bangweulu Block and the Tanzania Craton: Precambrian Research, v. 208–211, p. 72–89.

Bucci, L.A., McNaughton, N.J., Fletcher, I.R., Groves, D.I., Kositcin, N., Stein, H.J., and Hagemann, S.G., 2004, Timing and duration of high-temperature gold mineralization and spatially associated granitoid magmatism at Chalice, Yilgarn Craton, Western Australia: Economic Geology, v. 99, p. 1123–1144.

Crowley, J.L., Schoene, B., and Bowring, S.A., 2007, U-Pb dating of zircon in the Bishop Tuff at the millennial scale: Geology, v. 35, p. 1123–1126.

Daly, M.C., 1988, Crustal shear zones in central Africa a kinematic approach to Proterozoic tectonics: Episodes, v. 11, p. 5–11.

Davis, D.W., and Lin, S.F., 2003, Unraveling the geologic history of the Hemlo Archean gold deposit, Superior province, Canada; a U-Pb geochronological study: Economic Geology, v. 98, p. 51–67.

Dziggel, A., Poujol, M., Otto, A., Kisters, A.F.M., Trieloff, M., Schwarz, W.H., and Meyer, F.M., 2010, New U-Pb and Ar-40/Ar-39 ages from the northernmargin of the Barberton

greenstone belt, South Africa: Implication for the formation of Mesoarchaean gold deposits: Precambrian Research, v. 179, p. 206–220.

Frost, B.R., Chamberlain, K.R., and Schumacher, J.C., 2000, Sphene (titanite): phase relations and role as a geochronometer: Chemical Geology, v. 172, p. 131–148.

Groves, D.I., Goldfarb, R.J., Gebre-Mariam, M., Hagemann, S.G., and Robert, F., 1998, Orogenic gold deposits: a proposed classification in the context of their crustal distribution and relationships to other gold deposit types: Ore Geology Reviews, v. 13, p. 7–27.

Groves, D.I., Goldfarb, R.J., Knox-Robinson, C.M., Ojala, J., Gardoll, S., Yun, G.Y., and Holyland, P., 2000, Late-kinematic timing of orogenic gold deposits and significance for computer-based exploration techniques with emphasis on the Yilgarn Block, Western Australia: Ore Geology Reviews, v. 17, p. 1–38.

Groves, D.I., Goldfarb, R.J., Robert, F., and Hart, C.J.R., 2003, Gold deposits in metamorphic belts: overview of current understanding, outstanding problems, future research and exploration strategies: Economic Geology, v. 98, p. 1–29.

Harlov, D.E., Tropper, P., Seifert, W., Nijland, T. and Förster, H.J., 2006, Formation of Al-rich titanite ($CaTiSiO_4O$-$CaAlSiO_4OH$) reaction rims on ilmenite in metamorphic rocks as a function of fH2O and fO2: Lithos, v. 88, p. 72–84.

Hiess, J., Condon, D. J., McLean, N., and Noble, S. R., 2012. $^{238}U/^{235}U$ Systematics in Terrestrial Uranium-Bearing Minerals. Science 335 (no. 6076), 1610-1614.

Hronsky, J.M.A., Groves, D.I., Loucks, R.R., and Begg, G.C., 2012, A unified model for gold mineralization in accretionary orogens and implications for regional-scale exploration targeting methods: Mineralium Deposita, v. 47, p. 339–358.

Jaffey, A. H., Flynn, K. F., Glendenin, L. E., Bentley, W. C., and Essling, A. M., 1971, Precision measurement of half-lives and specific of 235U and 238U: Physics Reviews C4, p. 1889-1906.

Jung, S., and Hellebrand, E., 2007, Textural, geochronological and chemical constraints from polygenetic titanite and monogenetic apatite from a mid-crustal shear zone; an integrated EPMA, SIMS, and TIMS study: Chemical Geology, v. 241, p. 88–107.

Kerrich, R., and Kyser, T.K., 1994, 100 Ma timing paradox of Archean gold, Abitibi greenstone-belt (Canada) – new evidence from U-Pb and Pb-Pb evaporation ages of hydrothermal zircons: Geology, v. 22, p. 1131–1134.

Kerrich, R., and Cassidy, K.F., 1994, Temporal relationship of lode gold mineralization to accretion, magmatism, metamorphism and deformation – Archean to present: a review: Ore Geology Reviews, v. 9, p. 263–310.

Kerrich, R., and Wyman, D., 1990, Geodynamic setting of mesothermal gold deposits; an association with accretionary tectonic regimes: Geology, v. 18, p. 882–885.

Kreuzer, O.P., 2005, Intrusion-hosted mineralization in the charters towers goldfield, North Queensland; new isotopic and fluid inclusion constraints on the timing and origin of the

auriferous veins: Economic Geology, v. 100, p. 1583–1603.

Lucassen, F., and Becchio, R., 2003, Timing of high-grade metamorphism: early Palaeozoic U-Pb formation ages of tianite indicate long-standing high-T conditions at the western margin of Gondwana (Argentina, 26–29ºS): Journal of Metamorphic Geology, v. 21, p. 649–662.

Mattinson, J.M., 2005, Zircon U-Pb chemical abrasion ("CA-TIMS") method: combined annealing and multi-step partial dissolution analysis for improved precision and accuracy of zircon ages: Chemical Geology, v. 220, p. 47–66.

McFarlane, C.R.M., Mavrogenes, J., Lentz, D., King, K., Allibone, A., and Holcombe, R., 2011, Geology and intrusion-related affinity of the Morila Gold Mine, southeast Mali: Economic Geology, v. 106, p. 727–750.

Morelli, R., Creaser, R.A., Seltmann, R., Stuart, F.M., Selby, D., and Graupner, T., 2007, Age and source constraints for the giant Muruntau gold deposit, Uzbekistan, from coupled Re-Os-He isotopes in arsenopyrite: Geology, v. 35, p. 795-798.

Oberthur, T., Vetter, U., Davis, D.W., and Amanor, J.A., 1998, Age constraints on gold mineralization and Paleoproterozoic crustal evolution I nthe Ashanti belt of southern Ghana: Precambrian Research, v. 89, p. 129–143.

Ootes, L., Lentz, D.R., Creaser, R.A., Ketchum, J.W., and Falck, H., 2007, Re-Os molybdenite ages from the Archean Yellowknife greenstone belt comparison to U-Pb ages and evidence for metal introduction at similar to 2675 Ma: Economic Geology, v. 102, p. 511–518.

Ootes, L., Morelli, R.M., Creaser, R.A., Lentz, D.R., Falck, H., and Davis, W.J., 2011, The timing of Yellowknife gold mineralization a temporal relationship with crustal anatexis: Economic Geology, v. 106, p. 713–720.

Phillips, G.N., and Powell, R., 2010, Formation of gold deposits; a metamorphic devolatilization model: Journal of Metamorphic Geology, v. 28, p. 689–718.

Richards, J.P., 2009, Postsubduction poryphyry Cu-Au and epithermal Au deposits: products of remelting of subduction-modified lithosphere: Geology, v. 37, p. 246–250.

Schmitz, M.D., and Schoene, B., 2007, Derivation of isotope ratios, errors, and error correlations for U-Pb geochronology using ^{205}Pb-^{235}U(^{233}U)-spiked isotope dilution thermal ionization mass spectrometric data: Geochemistry, Geophysics, Geosystems, v. 8, 20 p.

Schoene, B., and Bowring, S.A., 2007, Determining accurate temperature-time paths from u-Pb thermochronology; an example from the Kaapvaal craton, southern Africa: Geochimica et Cosmochimica Acta, v. 71, p. 165–185.

Scholz, C.H., 1988, The brittle-plastic transition and the depth of seismic faulting: Geologische Rundschau, v. 77, p. 319–328.

Sillitoe, R.H., and Thompson, F.H., 1998, Intrusion-related vein gold deposits: types, tectonomagmatic settings and difficulties of distinction from orogenic gold deposits: Resource Geology, v. 48, pp. 237–250.

Stacey, J.S., and Kramers, J.D., 1975, Approximation of terrestrial lead isotope evolution by a 2-Stage Model: Earth and Planetary Science Letters, v. 26, p. 207–221.

Stendal, H., Frei, R., Muhongo, S., Ramussen, T.M., Mnali, S., Petro, F., and Temu, E.B., 2004, Gold potential of the Mpanda Mineral Field, SW Tanzania: evaluation based on geological, lead isotopic and aeromagnetic data: Journal of African Earth Sciences, v. 38, p. 437–447.

Theunissen, K., Klerkx, J., Melnikov, A., and Mruma, A., 1996, Mechanisms of inheritance of rift faulting in the western branch of the east African Rift, Tanzania: Tectonics, v. 15, p. 776–790.

Von Quadt, A., Erni, M., Martinek, K., Moll, M., Peytcheva, I., Heinrich, C.A., 2011, Zircon crystallization and the lifetimes of ore-forming magmatic-hydrothermal systems: Geology, v. 39, p. 731–734.

Witt, W.K., Vanderhor, F., 1998, Diversity within a unified model for Archaean gold mineralization in the Yilgarn Craton of Western Australia: an overview of the late-orogenic, structurally controlled gold deposits: Ore Geology Reviews, v. 13, p. 29–64.

– Chapter Seven –

Conclusions, Mineral Exploration Implications and Future Research

7.1 Conclusions

7.1.1 Chapter Two

- U-Pb results demonstrate that previously considered Proterozoic granitoids are in fact Archean and imply that significant portions of the Ubendian Belt represent re-worked Archean crust. Archean granitoids (ca. 2740 Ma) possess inherited zircon cores (ca. 2850 Ma) and are thought to represent melting of ≥3.1 Ga crust based on $^{176}Hf/^{177}Hf$ results that are inconsistent with melting of Neoarchean mantle. The U-Pb and Lu-Hf results are compatible with a growing number of deep seismic studies, which demonstrate laterally extensive Archean lithosphere underlying many other Proterozoic accretionary orogens (Snyder, 2002; Begg et al., 2009; Hammer et al., 2010).

- Paleoproterozoic felsic-mafic plutons/dikes (1960–1880 Ma) possess trace element characteristics that are typical of modern-day continental arcs and suggest the Lupa Terrane represented a Paleoproterozoic continental magmatic arc onto which the other Ubendian Terranes were accreted. The U-Pb results are consistent with previously reported U-Pb ages from other Ubendian Terranes and provide evidence for a protracted and diachronous magmatic history during the Paleoproterozoic Ubendian orogenic cycle (Boniface et al., 2011; Boniface and Schenk, 2012). The juxtaposition of contemporaneous greenschist and granulite-amphibolite facies metamorphism implies significant displacement along the terrane-bounding shear zones.

7.1.2 Chapter Three

- Re-Os systematics are not affected by exposure to HF at room temperature and the HF mineral separation technique can be used to isolate sufficient quantities of ultrafine molybdenite samples for Re-Os geochronology that were previously unsuitable using conventional mineral separation techniques.

7.1.3 Chapter Four

- Re-Os molybdenite, pyrite and chalcopyrite geochronology provides evidence for contemporaneous sulphide deposition (ca. 1885 Ma) at all five of the studied Au occurrences (Fig. 7.1). The results suggest shear zones acted as a connected network of permeable fluid conduits during the Paleoproterozoic. Re-Os sulphide ages at ca. 1950,

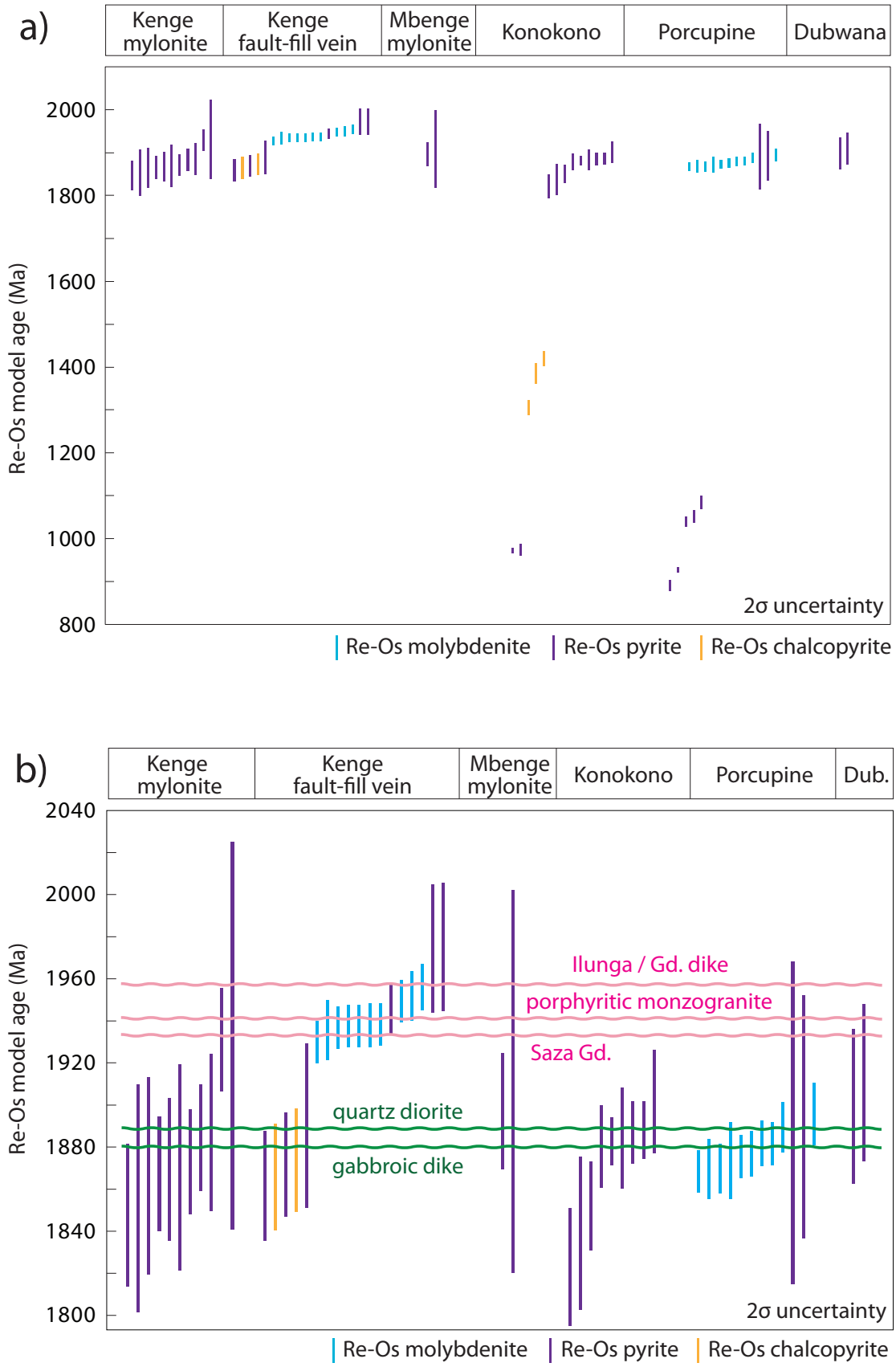

Figure 7.1 – (a) All Re-Os molybdenite (blue), pyrite (purple) and chalcopyrite (yellow) model ages reported in Chapter Four. Uncertainties are reported at 2σ; (b) Paleoproterozoic Re-Os molybdenite (blue), pyrite (purple) and chalcopyrite (yellow) model ages reported in Chapter Four. Uncertainties are reported at 2σ. With interpreted U-Pb zircon ages, minus their associated analytical uncertainties, reported in Chapter Two (Gd. = granodiorite; Ilunga = Ilunga Syenogranite)

1940 Ma and ca. 1885 Ma provides evidence for a protracted, but episodic metallogenic history spanning at least 70 Myr (Fig. 7.1). A complex metallogenic history is also inferred from vein textures and suggests individual vein histories comprising each of the broadly defined metallogenic events occurred at a time scale less than the resolution of the Re-Os method. The temporal overlap between Re-Os ages reported in this thesis and U-Pb ages of eclogites (1890–1860 Ma; Boniface et al., 2012) in other Ubendian Terranes supports a genetic link between subduction processes and orogenic Au.

- The protracted metallogenic history at Kenge (ca. 70 Myr) provides an example of a long lived and periodically reactivated mylonitic shear zone. Shear zone reactivation was likely coupled with increased permeability, which may explain the complex sulphide paragenesis inferred from outcrop exposures. The resolution of Re-Os sulfide geochronology is not sufficient to resolve disparate sulphide events occurring at time scale less than ca 10 Myr (i.e., the typical 2σ uncertainty of Re-Os molybdenite ages).

- Re-Os sulphide geochronology from Kenge and Porcupine provides evidence for broadly contemporaneous brittle and ductile deformation processes. The results suggest that Kenge and Porcupine should be regarded as part of the same mineralizing event despite the geologic differences between the two Au occurrence types (Chapters Four and Five).

- U-Pb zircon ages provide evidence for a protracted, but episodic Paleoproterozoic magmatic history (1960–1880 Ma) that broadly overlaps with the metallogenic history (1950–1880 Ma) determined by Re-Os sulphide geochronology (Fig. 7.2). High-precision U-Pb zircon ID-TIMS ages for the Saza Granodiorite overlap with Re-Os molybdenite model ages and provide unequivocal evidence for magmatism concomitant with mineralization at the Myr time scale (Fig. 7.1). However, none of the dated intrusions can

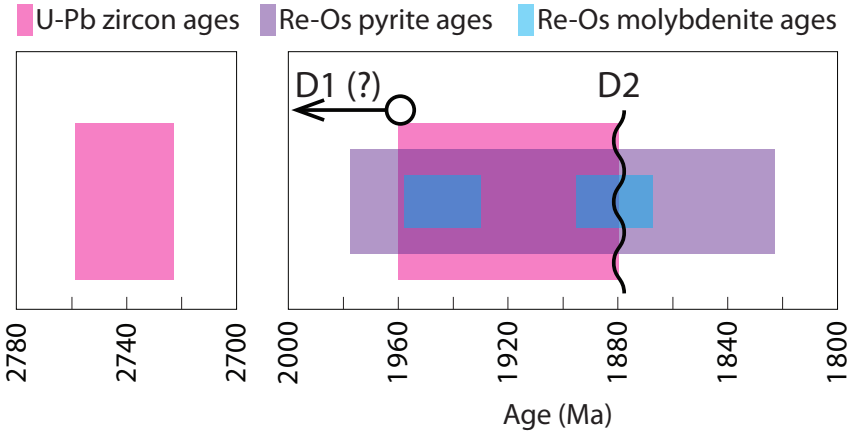

Figure 7.2 – Diagram summarizing the U-Pb and Re-Os age ranges reported in Chapters Two and Four. Note the broad temporal overlap between magmatism and mineralization.

explain the range of Re-Os ages observed at each Au occurrence and thus are inconsistent with the "intrusion related" deposit model. For example, the high precision U-Pb zircon age of the Saza Granodiorite overlaps with several Re-Os molybdenite ages at Kenge, but is clearly outside of analytical uncertainty with Re-Os molybdenite ages at Porcupine (Fig. 7.1).

- Calculated $^{187}Os/^{188}Os_{initial}$ (0.04 ± 0.18) for Kenge and Mbenge pyrite samples overlap with mantle values and are inconsistent with a significantly radiogenic source (e.g., crustal contribution) of Os to the hydrothermal system.

- Meso- and Neoproterozic Re-Os ages may suggest the metallogenic history of the Lupa goldfield spans two distinct orogenic cycles (Ubendian and Kibaran Orogeny; Fig. 7.1).

- The overlap between Re-Os molybdenite and Re-Os pyrite and chalcopyrite ages demonstrate pyrite and chalcopyrite can provide robust age determinations despite having undergone greenschist facies metamorphism.

7.1.4 Chapter Five

- Asymmetric fabrics on sub-horizontal and sub-vertical planes perpendicular to the mylonitic foliation imply a transpressional deformation setting and reverse oblique movement along the examined shear zones. Transpressional deformation is consistent with the flattening strain inferred from oblate-shaped porphyroclasts, variably oriented mineral elongation lineations, quartz veins boudinaged in plan and section views and the prevalence of S-type tectonites.

- Hydrothermal alteration, related to pre-D2 brittle deformation, led to the replacement of strong, load-bearing feldspars (plagioclase and K feldspar) with weak phyllosilicates and local produced the ideal conditions for strain localization, mylonitization and further fluid flow. Pre-existing structural weaknesses (e.g., D1 foliation, lithologic contacts) also likely played a key role during the initial localization of hydrothermal fluids and strain.

- The three-dimensional distribution of pyrite, as determined by X-ray Computed Tomography scanning, highlights the importance of the mylonitic fabric and associated shear band cleavages as fluid pathways during sulphidation. Intergranular flow explains the disseminated style of mineralization and was likely facilitated by shear zone normal dilation during episodic fluid overpressures.

7.1.5 Chapter Six

- Titanite crystals sampled from an Archean granitoid (ca. 2750 Ma) possess Paleoproterozoic U-Pb ages (ca. 1950 Ma) and are interpreted to constrain the onset of greenschist facies

metamorphism. In contrast, titanite crystals from the Saza Granodiorite possess U-Pb ages that are indistinguishable from U-Pb zircon ID-TIMS age for the same sample.

- The results presented in Chapters Two, Four, and Six imply that Au mineralization in the Lupa goldfield occurred at greenschist-facies pressure-temperature conditions in an evolving Paleoproterozoic continental arc and was concomitant with, but not genetically related to, calc-alkaline plutonism. The geologic setting of the Lupa goldfield contrasts with contemporaneous eclogite-amphibolte facies metamorphism that is characteristic of other Ubendian Terranes (Lenoir et al., 1994; Boniface et al., 2012).

- Mesoproterozoic Re-Os ages and a U-Pb zircon lower intercept age are similar to ages reported for the Kibaran Orogeny (and/or Irumide Orogeny). Three Pan-African lower intercept ages also provide evidence for a Pb-loss event during the Neoproterozoic–Paleozoic. The location of the Lupa goldfield at a cratonic margin was likely an important factor in the tectono-thermal evolution of the goldfield spanning multiple orogenic episodes.

7.2 Geologic evolution of the field area

The geologic evolution of the field area is summarized in a series of schematic block diagrams (Fig. 7.3). U-Pb ages of inherited zircons and in-situ Lu-Hf zircon geochemistry suggest that Archean granitoids (2760–2720 Ma) intruded into older Archean crust at depth (ca. 3.1 Ga). These Archean granitoids were later deformed, potentially during the Paleoproterozoic (ca. U-Pb titanite metamorphic age at ca. 1950 Ma; D1; Chapters Five and Six), and were intruded by non-foliated granitoids at ca. 1960 Ma. The regionally important Ilunga Syenogranite (CL0972; Chapter Two) represents an example of this Paleoproterozoic magmatic event along with non-foliated granodiorite-tonalite dikes (CL0911; Chapter Two). Dioritic-gabbroic dikes/intrusions are observed cross cutting the Ilunga Syenogranite, but intermediate-mafic enclaves/xenoliths suggest that the Ilunga Syenogranite is also pre-dated by intermediate-mafic magmatism. The Saza Granodiorite intruded at ca. 1935 Ma (CL0975 Ma; Chapter Two) and is pre-dated by porphyritic monzogranite (ca. 1942 Ma; CL1019; Chapter Two) and dioritic-gabbroic dikes/intrusions. Younger U-Pb zircon ages of intermediate-mafic dikes/intrusions post-date the Saza Granodiorite and are consistent with cross cutting relationships observed in the field. In particular, a U-Pb zircon age for a quartz diorite intrusion (ca. 1890 Ma; CL1021; Chapter Two) overlaps within analytical uncertainty with a U-Pb zircon age for a gabbroic dike (ca. 1880 Ma; CL1022; Chapter Three) and both are younger than any of the dated granitic intrusives. The U-Pb ages reported as part of this thesis are thus consistent with field relationships and collectively record a complex and protracted history of granitic-gabbroic magmatism. The unpublished aeromagnetic map flown by Helio Resource Corp. also shows magnetic lineaments that are interpreted to be mafic dikes cross cutting all of the dated intrusions and provide

evidence for undated, but younger magmatic events (also supported by undated aplite dikes cross cutting each of the main intrusive bodies in the field area).

Re-Os sulphide ages directly date brittle-deformation events and further constrain the geologic evolution of the field area. Molybdenite- and pyrite-bearing quartz veins record a protracted metallogenic history at Kenge (1960–1880 Ma), whereas Re-Os sulphide ages at all five of the dated Au occurrences demonstrate a broad and regional mineralizing event(s) at ca. 1885 Ma (Chapter Four). The economic significance of these disparately older Re-Os

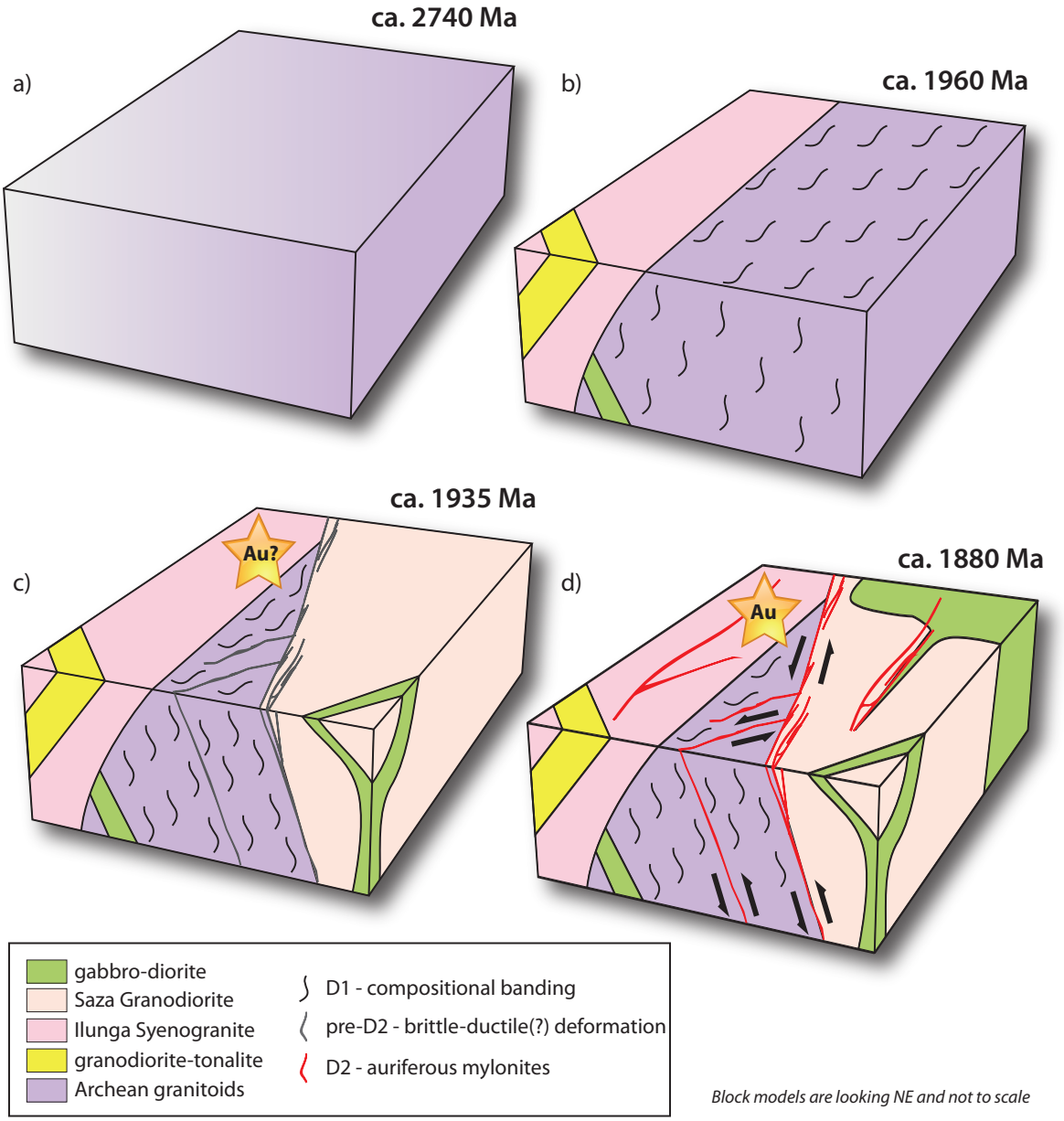

Figure 7.3 – Schematic block models showing the geologic evolution of the Lupa goldfield from the Archean to the Paleoproterozoic (based on U-Pb and Re-Os ages presented in Chapters Two, Four and Six). The geologic history of the Lupa extends beyond the Paleoproteorozoic (e.g., Meso- and Neoproterozoic Re-Os ages, Neoproterozoic and Paleozoic U-Pb lower intercept ages, fauting cross cutting ca. 1880 Ma shear zones, etc.), however the timing and characteristics of these events remain poorly understood. See text for more details.

pyrite and molybdenite ages (ca. 1950 and 1940 Ma; pre-D2 structures) from Kenge remains equivocal, whereas auriferous mylonites at Kenge (ca. 1880 Ma; D2), represent the closest paragenetic relationship to Au (Chapter Four). Kinematic indicators from auriferous mylonites are consistent with a transpressional setting and record reverse oblique movements along the Saza shear zone and subsidiary structures at ca. 1880 Ma.

Anomalously younger Re-Os ages (Meso- and Neoproterozoic), U-Pb lower intercept ages (Neoproterozoic and Paleozoic) and cross cutting field relationships all suggest the geologic evolution of the Lupa goldfield continues beyond the Paleoproterozoic. However, the characteristics and exact timing of these younger (<1880 Ma) magmatic-tectono-metallogenic events remains poorly understood.

7.3 Mineral exploration implications

The results and conclusions presented in Chapters Two, Three, Four, Five and Six have implications for on-going mineral exploration efforts in SW Tanzania. Several of these implications apply to regional and district scale mineral exploration for a variety of deposit types, whereas other implications are specific to orogenic Au deposits within the Lupa goldfield (Fig. 7.4).

7.3.1 Regional scale implications

- One of the important results of Chapter Two is the identification of Archean granitoids that cast doubt on the currently accepted SW extent of the Tanzanian cratonic margin. Establishing the extent of the Tanzanian Craton places important constraints on the prospectivity of SW Tanzania for deposits associated with Archean Cratons. The results imply the Tanzanian Craton is larger than previously suggested and provide the first evidence to propose that portions of the Ubendian Belt represent re-worked Archean crust. SW Tanzania may be prospective for previously unconsidered deposits associated with Archean Cratons.

- The results and conclusions presented in Chapter Two suggest the Lupa Terrane represented a Paleoproterozoic continental arc at the Tanzanian cratonic margin. This tectonic setting is distinct from other Tanzanian orogenic Au deposits that are associated with allochtonous terranes (Kuehn et al., 1990). Continental arcs are relatively under represented in the literature as important tectonic settings for Precambrian orogenic Au deposits (Groves et al., 1998). The results highlight the need to re-evaluate the importance of the position of orogenic Au deposit formation relative to the position of the evolving arc.

- The ages reported in Chapters Two, Four and Six record evidence for at least three orogenic cycles in the Lupa goldfield. This protracted geologic history is likely related to the Lupa goldfield's position at the Tanzanian Cratonic margin and may be an important

factor in orogenic Au deposit formation (Hronsky, 2012). A long-lived source, such as a fertile upper mantle / lower crust, could be repeatedly tapped during multiple orogenic cycles (Richards, 2009). As a result, cratonic margins bordering the Ubendian Belt are particularly attractive mineral exploration targets for orogenic Au deposits that may have developed during three discrete orogenic cycles.

- The tectono-magmatic evolution of the Lupa goldfield proposed in Chapter Two possesses many similarities with magmatic ages reported from the western limit of the Ubendian Belt (eastern Congo Craton and the Bangweulu block). Very few geologic constraints are currently available, but these areas appear to possess granitic plutons of comparable age and may also represent important settings for orogenic Au deposits (Cahen et al., 1984; Ring, 1993). In particular, the Bangweulu Block has undergone low grade metamorphism similar to the Lupa goldfield and contrasts with the high grade metamorphic rocks characteristic of the Ubendian Terranes (De Waele, 2006).

7.3.2 Goldfield and deposit scale implications

- The results and conclusions presented in Chapter Four provide evidence for contemporaneous sulphidation at five Au occurrences across the field area. These ore

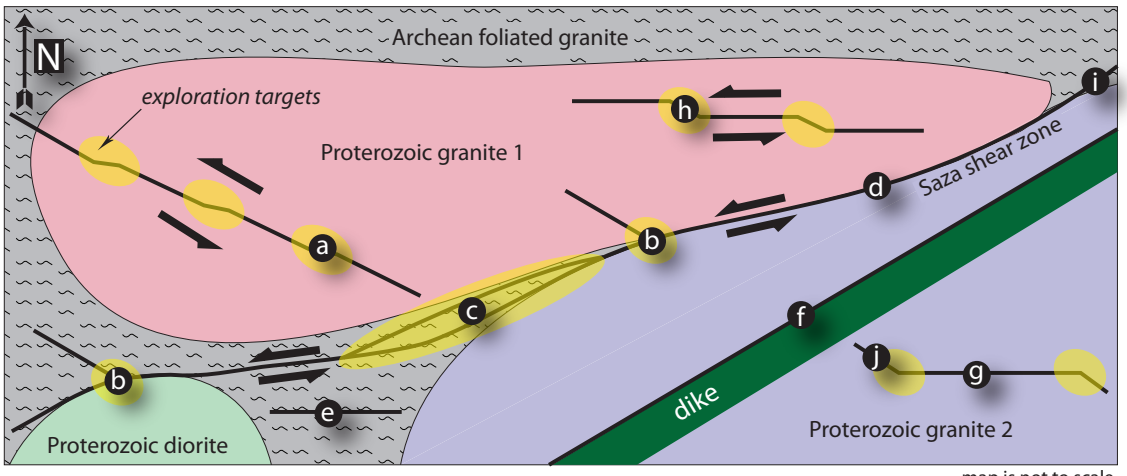

map is not to scale

a dilational jogs and step-overs in NW-SE trending shear zones
b shear zone intersection between NW-SE trending and Saza shear zones
c dilational jogs in Saza shear zone
d shear zone geometry is locally controlled by lithologic contatcs
e pre-existing deformation may control Au-bearing shear zone geometry
f shear zone geometry is controlled by dike-host rock contacts
g shear zones apparently isolated form the Saza shear zone are still prospective
h mis-oriented shear zones appear to be important for the development of oblique-extension veins
i curved shear zone segments may exhibit variations in finite strain
j E-W trending shear zones are associated with NW-SE trending splays

Figure 7.4 – Schematic plan view of the field area highlighting potential exploration targets.

bodies are hosted by disparately oriented shear zones of various scales (second order shear zones possess strike lengths >10 km, whereas third order shear zones possess strike lengths <10 km) and suggest that mylonitic shear zones represented an interconnected network of permeable fluid conduits during the Paleoproterozoic. Therefore, second- and third-order shear zones are equally prospective for the focusing of auriferous hydrothermal fluids. Flow localization also likely occurred at the intersection between large-scale faults and contemporaneous subsidiary structures (Cox et al., 2001).

- The unpublished aeromagnetic map flown by Helio Resource Corp. clearly shows magnetic lineaments, corresponding to mylonitic shear zones, cross cutting all of the major lithologies in the field area. However, several Re-Os pyrite and molybdenite ages at Kenge are older than the U-Pb age of the Saza Granodiorite (Fig. 7.1b). One of the implications of these older Re-Os ages to mineral exploration is that not all of the identified metallogenic/deformation events will be preserved within all of the intrusive phases. Foliated Archean granitoids are the only dated intrusive phases which pre-date all of the Re-Os ages and if the ca. 1950 Ma sulphidation event was associated with Au mineralization than Archean granitoids may represent favourable exploration targets. The regional metallogenic event dated at ca. 1885 Ma is consistent with the traces of mylonitic shears cross cutting all of the major intrusive phases on the aeromagnetic map and also represents the closest paragenetic relationship with Au.

- Comparison between structural mapping completed as part of this study and previously reported lithologic maps (e.g., Kimambo, 1984) highlight two goldfield-wide structural trends for Au-bearing shear zones: 1) NW-SE trending (ca. 120º); and 2) E-W trending (ca. 90º). N-S and NE-SW trending shear zones are also present but are generally subordinate in the field area. Re-Os results suggest that NW-SE and E-W trending shear zones were kinematically linked during reverse oblique movement and transpressional deformation

- One of the striking differences between the Kenge, Mbenge and Porcupine ore bodies is the absence of oblique-extension veins at Kenge and Mbenge. This is of particular interest to mineral exploration as oblique-extension veining significantly widen the mineralized zone and produce ore bodies more amenable to open-pit mining methods. The prevalence of oblique-extension veins at Porcupine is poorly understood, but could be related to the orientation of the shear zone hosting Porcupine relative to the regional stress field and/or the discontinuous nature of the host shear zone. Sibson (1988) proposed that supralithostatic fluid pressures are required for the development of oblique-extension quartz veins. In this model, favourably oriented low-cohesion shear zones are reactivated under conditions of low differential stress and prevent fluid pressure build-up. This is in contrast to mis-oriented and discontinuous shear zones where fluid pressure is expected to increase in the absence of shear zone reactivation. If correct, ENE-WSW trending shear

zones and other mis-oriented shear zones may be more attractive exploration targets.

- The location of Razorback mine at the termination of one of the left-stepping shear zone segments suggest that dilational jogs and shear zone step-overs are important in significantly widening the mineralized zone of Au-bearing shear zones (Fig. 7.4).

7.4 Future research

- Limited SEM work completed in this thesis supports previous findings that report Au as free native Au grains and as inclusions hosted by pyrite (Simpson, 2012). Native Au is also observed concentrated within pyrite fractures and could suggest Au deposition at least locally post-dated sulphidation. More work is needed to assess the mineralogy and occurrence of Au in the Lupa goldfield. This sort of study is important from a metallurgical perspective and would also further constrain ore deposit models.

- The structural data reported in this thesis represents a first step in understanding the structural setting of Au mineralization in the Lupa goldfield. Many questions remain unanswered due to complex cross cutting relationships, three-dimensional transpressional deformation paths, intense surface weathering and limited outcrop exposures (predominately within artisanal mines). The thesis focused on the economically important D2 event, however many outstanding questions are also associated with the nature and significance of the D1 and D3 deformation events. Future structural studies would benefit from access to on-going mineral exploration drilling, expansion of artisanal mines and/or increased rock exposure after commercial exploitation of the delineated ore bodies.

- Many of the outstanding questions in the Lupa goldfield are a consequence of a dearth of constraints on the regional evolution of the Ubendian and Usagaran Belts. Recent geologic studies have demonstrated the current configuration of the Ubendian Belt developed through at least three discrete orogenic cycles and was likely further modified by Tertiary rifting (Boniface et al., 2012; Boniface and Schenk, 2012; this thesis). The relationship between the tectono-magmatic evolution of the Lupa and other Ubendian litho-tectonic terranes awaits an improved understanding of this >2 Byr of tectonism. In particular, the area of SW Tanzania between the Lupa Terrane and the Dodoma Schist Belt of the Tanzanian Craton has not been previously studied. The relationship between the tectono-magmatic history of the Tanzanian Craton and the Lupa goldfield also needs to be re-examined in light of the results presented as part of this thesis.

- One of the outstanding questions regarding orogenic Au deposit formation in the Lupa goldfield is the source(s) of hydrothermal fluids. Calculated $^{187}Os/^{188}Os_{initial}$ provides evidence for a mantle Os contribution but the source of fluid(s) remains equivocal. A detailed fluid inclusion study integrated with novel and in-situ isotopic study (e.g., He)

could provide insight into the composition of the auriferous fluids and also may elucidate potential fluid source(s).

7.5 References

Begg, G.C., Griffin, W.L., Natapov, L.M., O'Reilly, S.Y., Grand, S.P., O'Neill, C.J., Hronsky, J.M.A., Poudjom Djomani, Y., Swain, C.J., Deen, T., and Bowden, P., 2009, The lithospheric architecture of Africa: seismic tomography, mantle petrology, and tectonic evolution: Geosphere, v. 5, p. 23–50.

Boniface, N., Schenk, V., and Appel, P., 2012, Paleoproterozoic eclogites of MORB-type chemistry and three Proterozoic orogenic cycles in the Ubendian Belt (Tanzania): evidence from monazite and zircon geochronology, and geochemistry: Precambrian Research, v. 192–195, p. 16–33.

Boniface, N., and Schenk, V., 2012, Neoproterozoic eclogites in the Paleoproterozoic Ubendian Belt of Tanzania: evidence for a Pan-African suture between the Bangweulu Block and the Tanzania Craton: Precambrian Research, v. 208–211, p. 72–89.

Cahen, L., Snelling, N.J., Delhal, J., and Vail, J., 1984, The geochronology and evolution of Africa, Clarendon Press, Oxford, 512 p.

Cox, S.F., Knackstedt, M.A., and Braun, J., 2001, Principles of structural control on permeability and fluid flow in hydrothermal systems, *in* Richards, J.P., and Tosdal, R.M., eds, Structural controls on ore genesis, Society of Economic Geology Reviews, v. 14, p. 1–24.

De Waele, B., Liégeois, J.P., Nemchin, A.A., and Tembo, F., 2006, Isotopic and geochemical evidence of Proterozoic episodic crustal reworking within the irumide belt of south-central Africa, the southern metacratonic boundary of an Archaean Bangweulu Craton: Precambrian Research, v. 148, p. 225–256.

Groves, D.I., Goldfarb, R.J., Gebre-Mariam, M., Hagemann, S.G., and Robert, F., 1998, Orogenic gold deposits: a proposed classification in the context of their crustal distribution and relationships to other gold deposit types: Ore Geology Reviews, v. 13, p. 7–27.

Hammer, P.T.C., Clowes, R.M., Cook, F.A., van der Velden, A.J. and Vasudevan, K., 2010, The Lithoprobe trans-continental lithospheric cross sections: imagine the internal structure of the North American continent: Canadian Journal of Earth Sciences, v. 47, p. 821–857.

Hronsky, J.M.A., Groves, D.I., Loucks, R.R., and Begg, G.C., 2012, A unified model for gold mineralisation in accretionary orogens and implications for regional-scale exploration targeting methods: Mineralium Deposita, v. 47, p. 339–358.

Kuehn, S., Ogola, J., and Sango, P., 1990, Regional setting and nature of gold mineralization in Tanzania and southeast Kenya: Precambrian Research, v. 46, p. 71–82.

Kimambo, R.H.N., 1984, Mining and mineral prospects in Tanzania, Eastern Africa Publications Ltd., Arusha, 250 p.

Lenoir, J.L., Liégeois, J.P., Theunissen, K., and Klerkx, J., 1994, The Palaeoproterozoic Ubendian

shear Belt in Tanzania; geochronology and structure: Journal of African Earth Sciences, v. 19, p. 169–184.

Richards, J.P., 2009, Postsubduction poryphyry Cu-Au and epithermal Au deposits: products of remelting of subduction-modified lithosphere: Geology, v. 37, p. 246–250.

Ring, U., 1993, Aspects of the kinematic history and mechanisms of superposition of the Proterozoic mobile Belts of eastern Central Africa (northern Malawi and southern Tanzania): Precambrian Research, v. 62, p. 207–226.

Sibson, R.H., Robert, F., and Poulsen, H., 1988, High-angle reverse faults, fluid-pressure cycling, and mesothermal gold-quartz deposits: Geology, v. 16, p. 551–555.

Simpson, R., 2012, NI 43-101 mineral resource estimate update for the Saza-Makongolosi gold project, Tanzania: Unpublished company report, SRK consulting, 217 p.

Snyder, D.B., 2002, Lithospheric growth at margins of cratons: Tectonophysics, v. 355, p. 7–22.

Theunissen, K., Klerkx, J., Melnikov, A., and Mruma, A., 1996, Mechanisms of inheritance of rift faulting in the western branch of the east African Rift, Tanzania: Tectonics, v. 15, pp. 776–790.

van Straaten, V.P., 1984, Gold Mineralization in Tanzania – a review, *in* Foster, R.P., eds., Gold '82; the geology, geochemistry and genesis of gold deposits, A.A. Balkema, Rotterdam, p. 673–685.

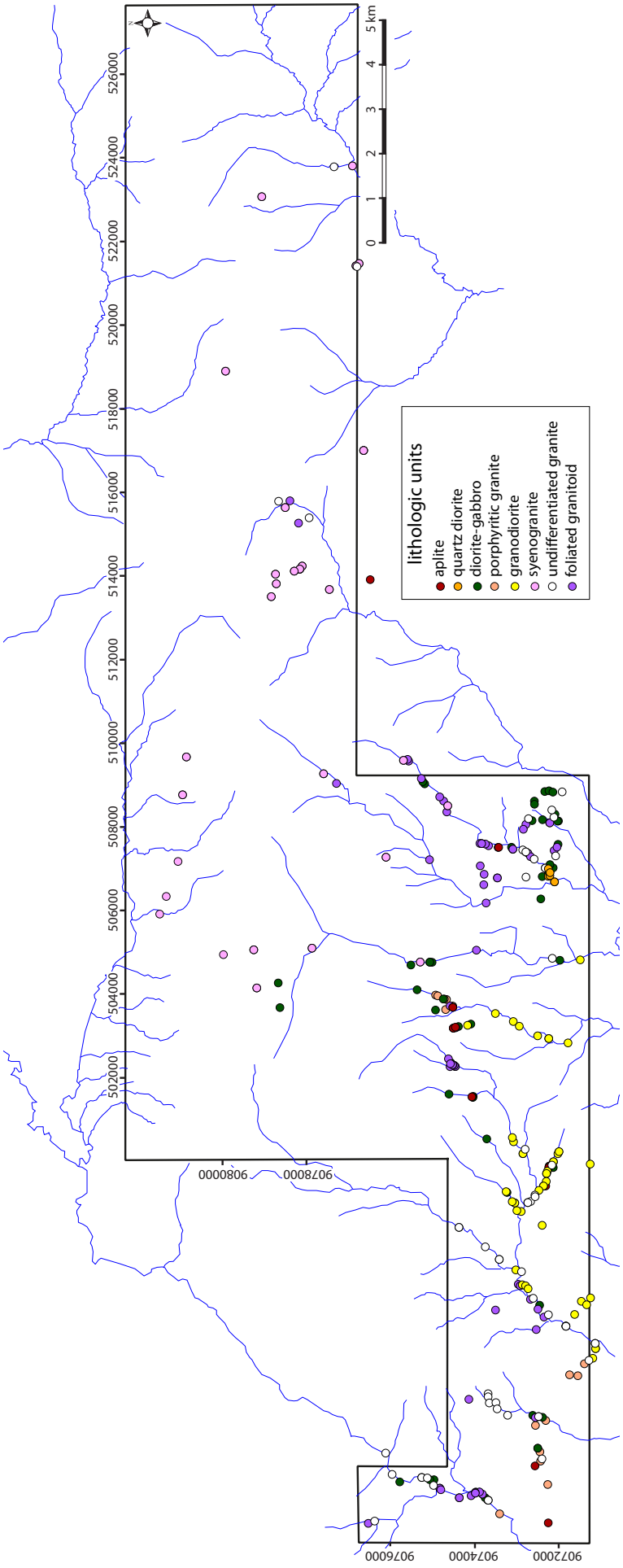
5 km
0
1
2
3
4
526000
524000
522000
520000
518000
516000
514000
512000
510000
508000
506000
504000
502000
908000
907800
907600
907400
907200
lithologic units
aplite
quartz diorite
diorite-gabbro
porphyritic granite
granodiorite
syenogranite
undifferentiated granite
foliated granitoid

Mapping localities and field descriptions

Easting	Northing	Lithology	Field Notes
491200	9073992	foliated granitoid	foliated granite-diorite contact
491368	9076548	foliated granitoid	foliated granite?; medium grained; K feldspar rich bands; weathers pink
491379	9072252	aplite	aplite; 5 m wide; @ rift
491422	9076396	undifferentiated granitoid	extremely silicified unit; purple; sheared?
491595	9073412	porphyritic granite	porphyritic granitoid cross cut by medium grained, muscovite and biotite granodiorite; at top of river
491919	9073684	undifferentiated granitoid	complex relationships between granite and diorite; mostly foliated; spectacular outcrop; epidote throughout
491929	9073701	porphyritic granite	porphyritic granite intruding diorite; granite looks strange at contact
491978	9074375	foliated granitoid	diorite cross cutting foliated granite
491982	9073760	diorite	sample for lithogeochemistry; fine to medium grained; massive; black-dark green; cross cut by aplite dikes and intruded by porphyritic granite?; locally porphyritic; with pyroxene phenocrysts; grades back into foliated granite along river
492027	9074093	foliated granitoid	foliated granite; strongly foliated; great outcrop
492065	9073825	foliated granitoid	foliated granite; no k feldspar phenocrysts; weakly foliated
492103	9073994	foliated granitoid	large foliated granite outcrop
492116	9073893	foliated granitoid	massive diorite interlayered with foliated granite
492170	9074816	foliated granitoid	back into foliated granite; river losses outcrop for several 100 m
492207	9074842	foliated granitoid	foliated granite intrudes diorite
492273	9074990	undifferentiated granitoid	coarse grained granite; weak jointing; cross cut by aplite dike
492295	9072264	porphyritic granite	U-Pb sample; hill overlooking rift; very coarse grained; k feldspar phenocrysts
492409	9074980	diorite	5 m wide dike; magnetic; diorite?; fine grained; massive; black; strongly jointed
492451	9075139	undifferentiated granitoid	strongly jointed granite
492462	9075272	granodiorite	walking south from last stop has been diorite with more felsic layers; cross cut by aplite; massive; plagioclase rich; mica rich; medium grained
492536	9075979	granodiorite	biotite granite; coarse granite; massive; u-pb sample
492738	9072568	aplite	aplite; muscovite; bleached; no contacts; fine grained
492852	9072435	porphyritic granite	very coarse grained; same porphyritic granite; giant k feldspar crystals 3 cm
492906	9072402	granodiorite	medium grained; granodiorite; muscovite; rare mafic minerals; massive
493044	9076133	granodiorite	massive; medium grained; mica rich; plagioclase rich; fresh biotite; chlorite altered; white
493075	9072451	porphyritic granite	porphyritic granite in contact with medium grained aplite; several 100 meters exposed
493160	9072502	porphyritic granite	spectacular porphyritic granite outcrop where porphyritic granite is cut by numerous <1m wide dikes; mostly massive
493705	9072557	porphyritic granite	megacrystic granite; massive
493822	9072312	porphyritic granite	megacrystic granite; massive
493892	9072558	foliated granitoid	sheared granite; strong foliation
493916	9072483	undifferentiated granitoid	granite and diorite; massive
493947	9073222	granodiorite	coarse grained granodiorite; warty weathering; plagioclase dominated; minor mafics; massive
494099	9073472	undifferentiated granitoid	granite outcrop; with quartz throughout; massive; medium to coarse grained; minor k feldspar; light grey; white; minor alteration
494241	9073659	undifferentiated granitoid	extremely altered granite; pyrite; back to granodiorite
494248	9073501	undifferentiated granitoid	extremely altered float; with sheared granite; slickensides on quartz vein; what is this?!?
494328	9074147	foliated granitoid	foliation; mylonitized granite; rubble; very similar to black tree
494388	9073688	undifferentiated granitoid	medium-coarse grained; bleached; plagioclase dominated; no mafics; locally chloritized; minor k feldspar
494461	9073688	undifferentiated granitoid	massive; medium-coarse grained; bleached granite; brown mica; looks like granodiorite in Luika river; plagioclase dominated
494890	9071545	porphyritic granite	sample of mega crystic granite for lithogeochemistry
494912	9071742	porphyritic granite	good outcrop down here; mostly porphyritic granite but some fine-medium grained light grey granite
495175	9071389	porphyritic granite	K feldspar porphyritic granite; massive; coarse very coarse grained; is this related to Saza granodiorite?
495257	9071280	undifferentiated granitoid	altered granite; fracture cleavage; bleached; K feldspar alteration; hard to tell protolith; mostly subcrop
495307	9071188	Saza Granodiorite	saza granite outcrop
495537	9071122	Saza Granodiorite	saza granite; coarse grained; massive; plagioclase dominated with abundant K feldspar; and mafic enclaves; saza is cross cut by aplite and may be coeval with diorite in river
495537	9071122	Saza Granodiorite	saza granite; subcrop and outcrop
495661	9071131	granodiorite	mixed granodiorite-diorite unit; mixing textures
495992	9072539	foliated granitoid	foliated granite; fracture cleavage; medium grained; K feldspar, quartz, plagioclase, chloritized, what granite is this?
496070	9071829	undifferentiated granitoid	in river spectacular outcrops; granite is medium grained; white; plagioclase dominated; minor mafics; minor K feldspar; cross cut by fine grained black dikes; also cross cut by aplite
496071	9071830	diorite	dikes cross cutting medium grained white granite; fine grained black
496074	9071830	granodiorite	spectacular outcrop with two big mafic dikes; massive; plagioclase rich
496075	9071830	diorite	spectacular giant outcrop with two big mafic dikes cross cutting plagioclase rich massive granite
496290	9072353	foliated granitoid	very strange outcrop; with folds; or just strongly sheared?; pretty sure it is similar to foliated granite elsewhere; coarse grained K feldspar
496345	9072248	granodiorite	medium grained; light grey-white; massive; muscovite; minor mafics; may be same unit down stream; not sure

496352	9071622	Saza Granodiorite	saza granodiorite; large boulders; massive; coarse grained; mafic xenoliths; plagioclase dominated
496457	9073511	foliated granitoid	strongly cleavage; abundant sheared float; intense quartz veining
496478	9072498	foliated granitoid	foliated granite; before was mostly granite (massive; coarse grained); here the granite is strongly hematized
496573	9072458	diorite	dike; WNW trending; mafic; massive; fine grained
496583	9071335	Saza Granodiorite	very large saza granodiorite outcrop; massive; coarse grained; plagioclase dominated; minor K feldspar; equigranular; no pervasive joints
496666	9071462	Saza Granodiorite	coarse grained; massive; K feldspar; porphyritic; looks like saza?; epidote and chlorite alteration; pretty sure of saza
496713	9072677	foliated granitoid	back into foliated granodiorite like rock; foliated; chlorite veins parallel to foliation
496738	9072611	undifferentiated granitoid	outcrop with intense E-W quartz veins; lots of veins; look barren; altered; silicified; plagioclase rich
496747	9071242	Saza Granodiorite	saza granite; coarse grained; mafic enclaves; massive; K feldspar poor; minor E-W trending veins with epidote alteration
496966	9072733	Saza Granodiorite	massive; medium grained; white; plagioclase rich; harder than saza; could be saza
497036	9072793	Saza Granodiorite	saza granite
497037	9072922	foliated granitoid	hematite-chlorite altered; foliated; large K feldspar crystals
497060	9072872	Saza Granodiorite	saza granite cross cut by quartz vein
497072	9072968	foliated granitoid	strongly sheared; gneiss-like; chloritized; quartz lenses parallel with foliation; epidote veins crosscut
497373	9072890	granodiorite	indurated granite; not saza granite; massive; medium-coarse grained; plagioclase rich; more altered
497415	9073026	Saza Granodiorite	saza granite; coarse grained; warty weathering; plagioclase rich; strongly jointed
497665	9073421	diorite	fine grained; black; dike; cross cuts granite; diorite?; joints appear more random and less pervasive; strongly magnetic; cross cuts massive diorite
497666	9073422	undifferentiated granitoid	black dike cross cuts undifferentiated granite
497965	9073755	granodiorite	granite; plagioclase rich; massive; medium-coarse grained
498430	9074383	granodiorite	granodiorite; medium-coarse grained; white; plagioclase dominated
498479	9072397	Saza Granodiorite	saza granite; outcrop; coarse grained; massive; quartz, plagioclase, K feldspar, chlorite clots; epidote veins
498809	9072898	Saza Granodiorite	coarse grained; massive; equigranular; plagioclase, K feldspar, chlorite, quartz; saza
498831	9073001	Saza Granodiorite	saza granite with chlorite stringers throughout
499012	9073051	Saza Granodiorite	saza granite cross cut by mafic dike
499013	9073052	diorite	dike cross cuts saza near magnetic anomaly
499021	9072739	undifferentiated granitoid	granite cross cut by mafic dike
499022	9072740	diorite	diorite cross cuts granite
499044	9073112	Saza Granodiorite	back into saza granite; coarse grained; massive
499048	9072673	granodiorite	coarse grained; massive; plagioclase rich; equigranular
499162	9072565	undifferentiated granitoid	altered dike; bleached granite
499200	9072570	undifferentiated granitoid	granite; medium grained; massive; strongly jointed; hard; much more K feldspar, chlorite, muscovite
499263	9073236	diorite	2m wide dike; massive; fine grained; magnetic anomaly?
499282	9073258	Saza Granodiorite	saza shear; 30 m long; but only 5 m where intense; shearing saza
499314	9072474	Saza Granodiorite	saza granite; coarse grained; massive
499418	9072364	Saza Granodiorite	saza granite cross cut by microgranite
499418	9072312	aplite	aplite dike
499419	9072365	aplite	microgranite cross cutting saza
499527	9072299	Saza Granodiorite	coarse grained; massive; plagioclase dominated; minor K feldspar, quartz; equigranular
499714	9072292	aplite	aplite dike; cross cutting saza; sharp contacts
499715	9072293	Saza Granodiorite	aplite dike cross cutting saza granite
499771	9072272	Saza Granodiorite	coarse grained; massive; equigranular; mostly plagioclase; minor quartz and K feldspar; epidote veins; minor aplite
499857	9072132	diorite	bleached granite cross cutting diorite
499857	9072241	aplite	massive; pink-purple; siliceous; felsite; fine grained
499892	9072232	diorite	mafic dike cross cut by aplite; complex relationships; dark; mafic; massive; fine grained
499898	9072210	aplite	aplite dike; fine grained; massive; equigranular; felsic; pinkish; K feldspar, quartz, chlorite
499915	9072165	undifferentiated granitoid	coarse grained; massive; equigranular; plagioclase, K feldspar, quartz; strongly jointed
499940	9071250	Saza Granodiorite	coarse grained; massive; equigranular; plagioclase, K feldspar; warty weathering; weakly jointed
499995	9072127	aplite	fine-medium grained; aplite dike; cross cutting granite
499996	9072128	Saza Granodiorite	saza cross cut by aplite
500187	9072021	Saza Granodiorite	coarse grained; massive; equigranular; plagioclase, K feldspar, quartz, chlorite; saza
500189	9072856	Saza Granodiorite	dark mafic dike cross cutting saza
500189	9072856	diorite	dark; mafic; massive; cross cutting saza; 10 m wide
500232	9071998	Saza Granodiorite	coarse grained; massive; equigranular; plagioclase, K feldspar, quartz, chlorite
500237	9071994	Saza Granodiorite	saza; massive; chlorite alteration; cross cut by alaskite; distinct weathering
500293	9072804	undifferentiated granitoid	coarse grained; massive; plagioclase rich; very coarse grained K feldspar; pervasive epidote alteration; jointing throughout
500472	9073080	Saza Granodiorite	saza granite; coarse grained; massive; plagioclase rich; minor K feldspar; abundant xenoliths
500573	9073109	Saza Granodiorite	saza granite; chloritized with lots of mafic xenoliths; cross cut by aplite dikes
501545	9074076	aplite	2 m wide aplite/felsite
501555	9074044	diorite	mafic outcrop; mostly fine grained.
501609	9074622	diorite	dike sample; lithogeochemistry sample

502265	9074596	foliated granitoid	great foliated granite outcrop in stream; strongly developed foliation
502269	9074471	foliated granitoid	diorite-foliated granite contact
502293	9074496	foliated granitoid	strongly foliated granite
502293	9074496	diorite	diorite contact
502306	9074530	foliated granitoid	strongly foliated granite
502309	9074537	foliated granitoid	strongly foliated granite
502335	9074588	foliated granitoid	foliated granite?; mostly massive; slightly porphyritic; lots of chlorite; K feldspar rich
502452	9074635	foliated granitoid	foliated granite; porphyritic; K feldspar phenocrysts; slightly foliated
502831	9071780	Saza Granodiorite	saza; i have decided to stop walking along this river here and head west; it has been all saza except for diorite as shown on radiometrics
502935	9072240	Saza Granodiorite	mafic sill cross cuts saza
502935	9072240	diorite	sill cross cuts saza; fine grained
503000	9072505	Saza Granodiorite	saza; coarse grained; massive; with aplite dikes
503184	9074518	foliated granitoid	foliation; strong banded appearance
503184	9074518	foliated granitoid	foliation; banded rock; does not look like foliated granite; bleached
503184	9074518	aplite	aplite/felsite; 5 cm wide
503193	9074459	foliated granitoid	sheared rock; looks like bleached granite; not foliated granite at Kenge; not coarse grained or texture
503207	9074468	aplite	aplite; fine grained; massive; equigranular
503222	9074396	diorite	gabbro; coarse grained; massive; green; equigranular
503229	9072943	Saza Granodiorite	grey saza? sheared with E-W trending foliation; good cleavage
503251	9074178	Saza Granodiorite	saza; chlorite alteration; coarse grained; warty weathering
503281	9074099	diorite	diorite; fine grained; black; very hard
503342	9073087	Saza Granodiorite	saza?; coarse grained; more pink than usual; but i suspect weathering; cross cut by aplite
503533	9073514	Saza Granodiorite	saza granite; as i have walked south along the river i have found rock that looks like saza granite; here i am sure it is saza; fresh; 10-15% biotite; plagioclase rich; hornblende bearing; coarse grained
503616	9074943	diorite	mafic rocks; slight foliation; sheared metabasalt?
503627	9074702	porphyritic granite	porphyritic granite float
503679	9074530	foliated granitoid	aplite cross cuts foliated granite
503680	9074531	aplite	aplite cross cut foliated granite
503711	9074532	porphyritic granite	porphyritic granite float
503713	9074595	foliated granitoid	weakly foliated granite
503868	9074681	porphyritic granite	porphyritic granite float
503878	9074733	porphyritic granite	porphyritic granite float
503954	9074890	porphyritic granite	porphyritic granite float
503973	9074940	porphyritic granite	porphyritic granite float
504099	9075383	diorite	coarse grained diorite
504142	9079210	syenogranite	fine grained Ilunga?; sample of acid volcanics? Or felsite?
504758	9075081	diorite	good outcrop where Ilunga granite? comes into contact with diorite; took lithogeochemistry samples; can see injections
504761	9075308	syenogranite	Ilunga; medium grained; massive; pink; equigranular; homogeneous
504813	9071488	Saza Granodiorite	Saza; coarse grained; white; mafic xenoliths; amphibole; chlorite; massive
504850	9072155	granodiorite	more leucogranite; doesn't look like Saza; late granodiorite; coarse grained; massive; light grey; minor mafics; no xenoliths
504942	9080004	foliated granitoid	sheared granite
505044	9073967	foliated granitoid	foliated granite sample for U-Pb
505053	9079282	syenogranite	fine grained Ilunga?
505092	9077892	syenogranite	Ilunga? pink granite; minor hematization; massive
505894	9081525	foliated granitoid	sheared granite; incredible ouctrop with folded foliation; veins
506169	9073736	foliated granitoid	foliated granite; coarse grained; trends EW; cross cut by aplite
506267	9072429	diorite	lithogeochemistry sample; gabbro from hill
506325	9081374	foliated granitoid	oriented sample of sheared granite
506606	9073791	foliated granitoid	granite; strongly foliated; almost gneiss; cross cut by mafic dike which is cross cut by aplite and veins/foliation trends E-W
506673	9072102	foliated granitoid	changes from mafic rich granite to foliated granite; slightly foliated
506674	9072103	quartz diorite	changes from mafic rich granite into foliated granite; slightly foliated
506768	9073466	foliated granitoid	outcrop of weakly foliated granite; equigranular; K feldspar, quartz, plagioclase; cross cut by microgranite and mafic dike
506769	9073467	diorite	mafic dike cross cutting weakly foliated granite
506788	9072784	undifferentiated granitoid	coarse grained; pink-green; silicified; epidote alteration; massive; coarse grained feldspar; tumbili
506806	9072251	quartz diorite	coarse grained; 20% mafics; chloritized; looks like diorite but locally weathers pink; suggestive of K feldspar?
506822	9072213	quartz diorite	coarse grained; 20% mafics; chloritized; looks like diorite
506855	9073783	foliated granitoid	foliated granite with more felsic lenses
506894	9072209	quartz diorite	U-Pb sample; quartz diorite; 20% mafics; chloritized; may be lineated; think this is the high thorium and low potassium unit near tumbili; cross cut by aplite
506951	9072200	diorite	fine grained; massive; black; weather orange; subcrop
506986	9072250	quartz diorite	diorite? chlorite rich; 20% mafic; massive to slightly foliated
507002	9072324	granodiorite	foliated; granodiorite; not sure what unit this is; but has amphibole; medium-coarse grained; strong foliation
507003	9072322	granodiorite	magnetic granite with chlorite clots; black/white; foliated; chlorite throughout; epidote veins
507056	9073875	foliated granitoid	sheared; strong foliation; gneiss?

507153	9081105	foliated granitoid	sheared granite
507202	9075086	foliated granitoid	foliated granite outcrop; boulders; good foliation; porphyritic; K feldspar phenocrysts
507217	9072589	undifferentiated granitoid	coarse grained; massive; plagioclase, pink K feldspar; chlorite; epidote; finer grained version of foliated granite? or new granite? looks new to me; massive; oscillatory zoning in plagioclase
507262	9076125	syenogranite	Ilunga no outcrop between here and last
507275	9072675	foliated granitoid	new granite? extremely hematized with large chlorite clots; looks similar to Mbenge
507293	9072076	undifferentiated granitoid	spectacular outcrop; very large; well exposed; strong cleavage locally; slightly more coarse grained than previous; still mafic rich; more abundant K feldspar; but still plagioclase dominated
507356	9072735	foliated granitoid	foliated; epidotized; chlorite granite; new unit?
507388	9072786	diorite	dike cross cutting medium grained pink granite contact
507389	9072787	undifferentiated granitoid	medium grained; pink; granite; in contact with dike
507422	9072112	foliated granitoid	subcrop of strongly foliated granite; K feldspar rich; not sure what this is
507436	9072860	undifferentiated granitoid	folded; medium grained; pink; granite; gentle folds; with moderately dipping hinge
507450	9073098	foliated granitoid	U-Pb foliated granite sample
507455	9073096	foliated granitoid	more fine grained than typical foliated granite; w/ K feldspar megacrysts; almost massive
507496	9073449	foliated granitoid	foliated granite?
507497	9073436	aplite	aplite; siliceous; fine grained; indurated
507500	9073129	diorite	fine-medium grained; mafic; dark green-black; minor plagioclase; minor veins; no jointing
507502	9072043	foliated granitoid	strongly foliated granite?; K feldspar phenocrysts/ sheared quartz and K feldspar
507536	9073677	foliated granitoid	foliated granite?
507569	9072018	diorite	hill; fine grained; massive; black
507577	9073753	foliated granitoid	strongly altered foliated granite? With quartz veins
507587	9073841	foliated granitoid	foliated granite looks like it is cross cutting mafic dike with granodiorite fingers
507588	9073842	diorite	non foliated mafic dike cross cutting foliated granite
507591	9073883	foliated granitoid	foliated granite with gneiss like foliation
507929	9072846	foliated granitoid	subcrop of foliated granite
508045	9072785	foliated granitoid	coarse grained; foliated granite; K feldspar, plagioclase, quartz, chloritized mafics
508081	9072214	foliated granitoid	strong foliation; coarse grained feldspar; mostly giant boulders
508181	9072724	undifferentiated granitoid	coarse grained; massive; chloritized; abundant k feldspar; some coarse grained K feldspar
508216	9072117	undifferentiated granitoid	subcrop?; coarse grained; K feldspar rich; minor mafics; mafic clots; epidote and chlorite alteration; much more free quartz than granodiorite
508342	9074674	foliated granitoid	foliated granite outcrop; K feldspar; coarse grained; weak foliation; all along river much harder and more indurated than Saza; different weathering
508389	9072167	undifferentiated granitoid	subcrop of coarse grained massive granite with K feldspar
508489	9074651	foliated granitoid	foliated granite
508602	9074749	foliated granitoid	foliated granite outcrop; cross cut by mafic dike; plagioclase; porphyritic; K feldspar rich; poorly defined foliation; chlorite clots
508701	9074843	foliated granitoid	sheared granite
508751	9080981	syenogranite	foliated Ilunga?
508821	9071920	undifferentiated granitoid	granite; coarse grained; massive; pink; K feldspar rich
509022	9077308	foliated granitoid	granite in river; strongly foliated; strongly sheared; pink/black; coarse grained; bleached at surface; quartz still visible; looks different than Saza
509139	9075282	foliated granitoid	shearing; gneiss like fabric
509253	9077615	syenogranite	Ilunga; large massive outcrop; equigranular
509555	9075584	foliated granitoid	foliated granite
509573	9075708	syenogranite	hematized; Ilunga granite; very pink; K feldspar rich; may be hematized foliated granite
509596	9075609	foliated granitoid	foliated granite
509654	9080890	syenogranite	foliated Ilunga?
513479	9078864	syenogranite	Ilunga; poor cleavage
513650	9077477	syenogranite	massive; outcrop of Ilunga; with strong jointing
513786	9078744	syenogranite	Ilunga; slightly sheared
513885	9076502	aplite	aplite; felsite; fine grained; K feldspar rich; sugary
514015	9078763	syenogranite	Ilunga; subcrop
514088	9078315	syenogranite	Ilunga; subtle foliation
514134	9078183	syenogranite	Ilunga; massive; in river
514138	9078183	syenogranite	Ilunga
514209	9078126	syenogranite	Ilunga; massive; with cleavage
515234	9078213	foliated granitoid	lots of altered granite; all subcrop
515360	9077960	undifferentiated granitoid	extremely altered granite
515605	9078531	syenogranite	Ilunga
515755	9078689	undifferentiated granitoid	altered granite; maybe foliated
515766	9078419	foliated granitoid	small hill of sheared rock
516966	9076658	aplite	aplite; cross cutting Ilunga
516967	9076659	syenogranite	aplite cross cutting Ilunga
518859	9079955	syenogranite	foliated Ilunga
521354	9076818	undifferentiated granitoid	sheared; silicified; hematized; granite
521372	9076843	syenogranite	sheared Ilunga
521427	9076768	syenogranite	hematized Ilunga
523022	9079091	syenogranite	went looking for rapikivi granite; here is regular Ilunga
523735	9077366	undifferentiated granitoid	pink granite; medium-coarse grained
523757	9076925	syenogranite	Ilunga? coarse grained; plagioclase and K feldspar; weather pink

N.B. eastings and northings are reported as UTM coordinates (WGS84, Zone 36S)

Lithogeochemistry results

Analyte	Analysis Method[1]	Unit	D.L.[2]	CL099	CL0913	CL0915	CL0921	CL0923	CL0925	CL0928
SiO_2	FUS-ICP	%	0.01	65.68	50.88	71.72	75.41	58.85	67.99	53.98
Al_2O_3	FUS-ICP	%	0.01	14.57	16.36	15.53	13.32	16.2	14.06	16.71
Fe_2O_3(T)	FUS-ICP	%	0.01	4.67	9.31	1.22	1.11	7.07	2.56	8.7
MnO	FUS-ICP	%	0.001	0.095	0.13	0.023	0.028	0.097	0.028	0.123
MgO	FUS-ICP	%	0.01	0.9	5.11	0.31	0.22	2.81	0.7	5.16
CaO	FUS-ICP	%	0.01	2.51	7.27	1.95	1.02	5.9	1.91	7.18
Na_2O	FUS-ICP	%	0.01	4.23	3.78	4.93	4.03	4.04	5.39	4.07
K_2O	FUS-ICP	%	0.01	3.74	1.06	2.65	3.19	0.95	3.4	0.63
TiO_2	FUS-ICP	%	0.001	0.717	1.234	0.123	0.107	1.003	0.339	1.014
P_2O_5	FUS-ICP	%	0.01	0.29	0.26	0.02	0.02	0.3	0.11	0.19
LOI	FUS-ICP	%		1.41	3.23	1.38	1.55	2.49	1.92	2.58
Total	FUS-ICP	%	0.01	98.79	98.63	99.87	100	99.72	98.4	100.3
Au	INAA	ppb	1	2	2	< 1	< 1	< 1	< 1	< 1
Ag	TD-ICP	ppm	0.5	< 0.5	< 0.5	< 0.5	< 0.5	< 0.5	< 0.5	< 0.5
As	INAA	ppm	1	< 1	2	2	< 1	2	2	2
Ba	FUS-ICP	ppm	1	1117	433	2128	1550	596	1804	278
Be	FUS-ICP	ppm	1	2	< 1	< 1	< 1	1	< 1	< 1
Br	INAA	ppm	0.5	< 0.5	< 0.5	2.9	< 0.5	1.9	2.9	1
Cd	TD-ICP	ppm	0.5	< 0.5	< 0.5	< 0.5	< 0.5	< 0.5	< 0.5	< 0.5
Co	INAA	ppm	0.1	25.1	46.2	23.9	31.6	24.6	18.1	41
Cr	INAA	ppm	0.5	< 0.5	116	1.6	< 0.5	20.6	13	97.6
Cu	TD-ICP	ppm	1	15	39	17	4	15	14	33
Hg	INAA	ppm	1	< 1	< 1	< 1	< 1	< 1	< 1	< 1
Ir	INAA	ppb	1	< 1	< 1	< 1	< 1	< 1	< 1	< 1
Ni	TD-ICP	ppm	1	6	70	4	6	22	17	59
Pb	TD-ICP	ppm	5	10	< 5	12	8	6	6	< 5
Sb	INAA	ppm	0.1	0.3	1.1	0.2	0.3	0.4	0.3	0.5
S	TD-ICP	%	0.001	0.075	0.189	0.079	0.006	0.065	0.021	0.1
Sc	INAA	ppm	0.01	6.26	18.1	1.16	1.21	11.9	4.73	22.8
Se	INAA	ppm	0.5	< 0.5	< 0.5	< 0.5	< 0.5	< 0.5	< 0.5	< 0.5
Sr	FUS-ICP	ppm	2	316	545	481	197	650	176	500
V	FUS-ICP	ppm	5	39	190	8	< 5	120	27	158
W	INAA	ppm	1	224	71	185	254	60	107	63
Y	FUS-ICP	ppm	1	24	11	4	5	11	6	17
Zn	TD-ICP	ppm	1	60	66	21	11	52	22	55
Mass	INAA	g		1.577	1.603	1.448	1.443	1.605	1.531	1.656
Bi	FUS-MS	ppm	0.1	< 0.1	< 0.1	< 0.1	< 0.1	< 0.1	< 0.1	< 0.1
Cs	FUS-MS	ppm	0.1	0.2	0.3	0.3	0.7	0.4	0.2	0.2
Ga	FUS-MS	ppm	1	20	17	15	13	18	14	17
Ge	FUS-MS	ppm	0.5	1.3	1.3	1	1.1	1.3	0.6	1.3
Hf	FUS-MS	ppm	0.1	7.3	2	1.7	2.1	2.7	3.7	2.3
In	FUS-MS	ppm	0.1	< 0.1	< 0.1	< 0.1	< 0.1	< 0.1	< 0.1	< 0.1
Mo	FUS-MS	ppm	2	< 2	< 2	< 2	< 2	< 2	< 2	< 2
Nb	FUS-MS	ppm	0.2	17.6	1.9	2.2	4.1	3.7	7.3	1.5
Rb	FUS-MS	ppm	1	54	23	47	55	22	41	17
Sn	FUS-MS	ppm	1	2	< 1	< 1	< 1	< 1	1	< 1
Ta	FUS-MS	ppm	0.01	1.51	0.33	0.77	1.08	0.52	0.78	0.3
Th	FUS-MS	ppm	0.05	3.75	1.45	3.2	4.83	4.53	16.3	0.75
U	FUS-MS	ppm	0.01	1.05	0.52	0.62	0.78	2.22	1.23	0.29
Zr	FUS-MS	ppm	1	330	98	80	82	134	169	96
La	FUS-MS	ppm	0.05	61.6	12	32.2	28.5	22.3	52.2	9.84
Ce	FUS-MS	ppm	0.05	135	24.8	50.6	47.9	43.8	91.1	21
Pr	FUS-MS	ppm	0.01	16.6	3.17	4.8	4.68	5.14	9.47	2.81
Nd	FUS-MS	ppm	0.05	60.1	13.1	13.7	13.7	18.8	29.2	11.9
Sm	FUS-MS	ppm	0.01	10.5	2.8	1.78	1.83	3.58	4.15	3.04
Eu	FUS-MS	ppm	0.005	1.88	1.28	0.625	0.479	1.39	0.968	1.12
Gd	FUS-MS	ppm	0.01	7.36	2.67	1.07	1.26	2.9	2.53	3.13
Tb	FUS-MS	ppm	0.01	1.01	0.42	0.14	0.17	0.43	0.3	0.54
Dy	FUS-MS	ppm	0.01	5.28	2.33	0.72	0.92	2.28	1.45	3.28
Ho	FUS-MS	ppm	0.01	0.97	0.44	0.14	0.19	0.43	0.26	0.65
Er	FUS-MS	ppm	0.01	2.54	1.23	0.45	0.58	1.21	0.73	1.84
Tl	FUS-MS	ppm	0.05	0.06	< 0.05	< 0.05	0.08	< 0.05	< 0.05	< 0.05
Tm	FUS-MS	ppm	0.005	0.344	0.175	0.07	0.091	0.178	0.098	0.276
Yb	FUS-MS	ppm	0.01	2.11	1.12	0.5	0.66	1.17	0.58	1.8
Lu	FUS-MS	ppm	0.002	0.316	0.176	0.092	0.121	0.184	0.085	0.29

[1]Analysis method abbreviations: FUS-ICP = Fusion Inductively Coupled Plasma Mass Spectrometry; INAA = Instrumental Neutron Activation Analysis; TD-ICP = Total Dissolution Inductively Coupled Plasma Mass Spectrometry; D.L. = detection limit

Lithogeochemistry Samples											
CL0931	CL0932	CL0934	CL0947	CL0956	CL0957	CL0958	CL0959	CL0977	CL0981	CL0984	CL0996
73.64	75.94	74.91	66.83	47.58	55.5	72.94	77.46	68.23	52.09	50.22	42.13
12.08	12.59	12.26	14.4	14.71	17.02	14.22	11.02	14.67	13.41	14.99	9.51
3.12	1.76	2.85	4.1	14.57	7.78	1.92	1.79	3.27	7.8	9.46	13.39
0.046	0.022	0.04	0.033	0.312	0.112	0.032	0.012	0.048	0.146	0.159	0.338
0.54	0.11	0.18	0.72	4.95	3.9	0.4	0.07	1.32	10.53	9.72	17.42
0.76	0.38	0.95	2.26	4.05	6.8	1.99	0.19	2.5	7.62	8.96	8.9
3.42	3.62	3.54	4.7	3.1	3.87	4.5	3.28	4.11	2.09	2.44	0.89
4.42	4.8	4.54	4.22	2.62	1.19	2.3	4.83	2.9	2.59	1.52	0.2
0.332	0.154	0.277	0.614	2.503	0.957	0.168	0.105	0.406	0.621	0.7	1.47
0.02	0.02	0.02	0.23	0.43	0.2	0.04	< 0.01	0.11	0.18	0.13	0.16
1.25	0.62	1.21	2.03	3.55	2.37	0.93	0.48	2.4	2.94	2.61	6.3
99.63	100	100.8	100.1	98.36	99.71	99.44	99.23	99.95	100	100.9	100.7
< 1	< 1	< 1	< 1	5	2	2	< 1	< 1	< 1	< 1	< 1
< 0.5	< 0.5	< 0.5	< 0.5	< 0.5	< 0.5	< 0.5	< 0.5	< 0.5	< 0.5	< 0.5	< 0.5
< 1	< 1	< 1	2	5	2	< 1	< 1	2	2	< 1	6
896	811	714	1184	1266	492	1458	142	1258	836	442	55
2	2	3	1	2	1	1	4	1	1	< 1	< 1
< 0.5	< 0.5	1.8	4.3	< 0.5	< 0.5	< 0.5	< 0.5	< 0.5	1.2	< 0.5	1.8
< 0.5	< 0.5	< 0.5	< 0.5	< 0.5	< 0.5	< 0.5	< 0.5	< 0.5	< 0.5	< 0.5	0.6
27.9	22.8	25.4	19.5	50.8	33.5	21	25.7	22.5	44.9	48.2	85.5
< 0.5	< 0.5	< 0.5	< 0.5	113	50.7	< 0.5	< 0.5	17.5	679	655	1840
8	1	5	2	101	46	18	15	12	12	21	135
< 1	< 1	< 1	< 1	< 1	< 1	< 1	< 1	< 1	< 1	< 1	< 1
< 1	< 1	< 1	< 1	< 1	< 1	< 1	< 1	< 1	< 1	< 1	< 1
5	4	4	5	77	35	5	5	15	360	186	817
10	12	18	< 5	< 5	< 5	12	10	7	11	< 5	7
< 0.1	0.2	0.2	0.3	1	0.4	< 0.1	< 0.1	0.9	0.9	< 0.1	0.8
0.008	0.001	0.015	0.036	0.039	0.053	0.003	0.002	0.002	0.003	0.01	0.111
3.89	2.74	3.94	5.67	34.9	16.4	1.73	0.39	5.63	22.1	30	23.2
< 0.5	< 0.5	< 0.5	< 0.5	< 0.5	< 0.5	< 0.5	< 0.5	< 0.5	< 0.5	< 0.5	< 0.5
51	41	60	181	251	548	464	33	385	298	271	105
8	< 5	5	37	332	155	14	< 5	47	126	185	220
216	196	198	117	7	71	175	213	126	23	20	5
68	42	88	17	33	16	8	94	8	9	19	13
51	29	73	25	154	72	31	42	40	91	99	223
1.447	1.269	1.322	1.298	1.443	1.479	1.424	1.39	1.436	1.431	1.527	1.689
< 0.1	< 0.1	< 0.1	< 0.1	< 0.1	< 0.1	< 0.1	< 0.1	< 0.1	< 0.1	< 0.1	< 0.1
0.3	0.2	0.3	0.2	1	0.3	0.5	0.2	0.8	0.4	0.4	2
21	17	22	17	20	18	15	23	15	14	14	13
1.5	1.4	1.7	1	1.6	1.3	1.3	1.7	1.1	1.4	1.4	1.5
10	6.7	12.6	6.6	4.6	2.6	2.3	13.7	3.7	1.7	1.6	2.7
< 0.1	< 0.1	< 0.1	< 0.1	< 0.1	< 0.1	< 0.1	< 0.1	< 0.1	< 0.1	< 0.1	< 0.1
2	2	2	< 2	< 2	< 2	< 2	< 2	< 2	< 2	< 2	< 2
15.3	9.7	20.5	13.9	12.8	3.4	5.9	25.5	4	2.5	1.6	11.7
88	124	112	68	74	37	53	131	71	85	62	6
4	3	4	2	2	2	< 1	8	< 1	1	2	2
1.73	1.09	1.85	0.99	0.87	0.63	0.98	1.65	0.68	0.22	0.31	0.76
15.5	13.3	12.4	6.73	2.55	4.97	2.75	17.7	5.09	1.39	1.18	1.15
3.17	2.31	3.92	1.2	0.46	1.32	0.62	3.86	1.25	0.45	0.5	0.28
396	237	474	300	199	114	98	337	163	80	62	115
88.6	73.7	60	61.1	28.8	19	21.9	57.2	25.2	15.2	8.91	14.2
171	134	124	124	60.4	35.7	36.9	131	47	32.3	19.1	31.2
19.6	15.3	15.4	14.2	7.79	4.26	3.74	13.7	5.24	4.27	2.51	4.12
68	50.6	56.6	48.5	31.4	16.2	11.4	47	17.2	17	10.6	17
13.2	9	13.4	8	6.94	3.45	1.87	11.7	2.86	3.34	2.6	3.9
1.46	0.847	1.08	1.61	2.12	1.28	0.492	0.313	0.732	1.03	0.833	1.27
11.5	7.3	12.9	5.24	6.71	3.1	1.42	11.7	2.04	2.61	2.83	3.38
2.01	1.23	2.47	0.73	1.14	0.49	0.23	2.46	0.28	0.35	0.52	0.5
12.2	7.64	15.8	3.68	6.57	2.91	1.36	16.9	1.52	1.9	3.28	2.93
2.46	1.52	3.18	0.66	1.27	0.57	0.27	3.67	0.29	0.36	0.68	0.52
7.2	4.5	9.39	1.81	3.59	1.7	0.81	11	0.86	0.95	2.07	1.38
0.16	0.34	0.24	0.09	0.15	< 0.05	0.09	0.32	0.12	0.11	< 0.05	< 0.05
1.08	0.705	1.43	0.243	0.519	0.254	0.135	1.72	0.125	0.132	0.312	0.188
7.14	4.78	9.3	1.52	3.35	1.75	1.1	11.4	0.83	0.83	2.11	1.18
1.14	0.747	1.43	0.241	0.525	0.288	0.192	1.72	0.139	0.141	0.356	0.181

CL1021	CL1022	CL1029	CL1030
59.96	49.6	67.55	67.63
14.51	17.29	15.09	14.89
6.86	11.36	3.5	3.51
0.103	0.139	0.048	0.057
4.88	5.93	1.46	1.31
6.11	7.85	2.4	3.19
3.71	3.18	3.78	4
2.5	1.03	3.84	2.53
0.673	1.433	0.444	0.405
0.25	0.22	0.16	0.12
1.36	2.62	1.59	1.21
100.9	100.7	99.86	98.84
< 1	< 1	< 1	< 1
< 0.5	< 0.5	< 0.5	< 0.5
2	4	2	3
1187	558	1272	1008
1	< 1	2	1
< 0.5	< 0.5	1.8	< 0.5
< 0.5	< 0.5	< 0.5	< 0.5
21.1	40.1	9	7.5
226	119	115	13.8
55	51	157	49
< 1	< 1	< 1	< 1
< 1	< 1	< 1	< 1
65	113	23	13
11	6	11	9
0.3	0.5	0.4	0.6
0.006	0.046	0.005	0.024
15.4	17.9	5.45	4.8
< 0.5	< 0.5	< 0.5	< 0.5
638	561	446	472
143	268	60	54
< 1	< 1	< 1	< 1
19	10	13	9
65	77	49	45
1.48	1.634	1.409	1.714
0.4	< 0.1	0.3	0.2
0.7	0.4	0.7	0.6
17	17	18	17
1.2	1.2	1.1	1.2
4.2	1.2	4.3	3.2
< 0.1	< 0.1	< 0.1	< 0.1
< 2	< 2	< 2	4
6.1	1.6	8.2	4.6
51	25	65	57
1	< 1	2	< 1
0.4	0.09	0.73	0.36
8.69	0.99	7.97	9.05
1.73	0.25	1.86	2.22
176	55	181	132
43.8	8.85	44.8	33
94.4	19.4	93	59.2
10.7	2.47	10	5.98
41.7	10.7	34.9	20.1
7.8	2.38	5.53	3.24
1.89	1.07	1.09	0.842
5.49	2.05	3.55	2.23
0.75	0.31	0.51	0.3
3.71	1.81	2.61	1.59
0.66	0.35	0.47	0.31
1.8	1	1.34	0.85
0.2	0.11	0.18	0.2
0.254	0.139	0.196	0.126
1.58	0.84	1.29	0.87
0.241	0.127	0.199	0.146

TIMS U-Th-Pb zircon isotopic data

							Radiogenic Isotope Ratios								Isotopic Ages					
Sample (a)	Th/U (d)	^{206}Pb* x10^{-13} mol (e)	mol % ^{206}Pb* (e)	Pb*/Pbc (e)	Pbc (pg) (e)	^{206}Pb/^{204}Pb (f)	208Pb/206Pb (g)	207Pb/206Pb (g)	% err (h)	207Pb/235U (g)	% err (h)	206Pb/238U (g)	% err (h)	corr. coef.	207Pb/206Pb (i)	± (h)	207Pb/235U (i)	± (h)	206Pb/238U (i)	± (h)
CL0975																				
z1	0.728	2.9490	99.01%	33	2.42	1871	0.211	0.118658	0.121	5.710455	0.211	0.349194	0.119	0.881	1935.25	2.16	1932.95	1.83	1930.81	1.98
z2	0.816	6.7791	99.81%	181	1.05	9832	0.236	0.118666	0.084	5.693951	0.325	0.348162	0.292	0.969	1935.37	1.51	1930.45	2.81	1925.87	4.87
z4	0.734	3.1318	99.49%	65	1.33	3605	0.212	0.118544	0.099	5.704957	0.235	0.349194	0.176	0.924	1933.52	1.77	1932.12	2.03	1930.81	2.93
z5	0.756	7.9483	99.89%	306	0.72	16872	0.219	0.118647	0.087	5.718879	0.219	0.349741	0.165	0.935	1935.09	1.56	1934.22	1.89	1933.42	2.76
z6	0.739	3.0479	99.48%	64	1.32	3534	0.214	0.118498	0.103	5.716807	0.198	0.350056	0.119	0.906	1932.82	1.84	1933.91	1.71	1934.93	1.99
CL0972																				
z1	0.596	1.9882	98.84%	28	1.92	1591	0.172	0.120329	0.136	5.871719	0.269	0.354069	0.158	0.928	1960.24	2.43	1957.06	2.34	1954.07	2.66
z2	0.573	4.2370	99.11%	36	3.12	2085	0.165	0.120334	0.116	5.886840	0.308	0.354967	0.241	0.940	1960.31	2.07	1959.30	2.67	1958.34	4.07
z3	0.682	4.9160	98.96%	31	4.29	1748	0.197	0.120384	0.125	5.881774	0.241	0.354515	0.133	0.938	1961.05	2.24	1958.55	2.09	1956.19	2.24
z4	0.644	2.2706	98.56%	23	2.72	1289	0.186	0.120182	0.152	5.873756	0.314	0.354627	0.196	0.924	1958.05	2.72	1957.36	2.72	1956.72	3.31
z5	0.551	6.7095	99.42%	55	3.21	3196	0.159	0.120200	0.105	5.873079	0.296	0.354533	0.243	0.942	1958.31	1.88	1957.26	2.57	1956.27	4.11
z6	0.616	4.2502	99.41%	55	2.09	3114	0.179	0.120275	0.109	5.800768	0.228	0.349950	0.150	0.914	1959.43	1.95	1946.53	1.98	1934.42	2.51
CL0911																				
z2	0.586	7.7665	99.51%	66	3.13	3776	0.170	0.120238	0.101	5.866255	0.215	0.354008	0.143	0.921	1958.89	1.80	1956.26	1.87	1953.77	2.41
z3	0.572	5.3108	99.68%	102	1.38	5867	0.165	0.120186	0.090	5.869737	0.178	0.354371	0.095	0.962	1958.11	1.61	1956.77	1.54	1955.50	1.60
z4	0.792	12.0659	99.41%	55	6.16	2844	0.232	0.117953	0.095	5.514513	0.210	0.339228	0.141	0.930	1924.57	1.69	1902.86	1.81	1883.01	2.30
z5	0.561	3.1647	99.10%	35	2.37	2045	0.163	0.119632	0.166	5.771288	0.260	0.350042	0.128	0.851	1949.85	2.96	1942.11	2.25	1934.87	2.14
z6	0.565	5.7663	99.24%	41	3.70	2342	0.163	0.119818	0.115	5.824825	0.218	0.352739	0.126	0.912	1952.64	2.05	1950.11	1.89	1947.73	2.12

(a) z1, z2 etc. are labels for fractions composed of single zircon grains or fragments; all fractions annealed and chemically abraded after Mattinson (2005).
(d) Model Th/U ratio calculated from radiogenic ^{208}Pb/^{206}Pb ratio and ^{207}Pb/^{235}U age.
(e) Pb* and Pbc represent radiogenic and common Pb, respectively; mol % ^{206}Pb* with respect to radiogenic, blank and initial common Pb.
(f) Measured ratio corrected for spike and fractionation only.
Daly analyses, based on analysis of NBS-981 and NBS-982.
(g) Corrected for fractionation, spike, and common Pb; up to 1 pg of common Pb was assumed to be procedural blank: ^{206}Pb/^{204}Pb = 18.60 ± 0.80%; ^{207}Pb/^{204}Pb = 15.69 ± 0.32%; ^{208}Pb/^{204}Pb = 38.51 ± 0.74% (all uncertainties 1-sigma). Excess over blank was assigned to initial common Pb.
(h) Errors are 2-sigma, propagated using the algorithms of Schmitz and Schoene (2007) and Crowley et al. (2007).
(i) Calculations are based on the decay constants of Jaffey et al. (1971). ^{206}Pb/^{238}U and ^{207}Pb/^{206}Pb ages corrected for initial disequilibrium in ^{230}Th/^{238}U using Th/U [magma] = 3.
(j) Corrected for fractionation, spike, and blank Pb only.

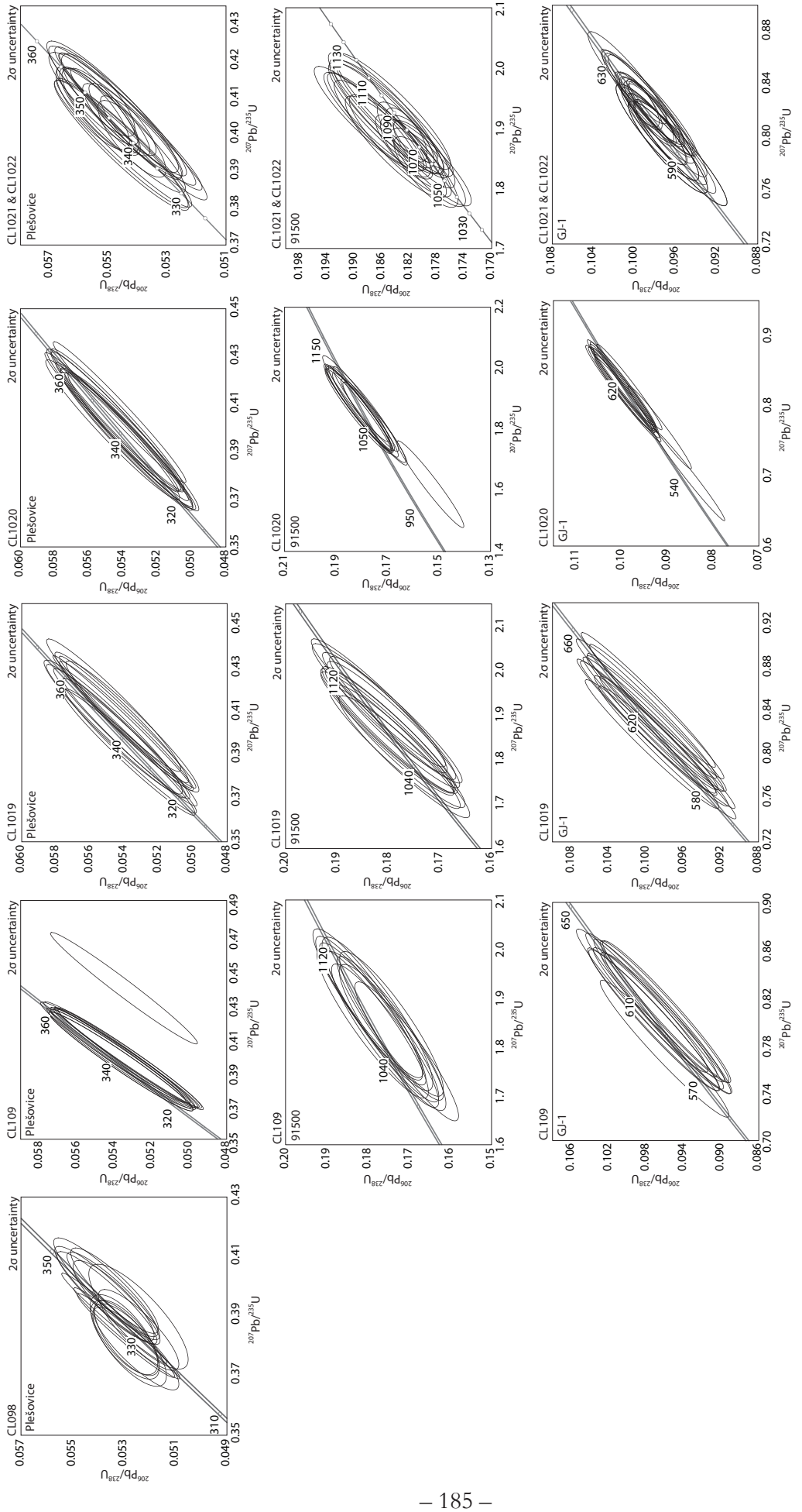
CL1021 & CL1022
Plešovice
2σ uncertainty
CL1021 & CL1022
91500
2σ uncertainty
CL1021 & CL1022
GJ-1
2σ uncertainty
CL1020
Plešovice
2σ uncertainty
CL1020
91500
2σ uncertainty
CL1020
GJ-1
2σ uncertainty
CL1019
Plešovice
2σ uncertainty
CL1019
91500
2σ uncertainty
CL1019
GJ-1
2σ uncertainty
CL109
Plešovice
2σ uncertainty
CL109
91500
2σ uncertainty
CL109
GJ-1
2σ uncertainty
CL098
Plešovice
2σ uncertainty
$^{206}Pb/^{238}U$
$^{207}Pb/^{235}U$

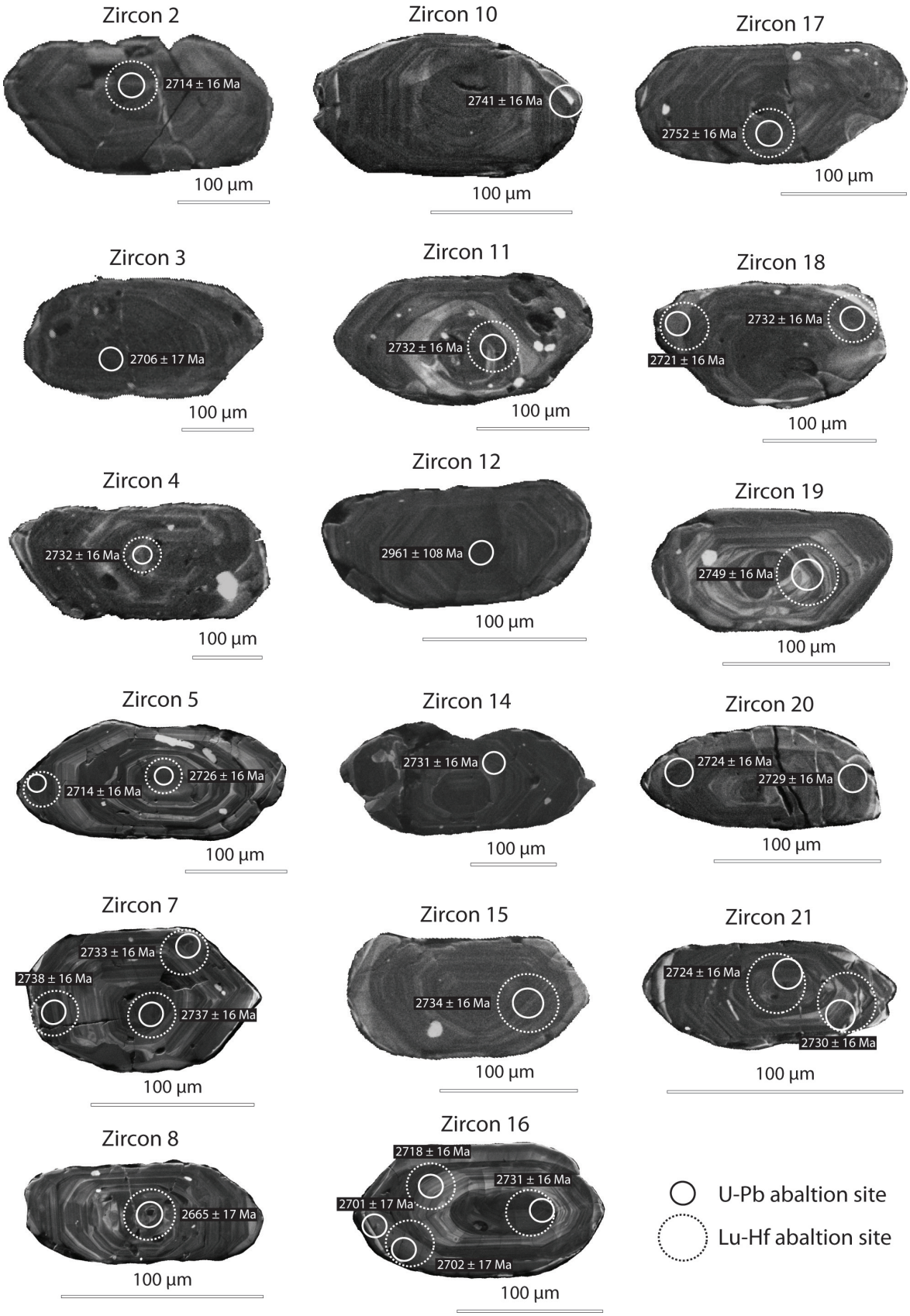
Zircon 2
2714 ± 16 Ma
100 µm
Zircon 10
2741 ± 16 Ma
100 µm
Zircon 17
2752 ± 16 Ma
100 µm
Zircon 3
2706 ± 17 Ma
100 µm
Zircon 11
2732 ± 16 Ma
100 µm
Zircon 18
2732 ± 16 Ma
2721 ± 16 Ma
100 µm
Zircon 4
2732 ± 16 Ma
100 µm
Zircon 12
2961 ± 108 Ma
100 µm
Zircon 19
2749 ± 16 Ma
100 µm
Zircon 5
2714 ± 16 Ma
2726 ± 16 Ma
100 µm
Zircon 14
2731 ± 16 Ma
100 µm
Zircon 20
2724 ± 16 Ma
2729 ± 16 Ma
100 µm
Zircon 7
2733 ± 16 Ma
2738 ± 16 Ma
2737 ± 16 Ma
100 µm
Zircon 15
2734 ± 16 Ma
100 µm
Zircon 21
2724 ± 16 Ma
2730 ± 16 Ma
100 µm
Zircon 8
2665 ± 17 Ma
100 µm
Zircon 16
2718 ± 16 Ma
2731 ± 16 Ma
2701 ± 17 Ma
2702 ± 17 Ma
100 µm
U-Pb abaltion site
Lu-Hf abaltion site

LA-MC-ICP-MS U-Pb zircon data for CL098

	Signals						Data for Tera-Wasserburg plot[3]				Data for Wetherill plot[3]					Ages						
Sample	f206c[1]	^{206}Pb mV	^{207}Pb mV	^{238}U mV	Pb ppm[2]	Uppm[2]	^{238}U/^{206}Pb	1s %	^{207}Pb/^{206}Pb	1s %	^{207}Pb/^{235}U	1s %	^{206}Pb/^{238}U	1s %	Rho	^{207}Pb/^{206}Pb	2s abs	^{206}Pb/^{238}U	2s abs	^{207}Pb/^{235}U	2s abs	Conc.[4]
Ples 4	-0.8	8.5	0.4	102	77	1468	18.91	1.59	0.0527	0.50	0.3840	1.67	0.0529	1.59	0.95	314	23	332	10	330	9	106
Ples 5	-0.8	8.5	0.4	103	77	1487	18.89	1.46	0.0525	0.50	0.3832	1.55	0.0529	1.46	0.95	308	23	332	9	329	9	108
Ples 6	-0.5	9.7	0.4	117	88	1688	18.73	1.57	0.0529	0.50	0.3890	1.64	0.0534	1.57	0.95	322	23	335	10	334	9	104
Lupa_2-1	0.1	21.0	3.2	27	190	394	1.97	1.26	0.1868	0.50	13.0569	1.35	0.5070	1.26	0.93	2714	16	2644	54	2684	25	97
Ples 20um 1	1.3	2.4	0.1	30	21	438	18.88	1.02	0.0523	0.97	0.3818	1.41	0.0530	1.02	0.72	298	44	333	7	328	8	112
Ples 20um 2	-3.7	2.3	0.1	30	21	426	18.94	1.11	0.0522	1.00	0.3800	1.49	0.0528	1.11	0.74	295	46	332	7	327	8	113
Ples 20um 3	0.7	2.3	0.1	30	21	425	18.87	1.01	0.0525	1.01	0.3835	1.43	0.0530	1.01	0.71	306	46	333	7	330	8	109
Ples 20um 4	-0.2	2.6	0.1	33	24	480	18.90	0.97	0.0525	0.94	0.3824	1.35	0.0529	0.97	0.72	304	43	332	6	329	8	109
Lupa 3-1	0.1	18.3	2.8	25	165	358	1.91	2.01	0.1860	0.50	13.4494	2.07	0.5247	2.01	0.97	2706	17	2719	88	2712	38	100
Lupa 4-1	0.0	11.8	1.8	16	106	229	1.94	1.19	0.1889	0.50	13.4204	1.29	0.5155	1.19	0.92	2732	16	2680	52	2710	24	98
Lupa 5-1	0.8	8.9	1.4	12	81	173	1.95	1.14	0.1882	0.50	13.3260	1.24	0.5137	1.14	0.92	2726	16	2673	49	2703	23	98
Lupa 5-2	0.3	15.8	2.4	20	143	294	1.83	1.86	0.1869	0.50	14.0951	1.92	0.5472	1.86	0.97	2714	16	2813	84	2756	36	104
Lupa 7-1	0.1	10.5	1.6	14	95	200	1.91	1.38	0.1895	0.50	13.6632	1.47	0.5233	1.38	0.94	2737	16	2713	61	2727	27	99
Lupa 7-2	0.8	8.6	1.3	11	78	154	1.81	1.99	0.1890	0.50	14.4266	2.05	0.5538	1.99	0.97	2733	16	2841	91	2778	38	104
Lupa 7-3	0.3	8.3	1.3	11	75	157	1.90	1.24	0.1896	0.50	13.7869	1.34	0.5276	1.24	0.93	2738	16	2731	55	2735	25	100
Lupa 8-1	0.3	9.3	1.4	13	84	187	1.95	1.99	0.1814	0.50	12.8033	2.06	0.5122	1.99	0.97	2665	17	2666	87	2665	38	100
Ples-1	-2.1	3.5	0.2	46	31	667	18.64	1.56	0.0537	0.66	0.3967	1.69	0.0536	1.56	0.92	355	30	337	10	339	10	95
Ples-2	-1.0	3.3	0.1	44	30	630	18.74	1.31	0.0542	0.67	0.3983	1.47	0.0534	1.31	0.89	376	30	335	9	340	8	89
Ples-3	0.3	3.2	0.1	42	29	609	18.72	1.21	0.0536	0.71	0.3948	1.40	0.0534	1.21	0.86	355	32	335	8	338	8	95
Lupa 10-1	0.0	13.5	2.1	19	122	275	1.95	0.97	0.1900	0.50	13.4276	1.09	0.5128	0.97	0.89	2741	16	2669	42	2710	20	97
Lupa 11-1	0.4	13.1	2.0	18	119	263	1.90	1.49	0.1889	0.50	13.6697	1.57	0.5249	1.49	0.95	2732	16	2720	66	2727	29	100
Lupa 12-1	3.8	10.1	1.8	14	92	197	1.84	2.35	0.2175	3.36	16.3220	4.10	0.5445	2.35	0.57	2961	108	2802	106	2896	76	95
Lupa 14-1	0.9	8.9	1.4	11	80	158	1.67	1.79	0.1888	0.50	15.5960	1.86	0.5994	1.79	0.96	2731	16	3027	86	2852	35	111
Lupa 15-1	0.4	12.7	2.0	18	115	260	1.95	2.85	0.1892	0.50	13.3759	2.89	0.5130	2.85	0.98	2734	16	2669	123	2707	53	98
Lupa 16-1	0.1	15.4	2.4	22	139	312	1.91	1.10	0.1888	0.50	13.5987	1.21	0.5226	1.10	0.91	2731	16	2710	49	2722	23	99
Lupa 16-2	0.9	5.8	0.9	8	52	118	1.91	1.32	0.1873	0.50	13.5269	1.41	0.5239	1.32	0.94	2718	16	2716	58	2717	26	100
Lupa 16-3	0.0	8.9	1.3	13	80	184	1.97	1.52	0.1854	0.50	12.9954	1.60	0.5085	1.52	0.95	2701	17	2650	66	2679	30	98
Lupa 16-4	0.1	5.9	0.9	9	54	123	1.96	1.33	0.1855	0.50	13.0741	1.42	0.5115	1.33	0.94	2702	17	2663	58	2685	26	99
Ples-1	0.8	3.8	0.2	53	35	763	18.62	1.54	0.0540	0.70	0.3994	1.70	0.0537	1.54	0.91	368	32	337	10	341	10	92
Ples-2	-1.0	3.9	0.2	54	35	776	18.63	1.48	0.0535	0.60	0.3959	1.60	0.0537	1.48	0.93	350	27	337	10	339	9	96
Ples-3	-1.2	3.8	0.2	52	34	746	18.72	1.38	0.0539	0.63	0.3965	1.52	0.0534	1.38	0.91	364	28	335	9	339	9	92
Lupa 17-1	-0.3	12.0	1.9	17	108	246	1.91	1.62	0.1912	0.50	13.8114	1.69	0.5240	1.62	0.96	2752	16	2716	71	2737	32	99
Lupa 18-1	-0.4	17.7	2.7	24	160	346	1.83	2.35	0.1889	0.50	14.1961	2.40	0.5453	2.35	0.98	2732	16	2805	106	2763	45	103
Lupa 18-2	-1.7	6.9	1.1	10	62	140	1.87	1.79	0.1876	0.50	13.8424	1.86	0.5353	1.79	0.96	2721	16	2764	80	2739	35	102
Lupa 19-1	-1.1	4.2	0.7	6	38	90	1.95	1.12	0.1909	0.50	13.4675	1.23	0.5119	1.12	0.91	2749	16	2665	49	2713	23	97
Lupa 20-1	-0.2	7.8	1.2	11	71	165	1.93	1.12	0.1886	0.50	13.4730	1.22	0.5183	1.12	0.91	2729	16	2692	49	2713	23	99
Lupa 20-2	0.3	11.0	1.7	16	100	236	1.96	1.09	0.1880	0.50	13.2377	1.20	0.5108	1.09	0.91	2724	16	2660	47	2697	22	98
Lupa 21-1	-0.1	10.8	1.7	15	98	222	1.87	1.63	0.1880	0.50	13.8337	1.70	0.5340	1.63	0.96	2724	16	2758	73	2738	32	101
Lupa 21-2	-0.5	10.5	1.6	15	95	219	1.91	1.87	0.1887	0.50	13.6040	1.94	0.5231	1.87	0.97	2730	16	2712	82	2723	36	99
Ples-1	-0.1	3.1	0.1	45	28	646	19.07	1.22	0.0533	0.77	0.3851	1.44	0.0524	1.22	0.85	340	35	329	8	331	8	97
Ples-2	-0.7	3.1	0.1	46	28	668	19.07	1.51	0.0539	1.07	0.3896	1.85	0.0524	1.51	0.82	366	48	329	10	334	10	90
Ples-3	0.3	3.0	0.1	45	28	648	19.04	1.29	0.0523	0.76	0.3788	1.50	0.0525	1.29	0.86	299	35	330	8	326	8	110

[1] f^{206}c% = % ^{206}Pb that is common, calculated as Stacey-Kramers ^{206}Pb/^{204}Pb at ^{207}Pb/^{206}Pb age / measured ^{208}Pb/^{203}Pb * 100

[2] concentration uncertainty c.20%

[3] data not corrected for common-Pb

[4] Concordance calculated as (^{206}Pb/^{238}U age/^{207}Pb/^{206}Pb age)*100

Decay constants of Jaffey et al 1971 used; Ratio data normalised to GJ1, concentrations normalised to 91500

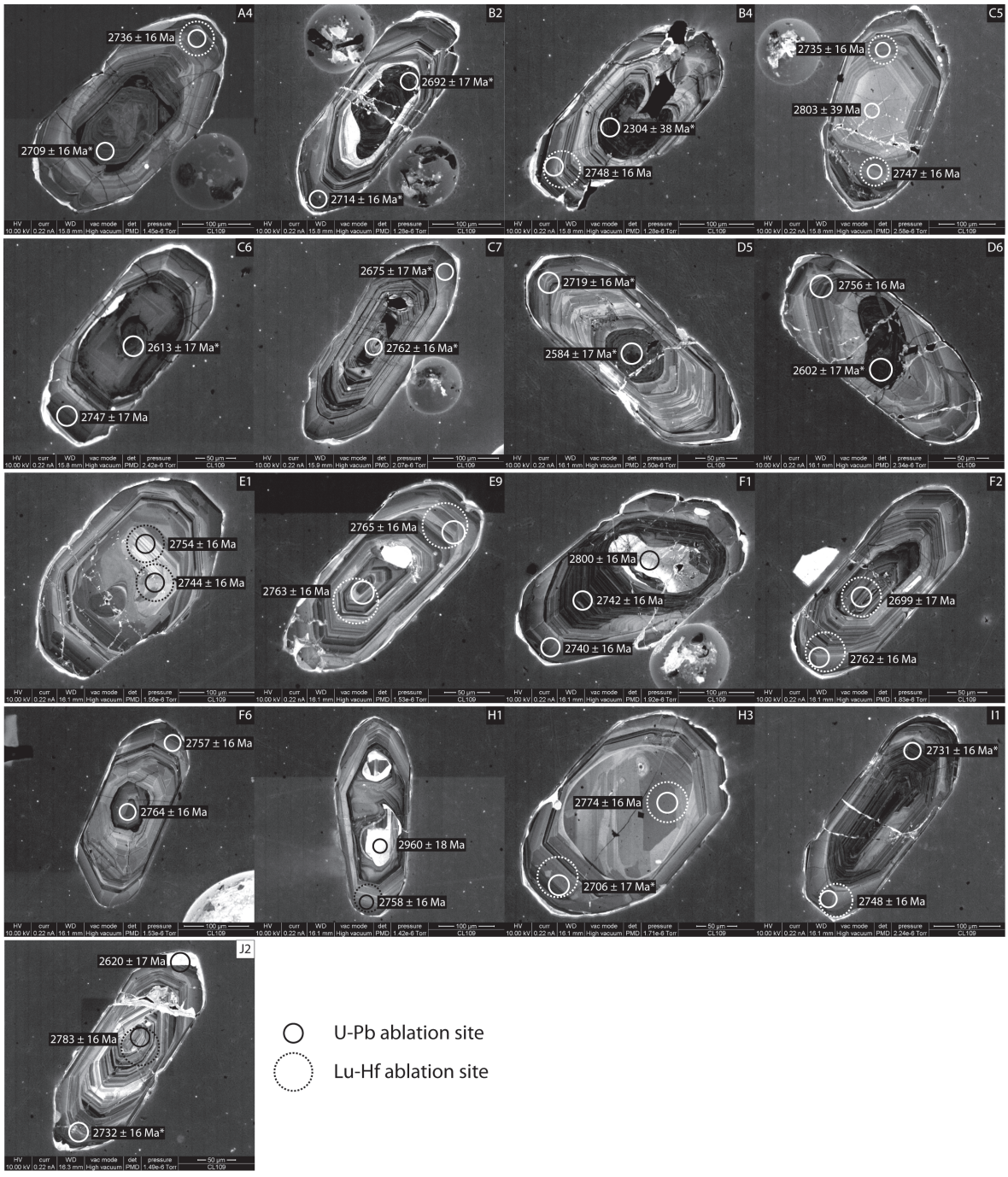
A4
2736 ± 16 Ma
2709 ± 16 Ma*
B2
2692 ± 17 Ma*
2714 ± 16 Ma*
B4
2304 ± 38 Ma*
2748 ± 16 Ma
C5
2735 ± 16 Ma
2803 ± 39 Ma
2747 ± 16 Ma
C6
2613 ± 17 Ma*
2747 ± 17 Ma
C7
2675 ± 17 Ma*
2762 ± 16 Ma*
D5
2719 ± 16 Ma*
2584 ± 17 Ma*
D6
2756 ± 16 Ma
2602 ± 17 Ma*
E1
2754 ± 16 Ma
2744 ± 16 Ma
E9
2765 ± 16 Ma
2763 ± 16 Ma
F1
2800 ± 16 Ma
2742 ± 16 Ma
2740 ± 16 Ma
F2
2699 ± 17 Ma
2762 ± 16 Ma
F6
2757 ± 16 Ma
2764 ± 16 Ma
H1
2960 ± 18 Ma
2758 ± 16 Ma
H3
2774 ± 16 Ma
2706 ± 17 Ma*
I1
2731 ± 16 Ma*
2748 ± 16 Ma
J2
2620 ± 17 Ma
2783 ± 16 Ma
2732 ± 16 Ma*
U-Pb ablation site
Lu-Hf ablation site

LA-MC-ICP-MS U-Pb zircon results for CL109

	Signals						Data for Tera-Wasserburg plot[3]				Data for Wetherill plot[3]					Ages						
Sample	f206c[1]	^{206}Pb mV	^{207}Pb mV	^{238}U mV	Pb ppm[2]	Uppm[2]	^{238}U/^{206}Pb	1s %	^{207}Pb/^{206}Pb	1s %	^{207}Pb/^{235}U	1s %	^{206}Pb/^{238}U	1s %	Rho	^{207}Pb/^{206}Pb	2s abs	^{206}Pb/^{238}U	2s abs	^{207}Pb/^{235}U	2s abs	Conc.[4]
GJ1_1	-2.7	2.6	0.1	30	26	278	10.32	0.9	0.0605	0.7	0.8077	1.2	0.0969	0.9	0.79	621	31	596	11	601	11	96
GJ1_2	-1.8	2.7	0.1	31	26	283	10.29	1.0	0.0610	0.7	0.8179	1.2	0.0972	1.0	0.81	640	30	598	11	607	11	94
GJ1_3	-0.6	2.7	0.1	31	27	285	10.31	1.0	0.0612	0.7	0.8179	1.2	0.0970	1.0	0.80	644	31	597	11	607	11	93
91500_1	-1.2	1.0	0.1	6	10	55	5.67	1.0	0.0768	1.4	1.8682	1.8	0.1765	1.0	0.59	1115	57	1048	20	1070	23	94
91500_2	-0.6	1.1	0.1	7	11	64	5.66	1.2	0.0763	1.2	1.8591	1.8	0.1768	1.2	0.70	1102	50	1049	24	1067	23	95
91500_3	2.8	1.1	0.1	7	11	63	5.49	1.3	0.0761	1.3	1.9110	1.8	0.1823	1.3	0.70	1096	52	1079	25	1085	24	98
Ples_1	-0.3	3.6	0.2	77	36	707	18.59	1.1	0.0541	0.6	0.4014	1.3	0.0538	1.1	0.89	376	27	338	7	343	7	90
Ples_2	0.0	3.9	0.2	84	39	768	18.50	1.0	0.0540	0.6	0.4020	1.2	0.0540	1.0	0.88	369	26	339	7	343	7	92
Ples_3	-0.4	4.6	0.2	98	46	904	18.52	1.1	0.0541	0.5	0.4026	1.2	0.0540	1.1	0.91	374	23	339	7	344	7	91
GJ1_4	-1.6	2.8	0.1	32	28	296	10.03	0.9	0.0602	0.7	0.8272	1.2	0.0997	0.9	0.79	610	32	612	11	612	11	100
GJ1_5	0.0	2.8	0.1	33	28	305	10.22	1.0	0.0607	0.7	0.8189	1.2	0.0978	1.0	0.83	629	30	602	12	607	11	96
91500_4	-9.8	1.1	0.1	7	11	66	5.60	1.5	0.0756	1.3	1.8621	2.0	0.1786	1.5	0.76	1085	53	1059	30	1068	26	98
91500_5	-3.3	0.9	0.1	6	9	55	5.56	1.4	0.0762	1.5	1.8891	2.0	0.1799	1.4	0.68	1099	60	1067	27	1077	27	97
Ples_4	0.0	3.7	0.2	81	37	747	18.47	1.2	0.0594	0.6	0.4437	1.3	0.0542	1.2	0.90	583	25	340	8	373	8	58
Ples_5	-1.5	3.8	0.2	82	38	751	18.57	1.1	0.0542	0.6	0.4022	1.2	0.0539	1.1	0.88	378	26	338	7	343	7	90
A4 1	-0.1	20.3	3.3	51	202	466	2.14	1.1	0.1863	0.5	12.0032	1.2	0.4676	1.1	0.92	2709	16	2473	47	2605	23	91
A4 2	-0.2	9.2	1.5	21	91	191	1.93	0.9	0.1893	0.5	13.5412	1.1	0.5190	0.9	0.88	2736	16	2695	41	2718	20	99
B2 1	0.1	19.5	3.1	48	194	442	2.08	1.0	0.1844	0.5	12.2433	1.1	0.4818	1.0	0.89	2692	17	2535	42	2623	21	94
B2 2	-0.1	10.2	1.6	25	102	228	2.07	1.0	0.1868	0.5	12.4664	1.1	0.4842	1.0	0.89	2714	16	2545	42	2640	21	94
B4 1	1.1	19.3	2.5	116	192	1065	5.06	1.2	0.1465	1.1	3.9911	1.6	0.1977	1.2	0.73	2304	38	1163	25	1632	26	50
B4 2	0.1	8.7	1.4	19	87	177	1.87	1.7	0.1907	0.5	14.0219	1.8	0.5335	1.7	0.96	2748	16	2756	75	2751	33	100
C6 1	1.7	23.5	3.5	130	234	1190	4.66	1.1	0.1758	0.5	5.1976	1.2	0.2145	1.1	0.91	2613	17	1253	26	1852	21	48
C6 2	0.2	8.7	1.4	20	86	187	1.99	1.0	0.1907	0.5	13.2374	1.1	0.5037	1.0	0.89	2747	16	2630	41	2697	20	96
D5 1	-0.1	17.7	2.6	58	176	532	2.72	1.2	0.1728	0.5	8.7695	1.3	0.3682	1.2	0.93	2584	17	2021	42	2314	24	78
D5 2	0.2	8.7	1.4	22	87	205	2.17	1.9	0.1874	0.5	11.8890	2.0	0.4602	1.9	0.97	2719	16	2441	77	2596	36	90
GJ1_6	-2.0	2.7	0.1	33	27	301	10.16	1.0	0.0598	0.7	0.8107	1.2	0.0984	1.0	0.79	595	32	605	11	603	11	102
GJ1_7	2.2	2.7	0.1	34	27	309	10.21	1.0	0.0602	0.7	0.8121	1.2	0.0979	1.0	0.82	609	31	602	12	604	11	99
GJ1_8	1.7	2.7	0.1	34	27	309	10.30	1.1	0.0604	0.7	0.8081	1.3	0.0971	1.1	0.84	617	30	597	12	601	11	97
9500_6	1.0	1.0	0.1	6	9	59	5.68	1.3	0.0758	1.4	1.8401	1.9	0.1762	1.3	0.67	1088	57	1046	25	1060	25	96
9500_7	1.6	1.0	0.1	7	10	62	5.52	1.4	0.0749	1.4	1.8694	2.0	0.1811	1.4	0.70	1065	56	1073	27	1070	26	101
9500_8	-1.4	1.1	0.1	7	11	67	5.62	1.2	0.0752	1.3	1.8439	1.8	0.1780	1.2	0.69	1072	52	1056	24	1061	23	99
Ples_1	1.2	3.4	0.2	75	34	690	18.41	1.0	0.0535	0.7	0.4002	1.2	0.0543	1.0	0.83	347	30	341	7	342	7	98
Ples_6	1.2	3.4	0.2	75	34	690	18.41	1.0	0.0535	0.7	0.4002	1.2	0.0543	1.0	0.83	347	30	341	7	342	7	98
Ples_7	-0.2	3.1	0.1	69	31	634	18.38	1.0	0.0536	0.7	0.4022	1.2	0.0544	1.0	0.83	355	31	342	7	343	7	96
Ples_8	0.5	3.3	0.2	74	33	676	18.27	1.0	0.0538	0.6	0.4056	1.2	0.0547	1.0	0.84	361	29	344	7	346	7	95
H1 2 c	1.8	2.5	0.5	5	25	47	1.81	2.0	0.2173	0.6	16.5759	2.0	0.5535	2.0	0.96	2960	18	2840	90	2911	38	96
H1 1 c	-0.7	6.7	1.1	15	67	137	1.85	1.0	0.1919	0.5	14.2991	1.2	0.5405	1.0	0.90	2758	16	2786	47	2770	22	101
H3 2 c	0.4	9.4	1.5	28	94	261	2.51	1.0	0.1859	0.5	10.2108	1.1	0.3985	1.0	0.90	2706	17	2162	37	2454	21	80
H3 1 c	-0.3	7.1	1.2	16	71	148	1.88	1.0	0.1939	0.5	14.2227	1.1	0.5324	1.0	0.90	2774	16	2751	45	2765	21	99
F6 2 c	0.4	8.9	1.5	21	89	193	1.99	1.1	0.1918	0.5	13.2936	1.2	0.5030	1.1	0.91	2757	16	2627	47	2701	22	95
F6 1 c	0.1	7.5	1.2	17	75	156	1.93	1.3	0.1926	0.5	13.7628	1.4	0.5184	1.3	0.93	2764	16	2692	56	2734	26	97
F2 2 c	-0.8	8.3	1.4	18	83	170	1.91	1.1	0.1924	0.5	13.9165	1.2	0.5248	1.1	0.91	2762	16	2720	49	2744	23	98
F2 1 c	0.3	12.3	2.0	30	123	274	2.00	1.2	0.1852	0.5	12.7641	1.3	0.5002	1.2	0.92	2699	17	2614	50	2662	23	97
F1 3 c	-0.5	7.6	1.2	17	76	160	1.95	1.1	0.1899	0.5	13.4310	1.2	0.5132	1.1	0.91	2740	16	2670	48	2710	23	97
F1 2 c	-0.1	23.0	3.8	53	229	487	1.97	1.2	0.1900	0.5	13.2624	1.3	0.5064	1.2	0.92	2742	16	2641	50	2699	23	96

F1 1 c	-0.3	4.4	0.8	10	44	91	1.94	1.1	0.1969	0.5	13.9634	1.2	0.5147	1.1	0.91	2800	16	2677	49	2747	23	96
E9 2 c	-0.4	6.4	1.1	14	64	133	1.91	1.0	0.1928	0.5	13.9022	1.2	0.5232	1.0	0.90	2765	16	2713	46	2743	22	98
E9 1 c	0.1	8.6	1.4	19	85	176	1.90	1.0	0.1926	0.5	13.9389	1.1	0.5253	1.0	0.89	2763	16	2721	44	2746	21	98
D6 2 c	0.0	9.2	1.5	21	92	193	1.94	1.1	0.1917	0.5	13.6420	1.2	0.5165	1.1	0.91	2756	16	2684	49	2725	23	97
D6 1 c	0.9	16.8	2.5	80	167	738	3.99	1.9	0.1746	0.5	6.0327	2.0	0.2507	1.9	0.97	2602	17	1442	50	1981	34	55
C5 -1	1.5	3.1	0.5	7	31	67	1.93	1.3	0.1973	1.2	14.1013	1.8	0.5186	1.3	0.74	2803	39	2693	58	2757	33	96
C5 -2	-0.1	7.0	1.1	16	70	150	1.94	1.1	0.1893	0.5	13.4303	1.2	0.5148	1.1	0.91	2735	16	2677	46	2710	22	98
C5 -3	-0.5	6.7	1.1	16	66	144	1.95	1.2	0.1906	0.5	13.4677	1.3	0.5127	1.2	0.92	2747	16	2668	51	2713	24	97
C7 1	0.2	9.7	1.6	24	97	225	2.27	1.2	0.1924	0.5	11.6550	1.3	0.4396	1.2	0.93	2762	16	2349	49	2577	25	85
C7 2	-0.3	8.8	1.4	28	88	257	2.68	1.2	0.1825	0.5	9.3826	1.3	0.3731	1.2	0.92	2675	17	2044	42	2376	24	76
E1 1	-0.2	6.3	1.0	14	63	132	1.91	1.1	0.1903	0.5	13.7021	1.2	0.5226	1.1	0.91	2744	16	2710	49	2729	23	99
E1 2	-0.6	6.9	1.1	16	69	145	1.90	1.1	0.1915	0.5	13.8836	1.3	0.5261	1.1	0.92	2754	16	2725	51	2742	23	99
I1 1	-0.1	13.0	2.1	29	130	268	2.08	1.2	0.1889	0.5	12.5221	1.3	0.4811	1.2	0.93	2731	16	2532	51	2644	24	93
I1 2	-0.3	10.0	1.6	23	100	208	1.91	1.0	0.1908	0.5	13.7849	1.1	0.5243	1.0	0.89	2748	16	2718	44	2735	21	99
J2 1	-0.1	3.3	0.5	8	33	70	1.97	1.1	0.1765	0.5	12.3385	1.2	0.5071	1.1	0.90	2620	17	2644	46	2631	22	101
J2 2	-0.3	9.0	1.5	20	89	182	1.85	1.0	0.1948	0.5	14.5183	1.2	0.5407	1.0	0.90	2783	16	2786	47	2784	22	100
J2 3	-0.4	18.3	3.0	44	182	408	2.16	1.7	0.1889	0.5	12.0260	1.7	0.4619	1.7	0.96	2732	16	2448	68	2606	32	90
GJ1 9	1.1	2.7	0.1	34	27	312	10.16	1.1	0.0598	0.7	0.8113	1.3	0.0984	1.1	0.84	596	31	605	13	603	12	102
GJ1 10	0.3	2.8	0.1	34	27	314	10.14	1.0	0.0606	0.7	0.8236	1.2	0.0987	1.0	0.82	623	30	607	12	610	11	97
GJ1 11	-0.2	2.7	0.1	34	27	308	10.28	1.0	0.0587	0.8	0.7864	1.2	0.0972	1.0	0.79	554	33	598	11	589	11	108
9500 1	-2.7	1.1	0.1	8	11	72	5.79	1.2	0.0761	1.2	1.8114	1.7	0.1727	1.2	0.71	1097	48	1027	23	1050	22	94
9500 10	-2.0	1.2	0.1	8	12	72	5.52	1.0	0.0757	1.2	1.8889	1.6	0.1811	1.0	0.66	1086	48	1073	21	1077	21	99
9500 11	3.5	1.1	0.1	8	11	70	5.50	1.0	0.0758	1.2	1.9007	1.6	0.1820	1.0	0.64	1089	50	1078	21	1081	21	99
Ples 9	0.9	3.4	0.2	77	34	708	18.45	1.1	0.0537	0.6	0.4013	1.2	0.0542	1.1	0.86	358	29	340	7	343	7	95
Ples 10	1.0	3.4	0.2	78	34	714	18.34	1.1	0.0540	0.6	0.4055	1.3	0.0545	1.1	0.87	369	28	342	7	346	7	93
Ples 11	1.6	3.4	0.2	77	34	705	18.44	1.0	0.0538	0.7	0.4025	1.2	0.0542	1.0	0.85	364	30	340	7	343	7	94

[1] $f^{206}c\% = \%\ ^{206}Pb$ that is common, calculated as Stacey-Kramers $^{206}Pb/^{204}Pb$ at $^{207}Pb/^{206}Pb$ age / measured $^{206}Pb/^{204}Pb * 100$

[2] concentration uncertainty c.20%

[3] data not corrected for common-Pb

[4] Concordance calculated as $(^{206}Pb/^{238}U\ age/^{207}Pb/^{206}Pb\ age)*100$

Decay constants of Jaffey et al 1971 used

Ratio data normalised to GJ1, concentrations normalised to 91500

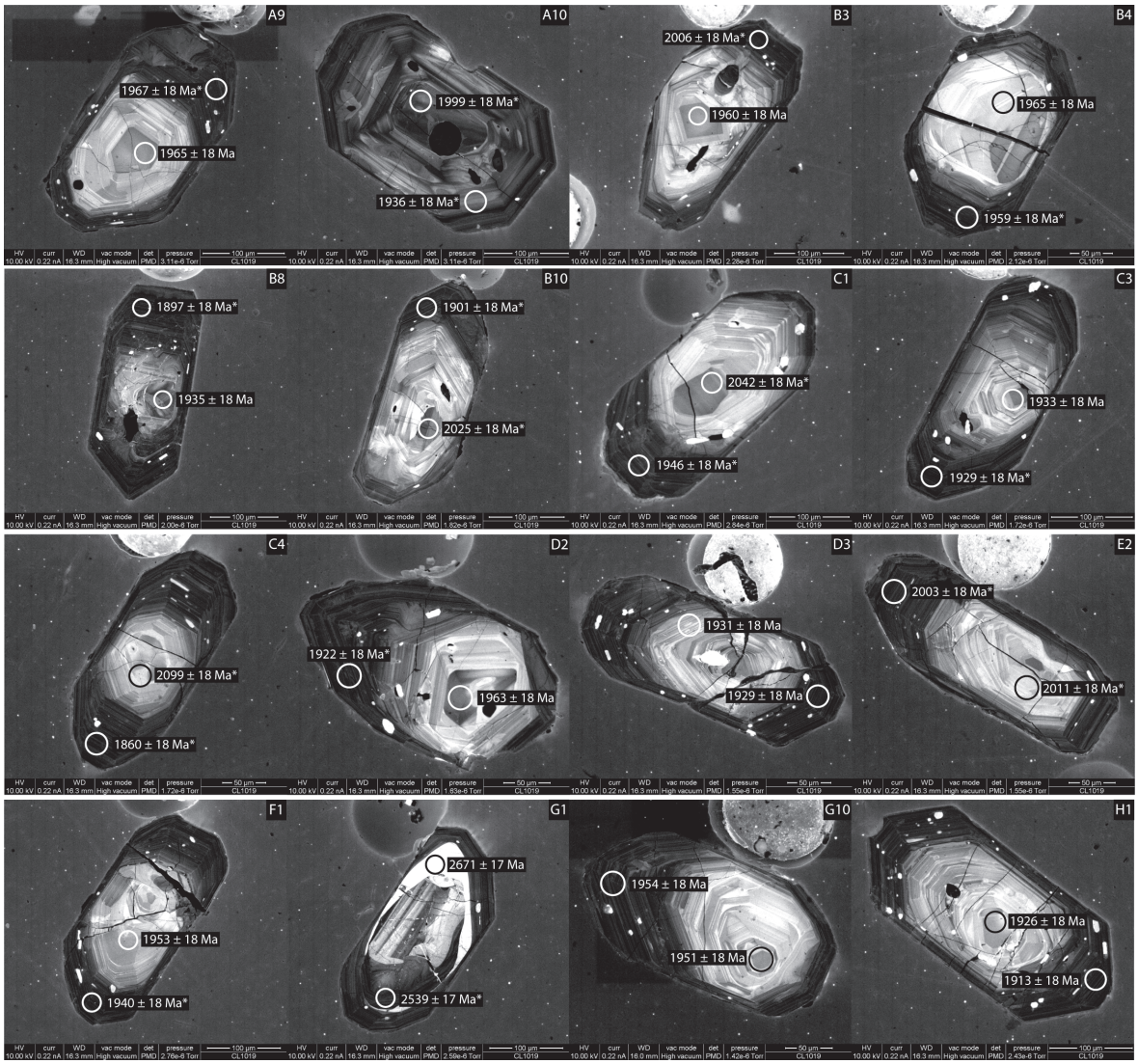
A9
1967 ± 18 Ma*
1965 ± 18 Ma
A10
1999 ± 18 Ma*
1936 ± 18 Ma*
B3
2006 ± 18 Ma*
1960 ± 18 Ma
B4
1965 ± 18 Ma
1959 ± 18 Ma*
B8
1897 ± 18 Ma*
1935 ± 18 Ma
B10
1901 ± 18 Ma*
2025 ± 18 Ma*
C1
2042 ± 18 Ma*
1946 ± 18 Ma*
C3
1933 ± 18 Ma
1929 ± 18 Ma*
C4
2099 ± 18 Ma*
1860 ± 18 Ma*
D2
1922 ± 18 Ma*
1963 ± 18 Ma
D3
1931 ± 18 Ma
1929 ± 18 Ma
E2
2003 ± 18 Ma*
2011 ± 18 Ma*
F1
1953 ± 18 Ma
1940 ± 18 Ma*
G1
2671 ± 17 Ma
2539 ± 17 Ma*
G10
1954 ± 18 Ma
1951 ± 18 Ma
H1
1926 ± 18 Ma
1913 ± 18 Ma

LA-MC-ICP-MS U-Pb zircon results for CL1019

	Signals						Data for Tera-Wasserburg plot[3]				Data for Wetherill plot[3]					Ages						
Sample	f206c[1]	^{206}Pb mV	^{207}Pb mV	^{238}U mV	Pb ppm[2]	Uppm[2]	^{238}U/^{206}Pb	1s %	^{207}Pb/^{206}Pb	1s %	^{207}Pb/^{235}U	1s %	^{206}Pb/^{238}U	1s %	Rho	^{207}Pb/^{206}Pb	2s abs	^{206}Pb/^{238}U	2s abs	^{207}Pb/^{235}U	2s abs	Conc.[4]
GJ1 12	-1.5	3.3	0.2	38	28	314	10.19	1.0	0.0604	0.6	0.8169	1.2	0.0981	1.0	0.86	618	26	603	12	606	11	98
GJ1 13	-0.5	3.4	0.2	39	28	322	10.26	1.0	0.0616	0.6	0.8277	1.2	0.0974	1.0	0.88	660	24	599	12	612	11	91
GJ1 14	-2.0	3.4	0.2	39	28	319	10.17	0.9	0.0619	0.6	0.8383	1.1	0.0983	0.9	0.86	668	24	605	11	618	10	91
91500 12	-6.2	1.6	0.1	10	13	82	5.68	1.0	0.0768	0.9	1.8620	1.3	0.1760	1.0	0.73	1114	36	1045	18	1068	17	94
91500 13	-5.3	1.6	0.1	10	13	85	5.64	0.9	0.0766	0.9	1.8706	1.3	0.1773	0.9	0.72	1109	36	1052	18	1071	17	95
91500 14	-7.1	1.6	0.1	10	14	84	5.58	0.9	0.0769	0.9	1.8995	1.2	0.1793	0.9	0.72	1117	35	1063	18	1081	16	95
PLES 12	-2.3	2.5	0.1	53	20	439	18.96	1.0	0.0546	0.8	0.3972	1.3	0.0527	1.0	0.77	396	37	331	6	340	7	84
PLES 13	-4.0	2.9	0.1	62	24	507	18.74	0.9	0.0546	0.7	0.4012	1.2	0.0534	0.9	0.79	393	32	335	6	343	7	85
PLES 14	-5.3	2.8	0.1	57	23	471	18.58	0.9	0.0548	0.8	0.4068	1.2	0.0538	0.9	0.76	405	34	338	6	347	7	84
A9 1	0.2	3.7	0.4	12	30	99	2.87	0.9	0.1207	0.5	5.7865	1.0	0.3480	0.9	0.87	1965	18	1925	29	1944	17	98
A9 2	0.4	16.4	1.7	59	136	487	3.14	0.9	0.1208	0.5	5.3021	1.0	0.3185	0.9	0.87	1967	18	1782	27	1869	17	91
A10 1	1.9	5.2	0.6	18	43	146	2.96	1.0	0.1230	0.5	5.7311	1.1	0.3381	1.0	0.90	1999	18	1878	33	1936	19	94
A10 2	0.9	8.0	0.8	35	67	287	3.66	2.5	0.1187	0.5	4.4726	2.5	0.2734	2.5	0.98	1936	18	1558	68	1726	41	80
B3 1	1.5	4.1	0.4	14	34	112	2.87	0.9	0.1203	0.5	5.7862	1.0	0.3489	0.9	0.87	1960	18	1929	29	1944	17	98
B3 2	0.8	13.0	1.4	50	108	414	3.34	1.0	0.1235	0.5	5.0950	1.1	0.2995	1.0	0.90	2006	18	1689	30	1835	19	84
B4 1	1.3	3.4	0.3	11	28	92	2.89	0.9	0.1206	0.5	5.7578	1.0	0.3464	0.9	0.87	1965	18	1917	29	1940	17	98
B4 2	0.4	18.6	1.9	73	155	603	3.39	0.9	0.1202	0.5	4.8936	1.0	0.2953	0.9	0.86	1959	18	1668	25	1801	16	85
B10 1	2.0	3.6	0.4	14	30	117	3.40	0.9	0.1248	0.5	5.0526	1.0	0.2938	0.9	0.86	2025	18	1660	25	1828	17	82
B10 2	0.6	15.4	1.5	76	128	623	4.26	0.9	0.1164	0.5	3.7659	1.0	0.2347	0.9	0.88	1901	18	1359	22	1585	17	71
C1 1	2.6	4.8	0.5	17	40	138	3.02	0.9	0.1260	0.5	5.7594	1.1	0.3316	0.9	0.88	2042	18	1846	30	1940	18	90
C1 2	0.0	19.5	2.0	69	162	566	3.03	1.0	0.1194	0.5	5.4254	1.1	0.3297	1.0	0.89	1946	18	1837	31	1889	18	94
D2 1	0.5	5.4	0.6	19	45	154	2.96	1.4	0.1205	0.5	5.6186	1.5	0.3384	1.4	0.94	1963	18	1879	45	1919	25	96
D2 2	-0.2	18.9	1.9	70	157	578	3.23	1.2	0.1178	0.5	5.0188	1.3	0.3092	1.2	0.93	1922	18	1737	37	1823	22	90
E2 1	2.0	2.1	0.2	8	18	66	3.29	1.3	0.1238	0.5	5.1896	1.4	0.3041	1.3	0.93	2011	18	1712	38	1851	23	85
E2 2	1.0	16.8	1.8	92	139	757	4.71	1.3	0.1232	0.5	3.6086	1.4	0.2125	1.3	0.94	2003	18	1242	30	1551	23	62
F1 1	0.9	3.3	0.3	11	28	90	2.86	1.7	0.1199	0.5	5.7697	1.8	0.3493	1.7	0.96	1953	18	1931	58	1942	31	99
F1 2	0.3	16.6	1.7	60	138	496	3.05	1.7	0.1190	0.5	5.3800	1.7	0.3281	1.7	0.96	1940	18	1829	53	1882	29	94
G10 1	1.9	3.1	0.3	10	25	86	2.90	0.9	0.1197	0.5	5.6805	1.0	0.3444	0.9	0.88	1951	18	1908	30	1928	18	98
G10 2	0.4	16.8	1.7	58	139	477	2.94	0.9	0.1199	0.5	5.6132	1.0	0.3397	0.9	0.87	1954	18	1885	29	1918	17	97
GJ1 15	1.3	3.2	0.2	38	26	310	10.24	1.2	0.0607	0.6	0.8168	1.3	0.0976	1.2	0.89	628	26	600	13	606	12	96
GJ1 16	0.1	3.2	0.2	39	27	322	10.26	1.3	0.0609	0.6	0.8179	1.4	0.0974	1.3	0.91	635	26	599	15	607	13	94
GJ1 17	-0.8	3.2	0.2	39	27	319	10.15	1.3	0.0611	0.6	0.8303	1.4	0.0985	1.3	0.90	643	26	606	15	614	13	94
91500 15	-2.4	1.5	0.1	10	12	81	5.67	0.9	0.0761	1.0	1.8513	1.3	0.1764	0.9	0.69	1098	39	1047	18	1064	18	95
91500 16	-1.8	1.5	0.1	10	12	82	5.64	0.9	0.0753	1.0	1.8404	1.3	0.1774	0.9	0.69	1075	39	1052	18	1060	18	98
91500 17	-3.5	1.5	0.1	10	13	82	5.58	1.0	0.0765	1.0	1.8876	1.4	0.1791	1.0	0.71	1107	38	1062	19	1077	18	96
PLES 17	0.9	4.1	0.2	89	34	734	18.86	1.2	0.0546	0.5	0.3991	1.3	0.0530	1.2	0.91	395	24	333	8	341	7	84
PLES 16	-0.3	5.0	0.2	109	42	898	18.75	1.3	0.0543	0.5	0.3993	1.4	0.0533	1.3	0.93	383	22	335	8	341	8	87
PLES 15	-0.4	3.8	0.2	84	32	692	18.83	1.0	0.0543	0.6	0.3974	1.2	0.0531	1.0	0.85	383	27	333	6	340	7	87
GJ1 18	-0.8	3.2	0.2	35	27	285	10.21	0.9	0.0591	0.6	0.7981	1.1	0.0979	0.9	0.83	571	27	602	11	596	10	106
GJ1 19	-1.5	3.2	0.2	35	26	285	10.31	1.0	0.0599	0.6	0.8009	1.2	0.0970	1.0	0.87	600	26	597	12	597	11	99
GJ1 20	-3.8	3.2	0.2	35	27	286	10.17	1.0	0.0600	0.6	0.8135	1.2	0.0984	1.0	0.86	603	26	605	12	604	11	100
91500 18	-3.3	1.4	0.1	9	12	71	5.74	0.9	0.0741	1.0	1.7800	1.4	0.1744	0.9	0.67	1043	41	1036	18	1038	18	99
91500 19	-6.6	1.5	0.1	9	12	73	5.71	0.9	0.0747	1.0	1.8034	1.3	0.1752	0.9	0.66	1059	40	1041	17	1047	17	98
91500 20	-5.1	1.5	0.1	9	12	73	5.67	0.9	0.0741	1.0	1.8006	1.3	0.1763	0.9	0.68	1044	38	1046	17	1046	17	100
PLES 18	-4.1	3.1	0.1	62	26	508	18.87	1.0	0.0528	0.7	0.3854	1.2	0.0530	1.0	0.83	318	31	333	6	331	7	105
PLES 19	-3.7	3.3	0.2	66	28	547	18.92	0.9	0.0530	0.7	0.3860	1.1	0.0528	0.9	0.80	327	30	332	6	331	6	101
PLES 20	-4.0	3.6	0.2	71	30	585	18.91	1.0	0.0535	0.6	0.3900	1.2	0.0529	1.0	0.86	349	28	332	7	334	7	95

B8 1	0.1	4.7	0.5	14	39	116	2.93	1.1	0.1187	0.5	5.5891	1.2	0.3417	1.1	0.91	1935	18	1895	37	1914	21	98
B8 2	0.2	23.5	2.4	100	195	823	4.11	1.0	0.1161	0.5	3.8968	1.1	0.2435	1.0	0.90	1897	18	1405	26	1613	18	74
C3 1	-0.8	3.3	0.3	10	28	83	2.94	0.9	0.1185	0.5	5.5520	1.1	0.3400	0.9	0.88	1933	18	1887	31	1909	18	98
C3 2	0.3	19.0	2.0	79	158	655	4.06	0.9	0.1182	0.5	4.0150	1.1	0.2464	0.9	0.88	1929	18	1420	24	1637	17	74
C4 1	2.7	3.7	0.4	12	31	102	3.28	0.9	0.1301	0.5	5.4664	1.1	0.3048	0.9	0.88	2099	18	1715	29	1895	18	82
C4 2	0.3	19.3	1.9	80	160	659	4.02	0.9	0.1138	0.5	3.9009	1.0	0.2487	0.9	0.88	1860	18	1432	23	1614	17	77
D3 1	-0.4	3.0	0.3	9	25	72	2.89	1.2	0.1184	0.5	5.6420	1.3	0.3458	1.2	0.92	1931	18	1915	39	1923	22	99
D3 2	-0.3	18.6	1.9	56	154	459	2.93	2.0	0.1182	0.5	5.5676	2.0	0.3417	2.0	0.97	1929	18	1895	65	1911	35	98
G1 1	0.4	2.9	0.5	6	24	49	2.03	1.1	0.1820	0.5	12.3292	1.2	0.4915	1.1	0.92	2671	17	2577	48	2630	23	96
G1 2	0.1	31.4	4.7	96	261	790	2.96	1.1	0.1682	0.5	7.8227	1.2	0.3375	1.1	0.91	2539	17	1874	35	2211	21	74
H1 1	-0.3	3.3	0.3	10	28	80	2.86	0.9	0.1180	0.5	5.6843	1.0	0.3494	0.9	0.88	1926	18	1932	30	1929	18	100
H1 2	-0.3	18.3	1.9	57	152	473	3.00	0.9	0.1172	0.5	5.3854	1.1	0.3334	0.9	0.88	1913	18	1855	30	1883	18	97
GJ1 21	-0.8	3.2	0.2	36	27	296	10.38	1.3	0.0596	0.6	0.7905	1.4	0.0963	1.3	0.91	586	26	593	14	591	13	101
GJ1 22	-0.5	3.3	0.2	36	27	301	10.15	1.3	0.0599	0.6	0.8134	1.4	0.0985	1.3	0.91	600	25	605	15	604	13	101
GJ1 23	-0.4	3.3	0.2	37	27	302	10.38	1.2	0.0602	0.6	0.7997	1.3	0.0963	1.2	0.90	611	25	593	13	597	12	97
91500 21	-3.8	1.6	0.1	10	13	79	5.66	0.9	0.0754	0.9	1.8363	1.3	0.1768	0.9	0.69	1077	37	1049	17	1059	17	97
91500 22	-0.6	1.6	0.1	10	13	81	5.63	0.9	0.0748	0.9	1.8313	1.3	0.1776	0.9	0.71	1063	35	1054	17	1057	16	99
91500 23	-2.5	1.6	0.1	10	13	80	5.63	0.9	0.0751	0.9	1.8372	1.3	0.1776	0.9	0.71	1069	36	1054	18	1059	17	99
PLES 21	-1.6	3.1	0.1	64	26	524	18.74	1.1	0.0536	0.7	0.3939	1.3	0.0534	1.1	0.86	351	30	335	7	337	7	95
PLES 22	-1.2	2.3	0.1	46	19	383	18.57	1.2	0.0535	0.9	0.3969	1.4	0.0539	1.2	0.80	348	39	338	8	339	8	97
PLES 23	-1.3	2.9	0.1	58	24	477	18.63	1.3	0.0534	0.7	0.3950	1.3	0.0537	1.1	0.86	344	30	337	7	338	7	98

[1] f_{206}% = % ^{206}Pb that is common, calculated as Stacey-Kramers $^{206}Pb/^{204}Pb$ at $^{207}Pb/^{206}Pb$ age / measured $^{206}Pb/^{204}Pb$ * 100

[2] concentration uncertainty c.20%

[3] data not corrected for common-Pb

[4] Concordance calculated as ($^{206}Pb/^{238}U$ age/$^{207}Pb/^{206}Pb$ age)*100

Decay constants of Jaffey et al 1971 used

Ratio data normalised to GJ1, concentrations normalised to 91500

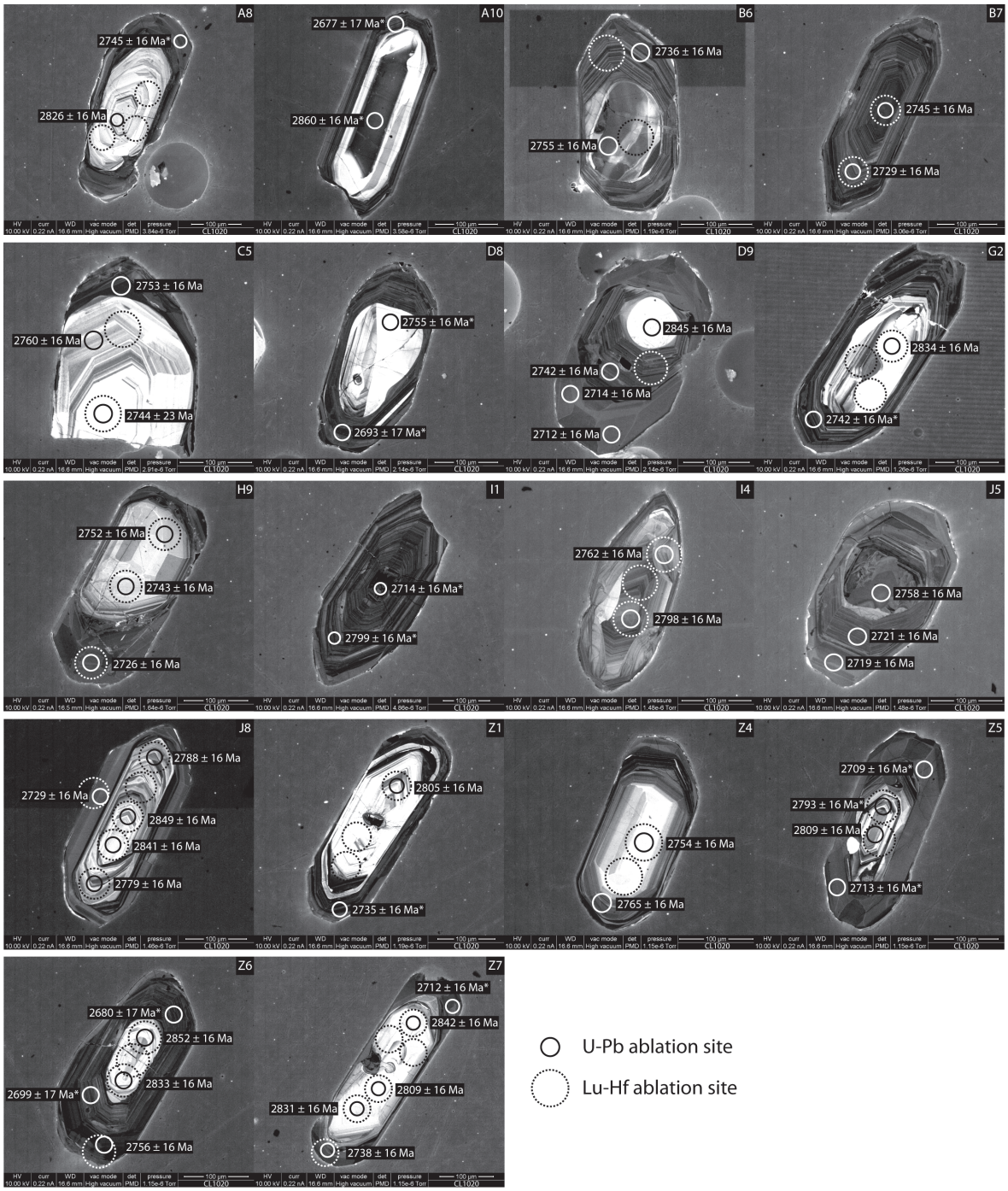
A8
2745 ± 16 Ma*
2826 ± 16 Ma
A10
2677 ± 17 Ma*
2860 ± 16 Ma*
B6
2736 ± 16 Ma
2755 ± 16 Ma
B7
2745 ± 16 Ma
2729 ± 16 Ma
C5
2753 ± 16 Ma
2760 ± 16 Ma
2744 ± 23 Ma
D8
2755 ± 16 Ma*
2693 ± 17 Ma*
D9
2845 ± 16 Ma
2742 ± 16 Ma
2714 ± 16 Ma
2712 ± 16 Ma
G2
2834 ± 16 Ma
2742 ± 16 Ma*
H9
2752 ± 16 Ma
2743 ± 16 Ma
2726 ± 16 Ma
I1
2714 ± 16 Ma*
2799 ± 16 Ma*
I4
2762 ± 16 Ma
2798 ± 16 Ma
J5
2758 ± 16 Ma
2721 ± 16 Ma
2719 ± 16 Ma
J8
2788 ± 16 Ma
2729 ± 16 Ma
2849 ± 16 Ma
2841 ± 16 Ma
2779 ± 16 Ma
Z1
2805 ± 16 Ma
2735 ± 16 Ma*
Z4
2754 ± 16 Ma
2765 ± 16 Ma
Z5
2709 ± 16 Ma*
2793 ± 16 Ma*
2809 ± 16 Ma
2713 ± 16 Ma*
Z6
2680 ± 17 Ma*
2852 ± 16 Ma
2833 ± 16 Ma
2699 ± 17 Ma*
2756 ± 16 Ma
Z7
2712 ± 16 Ma*
2842 ± 16 Ma
2809 ± 16 Ma
2831 ± 16 Ma
2738 ± 16 Ma
U-Pb ablation site
Lu-Hf ablation site

LA-MC-ICP-MS U-Pb results for CL1020

	Signals						Data for Tera-Wasserburg plot[3]				Data for Wetherill plot[3]					Ages						
Sample	f206c[1]	^{206}Pb mV	^{207}Pb mV	^{238}U mV	Pb ppm[2]	Uppm[2]	^{238}U/^{206}Pb	1s %	^{207}Pb/^{206}Pb	1s %	^{207}Pb/^{235}U	1s %	^{206}Pb/^{238}U	1s %	Rho	^{207}Pb/^{206}Pb	2s abs	^{206}Pb/^{238}U	2s abs	^{207}Pb/^{235}U	2s abs	**Conc.[4]**
GJ1 24	0.6	3.2	0.2	33	26	271	10.14	1.1	0.0597	0.6	0.8113	1.2	0.0986	1.1	0.86	592	27	606	12	603	11	102
GJ1 25	-1.8	3.2	0.2	33	26	272	11.06	1.4	0.0609	0.6	0.7585	1.5	0.0904	1.4	0.91	635	27	558	15	573	13	88
GJ1 26	-1.3	3.3	0.2	35	27	286	10.32	1.0	0.0610	0.6	0.8153	1.2	0.0969	1.0	0.86	640	26	596	12	605	11	93
91500 24	-4.7	1.6	0.1	9	13	77	5.78	0.9	0.0756	0.9	1.8022	1.3	0.1731	0.9	0.72	1082	36	1029	17	1046	17	95
91500 25	-3.6	1.6	0.1	9	13	76	6.61	2.1	0.0767	0.9	1.5972	2.3	0.1512	2.1	0.91	1111	37	908	35	969	28	82
91500 26	-1.1	1.7	0.1	10	14	80	5.63	0.8	0.0753	0.9	1.8424	1.2	0.1776	0.8	0.70	1075	35	1054	16	1061	16	98
PLES 24	-1.2	2.8	0.1	55	23	450	19.00	0.9	0.0536	0.7	0.3884	1.1	0.0526	0.9	0.76	352	33	331	6	333	6	94
PLES 25	-1.2	3.0	0.1	59	25	487	18.87	0.9	0.0532	0.7	0.3887	1.1	0.0530	0.9	0.78	337	31	333	6	333	6	99
PLES 26	-1.5	3.3	0.2	66	28	543	18.94	0.8	0.0534	0.6	0.3888	1.0	0.0528	0.8	0.80	346	28	332	5	333	6	96
A8 1 d	0.3	3.3	0.6	7	28	54	1.84	0.8	0.2001	0.5	14.9668	1.0	0.5427	0.8	0.86	2826	16	2795	38	2813	19	99
A8 2 d	0.4	15.3	2.6	34	127	279	2.06	1.0	0.1904	0.5	12.7500	1.1	0.4858	1.0	0.90	2745	16	2552	42	2661	21	93
A10 1 d	0.3	6.9	1.3	14	57	120	1.94	1.1	0.2043	0.5	14.4746	1.2	0.5142	1.1	0.91	2860	16	2674	49	2781	23	94
A10 2 d	0.3	16.3	2.6	47	136	388	2.67	0.9	0.1827	0.5	9.4207	1.0	0.3741	0.9	0.87	2677	17	2049	31	2380	18	77
B6 1 d	-0.1	13.4	2.3	27	111	224	1.89	0.9	0.1915	0.5	13.9857	1.1	0.5298	0.9	0.88	2755	16	2741	41	2749	20	99
B6 2 d	0.1	29.6	5.0	64	246	528	2.00	1.0	0.1893	0.5	13.0755	1.1	0.5011	1.0	0.89	2736	16	2618	42	2685	20	96
C5 1 d	1.7	0.9	0.1	2	7	15	1.92	1.1	0.1902	0.7	13.6766	1.3	0.5216	1.1	0.85	2744	23	2706	49	2728	24	99
C5 2 d	0.6	4.5	0.8	9	37	76	1.89	1.0	0.1921	0.5	13.9750	1.1	0.5277	1.0	0.89	2760	16	2732	44	2748	21	99
C5 3 d	0.2	9.8	1.7	21	82	170	1.93	0.9	0.1913	0.5	13.6570	1.0	0.5180	0.9	0.87	2753	16	2691	39	2726	19	98
D8 1 d	0.9	2.6	0.4	6	22	51	2.14	0.8	0.1916	0.5	12.3522	1.0	0.4678	0.8	0.86	2755	16	2474	35	2632	18	90
D8 2 d	0.2	23.7	3.9	64	197	525	2.47	0.8	0.1845	0.5	10.3063	1.0	0.4054	0.8	0.85	2693	17	2194	30	2463	18	81
D9 1 d	0.9	1.8	0.3	4	15	30	1.81	1.0	0.2024	0.5	15.4213	1.1	0.5529	1.0	0.89	2845	16	2837	44	2842	21	100
D9 2 d	0.1	13.4	2.2	27	111	227	1.89	0.9	0.1901	0.5	13.8961	1.0	0.5304	0.9	0.87	2742	16	2743	40	2743	19	100
D9 3 d	0.1	10.0	1.7	21	83	171	1.90	0.9	0.1868	0.5	13.5196	1.0	0.5251	0.9	0.88	2714	16	2721	40	2717	19	100
D9 4 d	0.1	9.9	1.6	21	82	170	1.92	0.9	0.1867	0.5	13.4234	1.0	0.5218	0.9	0.87	2712	16	2707	38	2710	19	100
B7 1 d	0.0	22.3	3.8	46	185	378	1.90	0.9	0.1905	0.5	13.8358	1.1	0.5271	0.9	0.88	2745	16	2729	41	2739	20	99
B7 2 d	0.2	14.7	2.4	31	122	258	1.96	0.9	0.1885	0.5	13.2777	1.0	0.5110	0.9	0.86	2729	16	2661	37	2700	18	98
GJ1 27	-1.6	3.2	0.2	35	27	286	10.26	0.9	0.0598	0.6	0.8028	1.1	0.0974	0.9	0.84	594	26	599	11	598	10	101
GJ1 28	-0.6	3.2	0.2	34	27	284	10.24	0.9	0.0602	0.6	0.8102	1.1	0.0977	0.9	0.83	609	26	601	10	603	10	99
GJ1 29	0.0	3.2	0.2	35	27	292	11.88	2.6	0.0596	0.6	0.6917	2.7	0.0842	2.6	0.97	589	27	521	26	534	22	88
91500 27	-5.6	1.7	0.1	10	14	83	5.80	0.9	0.0755	0.9	1.7928	1.2	0.1724	0.9	0.71	1080	35	1025	17	1043	16	95
91500 28	0.5	1.7	0.1	10	14	83	5.68	0.9	0.0759	0.9	1.8396	1.2	0.1760	0.9	0.71	1090	34	1045	16	1060	16	96
91500 29	-1.1	1.7	0.1	10	14	82	5.57	0.8	0.0756	0.9	1.8730	1.2	0.1797	0.8	0.69	1085	34	1065	16	1072	16	98
PLES 27	-0.7	3.2	0.2	64	27	525	18.86	0.9	0.0534	0.7	0.3904	1.1	0.0530	0.9	0.78	346	31	333	6	335	6	96
PLES 28	-0.4	3.7	0.2	73	31	602	18.72	0.9	0.0544	0.6	0.4007	1.0	0.0534	0.9	0.83	388	25	335	6	342	6	87
PLES 29	-1.0	3.2	0.1	62	26	510	18.68	0.8	0.0538	0.7	0.3967	1.1	0.0535	0.8	0.78	360	30	336	5	339	6	93
I4 1	0.0	12.7	2.2	26	106	218	1.91	1.1	0.1967	0.5	14.1845	1.2	0.5232	1.1	0.91	2798	16	2713	47	2762	22	97
I4 2	-0.8	8.6	1.5	18	71	148	1.93	0.9	0.1924	0.5	13.7257	1.1	0.5176	0.9	0.88	2762	16	2689	41	2731	20	97
J5 1	0.0	16.1	2.7	33	133	275	1.93	0.9	0.1919	0.5	13.7200	1.1	0.5188	0.9	0.88	2758	16	2694	41	2731	20	98
J5 2	-0.1	13.5	2.2	29	112	238	1.94	1.0	0.1877	0.5	13.3051	1.1	0.5144	1.0	0.89	2721	16	2675	42	2702	20	98
J5 3	-0.1	19.7	3.3	44	164	360	2.03	0.9	0.1874	0.5	12.7119	1.0	0.4921	0.9	0.86	2719	16	2580	36	2659	18	95
J8 1	0.6	2.6	0.5	5	22	42	1.76	1.0	0.2019	0.5	15.8363	1.1	0.5691	1.0	0.89	2841	16	2904	44	2867	20	102
J8 2	0.2	11.8	2.0	24	98	199	1.88	0.9	0.1886	0.5	13.8341	1.0	0.5324	0.9	0.87	2729	16	2751	39	2738	19	101
J8 3	-0.4	5.3	0.9	11	44	87	1.81	0.9	0.1954	0.5	14.9099	1.0	0.5536	0.9	0.88	2788	16	2840	42	2810	20	102
Z4 1	2.8	1.8	0.3	4	15	30	1.88	0.9	0.1915	0.5	14.0434	1.1	0.5322	0.9	0.88	2754	16	2751	42	2753	20	100
Z4 2	0.4	8.9	1.5	18	74	151	1.88	0.9	0.1927	0.5	14.1548	1.0	0.5329	0.9	0.87	2765	16	2754	39	2760	19	100
Z5 1	0.5	3.9	0.7	8	32	64	1.83	0.9	0.1980	0.5	14.9201	1.0	0.5468	0.9	0.88	2809	16	2812	41	2810	19	100
Z5 2	1.0	9.1	1.5	22	76	180	2.18	0.8	0.1863	0.5	11.7677	1.0	0.4583	0.8	0.86	2709	16	2432	34	2586	18	90

Z6 1	0.6	3.9	0.7	8	32	65	1.83	0.8	0.2010	0.5	15.1662	1.0	0.5476	0.8	0.86	2833	16	2815	38	2826	18	99
Z6 2	0.3	17.0	2.9	37	141	306	1.99	0.9	0.1917	0.5	13.3025	1.1	0.5036	0.9	0.88	2756	16	2629	41	2701	20	95
Z6 3	0.2	21.1	3.4	56	175	462	2.42	1.0	0.1831	0.5	10.4094	1.1	0.4125	1.0	0.89	2680	17	2226	36	2472	20	83
G2 1	1.5	2.8	0.5	6	23	46	1.84	1.1	0.2011	0.5	15.0972	1.2	0.5448	1.1	0.91	2834	16	2804	48	2821	22	99
G2 2	1.8	23.4	3.9	88	195	722	3.37	1.3	0.1900	0.5	7.7676	1.4	0.2966	1.3	0.94	2742	16	1675	39	2204	25	61
I1 1	0.1	25.0	4.1	58	208	479	2.11	0.9	0.1868	0.5	12.2173	1.0	0.4745	0.9	0.87	2714	16	2503	37	2621	19	92
I1 2	4.6	31.0	5.4	171	257	1409	4.94	1.2	0.1968	0.5	5.4906	1.3	0.2024	1.2	0.92	2799	16	1188	25	1899	21	42
GJ1 30	0.7	3.3	0.2	38	27	310	10.28	1.1	0.0595	0.6	0.7977	1.3	0.0972	1.1	0.89	586	25	598	13	596	11	102
GJ1 31	0.7	3.4	0.2	38	28	317	10.19	1.0	0.0600	0.6	0.8119	1.2	0.0982	1.0	0.86	603	25	604	12	604	10	100
GJ1 32	1.1	3.4	0.2	38	28	316	10.18	1.1	0.0602	0.6	0.8153	1.2	0.0983	1.1	0.88	610	25	604	12	605	11	99
91500 30	-0.4	1.7	0.1	10	14	86	5.62	0.8	0.0748	0.9	1.8358	1.2	0.1780	0.8	0.69	1063	35	1056	16	1058	16	99
91500 31	0.2	1.7	0.1	10	14	86	5.60	0.9	0.0748	0.9	1.8432	1.2	0.1787	0.9	0.69	1063	36	1060	17	1061	16	100
91500 32	1.1	1.7	0.1	11	14	88	5.59	0.8	0.0744	0.9	1.8321	1.2	0.1788	0.8	0.70	1051	35	1060	17	1057	16	101
PLES 30	-0.4	2.9	0.1	61	24	500	18.58	0.9	0.0530	0.7	0.3934	1.1	0.0538	0.9	0.77	330	33	338	6	337	6	103
PLES 31	0.5	2.9	0.1	59	24	487	18.60	0.9	0.0536	0.7	0.3974	1.2	0.0538	0.9	0.76	355	34	338	6	340	7	95
PLES 32	-0.4	3.0	0.1	61	25	499	18.68	0.9	0.0539	0.7	0.3976	1.1	0.0535	0.9	0.78	366	31	336	6	340	6	92
J8 4	-0.2	4.3	0.8	8	36	69	1.77	0.9	0.2029	0.5	15.8360	1.0	0.5664	0.9	0.87	2849	16	2893	41	2867	19	102
J8 5	-0.1	7.5	1.3	15	62	125	1.85	0.9	0.1944	0.5	14.5116	1.1	0.5418	0.9	0.88	2779	16	2791	43	2784	20	100
Z6 4	0.2	4.0	0.7	8	33	65	1.84	0.9	0.2033	0.5	15.2452	1.0	0.5442	0.9	0.87	2852	16	2801	40	2831	19	98
Z6 5	0.3	22.2	3.6	62	184	514	2.58	0.8	0.1852	0.5	9.8928	1.0	0.3876	0.8	0.86	2699	17	2112	30	2425	18	78
Z5 3	0.9	7.7	1.3	20	64	162	2.33	0.9	0.1961	0.5	11.5910	1.0	0.4289	0.9	0.87	2793	16	2301	34	2572	19	82
Z5 4	0.6	11.4	1.9	27	95	219	2.11	1.2	0.1868	0.5	12.2222	1.3	0.4748	1.2	0.92	2713	16	2505	48	2622	23	92
Z1 1	0.1	5.8	1.0	12	48	95	1.86	1.0	0.1975	0.5	14.6409	1.1	0.5378	1.0	0.89	2805	16	2774	43	2792	20	99
Z1 2	-0.2	18.7	3.1	41	156	342	2.05	0.9	0.1893	0.5	12.7562	1.1	0.4890	0.9	0.88	2735	16	2566	40	2662	20	94
H9 1	2.9	3.0	0.5	6	25	51	1.85	1.0	0.1912	0.5	14.2305	1.1	0.5399	1.0	0.89	2752	16	2783	44	2765	20	101
H9 2	1.0	3.0	0.5	6	25	50	1.86	0.9	0.1902	0.5	14.0990	1.1	0.5378	0.9	0.88	2743	16	2774	42	2756	20	101
H9 3	0.2	9.6	1.6	21	80	170	1.91	1.0	0.1882	0.5	13.5633	1.2	0.5229	1.0	0.90	2726	16	2712	46	2720	22	99
Z7 1	0.7	2.5	0.4	5	21	42	1.84	1.2	0.2020	0.5	15.1535	1.3	0.5443	1.2	0.92	2842	16	2801	54	2825	24	99
Z7 2	4.2	1.8	0.3	4	15	30	1.82	1.1	0.1980	0.5	15.0104	1.2	0.5500	1.1	0.92	2809	16	2825	52	2816	23	101
Z7 3	0.6	3.1	0.6	6	26	53	1.86	1.1	0.2007	0.5	14.8438	1.2	0.5366	1.1	0.92	2831	16	2769	51	2805	23	98
Z7 4	0.1	13.0	2.2	29	108	242	2.01	1.1	0.1896	0.5	13.0292	1.2	0.4986	1.1	0.91	2738	16	2608	46	2682	22	95
Z7 5	0.3	10.3	1.7	24	86	197	2.08	1.1	0.1866	0.5	12.3367	1.2	0.4797	1.1	0.92	2712	16	2526	47	2630	23	93
GJ1 33	0.2	3.1	0.2	35	26	290	10.08	0.9	0.0596	0.6	0.8142	1.1	0.0992	0.9	0.83	587	27	610	11	605	10	104
GJ1 34	0.0	3.1	0.2	35	26	291	10.11	0.9	0.0603	0.6	0.8219	1.1	0.0989	0.9	0.82	614	27	608	10	609	10	99
GJ1 35	0.8	3.1	0.2	35	26	290	10.17	0.9	0.0605	0.6	0.8189	1.1	0.0983	0.9	0.83	619	26	604	10	607	10	98
91500 33	2.5	1.6	0.1	10	14	86	5.68	0.9	0.0750	0.9	1.8205	1.2	0.1761	0.9	0.71	1068	36	1046	17	1053	16	98
91500 34	-0.7	1.7	0.1	11	14	89	5.58	0.9	0.0748	0.9	1.8470	1.2	0.1791	0.9	0.72	1063	34	1062	17	1062	16	100
91500 35	1.2	1.7	0.1	11	14	90	5.61	0.9	0.0748	0.8	1.8394	1.2	0.1784	0.9	0.71	1063	34	1058	17	1060	16	100
PLES 33	0.8	4.1	0.2	87	34	715	18.77	0.9	0.0535	0.6	0.3926	1.0	0.0533	0.9	0.85	348	25	335	6	336	6	96
PLES 34	1.2	2.9	0.1	62	24	510	18.86	0.9	0.0533	0.7	0.3897	1.2	0.0530	0.9	0.79	342	33	333	6	334	7	97
PLES 35	0.5	3.9	0.2	82	33	679	18.56	0.8	0.0534	0.6	0.3965	1.0	0.0539	0.8	0.83	345	25	338	6	339	6	98

[1] $f^{206}c\% = \%\ ^{206}Pb$ that is common, calculated as Stacey-Kramers $^{206}Pb/^{204}Pb$ at $^{207}Pb/^{206}Pb$ age / measured $^{206}Pb/^{204}Pb * 100$

[2] concentration uncertainty c.20%

[3] data not corrected for common-Pb

[4] Concordance calculated as $(^{206}Pb/^{238}U\ age/^{207}Pb/^{206}Pb\ age)*100$

Decay constants of Jaffey et al 1971 used

Ratio data normalised to GJ1, concentrations normalised to 91500

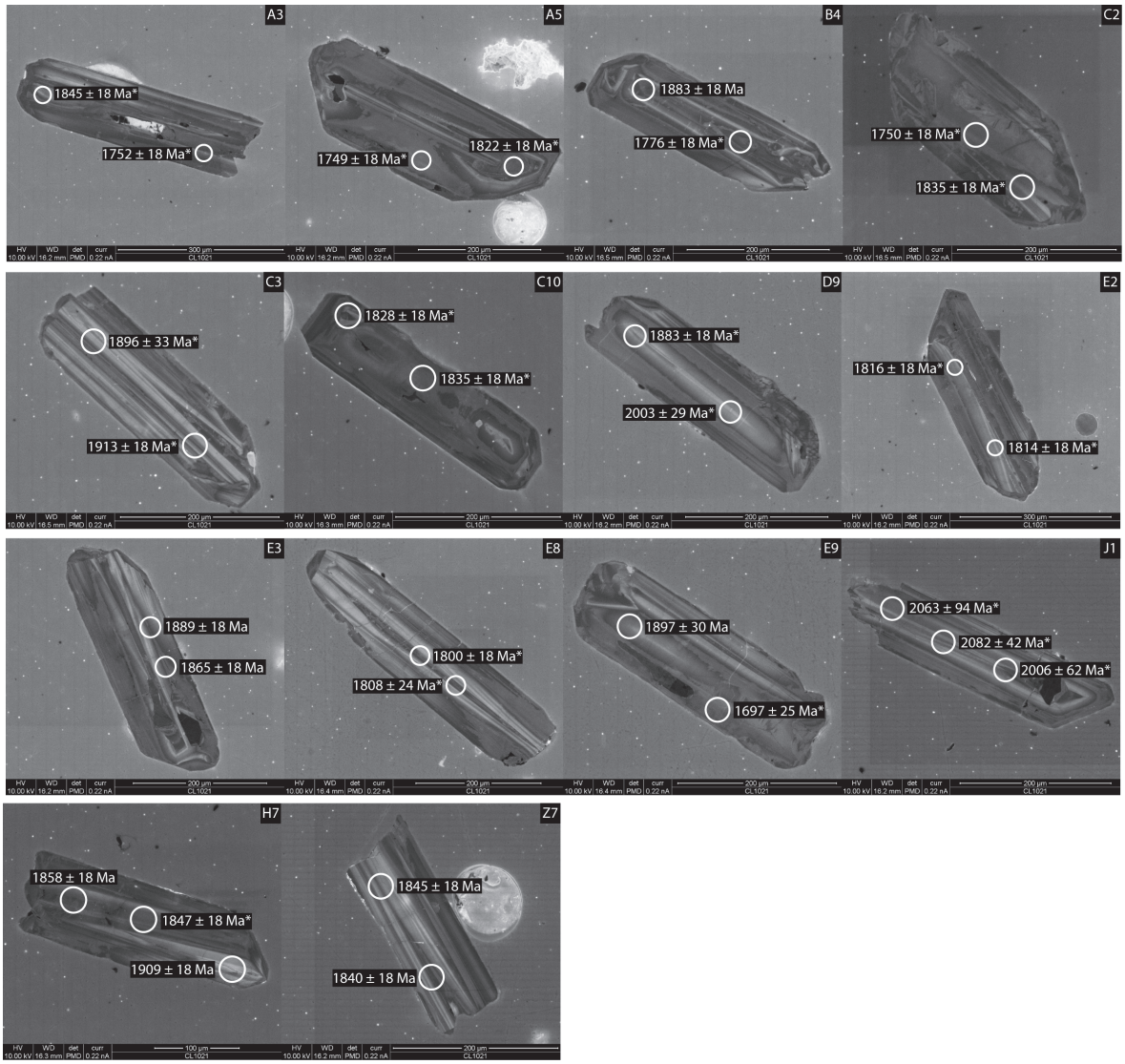
A3
1845 ± 18 Ma*
1752 ± 18 Ma*
A5
1749 ± 18 Ma*
1822 ± 18 Ma*
B4
1883 ± 18 Ma
1776 ± 18 Ma*
C2
1750 ± 18 Ma*
1835 ± 18 Ma*
C3
1896 ± 33 Ma*
1913 ± 18 Ma*
C10
1828 ± 18 Ma*
1835 ± 18 Ma*
D9
1883 ± 18 Ma*
2003 ± 29 Ma*
E2
1816 ± 18 Ma*
1814 ± 18 Ma*
E3
1889 ± 18 Ma
1865 ± 18 Ma
E8
1800 ± 18 Ma*
1808 ± 24 Ma*
E9
1897 ± 30 Ma
1697 ± 25 Ma*
J1
2063 ± 94 Ma*
2082 ± 42 Ma*
2006 ± 62 Ma*
H7
1858 ± 18 Ma
1847 ± 18 Ma*
1909 ± 18 Ma
Z7
1845 ± 18 Ma
1840 ± 18 Ma

LA-MC-ICP-MS U-Pb zircon results for CL1021

	Signals						Data for Tera-Wasserburg plot[3]				Data for Wetherill plot[3]					Ages						
Sample	f206c[1]	^{206}Pb mV	^{207}Pb mV	^{238}U mV	Pb ppm[2]	Uppm[2]	^{238}U/^{206}Pb	1s %	^{207}Pb/^{206}Pb	1s %	^{207}Pb/^{235}U	1s %	^{206}Pb/^{238}U	1s %	Rho	^{207}Pb/^{206}Pb	2s abs	^{206}Pb/^{238}U	2s abs	^{207}Pb/^{235}U	2s abs	Conc.[4]
91500 1	-2.4	1.7	0.1	12	13	71	5.41	1.8	0.0751	0.8	1.8639	2.0	0.1823	1.8	0.90	1045	34	1080	36	1068	26	103
91500 2	-3.9	1.8	0.1	12	14	73	5.43	1.9	0.0755	0.8	1.8647	2.1	0.1815	1.9	0.92	1055	32	1075	38	1069	27	102
91500 3	-0.8	1.7	0.1	12	13	73	5.38	1.7	0.0755	0.8	1.8825	1.9	0.1832	1.7	0.90	1056	34	1084	35	1075	26	103
PLES 1	-1.1	5.0	0.2	118	39	718	18.40	1.8	0.0539	0.5	0.3934	1.8	0.0536	1.8	0.96	340	23	336	12	337	11	99
PLES 2	-1.8	4.4	0.2	103	34	631	18.44	1.8	0.0540	0.5	0.3928	1.9	0.0535	1.8	0.96	341	23	336	12	336	11	98
PLES 3	-2.0	4.2	0.2	101	32	615	18.53	1.8	0.0538	0.5	0.3895	1.8	0.0532	1.8	0.96	333	24	334	12	334	11	100
GJI 1	0.4	4.3	0.2	55	53	565	9.79	0.8	0.0600	0.5	0.8445	1.8	0.1022	1.8	0.85	601	24	627	12	622	11	104
GJ1 2	0.5	4.3	0.2	54	52	554	9.81	0.8	0.0599	0.5	0.8420	1.8	0.1019	1.8	0.86	600	24	626	12	620	11	104
GJ1 3	0.4	4.1	0.2	52	51	536	9.80	0.9	0.0598	0.5	0.8408	1.8	0.1021	1.8	0.87	594	24	627	12	620	11	105
91500 4	-1.2	1.7	0.1	11	13	69	5.38	1.8	0.0749	0.9	1.8656	2.0	0.1831	1.8	0.90	1039	35	1084	36	1069	26	104
91500 5	0.1	1.6	0.1	12	13	70	5.39	1.8	0.0751	0.9	1.8686	2.0	0.1827	1.8	0.90	1046	35	1082	37	1070	27	103
91500 6	2.0	1.8	0.1	12	14	74	5.42	1.9	0.0758	0.8	1.8763	2.0	0.1817	1.9	0.91	1065	34	1076	37	1073	27	101
PLES 4	-1.8	3.6	0.2	86	28	525	18.26	1.7	0.0538	0.6	0.3954	1.8	0.0540	1.7	0.94	335	28	339	11	338	11	101
PLES 5	0.3	4.0	0.2	95	31	578	18.32	1.7	0.0540	0.6	0.3955	1.8	0.0538	1.7	0.95	342	25	338	11	338	10	99
PLES 6	1.5	3.2	0.2	77	25	472	18.23	1.7	0.0539	0.7	0.3967	1.8	0.0541	1.7	0.93	338	30	339	11	339	11	100
GJ1 4	1.3	3.2	0.2	43	25	263	10.13	1.9	0.0608	0.6	0.8045	2.0	0.0972	1.9	0.95	604	26	598	22	599	18	99
GJ1 5	0.1	3.1	0.2	42	24	255	10.18	1.8	0.0609	0.6	0.8023	1.9	0.0968	1.8	0.94	607	27	596	21	598	17	98
GJ1 6	0.3	3.1	0.2	41	24	249	10.10	1.6	0.0607	0.6	0.8071	1.7	0.0976	1.6	0.93	602	26	600	18	601	16	100
GJ1 7	1.4	2.9	0.2	40	23	244	10.20	1.6	0.0603	0.7	0.7934	1.7	0.0966	1.6	0.93	587	28	595	18	593	16	101
GJ1 8	1.8	2.7	0.1	36	21	222	10.09	1.7	0.0607	0.7	0.8074	1.8	0.0977	1.7	0.92	601	31	601	19	601	16	100
GJ1 9	0.8	3.0	0.2	39	23	241	9.93	1.6	0.0609	0.6	0.8227	1.7	0.0992	1.6	0.93	609	27	610	18	610	16	100
A3 1	-0.2	12.3	1.2	81	95	492	4.86	1.7	0.1072	0.5	3.0424	1.7	0.2059	1.7	0.96	1752	18	1207	44	1418	31	69
A3 2	0.0	15.3	1.5	77	119	471	3.76	1.9	0.1129	0.5	4.1349	1.9	0.2658	1.9	0.97	1845	18	1520	57	1661	35	82
A5 3	-0.1	18.3	1.8	93	141	570	3.80	1.6	0.1114	0.5	4.0409	1.6	0.2631	1.6	0.95	1822	18	1506	52	1642	32	83
A5 4	-0.3	19.8	1.9	112	153	683	4.21	2.0	0.1070	0.5	3.5029	2.1	0.2374	2.0	0.97	1749	18	1373	55	1528	35	79
B4 5	-0.5	12.4	1.2	63	96	385	3.76	1.6	0.1087	0.5	3.9868	1.7	0.2662	1.6	0.96	1776	18	1522	54	1632	33	86
B4 6	-0.1	12.8	1.3	54	99	328	3.10	2.0	0.1152	0.5	5.1177	2.1	0.3223	2.0	0.97	1883	18	1801	70	1839	38	96
C2 7	0.1	12.6	1.2	68	98	416	4.09	1.9	0.1071	0.5	3.6044	1.9	0.2442	1.9	0.97	1750	18	1409	54	1551	34	81
C2 8	-0.4	6.4	0.6	29	50	175	3.40	2.5	0.1122	0.5	4.5458	2.5	0.2940	2.5	0.98	1835	18	1661	74	1739	42	91
C3 9	0.3	9.0	0.9	38	70	234	3.13	2.1	0.1161	1.0	5.1181	2.3	0.3199	2.1	0.91	1896	33	1789	70	1839	40	94
C3 10	0.6	5.4	0.6	23	42	142	3.27	0.8	0.1172	0.5	4.9330	1.0	0.3054	0.8	0.85	1913	18	1718	47	1808	27	90
91500 7	-0.5	1.7	0.1	12	13	74	5.44	1.6	0.0737	0.9	1.8186	1.9	0.1813	1.6	0.88	1007	35	1074	33	1052	24	107
91500 8	1.7	1.7	0.1	13	14	78	5.45	1.7	0.0740	0.8	1.8205	1.9	0.1807	1.7	0.89	1016	34	1071	33	1053	24	105
91500 9	-2.5	1.8	0.1	13	14	82	5.38	1.6	0.0741	0.8	1.8466	1.8	0.1831	1.6	0.89	1018	33	1084	32	1062	23	107
PLES 7	0.3	4.3	0.2	104	33	633	18.33	1.7	0.0528	0.5	0.3868	1.8	0.0538	1.7	0.95	293	25	338	11	332	10	115
PLES 8	0.7	4.2	0.2	102	32	623	18.36	1.7	0.0530	0.5	0.3872	1.8	0.0537	1.7	0.96	299	24	337	11	332	10	113
PLES 9	0.9	3.5	0.2	85	27	519	18.33	1.7	0.0528	0.6	0.3865	1.8	0.0538	1.7	0.94	292	29	338	11	332	11	116
GJ1 10	-0.6	2.7	0.1	38	21	234	10.31	1.7	0.0603	0.7	0.7850	1.8	0.0956	1.7	0.93	588	30	588	19	588	17	100
GJ1 11	-0.2	2.8	0.1	39	22	236	10.30	1.7	0.0598	0.7	0.7798	1.9	0.0957	1.7	0.93	571	29	589	20	585	17	103
GJ1 12	-0.3	2.8	0.1	40	22	244	10.38	1.8	0.0599	0.7	0.7742	1.9	0.0949	1.8	0.94	572	29	585	20	582	17	102
E2 11	0.0	15.8	1.6	79	123	483	3.79	2.0	0.1109	0.5	4.0304	2.1	0.2637	2.0	0.97	1814	18	1509	59	1640	36	83
E2 12	0.5	15.1	1.5	73	117	445	3.66	2.1	0.1110	0.5	4.1761	2.1	0.2729	2.1	0.97	1816	18	1555	62	1669	37	86
E3 13	0.4	12.6	1.3	50	98	306	3.03	1.7	0.1157	0.5	5.2672	1.7	0.3304	1.7	0.96	1889	18	1841	64	1864	35	97
E3 14	0.0	14.3	1.5	60	111	365	3.17	1.7	0.1141	0.5	4.9614	1.8	0.3154	1.7	0.96	1865	18	1767	62	1813	34	95
D9 15	0.2	10.7	1.1	45	83	276	3.24	1.5	0.1152	0.5	4.9048	1.6	0.3088	1.5	0.95	1883	18	1735	58	1803	33	92
D9 16	1.5	6.1	0.7	26	47	158	3.14	2.8	0.1232	0.8	5.4011	3.0	0.3181	2.8	0.96	2003	29	1780	87	1885	48	89
E8 17	0.4	9.7	1.0	51	75	310	4.07	2.7	0.1101	0.5	3.7305	2.7	0.2458	2.7	0.98	1800	18	1417	68	1578	43	79

E8 18	-0.2	11.2	1.1	53	87	325	3.58	3.3	0.1105	0.7	4.2504	3.4	0.2790	3.3	0.98	1808	24	1586	88	1684	51	88
E9 19	0.1	9.6	1.0	37	74	224	2.91	2.2	0.1162	0.9	5.5046	2.4	0.3439	2.2	0.93	1897	30	1905	78	1901	42	100
E9 20	0.5	17.6	1.7	113	136	687	4.98	3.1	0.1037	0.7	2.8695	3.2	0.2007	3.1	0.98	1691	25	1179	65	1374	45	70
91500 10	-0.6	1.9	0.1	14	15	83	5.31	1.6	0.0739	0.8	1.8662	1.8	0.1856	1.6	0.91	1012	31	1097	34	1069	24	108
91500 11	0.7	2.0	0.1	14	15	84	5.34	1.6	0.0740	0.8	1.8593	1.8	0.1845	1.6	0.90	1017	30	1091	32	1067	23	107
91500 12	0.7	2.1	0.1	15	16	89	5.35	1.6	0.0742	0.7	1.8595	1.7	0.1841	1.6	0.91	1021	30	1089	32	1067	23	107
PLES 10	0.4	4.6	0.2	112	57	1157	18.56	1.0	0.0548	0.5	0.4068	1.7	0.0539	1.6	0.91	402	30	338	32	347	23	84
PLES 11	0.5	3.6	0.2	88	45	911	18.59	1.0	0.0527	0.6	0.3906	1.7	0.0538	1.6	0.86	315	30	338	32	335	23	107
PLES 12	0.4	3.8	0.2	92	47	955	18.75	0.9	0.0559	0.7	0.4111	1.7	0.0533	1.6	0.80	449	30	335	32	350	23	75
GJ1 13	0.2	2.6	0.1	36	20	222	10.47	1.9	0.0599	0.7	0.7672	2.1	0.0941	1.9	0.93	572	32	580	22	578	18	101
GJ1 14	1.7	2.4	0.1	32	19	198	10.23	1.7	0.0597	0.8	0.7827	1.9	0.0963	1.7	0.91	564	34	593	19	587	17	105
GJ1 15	1.2	2.5	0.1	34	20	208	10.34	1.6	0.0595	0.7	0.7717	1.8	0.0953	1.6	0.91	556	32	587	18	581	16	106
C10 21	0.1	14.3	1.4	68	111	417	3.60	1.1	0.1118	0.5	4.2776	1.2	0.2776	1.1	0.90	1828	18	1579	47	1689	28	86
C10 22	0.1	15.8	1.6	76	122	465	3.63	0.9	0.1122	0.5	4.2594	1.0	0.2753	0.9	0.87	1835	18	1568	45	1686	27	85
J1 23	2.1	12.5	1.4	57	97	349	3.26	3.2	0.1275	2.7	5.3905	4.2	0.3068	3.2	0.76	2063	94	1725	91	1883	67	84
J1 24	1.8	12.2	1.4	52	95	316	3.11	2.3	0.1289	2.0	5.7105	3.0	0.3215	2.3	0.75	2082	69	1797	74	1933	52	86
J1 25	1.1	10.9	1.2	45	84	272	3.07	1.5	0.1234	1.2	5.5356	1.9	0.3254	1.5	0.77	2006	42	1816	59	1906	37	91
Z7 26	-0.3	11.0	1.1	45	85	278	3.11	1.9	0.1128	0.5	5.0075	2.0	0.3220	1.9	0.97	1845	18	1800	68	1821	37	98
Z7 27	-1.0	9.0	0.9	37	69	223	3.04	2.7	0.1126	0.5	5.1015	2.7	0.3289	2.7	0.98	1840	18	1833	85	1836	45	100
H7 28	-0.1	13.8	1.4	57	107	346	2.99	3.6	0.1137	0.5	5.2321	3.7	0.3339	3.6	0.99	1858	18	1857	109	1858	57	100
H7 29	0.2	11.8	1.2	57	92	348	3.43	3.2	0.1130	0.5	4.5392	3.3	0.2915	3.2	0.99	1847	18	1649	89	1738	51	89
H7 30	-0.4	9.2	1.0	37	71	229	3.01	2.1	0.1170	0.5	5.3541	2.1	0.3322	2.1	0.97	1909	18	1849	72	1878	39	97

[1] $f^{206}c\% = \%\ ^{206}Pb$ that is common, calculated as Stacey-Kramers $^{206}Pb/^{204}Pb$ at $^{207}Pb/^{206}Pb$ age / measured $^{206}Pb/^{204}Pb * 100$

[2] concentration uncertainty c.20%

[3] data not corrected for common-Pb

[4] Concordance calculated as $(^{206}Pb/^{238}U\ age/^{207}Pb/^{206}Pb\ age)*100$

Decay constants of Jaffey et al 1971 used

Ratio data normalised to GJ1, concentrations normalised to 91500

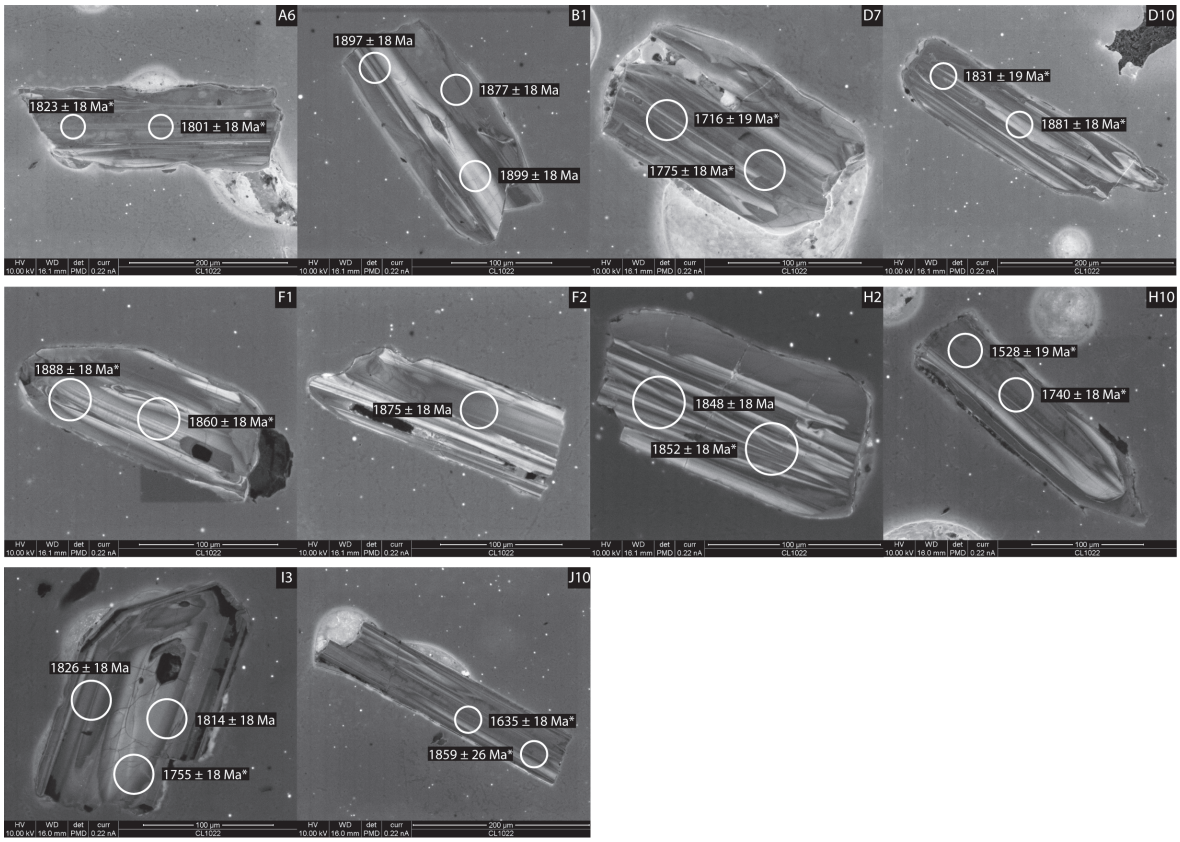
A6
1823 ± 18 Ma*
1801 ± 18 Ma*
B1
1897 ± 18 Ma
1877 ± 18 Ma
1899 ± 18 Ma
D7
1716 ± 19 Ma*
1775 ± 18 Ma*
D10
1831 ± 19 Ma*
1881 ± 18 Ma*
F1
1888 ± 18 Ma*
1860 ± 18 Ma*
F2
1875 ± 18 Ma
H2
1848 ± 18 Ma
1852 ± 18 Ma*
H10
1528 ± 19 Ma*
1740 ± 18 Ma*
I3
1826 ± 18 Ma
1814 ± 18 Ma
1755 ± 18 Ma*
J10
1635 ± 18 Ma*
1859 ± 26 Ma*

LA-MC-ICP-MS U-Pb zircon results for CL1022

	Signals						Data for Tera-Wasserburg plot[3]				Data for Wetherill plot[3]					Ages						
Sample	f206c[1]	^{206}Pb mV	^{207}Pb mV	^{238}U mV	Pb ppm[2]	Uppm[2]	^{238}U/^{206}Pb	1s %	^{207}Pb/^{206}Pb	1s %	^{207}Pb/^{235}U	1s %	^{206}Pb/^{238}U	1s %	Rho	^{207}Pb/^{206}Pb	2s abs	^{206}Pb/^{238}U	2s abs	^{207}Pb/^{235}U	2s abs	Conc.[4]
91500 13	-1.5	2.2	0.1	14	17	86	5.48	0.8	0.0742	0.7	1.8423	1.1	0.1835	0.8	0.75	1009	29	1086	16	1061	14	108
91500 14	-0.6	2.2	0.1	14	17	88	5.48	0.7	0.0751	0.7	1.8625	1.0	0.1834	0.7	0.69	1032	28	1085	13	1068	13	105
91500 15	-1.0	2.4	0.2	16	19	96	5.54	0.9	0.0751	0.6	1.8428	1.1	0.1813	0.9	0.83	1034	26	1074	18	1061	15	104
PLES 13	-1.1	4.9	0.2	109	38	663	18.34	0.9	0.0538	0.5	0.3986	1.0	0.0548	0.9	0.86	318	23	344	6	341	6	108
PLES 14	-1.3	5.0	0.2	109	39	663	18.56	1.0	0.0537	0.5	0.3937	1.2	0.0542	1.0	0.90	317	23	340	7	337	7	107
PLES 15	-2.2	4.5	0.2	98	35	600	18.27	0.9	0.0536	0.5	0.3985	1.0	0.0550	0.9	0.86	309	23	345	6	341	6	112
GJ1 16	-0.8	3.9	0.2	47	31	288	10.19	1.1	0.0606	0.5	0.8091	1.2	0.0987	1.1	0.90	585	22	607	12	602	11	104
GJ1 17	-2.6	3.8	0.2	47	29	286	10.27	1.3	0.0607	0.5	0.8034	1.4	0.0979	1.3	0.93	586	22	602	15	599	13	103
GJ1 18	-1.5	3.9	0.2	48	31	291	10.26	1.3	0.0605	0.5	0.8018	1.4	0.0980	1.3	0.93	579	22	603	15	598	13	104
A6 31	-0.4	18.9	1.9	90	147	549	3.89	1.9	0.1115	0.5	3.9534	2.0	0.2573	1.9	0.97	1823	18	1476	43	1625	28	81
A6 32	0.3	17.3	1.7	81	134	494	3.80	1.6	0.1101	0.5	3.9957	1.7	0.2632	1.6	0.95	1801	18	1506	37	1633	24	84
D7 33	0.2	14.5	1.3	78	112	474	4.38	3.5	0.1051	0.5	3.3075	3.5	0.2282	3.5	0.99	1716	19	1325	69	1483	45	77
D7 34	0.2	16.3	1.6	77	126	469	3.82	2.2	0.1086	0.5	3.9170	2.2	0.2617	2.2	0.97	1775	18	1499	50	1617	31	84
D10 35	0.5	19.8	2.0	88	153	539	3.69	2.3	0.1120	0.5	4.1831	2.4	0.2710	2.3	0.97	1831	19	1546	54	1671	33	84
D10 36	0.7	13.2	1.4	52	102	317	3.16	2.2	0.1151	0.5	5.0266	2.2	0.3168	2.2	0.97	1881	18	1774	57	1824	32	94
H10 37	0.0	26.2	2.2	204	203	1247	6.31	1.2	0.0951	0.5	2.0771	1.3	0.1585	1.2	0.92	1528	19	949	18	1141	16	62
H10 38	0.1	16.6	1.6	93	128	570	4.43	2.7	0.1065	0.5	3.3108	2.7	0.2256	2.7	0.98	1740	18	1311	53	1484	36	75
J10 39	0.4	21.3	1.9	152	165	926	5.61	2.1	0.1006	0.5	2.4737	2.2	0.1783	2.1	0.97	1635	18	1058	35	1264	27	65
J10 40	1.1	15.9	1.6	79	123	483	3.79	3.2	0.1137	0.8	4.1292	3.3	0.2635	3.2	0.97	1859	26	1508	72	1660	45	81
91500 16	2.2	2.0	0.1	14	15	85	5.58	1.2	0.0743	0.8	1.8093	1.5	0.1801	1.2	0.84	1010	32	1068	24	1049	19	106
91500 17	0.7	2.0	0.1	14	16	87	5.58	1.4	0.0746	0.8	1.8166	1.6	0.1801	1.4	0.88	1019	30	1067	27	1051	21	105
91500 18	1.0	2.2	0.1	15	17	94	5.56	1.0	0.0749	0.7	1.8305	1.2	0.1808	1.0	0.82	1026	28	1071	20	1056	16	104
PLES 16	0.3	4.0	0.2	91	31	557	18.01	1.1	0.0536	0.6	0.4042	1.3	0.0558	1.1	0.89	309	26	350	8	345	7	113
PLES 17	0.8	3.4	0.2	78	26	476	18.09	1.0	0.0533	0.7	0.4008	1.2	0.0556	1.0	0.84	299	30	349	7	342	7	117
PLES 18	-0.2	3.3	0.2	75	25	460	18.09	1.0	0.0533	0.6	0.4009	1.2	0.0556	1.0	0.83	300	29	349	6	342	7	116
GJ1 19	0.6	3.4	0.2	43	26	262	10.05	0.9	0.0603	0.6	0.8163	1.1	0.1000	0.9	0.84	575	25	614	11	606	10	107
GJ1 20	1.7	3.2	0.2	42	25	258	10.05	0.8	0.0604	0.6	0.8169	1.0	0.1001	0.8	0.80	575	26	615	9	606	9	107
GJ1 21	0.9	3.2	0.2	41	25	253	10.13	1.1	0.0603	0.6	0.8095	1.2	0.0992	1.1	0.87	573	26	610	12	602	11	106
B1 41	-0.4	10.4	1.1	41	81	251	3.03	1.1	0.1162	0.5	5.2870	1.2	0.3302	1.1	0.91	1897	18	1839	31	1867	19	97
B1 42	-0.5	9.3	1.0	35	72	215	2.91	1.3	0.1163	0.5	5.5124	1.4	0.3439	1.3	0.93	1899	18	1906	38	1903	21	100
B1 43	-0.6	19.6	2.0	75	152	457	2.96	1.1	0.1149	0.5	5.3478	1.2	0.3378	1.1	0.91	1877	18	1876	31	1877	18	100
F1 44	-0.5	14.4	1.5	58	112	353	3.08	1.3	0.1154	0.5	5.1722	1.4	0.3252	1.3	0.93	1886	18	1815	35	1848	20	96
F1 45	-0.2	14.8	1.5	60	115	366	3.11	1.0	0.1156	0.5	5.1194	1.1	0.3214	1.0	0.89	1888	18	1796	28	1839	17	95
F2 46	-0.9	11.1	1.1	41	86	250	2.85	1.1	0.1148	0.5	5.5479	1.2	0.3508	1.1	0.90	1875	18	1938	31	1908	18	103
H2 47	-0.9	10.9	1.1	44	84	268	3.06	1.5	0.1130	0.5	5.0912	1.6	0.3268	1.5	0.95	1848	18	1823	41	1835	24	99
H2 48	0.1	12.1	1.2	50	94	308	3.15	2.1	0.1133	0.5	4.9543	2.2	0.3173	2.1	0.97	1852	18	1776	56	1812	32	96
I3 49	-0.9	13.7	1.3	72	106	438	4.25	3.2	0.1074	0.5	3.4844	3.2	0.2354	3.2	0.99	1755	18	1363	66	1524	42	78
I3 50	-0.6	11.0	1.1	45	85	273	3.15	1.3	0.1109	0.5	4.8532	1.4	0.3175	1.3	0.93	1814	18	1777	34	1794	20	98
I3 51	-0.5	18.3	1.8	76	142	465	3.10	2.4	0.1117	0.5	4.9589	2.4	0.3222	2.4	0.98	1826	18	1800	63	1812	35	99
91500 19	-2.5	2.0	0.1	14	15	88	5.57	1.1	0.0738	0.8	1.8014	1.3	0.1805	1.1	0.81	997	32	1070	21	1046	17	107
91500 20	1.2	2.0	0.1	15	16	90	5.50	1.1	0.0742	0.7	1.8345	1.4	0.1828	1.1	0.84	1008	30	1082	22	1058	18	107
91500 21	-3.7	2.1	0.1	15	16	91	5.48	0.9	0.0750	0.7	1.8622	1.2	0.1835	0.9	0.78	1031	30	1086	18	1068	16	105
PLES 19	-1.3	3.2	0.1	75	25	458	18.01	0.9	0.0532	0.7	0.4016	1.1	0.0558	0.9	0.81	293	30	350	6	343	7	119
PLES 20	-0.4	3.4	0.2	80	26	487	18.07	0.9	0.0538	0.6	0.4051	1.1	0.0556	0.9	0.82	321	29	349	6	345	7	109
PLES 21	-1.0	3.6	0.2	87	28	533	18.45	0.9	0.0534	0.6	0.3933	1.1	0.0545	0.9	0.81	301	28	342	6	337	6	113
GJ1 22	-2.5	3.0	0.2	39	23	240	10.13	1.1	0.0603	0.6	0.8086	1.3	0.0992	1.1	0.87	572	28	610	13	602	12	107
GJ1 23	-2.0	3.0	0.2	40	23	246	10.23	1.2	0.0598	0.6	0.7954	1.4	0.0983	1.2	0.89	556	27	604	14	594	12	109
GJ1 24	-0.5	3.0	0.2	39	23	240	10.25	1.1	0.0598	0.6	0.7932	1.3	0.0980	1.1	0.86	555	28	603	12	593	11	109

[1] f^{206}c% = % ^{206}Pb that is common, calculated as Stacey-Kramers ^{206}Pb/^{204}Pb at ^{207}Pb/^{206}Pb age / measured ^{206}Pb/^{204}Pb * 100

[2] concentration uncertainty c.20%

[3] data not corrected for common-Pb

[4] Concordance calculated as (^{206}Pb/^{238}U age/^{207}Pb/^{206}Pb age)*100

Decay constants of Jaffey et al 1971 used

Ratio data normalised to GJ1, concentrations normalised to 91500

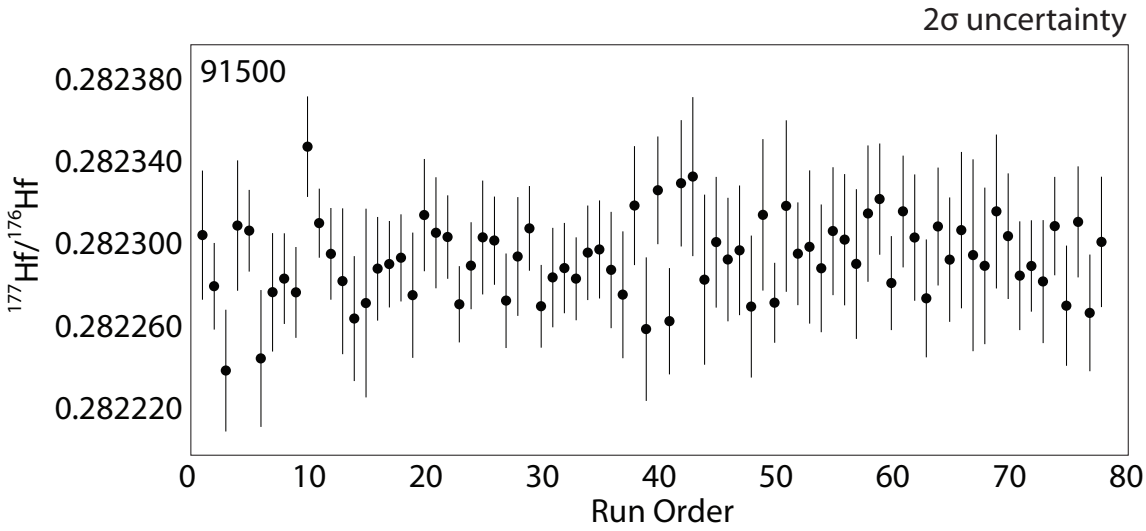
2σ uncertainty
91500
0.282380
0.282340
0.282300
0.282260
0.282220
$^{177}Hf/^{176}Hf$
0
10
20
30
40
50
60
70
80
Run Order

LA-MC-ICP-MS Lu-Hf zircon results for CL098, CL109, CL1020

		Measured Ratios									
Spot/grain	Sample	$^{176}Hf/^{177}Hf$	2σ	$^{178}Hf/^{177}Hf$	2σ	$^{179}Hf/^{177}Hf$	2σ	$^{180}Hf/^{177}Hf$	2σ	$^{176}Yb/^{177}Hf$	2σ
JMC475	Standard	0.280417	0.000008	1.476205	0.000032	0.741523	0.000016	1.921642	0.000038	-0.000002	0.000003
JMC475	Standard	0.280439	0.000009	1.476076	0.000029	0.741382	0.000017	1.921019	0.000038	0.000008	0.000003
JMC475	Standard	0.280452	0.000010	1.476024	0.000022	0.741319	0.000015	1.920859	0.000036	0.000001	0.000003
JMC475	Standard	0.280465	0.000008	1.475953	0.000026	0.741239	0.000019	1.920547	0.000035	0.000002	0.000003
JMC475	Standard	0.280484	0.000007	1.475819	0.000030	0.741092	0.000023	1.919977	0.000065	-0.000002	0.000002
JMC475	Standard	0.280522	0.000010	1.475723	0.000028	0.740995	0.000024	1.919550	0.000068	0.095598	0.000017
JMC475	Standard	0.280507	0.000011	1.475792	0.000030	0.741086	0.000017	1.919890	0.000036	0.095590	0.000014
JMC475	Standard	0.280540	0.000011	1.475555	0.000035	0.740839	0.000023	1.918866	0.000091	0.202219	0.000100
JMC475	Standard	0.280459	0.000013	1.475893	0.000028	0.741220	0.000018	1.920345	0.000053	0.203518	0.000050
JMC475	Standard	0.280393	0.000013	1.476173	0.000029	0.741491	0.000018	1.921531	0.000056	0.205022	0.000070
91500	Standard	0.280859	0.000030	1.474779	0.000084	0.740005	0.000043	1.915801	0.000069	0.008500	0.000035
91500	Standard	0.280826	0.000022	1.474785	0.000061	0.740035	0.000031	1.915897	0.000109	0.008487	0.000014
91500	Standard	0.280800	0.000020	1.474691	0.000080	0.739979	0.000046	1.915528	0.000125	0.008448	0.000016
91500	Standard	0.280872	0.000021	1.474718	0.000061	0.739888	0.000037	1.915313	0.000108	0.008405	0.000013
91500	Standard	0.280879	0.000018	1.474686	0.000061	0.739947	0.000024	1.915299	0.000071	0.008417	0.000013
91500	Standard	0.280879	0.000034	1.474435	0.000100	0.739654	0.000088	1.914322	0.000231	0.008404	0.000017
91500	Standard	0.280870	0.000036	1.474411	0.000084	0.739683	0.000049	1.914445	0.000114	0.008368	0.000016
91500	Standard	0.280812	0.000017	1.474812	0.000051	0.740141	0.000053	1.916014	0.000138	0.008451	0.000017
91500	Standard	0.280791	0.000023	1.474953	0.000111	0.740207	0.000031	1.916523	0.000152	0.008606	0.000041
91500	Standard	0.280795	0.000022	1.475357	0.000067	0.740507	0.000029	1.917684	0.000105	0.008629	0.000021
91500	Standard	0.280619	0.000016	1.475989	0.000092	0.741224	0.000060	1.920405	0.000147	0.008637	0.000028
91500	Standard	0.280592	0.000019	1.476054	0.000089	0.741353	0.000046	1.920862	0.000122	0.008736	0.000053
91500	Standard	0.280576	0.000028	1.476037	0.000098	0.741368	0.000054	1.920978	0.000132	0.008812	0.000031
91500	Standard	0.280546	0.000023	1.476221	0.000088	0.741429	0.000067	1.921187	0.000133	0.008900	0.000070
91500	Standard	0.280557	0.000038	1.476159	0.000072	0.741413	0.000044	1.921378	0.000121	0.008981	0.000068
91500	Standard	0.280548	0.000024	1.476402	0.000076	0.741589	0.000041	1.922033	0.000125	0.009206	0.000031
91500	Standard	0.280538	0.000021	1.476304	0.000061	0.741580	0.000044	1.921841	0.000101	0.009293	0.000025
91500	Standard	0.280536	0.000020	1.476266	0.000073	0.741565	0.000044	1.921709	0.000102	0.009157	0.000021
91500	Standard	0.280530	0.000024	1.476201	0.000074	0.741495	0.000036	1.921576	0.000094	0.009152	0.000036
91500	Standard	0.280590	0.000024	1.476236	0.000080	0.741468	0.000034	1.921389	0.000088	0.008950	0.000027
91500	Standard	0.280617	0.000024	1.475965	0.000084	0.741276	0.000040	1.920589	0.000096	0.008876	0.000027
91500	Standard	0.280638	0.000019	1.475897	0.000066	0.741133	0.000032	1.920150	0.000079	0.008792	0.000025
91500	Standard	0.280630	0.000015	1.475758	0.000069	0.741036	0.000044	1.919741	0.000088	0.008717	0.000010
91500	Standard	0.280671	0.000018	1.475652	0.000052	0.740966	0.000026	1.919357	0.000076	0.008729	0.000021
91500	Standard	0.280684	0.000026	1.475652	0.000080	0.740903	0.000044	1.919043	0.000128	0.008767	0.000014
A4-2	CL109	0.279415	0.000013	1.475787	0.000069	0.741105	0.000035	1.919893	0.000122	0.007184	0.000106
B4-2	CL109	0.279386	0.000012	1.475843	0.000036	0.741143	0.000028	1.920102	0.000115	0.007283	0.000078
C5-2	CL109	0.279388	0.000016	1.475796	0.000051	0.741073	0.000023	1.920027	0.000075	0.004363	0.000060
C5-3	CL109	0.279364	0.000010	1.475919	0.000034	0.741275	0.000024	1.920709	0.000056	0.003166	0.000016
E1-1	CL109	0.279399	0.000014	1.475959	0.000057	0.741233	0.000023	1.920464	0.000061	0.010047	0.000469

E1-2	CL109	0.279374	0.000010	1.475842	0.000041	0.741157	0.000027	1.920276	0.000057	0.003114	0.000070		
E9-1	CL109	0.279453	0.000021	1.475780	0.000050	0.741008	0.000030	1.919746	0.000090	0.012930	0.000167		
E9-2	CL109	0.279459	0.000018	1.475634	0.000061	0.740933	0.000036	1.919399	0.000081	0.010353	0.000111		
91500	Standard	0.280693	0.000022	1.475562	0.000071	0.740827	0.000028	1.918977	0.000069	0.008637	0.000020		
91500	Standard	0.280677	0.000021	1.475558	0.000070	0.740785	0.000033	1.918786	0.000063	0.008554	0.000013		
91500	Standard	0.280719	0.000026	1.475416	0.000073	0.740700	0.000032	1.918391	0.000076	0.008637	0.000013		
91500	Standard	0.280745	0.000019	1.475330	0.000061	0.740621	0.000030	1.918085	0.000119	0.008643	0.000016		
91500	Standard	0.280736	0.000019	1.475243	0.000060	0.740516	0.000026	1.917720	0.000106	0.008558	0.000015		
F2-1	CL109	0.279576	0.000012	1.475164	0.000054	0.740393	0.000034	1.917182	0.000102	0.016585	0.000506		
F2-2	CL109	0.279528	0.000011	1.475103	0.000044	0.740402	0.000021	1.917249	0.000086	0.006601	0.000058		
H1-1	CL109	0.279488	0.000020	1.474985	0.000069	0.740181	0.000053	1.916151	0.000139	0.002624	0.000440		
H3-1	CL109	0.279599	0.000015	1.475000	0.000049	0.740240	0.000027	1.916590	0.000073	0.010218	0.000294		
H3-2	CL109	0.279512	0.000013	1.475242	0.000042	0.740476	0.000030	1.917542	0.000114	0.004602	0.000322		
I1-2	CL109	0.279510	0.000016	1.475268	0.000038	0.740557	0.000023	1.917807	0.000075	0.008190	0.000082		
J2-2	CL109	0.279506	0.000014	1.475437	0.000050	0.740754	0.000028	1.918553	0.000079	0.015630	0.000759		
91500	Standard	0.280641	0.000026	1.475903	0.000055	0.741123	0.000036	1.920160	0.000077	0.008574	0.000010		
91500	Standard	0.280601	0.000020	1.476007	0.000064	0.741261	0.000031	1.920635	0.000087	0.008624	0.000020		
91500	Standard	0.280583	0.000017	1.476066	0.000066	0.741355	0.000029	1.920974	0.000078	0.008709	0.000014		
91500	Standard	0.280583	0.000019	1.476170	0.000075	0.741435	0.000031	1.921232	0.000080	0.008737	0.000019		
91500	Standard	0.280563	0.000017	1.476250	0.000065	0.741529	0.000038	1.921551	0.000088	0.008651	0.000019		
JMC475	Standard	0.280571	0.000007	1.475374	0.000022	0.740653	0.000011	1.918291	0.000028	-0.000003	0.000002		
JMC475	Standard	0.280579	0.000009	1.475363	0.000021	0.740642	0.000014	1.918191	0.000026	0.000004	0.000002		
JMC475	Standard	0.280585	0.000007	1.475324	0.000015	0.740619	0.000009	1.918146	0.000020	0.000000	0.000001		
JMC475	Standard	0.280583	0.000009	1.475322	0.000026	0.740620	0.000012	1.918113	0.000032	0.000000	0.000002		
JMC475	Standard	0.280591	0.000006	1.475317	0.000020	0.740614	0.000012	1.918099	0.000021	0.000002	0.000002		
Plesovice	Standard	0.280968	0.000016	1.475131	0.000052	0.740414	0.000023	1.917368	0.000063	0.013187	0.000173		
Plesovice	Standard	0.280966	0.000015	1.475186	0.000037	0.740398	0.000027	1.917351	0.000059	0.009607	0.000153		
Plesovice	Standard	0.280952	0.000009	1.475145	0.000045	0.740393	0.000034	1.917367	0.000076	0.010036	0.000208		
Plesovice	Standard	0.280951	0.000022	1.475111	0.000080	0.740402	0.000030	1.917067	0.000125	0.008633	0.000051		
Plesovice	Standard	0.280934	0.000016	1.474993	0.000050	0.740338	0.000032	1.916936	0.000083	0.009327	0.000028		
JMC475	Standard	0.280576	0.000012	1.475585	0.000028	0.740900	0.000012	1.919140	0.000034	0.240576	0.000108		
91500	Standard	0.280733	0.000024	1.475197	0.000075	0.740489	0.000053	1.917609	0.000098	0.011642	0.000037		
91500	Standard	0.280732	0.000031	1.475231	0.000093	0.740550	0.000038	1.917714	0.000101	0.011615	0.000038		
91500	Standard	0.280764	0.000025	1.475330	0.000090	0.740552	0.000055	1.917730	0.000100	0.011552	0.000037		
91500	Standard	0.280723	0.000031	1.475275	0.000074	0.740553	0.000040	1.917727	0.000106	0.011473	0.000031		
G2-1	CL1020	0.279481	0.000018	1.475201	0.000058	0.740386	0.000039	1.917484	0.000079	0.021400	0.001609		
H9-1	CL1020	0.279486	0.000015	1.475214	0.000074	0.740520	0.000044	1.917874	0.000172	0.005098	0.000130		
H9-2	CL1020	0.279489	0.000025	1.475168	0.000059	0.740488	0.000049	1.917574	0.000134	0.002261	0.000022		
H9-3	CL1020	0.279493	0.000018	1.475213	0.000047	0.740495	0.000041	1.917691	0.000163	0.009012	0.000207		
I4-1	CL1020	0.279502	0.000023	1.475214	0.000073	0.740434	0.000028	1.917372	0.000101	0.010950	0.000201		
I4-2	CL1020	0.279512	0.000021	1.475329	0.000067	0.740523	0.000025	1.917774	0.000089	0.005808	0.000042		
J8-1	CL1020	0.279476	0.000022	1.475190	0.000074	0.740502	0.000059	1.917870	0.000181	0.023924	0.000514		
J8-2	CL1020	0.279551	0.000025	1.474893	0.000094	0.740223	0.000074	1.916754	0.000278	0.011029	0.000411		
J8-3	CL1020	0.279467	0.000025	1.475305	0.000057	0.740566	0.000042	1.917915	0.000131	0.005612	0.000330		

J8-4	CL1020	0.279497	0.000019	1.475251	0.000079	0.740618	0.000051	1.918130	0.000153	0.026496	0.000758		
J8-5	CL1020	0.279473	0.000018	1.475267	0.000090	0.740587	0.000049	1.918090	0.000171	0.005549	0.000142		
91500	Standard	0.280778	0.000026	1.475218	0.000083	0.740502	0.000054	1.917640	0.000148	0.012105	0.000170		
91500	Standard	0.280726	0.000026	1.475252	0.000072	0.740464	0.000052	1.917736	0.000134	0.011671	0.000063		
91500	Standard	0.280764	0.000025	1.475301	0.000105	0.740588	0.000051	1.917976	0.000175	0.011905	0.000030		
91500	Standard	0.280774	0.000032	1.475389	0.000078	0.740592	0.000055	1.917857	0.000164	0.011992	0.000031		
91500	Standard	0.280739	0.000040	1.475158	0.000100	0.740529	0.000048	1.917578	0.000156	0.011961	0.000025		
Z1-1	CL1020	0.279570	0.000025	1.475139	0.000089	0.740470	0.000037	1.917517	0.000180	0.037175	0.000385		
Z4-1	CL1020	0.279506	0.000033	1.475188	0.000081	0.740445	0.000050	1.917478	0.000159	0.004655	0.000095		
Z5-1	CL1020	0.279532	0.000023	1.475249	0.000079	0.740572	0.000041	1.917953	0.000135	0.023927	0.000363		
Z6-1	CL1020	0.279550	0.000017	1.475094	0.000084	0.740439	0.000048	1.917500	0.000166	0.032431	0.002464		
Z6-2	CL1020	0.279518	0.000019	1.475117	0.000096	0.740520	0.000047	1.917692	0.000161	0.009812	0.000383		
Z6-4	CL1020	0.279520	0.000023	1.475159	0.000090	0.740471	0.000043	1.917581	0.000125	0.028751	0.001814		
Z7-1	CL1020	0.279488	0.000029	1.475124	0.000079	0.740420	0.000053	1.917410	0.000140	0.015824	0.000197		
Z7-2	CL1020	0.279510	0.000026	1.475189	0.000066	0.740497	0.000023	1.917664	0.000077	0.020341	0.001652		
Z7-3	CL1020	0.279487	0.000021	1.475257	0.000073	0.740493	0.000036	1.917604	0.000095	0.017890	0.000332		
Z7-4	CL1020	0.279519	0.000016	1.475242	0.000063	0.740502	0.000028	1.917812	0.000088	0.006706	0.000105		
91500	Standard	0.280741	0.000029	1.475292	0.000098	0.740635	0.000053	1.917939	0.000079	0.011532	0.000062		
91500	Standard	0.280727	0.000029	1.475416	0.000078	0.740660	0.000049	1.918068	0.000103	0.011538	0.000027		
91500	Standard	0.280744	0.000024	1.475239	0.000082	0.740592	0.000054	1.918013	0.000121	0.011544	0.000044		
91500	Standard	0.280721	0.000033	1.475230	0.000080	0.740556	0.000055	1.917897	0.000153	0.011518	0.000047		
91500	Standard	0.280746	0.000027	1.475286	0.000093	0.740586	0.000052	1.917895	0.000146	0.011584	0.000048		
A8-1	CL1020	0.279511	0.000026	1.475225	0.000078	0.740509	0.000038	1.917782	0.000151	0.017525	0.000168		
B6-1	CL1020	0.279515	0.000022	1.475184	0.000076	0.740490	0.000032	1.917650	0.000117	0.002080	0.000080		
B6-2	CL1020	0.279549	0.000026	1.475205	0.000074	0.740396	0.000037	1.917427	0.000078	0.022882	0.000733		
B7-1	CL1020	0.279536	0.000031	1.475302	0.000096	0.740538	0.000048	1.917764	0.000173	0.020749	0.000265		
B7-2	CL1020	0.279522	0.000018	1.475193	0.000058	0.740491	0.000036	1.917649	0.000105	0.011034	0.000062		
C5-1	CL1020	0.279499	0.000025	1.475120	0.000067	0.740444	0.000040	1.917349	0.000101	0.002381	0.000027		
C5-2	CL1020	0.279514	0.000021	1.475201	0.000079	0.740518	0.000044	1.917700	0.000108	0.011071	0.000118		
D9-2	CL1020	0.279524	0.000017	1.475284	0.000094	0.740568	0.000044	1.917915	0.000085	0.009388	0.000268		
G2-1	CL1020	0.279482	0.000021	1.475173	0.000070	0.740447	0.000030	1.917599	0.000091	0.022499	0.000887		
A8-1	CL1020	0.279470	0.000026	1.475269	0.000080	0.740540	0.000040	1.917916	0.000165	0.009805	0.000137		
91500	Standard	0.280729	0.000018	1.475288	0.000071	0.740573	0.000035	1.917955	0.000090	0.011794	0.000137		
91500	Standard	0.280756	0.000037	1.475308	0.000067	0.740627	0.000054	1.918234	0.000140	0.011570	0.000026		
91500	Standard	0.280729	0.000026	1.475276	0.000094	0.740570	0.000038	1.917987	0.000114	0.011528	0.000053		
91500	Standard	0.280743	0.000033	1.475299	0.000093	0.740555	0.000041	1.918046	0.000134	0.011513	0.000042		
91500	Standard	0.280741	0.000032	1.475267	0.000076	0.740568	0.000047	1.917965	0.000131	0.011429	0.000042		
JMC475	Standard	0.280714	0.000007	1.474586	0.000022	0.739883	0.000016	1.915220	0.000048	0.000005	0.000002		
JMC475	Standard	0.280753	0.000006	1.474426	0.000016	0.739704	0.000012	1.914586	0.000036	0.000003	0.000002		
JMC475	Standard	0.280777	0.000008	1.474334	0.000025	0.739599	0.000014	1.914226	0.000034	0.000003	0.000002		
JMC475	Standard	0.280788	0.000008	1.474263	0.000023	0.739524	0.000014	1.913905	0.000036	-0.000002	0.000002		
JMC475	Standard	0.280791	0.000008	1.474215	0.000024	0.739499	0.000014	1.913756	0.000036	-0.000001	0.000002		
91500	Standard	0.281125	0.000028	1.473390	0.000100	0.738628	0.000055	1.910291	0.000125	0.011034	0.000038		
91500	Standard	0.281115	0.000030	1.473327	0.000078	0.738657	0.000065	1.910450	0.000117	0.011050	0.000032		

91500	Standard	0.281106	0.000030	1.473400	0.000116	0.738688	0.000050	1.910592	0.000094	0.010897	0.000054		
91500	Standard	0.281120	0.000029	1.473494	0.000092	0.738663	0.000057	1.910403	0.000115	0.011074	0.000032		
91500	Standard	0.281150	0.000023	1.473387	0.000077	0.738593	0.000042	1.910331	0.000128	0.011013	0.000026		
Z2-1	CL098	0.279950	0.000023	1.473448	0.000066	0.738744	0.000047	1.910698	0.000122	0.034436	0.001028		
Z4-1	CL098	0.279855	0.000015	1.473536	0.000053	0.738831	0.000034	1.911223	0.000107	0.021457	0.000131		
Z5-1	CL098	0.279883	0.000017	1.473481	0.000080	0.738764	0.000026	1.910895	0.000072	0.038142	0.001386		
Z5-2	CL098	0.279873	0.000018	1.473524	0.000080	0.738748	0.000030	1.910885	0.000068	0.016208	0.000390		
Z7-1	CL098	0.279902	0.000020	1.473423	0.000071	0.738675	0.000036	1.910642	0.000101	0.032363	0.001080		
Z7-2	CL098	0.279863	0.000021	1.473441	0.000060	0.738687	0.000034	1.910729	0.000085	0.017221	0.000247		
Z7-3	CL098	0.279874	0.000015	1.473471	0.000066	0.738707	0.000020	1.910727	0.000074	0.018992	0.000194		
Z8-1	CL098	0.279872	0.000018	1.473451	0.000057	0.738761	0.000030	1.910848	0.000070	0.025542	0.001969		
Z11-1	CL098	0.279925	0.000016	1.473385	0.000068	0.738691	0.000051	1.910681	0.000065	0.049055	0.001299		
Z16-1	CL098	0.279926	0.000026	1.473542	0.000055	0.738766	0.000032	1.910995	0.000075	0.044973	0.000985		
Z16-2	CL098	0.279856	0.000021	1.473640	0.000064	0.738798	0.000035	1.911060	0.000096	0.020725	0.000026		
Z16-3	CL098	0.279864	0.000019	1.473506	0.000077	0.738812	0.000019	1.911022	0.000085	0.017609	0.000357		
91500	Standard	0.281071	0.000021	1.473545	0.000081	0.738754	0.000043	1.910969	0.000088	0.011216	0.000026		
91500	Standard	0.281120	0.000024	1.473553	0.000067	0.738745	0.000033	1.910899	0.000103	0.011244	0.000035		
91500	Standard	0.281108	0.000033	1.473605	0.000072	0.738758	0.000036	1.910908	0.000097	0.011145	0.000028		
91500	Standard	0.281083	0.000027	1.473437	0.000080	0.738718	0.000037	1.910792	0.000081	0.011182	0.000015		
91500	Standard	0.281094	0.000027	1.473609	0.000071	0.738816	0.000035	1.911068	0.000087	0.011468	0.000048		
Z15-1	CL098	0.279855	0.000026	1.473538	0.000069	0.738758	0.000037	1.910854	0.000093	0.030407	0.000990		
Z17-1	CL098	0.279855	0.000018	1.473616	0.000065	0.738877	0.000029	1.911355	0.000063	0.031203	0.000470		
Z18-1	CL098	0.279862	0.000019	1.473600	0.000074	0.738841	0.000047	1.911206	0.000114	0.018596	0.000441		
Z18-2	CL098	0.279855	0.000021	1.473619	0.000079	0.738971	0.000042	1.911786	0.000145	0.021537	0.001015		
Z19-1	CL098	0.279830	0.000020	1.473586	0.000047	0.738878	0.000037	1.911333	0.000085	0.019705	0.000514		
Z21-1	CL098	0.279895	0.000024	1.473569	0.000059	0.738841	0.000033	1.911161	0.000115	0.038919	0.001788		
Z21-2	CL098	0.279880	0.000016	1.473560	0.000080	0.738828	0.000040	1.911135	0.000123	0.019970	0.000269		
91500	Standard	0.281104	0.000027	1.473411	0.000072	0.738685	0.000041	1.910547	0.000109	0.011028	0.000036		
91500	Standard	0.281088	0.000034	1.473504	0.000081	0.738774	0.000035	1.910707	0.000095	0.010997	0.000045		
91500	Standard	0.281111	0.000036	1.473477	0.000094	0.738754	0.000049	1.910808	0.000134	0.010936	0.000019		
91500	Standard	0.281091	0.000036	1.473544	0.000082	0.738757	0.000047	1.910853	0.000095	0.010973	0.000020		
91500	Standard	0.281107	0.000031	1.473541	0.000073	0.738884	0.000038	1.911118	0.000127	0.010882	0.000018		
91500	Standard	0.281084	0.000029	1.473479	0.000088	0.738830	0.000044	1.911071	0.000150	0.010432	0.000101		
91500	Standard	0.281064	0.000017	1.473688	0.000096	0.738856	0.000042	1.911411	0.000136	0.010478	0.000064		
91500	Standard	0.281070	0.000018	1.473526	0.000062	0.738809	0.000039	1.911102	0.000089	0.010544	0.000051		
91500	Standard	0.281053	0.000025	1.473592	0.000085	0.738903	0.000028	1.911300	0.000100	0.010568	0.000084		
A8-1	CL1020	0.279796	0.000014	1.473638	0.000066	0.738874	0.000034	1.911374	0.000122	0.005364	0.000153		
G2-1	CL1020	0.279832	0.000019	1.473559	0.000055	0.738784	0.000025	1.910884	0.000085	0.019880	0.000085		
I4-1	CL1020	0.279803	0.000023	1.473525	0.000069	0.738766	0.000029	1.910880	0.000094	0.010178	0.000206		
J8-1	CL1020	0.279804	0.000020	1.473615	0.000054	0.738857	0.000042	1.911468	0.000117	0.013209	0.000773		
Z1-1	CL1020	0.279805	0.000019	1.473421	0.000049	0.738745	0.000035	1.910829	0.000089	0.010936	0.000608		
Z1-1	CL1020	0.279879	0.000021	1.473425	0.000070	0.738685	0.000047	1.910684	0.000141	0.028956	0.000271		
Z4-1	CL1020	0.279828	0.000019	1.473437	0.000059	0.738767	0.000037	1.910965	0.000102	0.003676	0.000027		
Z5-1	CL1020	0.279852	0.000024	1.473553	0.000079	0.738824	0.000037	1.911134	0.000153	0.017139	0.000484		

Z6-1	CL1020	0.279866	0.000027	1.473363	0.000063	0.738684	0.000049	1.910670	0.000120	0.032989	0.005933	
Z7-1	CL1020	0.279852	0.000029	1.473550	0.000073	0.738786	0.000041	1.911192	0.000158	0.037425	0.002889	
Z7-1	CL1020	0.279799	0.000021	1.473534	0.000081	0.738844	0.000039	1.911376	0.000115	0.041935	0.007881	
91500	Standard	0.281095	0.000023	1.473517	0.000055	0.738798	0.000039	1.911070	0.000106	0.010462	0.000063	
91500	Standard	0.281053	0.000026	1.473553	0.000059	0.738835	0.000035	1.911125	0.000124	0.010491	0.000043	
91500	Standard	0.281088	0.000023	1.473531	0.000080	0.738866	0.000036	1.911267	0.000105	0.010388	0.000038	
91500	Standard	0.281047	0.000026	1.473561	0.000060	0.738808	0.000034	1.911051	0.000095	0.010616	0.000053	
Spot/grain	Sample	0.281067	0.000030	1.473675	0.000078	0.738866	0.000043	1.911209	0.000104	0.010551	0.000044	

[1] $^{176}Hf/^{177}Hf_{initial}$ values were calculated using the ^{176}Lu decay constant of Söderlund et al. (2004) and the calculated $^{206}Pb/^{207}Pb$ age

[2] εHf was caculated by normalizing caculated $^{176}Hf/^{177}Hf_{initial}$ to the $^{176}Hf/^{177}Hf$ value of the present day bulk earth ($^{176}Hf/^{177}Hf = 0.28295$)

[3] two-stage model age, using measured $^{176}Lu/^{177}Hf$ to calculate the initial $^{176}Hf/^{177}Hf$ ratio of the zircon at the time of growth ($^{207}Pb/^{206}Pb$ age), and an average crustal $^{176}Lu/^{177}Hf$ ratio of 0.012 (Vervoort et al., 1999) to project back to the time of intersection with depleted mantle (with $^{176}Lu/^{177}Hf = 0.0384$, $^{176}Hf/^{177}Hf = 0.28325$: Chauvel and Blichert-Toft 2001)

Spot/grain	Sample	Age	Corrected Ratios								Calculated Values		
		$^{207}Pb/^{206}Pb$ age (Ma)	$^{176}Lu/^{177}Hf$	2σ	$^{176}Hf/^{177}Hf$	2σ	$^{178}Hf/^{177}Hf$	2σ	$^{180}Hf/^{177}Hf$	2σ	$^{176}Hf/^{177}Hf_{initial}$ [1]	εHf[2]	Model Age (Ma)[3]
JMC475	Standard	-	0.000000	0.000000	0.282159	0.000009	1.467175	0.000026	1.886747	0.000054	-	-	-
JMC475	Standard	-	0.000000	0.000000	0.282147	0.000010	1.467215	0.000023	1.886712	0.000045	-	-	-
JMC475	Standard	-	0.000000	0.000000	0.282150	0.000010	1.467190	0.000019	1.886750	0.000054	-	-	-
JMC475	Standard	-	0.000000	0.000000	0.282151	0.000010	1.467210	0.000029	1.886811	0.000056	-	-	-
JMC475	Standard	-	0.000000	0.000000	0.282141	0.000008	1.467222	0.000018	1.886821	0.000052	-	-	-
JMC475	Standard	-	0.000003	0.000000	0.282160	0.000011	1.467192	0.000022	1.886775	0.000051	-	-	-
JMC475	Standard	-	0.000003	0.000000	0.282164	0.000011	1.467210	0.000020	1.886730	0.000055	-	-	-
JMC475	Standard	-	0.000006	0.000000	0.282145	0.000011	1.467208	0.000022	1.886676	0.000042	-	-	-
JMC475	Standard	-	0.000006	0.000000	0.282133	0.000013	1.467182	0.000021	1.886696	0.000046	-	-	-
JMC475	Standard	-	0.000006	0.000000	0.282130	0.000013	1.467184	0.000025	1.886763	0.000047	-	-	-
91500	Standard	-	0.000313	0.000000	0.282307	0.000031	1.467247	0.000058	1.886840	0.000119	-	-	-
91500	Standard	-	0.000313	0.000000	0.282282	0.000021	1.467242	0.000054	1.886927	0.000101	-	-	-
91500	Standard	-	0.000312	0.000001	0.282241	0.000030	1.467237	0.000038	1.886673	0.000123	-	-	-
91500	Standard	-	0.000312	0.000000	0.282312	0.000032	1.467294	0.000060	1.886674	0.000138	-	-	-
91500	Standard	-	0.000313	0.000000	0.282309	0.000020	1.467257	0.000086	1.886579	0.000088	-	-	-
91500	Standard	-	0.000313	0.000000	0.282247	0.000033	1.467271	0.000033	1.886700	0.000204	-	-	-
91500	Standard	-	0.000312	0.000000	0.282279	0.000029	1.467190	0.000084	1.886616	0.000121	-	-	-
91500	Standard	-	0.000311	0.000001	0.282286	0.000022	1.467173	0.000073	1.886516	0.000143	-	-	-
91500	Standard	-	0.000310	0.000001	0.282279	0.000022	1.467259	0.000111	1.886665	0.000157	-	-	-
91500	Standard	-	0.000312	0.000001	0.282350	0.000024	1.467341	0.000059	1.886635	0.000123	-	-	-
91500	Standard	-	0.000311	0.000001	0.282313	0.000017	1.467304	0.000044	1.886700	0.000176	-	-	-
91500	Standard	-	0.000312	0.000001	0.282298	0.000022	1.467223	0.000081	1.886702	0.000116	-	-	-
91500	Standard	-	0.000313	0.000000	0.282285	0.000035	1.467164	0.000085	1.886714	0.000177	-	-	-
91500	Standard	-	0.000310	0.000001	0.282267	0.000030	1.467275	0.000057	1.886688	0.000177	-	-	-
91500	Standard	-	0.000307	0.000000	0.282274	0.000046	1.467275	0.000061	1.886888	0.000177	-	-	-
91500	Standard	-	0.000315	0.000000	0.282291	0.000025	1.467244	0.000069	1.886816	0.000117	-	-	-
91500	Standard	-	0.000317	0.000000	0.282293	0.000021	1.467228	0.000058	1.886809	0.000132	-	-	-
91500	Standard	-	0.000315	0.000000	0.282296	0.000021	1.467218	0.000060	1.886708	0.000139	-	-	-
91500	Standard	-	0.000315	0.000000	0.282278	0.000030	1.467215	0.000072	1.886793	0.000092	-	-	-
91500	Standard	-	0.000313	0.000001	0.282317	0.000027	1.467279	0.000060	1.886800	0.000133	-	-	-
91500	Standard	-	0.000315	0.000000	0.282308	0.000027	1.467185	0.000070	1.886663	0.000119	-	-	-
91500	Standard	-	0.000317	0.000000	0.282306	0.000020	1.467244	0.000067	1.886736	0.000126	-	-	-
91500	Standard	-	0.000318	0.000000	0.282274	0.000019	1.467198	0.000053	1.886701	0.000139	-	-	-
91500	Standard	-	0.000317	0.000000	0.282292	0.000021	1.467199	0.000059	1.886662	0.000120	-	-	-
91500	Standard	-	0.000318	0.000000	0.282306	0.000028	1.467263	0.000062	1.886615	0.000151	-	-	-
A4-2	CL109	2736	0.000256	0.000002	0.281062	0.000013	1.467225	0.000048	1.886675	0.000087	0.281049	0.6	3103
B4-2	CL109	2748	0.000267	0.000002	0.281046	0.000014	1.467190	0.000032	1.886734	0.000090	0.281032	0.2	3130
C5-2	CL109	2735	0.000159	0.000002	0.281041	0.000016	1.467200	0.000044	1.886883	0.000069	0.281032	-0.2	3137
C5-3	CL109	2747	0.000111	0.000001	0.281049	0.000012	1.467159	0.000027	1.886782	0.000068	0.281043	0.6	3109
E1-1	CL109	2744	0.000354	0.000016	0.281075	0.000016	1.467234	0.000048	1.886753	0.000110	0.281057	1.0	3084

E1-2	CL109	2754	0.000130	0.000003	0.281039	0.000011	1.467199	0.000042	1.886801	0.000089	0.281032	0.4	3127					
E9-1	CL109	2763	0.000494	0.000007	0.281090	0.000021	1.467241	0.000046	1.886785	0.000073	0.281064	1.8	3060					
E9-2	CL109	2765	0.000404	0.000002	0.281079	0.000018	1.467198	0.000040	1.886738	0.000100	0.281058	1.6	3071					
91500	Standard	-	0.000311	0.000000	0.282305	0.000021	1.467198	0.000053	1.886705	0.000125	-	-	-					
91500	Standard	-	0.000310	0.000001	0.282275	0.000023	1.467259	0.000067	1.886686	0.000143	-	-	-					
91500	Standard	-	0.000314	0.000000	0.282297	0.000029	1.467209	0.000056	1.886783	0.000133	-	-	-					
91500	Standard	-	0.000315	0.000000	0.282311	0.000021	1.467226	0.000043	1.886691	0.000089	-	-	-					
91500	Standard	-	0.000314	0.000000	0.282273	0.000020	1.467226	0.000049	1.886676	0.000087	-	-	-					
F2-1	CL109	2699	0.000603	0.000023	0.281086	0.000012	1.467246	0.000054	1.886675	0.000083	0.281055	-0.1	3107					
F2-2	CL109	2762	0.000254	0.000001	0.281052	0.000013	1.467175	0.000044	1.886774	0.000082	0.281038	0.8	3111					
H1-1	CL109	2758	0.000093	0.000009	0.280959	0.000020	1.467340	0.000066	1.886641	0.000144	0.280955	-2.8	3282					
H3-1	CL109	2774	0.000361	0.000011	0.281086	0.000017	1.467222	0.000049	1.886683	0.000099	0.281067	2.1	3050					
H3-2	CL109	2706	0.000185	0.000012	0.281041	0.000013	1.467245	0.000039	1.886793	0.000068	0.281031	-0.8	3151					
I1-2	CL109	2748	0.000330	0.000002	0.281056	0.000017	1.467226	0.000031	1.886707	0.000064	0.281039	0.5	3116					
J2-2	CL109	2783	0.000543	0.000018	0.281083	0.000016	1.467221	0.000037	1.886672	0.000088	0.281054	1.8	3072					
91500	Standard	-	0.000309	0.000001	0.282287	0.000024	1.467280	0.000053	1.886799	0.000134	-	-	-					
91500	Standard	-	0.000311	0.000000	0.282291	0.000022	1.467222	0.000049	1.886748	0.000101	-	-	-					
91500	Standard	-	0.000310	0.000000	0.282286	0.000020	1.467191	0.000058	1.886733	0.000085	-	-	-					
91500	Standard	-	0.000312	0.000000	0.282299	0.000023	1.467236	0.000059	1.886741	0.000099	-	-	-					
91500	Standard	-	0.000309	0.000001	0.282300	0.000024	1.467253	0.000058	1.886679	0.000114	-	-	-					
JMC475	Standard	-	0.000000	0.000000	0.282143	0.000008	1.467200	0.000023	1.886774	0.000043	-	-	-					
JMC475	Standard	-	0.000000	0.000000	0.282148	0.000010	1.467216	0.000021	1.886749	0.000041	-	-	-					
JMC475	Standard	-	0.000000	0.000000	0.282149	0.000008	1.467189	0.000015	1.886782	0.000030	-	-	-					
JMC475	Standard	-	0.000000	0.000000	0.282154	0.000011	1.467207	0.000022	1.886718	0.000032	-	-	-					
JMC475	Standard	-	0.000000	0.000000	0.282155	0.000007	1.467183	0.000015	1.886729	0.000045	-	-	-					
Plesovice	Standard	-	0.000247	0.000002	0.282501	0.000017	1.467168	0.000046	1.886772	0.000085	-	-	-					
Plesovice	Standard	-	0.000180	0.000002	0.282490	0.000017	1.467273	0.000036	1.886828	0.000075	-	-	-					
Plesovice	Standard	-	0.000185	0.000003	0.282476	0.000012	1.467229	0.000047	1.886948	0.000104	-	-	-					
Plesovice	Standard	-	0.000159	0.000000	0.282473	0.000022	1.467236	0.000088	1.886715	0.000123	-	-	-					
Plesovice	Standard	-	0.000166	0.000000	0.282447	0.000018	1.467146	0.000045	1.886594	0.000100	-	-	-					
JMC475	Standard	-	0.000006	0.000000	0.282192	0.000011	1.467200	0.000022	1.886732	0.000037	-	-	-					
91500	Standard	-	0.000320	0.000001	0.282290	0.000028	1.467191	0.000076	1.886706	0.000152	-	-	-					
91500	Standard	-	0.000320	0.000001	0.282278	0.000031	1.467172	0.000088	1.886549	0.000142	-	-	-					
91500	Standard	-	0.000319	0.000001	0.282322	0.000029	1.467269	0.000072	1.886659	0.000213	-	-	-					
91500	Standard	-	0.000320	0.000001	0.282262	0.000035	1.467221	0.000067	1.886756	0.000121	-	-	-					
G2-1	CL1020	2834	0.000611	0.000048	0.280997	0.000020	1.467289	0.000046	1.887057	0.000102	0.280964	-0.2	3221					
H9-1	CL1020	2752	0.000128	0.000003	0.281035	0.000017	1.467209	0.000062	1.886665	0.000134	0.281028	0.2	3135					
H9-2	CL1020	2743	0.000059	0.000000	0.281019	0.000028	1.467208	0.000064	1.886853	0.000161	0.281016	-0.5	3163					
H9-3	CL1020	2726	0.000238	0.000005	0.281038	0.000019	1.467201	0.000066	1.886788	0.000117	0.281025	-0.8	3158					
I4-1	CL1020	2798	0.000263	0.000005	0.281037	0.000023	1.467251	0.000059	1.886693	0.000119	0.281023	1.1	3124					
I4-2	CL1020	2762	0.000194	0.000002	0.281052	0.000022	1.467307	0.000058	1.886781	0.000114	0.281041	0.9	3105					
J8-1	CL1020	2841	0.000696	0.000016	0.281021	0.000024	1.467173	0.000052	1.886881	0.000170	0.280983	0.6	3181					
J8-2	CL1020	2729	0.000313	0.000007	0.281020	0.000027	1.467163	0.000070	1.886926	0.000136	0.281004	-1.2	3193					
J8-3	CL1020	2788	0.000189	0.000010	0.281018	0.000026	1.467193	0.000040	1.886825	0.000099	0.281008	0.3	3159					

J8-4	CL1020	2849	0.000810	0.000017	0.281057	0.000022	1.467123	0.000068	1.886823	0.000109	0.281013	1.9	3121					
J8-5	CL1020	2841	0.000185	0.000003	0.281027	0.000023	1.467171	0.000062	1.886776	0.000127	0.281017	1.9	3116					
91500	Standard	-	0.000313	0.000001	0.282329	0.000026	1.467179	0.000059	1.886694	0.000164	-	-	-					
91500	Standard	-	0.000312	0.000001	0.282265	0.000026	1.467277	0.000059	1.886873	0.000174	-	-	-					
91500	Standard	-	0.000314	0.000001	0.282333	0.000031	1.467230	0.000075	1.886711	0.000105	-	-	-					
91500	Standard	-	0.000314	0.000001	0.282336	0.000039	1.467240	0.000069	1.886676	0.000148	-	-	-					
91500	Standard	-	0.000312	0.000001	0.282286	0.000041	1.467155	0.000078	1.886608	0.000161	-	-	-					
Z1-1	CL1020	2805	0.000991	0.000007	0.281094	0.000026	1.467192	0.000088	1.886785	0.000135	0.281040	1.9	3088					
Z4-1	CL1020	2754	0.000125	0.000003	0.281033	0.000036	1.467179	0.000062	1.886723	0.000115	0.281026	0.2	3137					
Z5-1	CL1020	2809	0.000684	0.000007	0.281079	0.000029	1.467184	0.000057	1.886778	0.000131	0.281042	2.0	3083					
Z6-1	CL1020	2833	0.000906	0.000063	0.281090	0.000025	1.467198	0.000073	1.886831	0.000131	0.281041	2.5	3073					
Z6-2	CL1020	2756	0.000310	0.000008	0.281054	0.000020	1.467138	0.000074	1.886936	0.000118	0.281038	0.6	3116					
Z6-4	CL1020	2852	0.000799	0.000048	0.281072	0.000027	1.467141	0.000058	1.886701	0.000110	0.281028	2.5	3090					
Z7-1	CL1020	2842	0.000422	0.000004	0.281028	0.000029	1.467170	0.000047	1.886852	0.000118	0.281005	1.4	3139					
Z7-2	CL1020	2809	0.000534	0.000037	0.281060	0.000029	1.467164	0.000057	1.886679	0.000134	0.281032	1.6	3103					
Z7-3	CL1020	2831	0.000474	0.000007	0.281016	0.000021	1.467265	0.000057	1.886752	0.000112	0.280990	0.7	3172					
Z7-4	CL1020	2738	0.000195	0.000003	0.281064	0.000019	1.467219	0.000057	1.886806	0.000081	0.281054	0.8	3091					
91500	Standard	-	0.000317	0.000001	0.282304	0.000032	1.467171	0.000084	1.886619	0.000152	-	-	-					
91500	Standard	-	0.000317	0.000001	0.282295	0.000030	1.467226	0.000076	1.886647	0.000156	-	-	-					
91500	Standard	-	0.000318	0.000001	0.282300	0.000032	1.467170	0.000080	1.886765	0.000123	-	-	-					
91500	Standard	-	0.000317	0.000001	0.282273	0.000035	1.467227	0.000090	1.886819	0.000166	-	-	-					
91500	Standard	-	0.000314	0.000001	0.282317	0.000037	1.467187	0.000066	1.886782	0.000119	-	-	-					
A8-1	CL1020	2826	0.000488	0.000007	0.281062	0.000027	1.467170	0.000057	1.886816	0.000135	0.281036	2.2	3087					
B6-1	CL1020	2755	0.000049	0.000002	0.281037	0.000027	1.467177	0.000069	1.886784	0.000116	0.281035	0.5	3122					
B6-2	CL1020	2736	0.000676	0.000015	0.281068	0.000031	1.467273	0.000061	1.886993	0.000136	0.281033	0.0	3134					
B7-1	CL1020	2745	0.000607	0.000003	0.281076	0.000035	1.467264	0.000066	1.886762	0.000149	0.281044	0.6	3108					
B7-2	CL1020	2729	0.000321	0.000002	0.281045	0.000019	1.467216	0.000055	1.886937	0.000126	0.281029	-0.4	3145					
C5-1	CL1020	2744	0.000058	0.000001	0.281022	0.000025	1.467178	0.000051	1.886779	0.000169	0.281019	-0.3	3156					
C5-2	CL1020	2760	0.000285	0.000004	0.281052	0.000023	1.467189	0.000083	1.886786	0.000133	0.281037	0.7	3115					
D9-2	CL1020	2742	0.000300	0.000010	0.281078	0.000018	1.467216	0.000072	1.886622	0.000123	0.281062	1.2	3074					
G2-1	CL1020	2834	0.000630	0.000028	0.281016	0.000023	1.467208	0.000070	1.886830	0.000093	0.280981	0.4	3187					
A8-1	CL1020	2826	0.000291	0.000004	0.281009	0.000025	1.467195	0.000095	1.886809	0.000136	0.280993	0.6	3170					
91500	Standard	-	0.000314	0.000001	0.282274	0.000019	1.467202	0.000065	1.886665	0.000123	-	-	-					
91500	Standard	-	0.000315	0.000001	0.282321	0.000042	1.467197	0.000060	1.886891	0.000136	-	-	-					
91500	Standard	-	0.000316	0.000001	0.282298	0.000025	1.467208	0.000075	1.886798	0.000144	-	-	-					
91500	Standard	-	0.000312	0.000001	0.282302	0.000037	1.467208	0.000076	1.886911	0.000121	-	-	-					
91500	Standard	-	0.000315	0.000001	0.282291	0.000031	1.467196	0.000064	1.886759	0.000150	-	-	-					
JMC475	Standard	-	0.000000	0.000000	0.282139	0.000008	1.467216	0.000019	1.886704	0.000045	-	-	-					
JMC475	Standard	-	0.000000	0.000000	0.282141	0.000007	1.467228	0.000017	1.886759	0.000045	-	-	-					
JMC475	Standard	-	0.000000	0.000000	0.282149	0.000010	1.467214	0.000017	1.886787	0.000038	-	-	-					
JMC475	Standard	-	0.000000	0.000000	0.282145	0.000009	1.467220	0.000019	1.886737	0.000045	-	-	-					
JMC475	Standard	-	0.000000	0.000000	0.282142	0.000010	1.467203	0.000015	1.886721	0.000045	-	-	-					
91500	Standard	-	0.000316	0.000001	0.282309	0.000031	1.467277	0.000093	1.886572	0.000154	-	-	-					
91500	Standard	-	0.000315	0.000001	0.282305	0.000032	1.467175	0.000058	1.886723	0.000224	-	-	-					

91500	Standard	-	0.000312	0.000001	0.282293	0.000036	1.467166	0.000087	1.886655	0.000151	-	-	-					
91500	Standard	-	0.000322	0.000001	0.282318	0.000033	1.467308	0.000070	1.886647	0.000151	-	-	-					
91500	Standard	-	0.000321	0.000001	0.282325	0.000027	1.467224	0.000063	1.886677	0.000105	-	-	-					
Z2-1	CL098	2714	0.000892	0.000024	0.281155	0.000024	1.467233	0.000052	1.886693	0.000120	0.281108	2.2	2998					
Z4-1	CL098	2732	0.000586	0.000005	0.281078	0.000015	1.467181	0.000057	1.886784	0.000122	0.281048	0.4	3107					
Z5-1	CL098	2726	0.001038	0.000035	0.281086	0.000020	1.467218	0.000072	1.886708	0.000112	0.281032	-0.3	3139					
Z5-2	CL098	2714	0.000446	0.000013	0.281075	0.000020	1.467269	0.000058	1.886736	0.000099	0.281052	0.2	3106					
Z7-1	CL098	2737	0.000875	0.000021	0.281100	0.000024	1.467239	0.000063	1.886694	0.000128	0.281054	0.7	3093					
Z7-2	CL098	2733	0.000476	0.000005	0.281055	0.000025	1.467245	0.000058	1.886891	0.000087	0.281031	-0.2	3139					
Z7-3	CL098	2738	0.000534	0.000006	0.281060	0.000016	1.467251	0.000059	1.886788	0.000113	0.281032	0.0	3133					
Z8-1	CL098	2665	0.000712	0.000049	0.281086	0.000023	1.467171	0.000058	1.886801	0.000108	0.281050	-1.0	3132					
Z11-1	CL098	2732	0.001337	0.000030	0.281114	0.000017	1.467188	0.000061	1.886767	0.000187	0.281044	0.3	3114					
Z16-1	CL098	2731	0.001206	0.000024	0.281134	0.000028	1.467238	0.000051	1.886761	0.000110	0.281071	1.2	3062					
Z16-2	CL098	2718	0.000580	0.000002	0.281068	0.000024	1.467302	0.000058	1.886695	0.000101	0.281038	-0.3	3133					
Z16-3	CL098	2701	0.000494	0.000008	0.281076	0.000020	1.467222	0.000073	1.886689	0.000101	0.281050	-0.2	3116					
91500	Standard	-	0.000315	0.000001	0.282284	0.000023	1.467249	0.000071	1.886682	0.000159	-	-	-					
91500	Standard	-	0.000319	0.000001	0.282319	0.000027	1.467270	0.000061	1.886680	0.000144	-	-	-					
91500	Standard	-	0.000319	0.000001	0.282306	0.000031	1.467333	0.000074	1.886806	0.000124	-	-	-					
91500	Standard	-	0.000316	0.000001	0.282277	0.000029	1.467201	0.000078	1.886717	0.000150	-	-	-					
91500	Standard	-	0.000317	0.000001	0.282312	0.000029	1.467340	0.000052	1.886635	0.000154	-	-	-					
Z15-1	CL098	2734	0.000901	0.000024	0.281053	0.000027	1.467211	0.000079	1.886773	0.000128	0.281006	-1.0	3185					
Z17-1	CL098	2752	0.000921	0.000009	0.281080	0.000021	1.467242	0.000058	1.886738	0.000097	0.281031	0.3	3129					
Z18-1	CL098	2732	0.000571	0.000012	0.281077	0.000021	1.467204	0.000060	1.886749	0.000138	0.281047	0.4	3108					
Z18-2	CL098	2721	0.000644	0.000031	0.281108	0.000024	1.467195	0.000073	1.886741	0.000118	0.281074	1.1	3060					
Z19-1	CL098	2749	0.000599	0.000015	0.281047	0.000020	1.467224	0.000059	1.886732	0.000136	0.281016	-1.1	3176					
Z21-1	CL098	2724	0.001114	0.000050	0.281117	0.000025	1.467276	0.000072	1.886682	0.000103	0.281059	0.6	3090					
Z21-2	CL098	2730	0.000603	0.000005	0.281100	0.000016	1.467185	0.000068	1.886811	0.000127	0.281068	1.1	3068					
91500	Standard	-	0.000318	0.000001	0.282295	0.000030	1.467261	0.000048	1.886788	0.000150	-	-	-					
91500	Standard	-	0.000310	0.000001	0.282310	0.000038	1.467234	0.000075	1.886601	0.000121	-	-	-					
91500	Standard	-	0.000311	0.000001	0.282298	0.000047	1.467253	0.000080	1.886601	0.000132	-	-	-					
91500	Standard	-	0.000313	0.000001	0.282292	0.000038	1.467265	0.000060	1.886678	0.000166	-	-	-					
91500	Standard	-	0.000313	0.000001	0.282319	0.000037	1.467176	0.000085	1.886530	0.000135	-	-	-					
91500	Standard	-	0.000314	0.000001	0.282307	0.000031	1.467213	0.000078	1.886597	0.000130	-	-	-					
91500	Standard	-	0.000318	0.000001	0.282288	0.000026	1.467252	0.000067	1.886816	0.000157	-	-	-					
91500	Standard	-	0.000319	0.000001	0.282292	0.000022	1.467203	0.000054	1.886769	0.000127	-	-	-					
91500	Standard	-	0.000314	0.000001	0.282285	0.000030	1.467189	0.000066	1.886586	0.000082	-	-	-					
A8-1	CL1020	2826	0.000180	0.000003	0.281028	0.000017	1.467262	0.000057	1.886679	0.000079	0.281018	1.5	3121					
G2-1	CL1020	2834	0.000653	0.000003	0.281033	0.000020	1.467257	0.000043	1.886600	0.000102	0.280997	1.0	3158					
I4-1	CL1020	2798	0.000263	0.000004	0.281006	0.000025	1.467244	0.000054	1.886765	0.000105	0.280992	0.0	3183					
J8-1	CL1020	2841	0.000444	0.000024	0.281038	0.000020	1.467213	0.000047	1.886924	0.000117	0.281013	1.7	3123					
Z1-1	CL1020	2805	0.000346	0.000020	0.281000	0.000025	1.467165	0.000062	1.886707	0.000088	0.280981	-0.2	3201					
Z1-1	CL1020	2805	0.000913	0.000009	0.281066	0.000028	1.467234	0.000061	1.886858	0.000127	0.281017	1.0	3133					
Z4-1	CL1020	2754	0.000107	0.000002	0.281030	0.000022	1.467189	0.000060	1.886766	0.000107	0.281024	0.1	3142					
Z5-1	CL1020	2809	0.000525	0.000013	0.281071	0.000026	1.467207	0.000072	1.886760	0.000108	0.281043	2.0	3082					

Spot/grain	Sample														
Z6-1	CL1020	2833	0.000935	0.000146	0.281055	0.000030	1.467184	0.000082	1.886863	0.000154	0.281005	1.2	3144		
Z7-1	CL1020	2842	0.001053	0.000069	0.281063	0.000029	1.467257	0.000068	1.886786	0.000114	0.281006	1.5	3138		
Z7-1	CL1020	2842	0.000999	0.000188	0.281035	0.000020	1.467111	0.000055	1.886818	0.000095	0.280981	0.6	3186		
91500	Standard	-	0.000316	0.000001	0.282312	0.000024	1.467229	0.000053	1.886739	0.000126	-	-	-		
91500	Standard	-	0.000316	0.000001	0.282273	0.000029	1.467193	0.000058	1.886768	0.000122	-	-	-		
91500	Standard	-	0.000313	0.000001	0.282314	0.000027	1.467220	0.000084	1.886817	0.000122	-	-	-		
91500	Standard	-	0.000311	0.000000	0.282269	0.000028	1.467226	0.000063	1.886635	0.000141	-	-	-		
		-	0.000314	0.000001	0.282304	0.000032	1.467257	0.000074	1.886571	0.000161	-	-	-		

Economic Geology, v. 107, pp. 1499–1505

Re-Os GEOCHRONOLOGY OF QUARTZ-ENCLOSED ULTRAFINE MOLYBDENITE: IMPLICATIONS FOR ORE GEOCHRONOLOGY

C. J. M. Lawley† and D. Selby

Department of Earth Sciences, Durham University, Durham DH1 3LE, United Kingdom

Abstract

Re-Os molybdenite geochronology relies on the aliquant analysis taken from a mineral separate. Although suitable for coarse-grained molybdenite samples, traditional mineral separation techniques are not ideally suited for samples possessing fine-grained molybdenite (<50 μm) and thus hamper the application of Re-Os geochronology for such samples. Here, we demonstrate a room-temperature hydrofluoric acid (HF) chemical separation technique that is capable of isolating ultrafine molybdenite (i.e., <50 μm) for Re-Os geochronology. Six Re-Os molybdenite model ages from four molybdenite in-house control and NIST reference material (RM8599) samples exposed to concentrated HF are indistinguishable from the Re-Os molybdenite model ages for aliquants not exposed to HF. Thus, HF exposure at room temperature has no effect on Re-Os molybdenite systematics. Our HF chemical separation technique was then applied to six ultrafine molybdenite samples from the Lupa goldfield, southwest Tanzania. Three samples from the Kenge deposit provide a weighted average Re-Os molybdenite model age of 1953 ± 5 Ma (MSWD = 0.6; n = 3), whereas three samples and one repeat analysis from the Porcupine deposit provide a weighted average Re-Os molybdenite model age of 1886 ± 5 Ma (MSWD = 1.5; n = 4). Our proposed analytical protocol has allowed us to determine reproducible ages from ultrafine molybdenite samples within the Lupa goldfield that were previously unsuitable for molybdenite Re-Os geochronology using conventional mineral separation techniques.

Introduction

Molybdenite Re-Os geochronology is a well-established geochemical tool in the study of ore deposits (e.g., Stein et al., 1997; Selby and Creaser, 2001). The utility of molybdenite as a geochronometer stems from (1) its occurrence in a wide variety of ore deposit types (e.g., porphyry, epithermal, skarn, orogenic gold, and others), (2) its closed-system behavior during hydrothermal alteration and regional metamorphism (e.g., Stein et al., 1998; Selby and Creaser, 2001; Bingen and Stein, 2003; Ootes et al., 2007; Bingen et al., 2008), and (3) its geochemical tendency to incorporate ppm levels of Re and exclude Os upon crystallization (e.g., Stein et al., 2001, and references therein; Takahashi et al., 2007). The exclusion of Os during molybdenite precipitation simplifies the dating process as all measured Os is radiogenic ($^{187}Os^{r}$) and results from the in situ decay of ^{187}Re (cf. Markey et al., 2007, and references therein). As a result, Re-Os molybdenite model ages can be calculated from the following equation:

$$t = \ln(^{187}Os/^{187}Re + 1)/\lambda,$$

where t = model age and λ = ^{187}Re decay constant, 1.666 × 10^{-11} a^{-1} (Smoliar et al., 1996; Selby et al., 2007). The advantages of the molybdenite Re-Os geochronometer over more traditional radiogenic systems (e.g., K-Ar, Rb-Sr) have resulted in a proliferation of precise and robust age determinations that have greatly improved our understanding of ore deposit genesis (e.g., Stein et al., 1997; Ballard et al., 2001; Brown et al., 2002; Selby et al., 2002; Barra et al., 2003; Mao et al., 2008).

The starting point for any molybdenite Re-Os analysis is to acquire a pure molybdenite mineral separate. Molybdenite (MoS_2) is a soft, platy, hexagonal, and metallic mineral. Porphyry molybdenite deposits possess the largest concentrations of molybdenite and are the most important economic source for the element molybdenum; however, molybdenite is a common accessory sulfide phase for several other ore deposit types. Pure molybdenite mineral separates can be obtained using conventional mineral separation techniques. Rock samples are typically crushed and milled before passing through a sieve and being subjected to a combination of heavy liquids (e.g., methyl iodide), magnetic separation (e.g., Frantz isodynamic magnetic separator), and high-purity water flotation. These time-tested mineral separation techniques have proved to be extremely successful for samples where molybdenite crystals are abundant and coarse grained (commonly >0.5 mm). However, in many situations molybdenite crystals are fine grained and are lost within the clay size fraction during sieving or remain as composite grains encased by silicate minerals, particularly quartz. As a result, ultrafine molybdenite (i.e., molybdenite crystals with diameters less than <50 μm; Fig. 1) samples require a novel approach to mineral separation. Ultrafine molybdenite samples in this study were collected from orogenic gold deposits in the Lupa goldfield, southwest Tanzania, and similar molybdenite occurrences have been reported for other orogenic gold deposits (e.g., Ispolatov et al., 2008). In addition, very fine molybdenite has also been reported in porphyry and other deposit types (e.g., Stevenson, 1940). A potential solution for the difficulties of processing these samples lies in the contrasting solubility of sulfide and silicate minerals in hydrofluoric acid (HF; Neuerburg, 1961). Quartz and other silicates rapidly dissolve in HF, whereas most sulfide minerals (e.g., molybdenite) are noted to be resistant to dissolution (Neuerburg, 1961). The effect of HF on the Re-Os isotope composition of molybdenite has not been previously tested, despite the potential applicability to isolating ultrafine molybdenite. We approach this problem by exposing four previously dated molybdenite mineral separates (e.g., NIST RM8599, in-house standards) to concentrated HF. Herein, we demonstrate that the Re-Os isotope composition

†Corresponding author: e-mail, c.j.lawley@durham.ac.uk

0361-0128/12/4066/1499-7

Submitted: November 24, 2011
Accepted: January 29, 2012

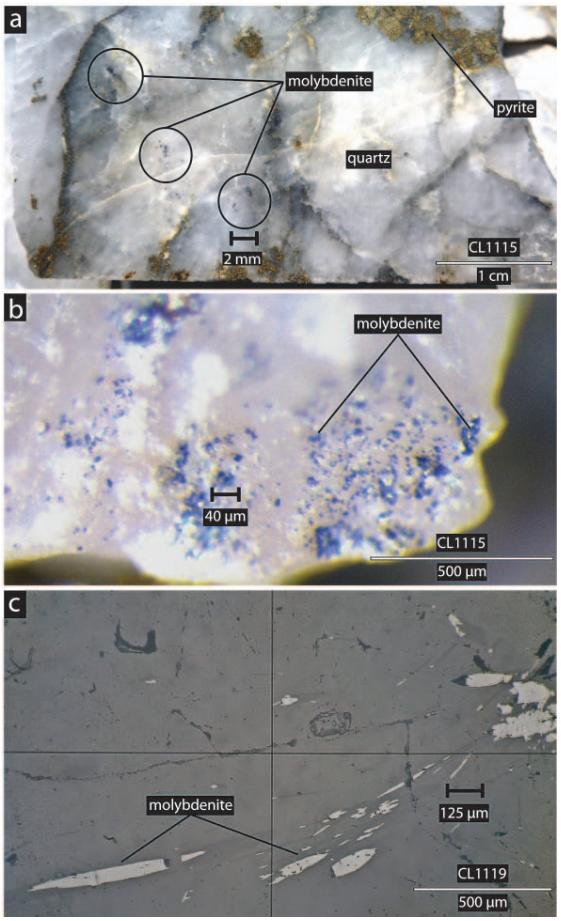

FIG. 1. (a) Ultrafine molybdenite within quartz vein; (b) ultrafine molybdenite coating and enclosed within quartz grains; (c) reflected-light photomicrograph of molybdenite within and along quartz grain boundaries.

of molybdenite is unaffected by exposure to HF. Further, we apply this approach to the study of ultrafine molybdenite.

Samples

Molybdenite control samples and NIST 8599

We tested the effect of HF exposure on Re-Os molybdenite systematics by comparing the Re-Os molybdenite model ages of four previously dated and well-constrained molybdenite mineral separates before and after exposure. The location and characteristics of each sample are presented in Table 1. Two of these samples, National Institute of Standards and Technology (NIST) RM8599 and HLP-5, have previously been reported as reference materials (cf. Markey et al., 1998, 2007; Du et al., 2004; Selby and Creaser, 2004). Both reference materials have also been analyzed using the facilities at the Northern Centre for Isotopic and Elemental Tracing (NCIET) in the TOTAL Laboratory for Source Rock Geochronology and Geochemistry at Durham University (e.g., Porter and Selby, 2010, and references therein). As a result, the Re-Os molybdenite model ages for these two samples are well constrained and have been reproduced by several laboratories using different analytical protocols. The RM8599 and HLP-5 molybdenite powder samples have been produced by mixing crushed ore rock with flotation oils at the Henderson and Huanglongpu deposit mills, respectively. The milling process produces fine-grained and extremely well mixed samples that are ideally suited for Re-Os analysis (Stein et al., 1998; Selby and Creaser, 2004). However, the Re-Os ages of milled samples represent an average age for ore mineralization and may mask subtle age variations related to the complex evolution of most ore systems (e.g., Selby and Creaser, 2001).

In addition to the reference material molybdenite samples, we have also utilized samples from the previously dated MAX (Lawley et al., 2010a) and Endako porphyry Mo deposits (Selby and Creaser, 2001). Molybdenite samples from the MAX and Endako deposits represent the potassic and phyllic stages of mineralization, respectively, and thus provide the absolute timing of that period of ore mineralization. The mineral separates were prepared using traditional mineral separation methods that included crushing, pulverizing, Frantz isodynamic magnetic separation, heavy liquids (i.e., lithium heteropolytungstates [LST] heavy liquid and methyl iodide), and MilliQ flotation.

Ultrafine molybdenite samples

Molybdenite samples are from the Lupa goldfield, southwest Tanzania. The Lupa goldfield is one of eight lithotectonic terranes that constitute the Paleoproterozoic Ubendian Belt (Daly, 1988). Gold is associated with pyrite, chalcopyrite, and trace molybdenite within quartz veins and mylonitic rocks. Sample locations and characteristics are reported in Table 1. Molybdenite is present as fracture coatings, monomineralic stringer veins, and ultrafine-grained disseminations within quartz veins and the granitic host rock (Fig. 1). The bulk of the molybdenite from these samples is <50 μm in diameter within quartz crystals and along quartz crystal boundaries (Fig. 1c). Samples were crushed, pulverized, sieved, and passed through a Frantz magnetic separator before heavy liquid separation. Composite grains (molybdenite encased by quartz) were concentrated in the light fraction of the density separation, whereas liberated pyrite and other sulfide grains were concentrated in the heavy fraction of the density separation.

Rhenium-osmium analytical methods utilize sealed borosilicate glass tubes and oxidizing acidic mediums, e.g., aqua regia, to achieve tracer solution (^{185}Re + isotopically normal Os) and sample Re and Os isotope equilibration. Aqua regia is not capable of digesting quartz, and thus any encased molybdenite is also not digested. As a result, ultrafine samples were then chemically separated using the method described below.

Analytical Protocol

Ultrafine molybdenite chemical separation method

Our series of HF tests indicates that approximately 8 ml of 32N HF will dissolve 0.750 g of quartz in 24 hr at room temperature and is adapted from Neuerburg (1961). For each

TABLE 1. Sample Locations, Characteristics, and Re-Os Results

Sample no.	Sample location	Brief sample description	Sample wt (g)	Re (ppm)	±	^{187}Re (ppm)	±	^{187}Os (ppb)	±	Model age (Ma)[1]	± (Ma)
			Control samples								
RM8599	Hendersen deposit, USA	Molybdenite powder; molybdenite reference material	0.092 0.103	11.39 11.36	0.04 0.04	7.16 7.14	0.02 0.02	3.30 3.29	0.01 0.01	27.6 27.6	0.1 0.1
HLP-5	Huanglongpu deposit, China	~1- × 500-m calcite-quartz-molybdenite veins	0.006	319.90	2.42	201.06	1.52	738.28	5.46	220.0	0.9
2706SWB	Endako deposit, Canada	Laminated quartz-molybdenite veins	0.016	32.85	0.14	20.65	0.09	50.19	0.18	145.7	0.6
CL100	MAX deposit, Canada	Quartz-molybdenite vein from high-grade zone	0.012 0.021	54.67 56.26	0.26 0.21	34.36 35.36	0.16 0.13	46.07 47.47	0.20 0.15	80.4 80.5	0.3 0.3
CL100 3 weeks			0.021	49.89	0.19	31.36	0.12	42.23	0.14	80.8	0.3
			Ultrafine molybdenite samples								
CL1115	Kenge deposit, Lupa goldfield, Tanzania	Disseminated molybdenite within quartz vein	0.022	7.40	0.03	4.65	0.02	153.65	0.50	1950	8
CL1116	Kenge deposit, Lupa goldfield, Tanzania	Disseminated molybdenite within quartz vein	0.015	8.55	0.04	5.37	0.02	177.64	0.75	1952	10
CL1117	Kenge deposit, Lupa goldfield, Tanzania	Disseminated molybdenite within quartz vein	0.023	13.35	0.06	8.39	0.04	278.02	0.85	1957	9
CL1118	Porcupine deposit, Lupa goldfield, Tanzania	Disseminated molybdenite within quartz-feldspar vein	0.023 0.019	1.96 1.72	0.01 0.01	1.23 1.08	0.01 0.01	39.26 34.66	0.13 0.13	1882 1890	9 10
CL1119	Porcupine deposit, Lupa goldfield, Tanzania	Disseminated molybdenite within granite	0.020	3.35	0.02	2.11	0.01	67.65	0.35	1896	13
CL1120	Porcupine deposit, Lupa goldfield, Tanzania	Disseminated molybdenite within granite	0.020	10.29	0.04	6.47	0.03	206.09	0.68	1882	8

Analytical uncertainties are reported at 2σ

[1]Model age calculated from the simplified isotope equation [$t = \ln(^{187}Os/^{187}Re + 1)/\lambda$, where t = model age and $\lambda = ^{187}$Re decay constant], assuming no initial radiogenic Os

control sample/reference material, a known amount of sample was placed into a Savillex Teflon digestion vessel with 8 ml of 32N HF (ROMIL Ltd. UpA high-purity HF) and left at room temperature for 24 hr. After this, the HF was removed by rinsing the molybdenite three times with 10 ml of MilliQ. Finally, the molybdenite was rinsed with ethanol and dried at 60°C. High-purity HF (trace element impurities at ppt levels) was used in this study in order to maintain low analytical blanks; however, we expect that less pure HF could also be used because the majority of HF is removed in the rinsing process and we expect that any Re and Os impurities within the HF are insignificant relative to the ppm and ppb levels of these elements within molybdenite. We estimate that sample recovery ranged from 80 to 90% during the rinsing procedure, based on the difference in sample weight before and after rinsing. Sample loss is explained by minor amounts of the sample adhering to the centrifuge tube and within the pipette during rinsing. This was particularly apparent for the two fine-grained mill samples, RM8599 and HLP-5. One of the control samples, "CL100 3 weeks," was exposed to the HF protocol for three weeks prior to analysis in order to assess the longer-term effects of HF on the Re-Os systematics.

The same protocol was followed to liberate molybdenite from enclosing quartz. After the silicate (quartz) digestion, the sample typically contained molybdenite plus trace pyrite. The grain size of these samples precluded handpicking as a means for removing trace amounts of pyrite. However, the Re and Os contribution of trace pyrite is insignificant relative to the much larger concentrations of Re and O present within molybdenite. Ultrafine molybdenite samples with more complicated mineralogy (e.g., quartz-feldspar-molybdenite veins) typically possessed HF-insoluble products after digestion. The majority of these HF-insoluble products were removed during the following MilliQ rinsing stage. Neuerburg (1961) reported that any remaining HF- and water-insoluble products can be removed by exposing the sample to aluminium chloride; however, this was not deemed necessary for our sample suite.

Re-Os isotope analytical method

The Re and Os abundance and isotope composition determinations for molybdenite mineral separates follow those previously published (e.g., Porter and Selby, 2010). In brief, a weighed aliquant of the molybdenite mineral separate and tracer solution (^{185}Re + isotopically normal Os) were then loaded into a Carius tube with 11N HCl (1 ml) and 15.5N HNO_3 (3 ml), sealed, and digested at 220°C for ~24 hr. Osmium was purified from the acid medium using solvent extraction ($CHCl_3$) at room temperature and microdistillation methods. The Re fraction was isolated using standard anion column chromatography. Rhenium and Os were loaded onto coated Ni and Pt filaments, respectively, and their isotopic compositions

were measured using negative thermal ionization mass spectrometry (Creaser et al., 1991; Völkening et al., 1991). Analyses were conducted on a Thermo Electron TRITON mass spectrometer, with the Re and Os isotope composition measured using static Faraday collection. Analytical uncertainties are propagated and incorporate uncertainties related to Re and Os mass spectrometer measurements, blank abundances and isotopic compositions, spike calibrations, and reproducibility of standard Re and Os isotope values. During the course of this study Re and Os blanks were <4 and 1 pg, respectively, with the $^{187}Os/^{188}Os$ of the blank being 0.25 ± 0.02.

Results

Re-Os control samples

All Re-Os results are listed in Table 1 and presented in Figure 2.

RM8599: Two aliquants of approximately 100 mg of RM8599 were analyzed and provided identical molybdenite Re-Os model ages of 27.6 ± 0.1 Ma. These ages are in excellent agreement with the arithmetic average of this sample, 27.7 ± 0.0 Ma (n = 48; Markey et al., 2007), and previously reported analyses of 27.6 ± 0.1 and 27.7 ± 0.1 Ma (Porter and Selby, 2010). The ^{187}Re and ^{187}Os concentrations are 7.2 ± 0.0 ppm and 3.3 ± 0.0 ppb, respectively, and overlap within uncertainty with previously reported values (Markey et al., 2007; Porter and Selby, 2010).

HLP-5: One aliquant of approximately 6 mg of HLP-5 was analyzed and provided a molybdenite model age of 220.0 ± 0.9 Ma. This age is in excellent agreement with the accepted weighted average age of 220.5 ± 0.2 Ma (MSWD = 1.3; n =17; Selby and Creaser, 2004) and also with the date reported by Porter and Selby (2010; 221.4 ± 0.9 Ma). The ^{187}Re and ^{187}Os concentrations are 201.1 ± 1.5 ppm and 738.3 ± 5.5 ppb, respectively, and are significantly higher than the ^{187}Re (~170 ppm) and ^{187}Os (~600 ppb) concentrations previously reported (Selby and Creaser, 2004, and references therein; Porter and Selby, 2010). The potential explanation for this discrepancy is discussed further below.

2706SWB: One aliquant of approximately 15 mg of 2706SWB was analyzed and provided a molybdenite model age of 145.7 ± 0.6 Ma. This age is identical, within analytical uncertainty, with the weighted average age of 145.8 ± 0.4 (MSWD = 2.8; n = 10; Selby and Creaser, 2004). The ^{187}Re and ^{187}Os concentrations are 20.7 ± 0.1 ppm and 50.2 ± 0.2 ppb, respectively, and are slightly higher (~19 ppm for ^{187}Re; 45 ppb for ^{187}Os) than those reported in Selby and Creaser (2004).

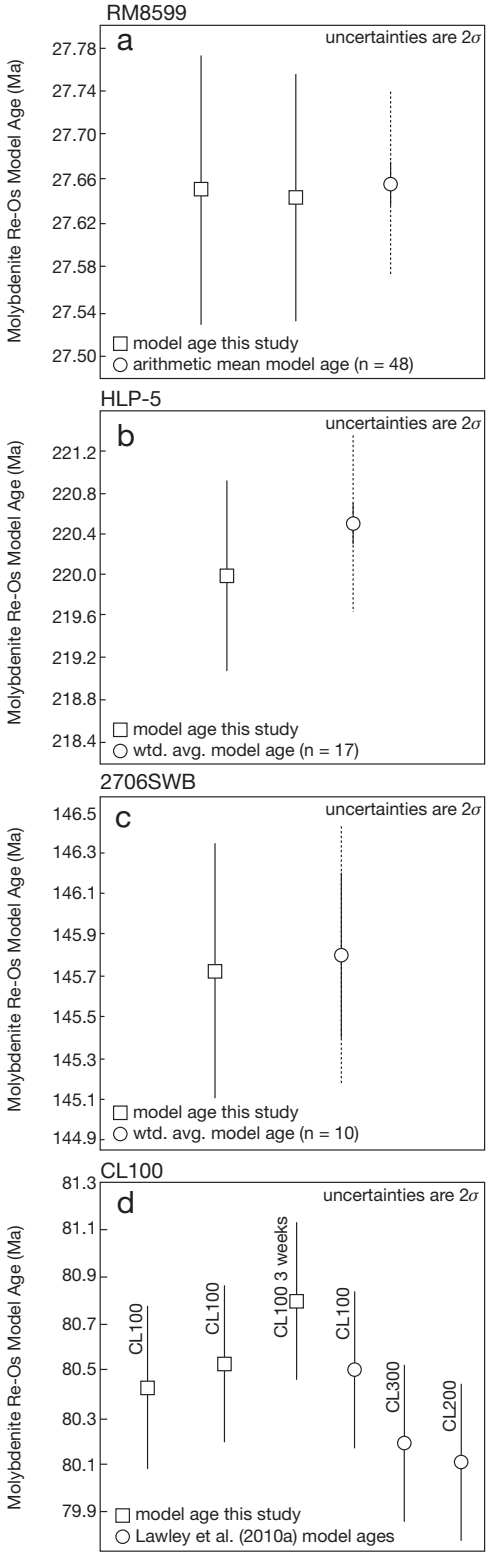

FIG. 2. (a) Molybdenite Re-Os model ages of RM8599 after exposure to HF and accepted age from Markey et al. (2007). Dotted error bars on arithmetic mean model age represent the typical uncertainty for an individual analysis. (b) Molybdenite Re-Os model age of HLP-5 after exposure to HF and accepted age from Selby and Creaser (2004). Dotted error bars on the weighted average model age represent the typical uncertainty for an individual analysis. (c) Molybdenite Re-Os model age of 2706SWB after exposure to HF and accepted age from Selby and Creaser (2004). Dotted error bars on the weighted average model age represent the typical uncertainty for an individual analysis. (d) Molybdenite Re-Os model ages of CL100 after exposure to HF and previously reported ages from Lawley et al. (2010a).

CL100: Three aliquants of molybdenite from the MAX porphyry deposit provide molybdenite model ages of 80.4 ± 0.3, 80.5 ± 0.3, and 80.8 ± 0.3 Ma. All three ages agree, within analytical uncertainty, with the previously reported Re-Os age for CL100 (80.5 ± 0.4 Ma) and two other Re-Os molybdenite dates from this deposit (80.1 ± 0.4 Ma; 80.2 ± 0.4 Ma; Lawley et al., 2010a). The ^{187}Re and ^{187}Os concentrations for the HF-treated CL100 sample are 34.4 ± 0.2, 35.4 ± 0.1, and 31.4 ± 0.1 ppm, and 46.1 ± 0.2, 47.5 ± 0.2, and 42.2 ± 0.1 ppb, respectively. All of these concentrations are slightly higher (^{187}Re = 27.8 ± 0.1 ppm; ^{187}Os = 37.3 ± 0.1 ppb) than those reported in Lawley et al. (2010a). One aliquant of sample CL100 was left in HF for three weeks at room temperature (CL100 3 weeks). The Re-Os model age for the latter is within uncertainty to ages of sample aliquants of CL100 that were only treated for 24 hr. However, the three-week-treated sample gave slightly lower Re and Os abundances, which are nonetheless similar to those published for this sample by Lawley et al. (2010a). In addition, our Re-Os results are also in good agreement with U-Pb and Ar-Ar ages of the host intrusion and associated hydrothermal alteration at MAX (Lawley et al., 2010a).

Re-Os ultrafine molybdenite

Ultrafine molybdenite results for the Kenge and Porcupine deposits are listed in Table 1 and presented in Figure 3. A weighted average Re-Os molybdenite model age for the three samples from the Kenge deposit is 1953 ± 5 Ma (MSWD = 0.6; n = 3). A weighted average Re-Os molybdenite model age for the three samples and one repeat analysis from the Porcupine deposit is 1886 ± 5 Ma (MSWD = 1.5; n = 4). Total Re concentrations for samples from the Kenge deposit range from 7 to 13 ppm, whereas total Re concentrations for samples from the Porcupine deposit range from 1 to 10 ppm. These ranges are comparable with previously reported values from samples prepared using conventional mineral separation techniques (Lawley et al., 2010b).

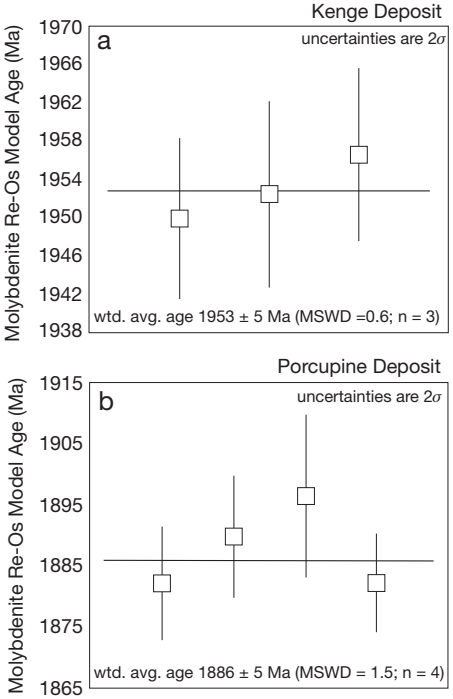

FIG. 3. (a) Molybdenite Re-Os model ages of ultrafine molybdenite samples from the Kenge deposit. (b) Molybdenite Re-Os model ages of ultrafine molybdenite samples from the Porcupine deposit.

Discussion

HF and Re-Os molybdenite systematics

We tested the effect of HF on Re-Os systematics by exposing previously dated molybdenite mineral separates (i.e., control samples) to HF and compared the molybdenite model age with and without HF exposure. Molybdenite model ages for analyses with and without exposure to HF overlap within analytical uncertainty and are shown graphically in Figure 2. In addition, one molybdenite mineral separate (i.e., CL100 3 weeks) was exposed to HF at room temperature for three weeks, and possesses an Re-Os molybdenite model age that is indistinguishable from samples prepared using conventional mineral separation techniques. This suggests that HF at room temperature does not affect the Re-Os isotope composition of molybdenite and that our analytical protocol is suitable for isolating molybdenite from silicate-enclosed molybdenite samples for Re-Os geochronology.

With the exception of RM8599, the control samples (CL100, 2706SWB, and HLP-5) possess ^{187}Re and ^{187}Os concentrations that are either slightly higher or significantly higher than previously reported values. However, any variation in ^{187}Re is coupled with ^{187}Os variation as all control samples yield Re-Os model ages that are in excellent agreement with previously reported ages. Interestingly, the analyses of sample CL100 reported in this study possess up to 7 ppm more ^{187}Re than the previously published analysis (Lawley et al., 2010a); however, the sample left in the HF for three weeks gave values very similar to those for CL100 reported by Lawley et al. (2010a).

Re and Os concentration variations such as this should be expected when analyzing aliquants of natural molybdenite mineral separates and do not necessarily affect molybdenite Re-Os model ages (Selby and Creaser, 2004). HLP-5 is one such example where previous workers have reported a range of total Re (240–290 ppm), whereas molybdenite Re-Os model ages for these analyses all overlap within analytical uncertainty (Markey et al., 1998; Suzuki et al., 2001; Du et al., 2004; Selby and Creaser, 2004). Our analysis of HLP-5 treated by HF prior to the traditional Re-Os analytical protocol possesses 320 ppm total Re and 738 ppb ^{187}Os, thus possessing ~40 ppm more total Re and ~98 ppb more ^{187}Os than reported by previous workers. However, as noted above, this difference in Re-Os abundance is coupled, as an Re-Os model age identical to reported values is determined for not only HLP-5, but all control samples. Previously, variations in Re and ^{187}Os abundance with repeat analysis were suggested to relate to the nonhomogeneous nature of Re and ^{187}Os in molybdenite (Selby and Creaser, 2004). Alternatively, the

variability of Re and Os abundances could relate to sample impurities within HLP-5. Atomic absorption, inductively couple plasma-mass spectrometry (ICP-MS), and inductively coupled plasma-atomic emission spectrometry (ICP-AES) analyses suggest HLP-5 contains significant (>1% m/m) Ca, Pb, Fe, and Al, which are unexpected in a pure MoS_2 (molybdenite) mineral separate (Markey et al., 1998; Du et al., 2004). These additional elements could be present as mineral inclusions within molybdenite crystals or as free mineral phases that were incorporated into the molybdenite mineral separate during froth flotation. We consider that our HF technique may have leached the sample and, thus, HLP-5 may contain higher Re and Os abundances than previously reported. This is supported by ICP-MS analyses of the HF used in HF treatment of HLP-5, completed as part of this study, which measured approximately 10 ppm Ca, 10 ppm Pb, 6 ppm Fe, 5 ppm Al, and 3 ppm K within the HF leachate. Our results suggest that HF dissolution removes HF-soluble mineral phases within HLP-5 or incorporated with the mineral separate and that our proposed method yields a better approximation of the true Re content of HLP-5.

Ultrafine molybdenite

Molybdenite from the Lupa goldfield is present as molybdenite-coated fractures, monomineralic stringer veins, and ultrafine disseminations within quartz veins and the host granite. Conventional mineral separation techniques were unable to separate sufficient quantities of molybdenite due to the ultrafine-grained nature of some molybdenite samples. The chemical separation technique developed here provided sufficient quantities (20–60 mg) of ultrafine molybdenite for Re-Os analysis. Three Re-Os molybdenite model ages from the Kenge deposit all overlap within uncertainty, as exemplified from the low MSWD of the weighted average calculation (i.e., 1953 ± 5 Ma; MSWD = 0.6). The four Re-Os molybdenite model ages from the Porcupine deposit also overlap within error of each other but possess slightly more scatter, resulting in a slightly higher MSWD (i.e., 1886 ± 5 Ma; MSWD = 1.5). Both ages are supported by Re-Os pyrite and U-Pb dating reported in Lawley et al. (2010b) and are part of a broader geologic study that will be reported in Lawley et al. (in prep).

Advantages of chemical mineral separation

Improved sample recovery is the greatest advantage of chemical mineral separation over conventional mineral separation techniques. High sample recovery is especially important for samples with low modal abundances of molybdenite or for small-volume samples. In the case of ultrafine molybdenite, chemical mineral separation maintains high sample recovery regardless of crystal size. Neuerberg (1961) measured that sulfide abundance is two to three times greater for mineral separates prepared using chemical mineral separation techniques when compared to mineral separates prepared by heavy media methods. The proposed method would likely generate higher sample recoveries than Neuerberg (1961) because our method requires less sample handling, which is where the majority of fine-grained sample material is lost.

Whole-rock samples can also be digested but typically require more time to digest and, depending on sample size, may require repeated applications of HF. The advantage of this approach is that molybdenite crystals are relatively undamaged when compared to mineral separates prepared using conventional techniques. Undamaged crystals are especially important for Re-Os molybdenite geochronology, as Re and Os are susceptible to intragrain decoupling (Stein et al., 2003). Selby and Creaser (2004) overcame Re-Os decoupling by increasing the analytical sample size utilized for Re-Os geochronology from a mineral separate. Larger sample sizes homogenize the sample and mask the decoupling, yielding more accurate and reproducible ages. Molybdenite mineral separates produced by chemical mineral separation provide another possible solution to Re-Os decoupling by preserving the original crystal morphology.

Another advantage of chemical mineral separation over conventional methods is the minimal time requirement. Once the samples are loaded with HF, no supervision is required during sample digestion. This differs from conventional techniques, where constant supervision is required through the mineral separation process. Additional time savings are gained by the ability to digest multiple samples at the same time. As a result, the number of samples that can be prepared at one time with chemical mineral separation is only limited by the number of digestion vessels.

Conclusions

Conventional mineral separation techniques are not ideally suited for samples possessing fine-grained molybdenite (<50 μm) and thus hamper the application of Re-Os geochronology for such samples. In this contribution we have demonstrated the following:

1. The Re and Os isotope composition of molybdenite is unaffected by exposure to HF at room temperature; thus, HF is capable of isolating ultrafine molybdenite for Re-Os geochronology.
2. The chemical mineral separation protocol described above is advantageous for samples with low modal abundances of molybdenite and/or samples containing ultrafine molybdenite (e.g., <50 μm).
3. Our proposed chemical mineral separation technique has produced six reproducible Re-Os molybdenite model ages from samples that were unsuitable for Re-Os analysis using traditional mineral separation techniques.

Acknowledgments

Funding and support was provided by a Durham Doctoral Fellowship at Durham University and a student research grant from the SEG to CJML. Chris MacKenzie and Helio Resource Corp. kindly provided funding and access to drill core/exploration licenses for sampling. Thank you to Chris Ottley at Durham University for helpful discussions regarding HF best practice and assistance with ICP-MS analyses. We also thank Massimo Chiaradia and the SEG editorial board for a constructive review.

REFERENCES

Ballard, J.R., Palin, J.M., Williams, I.S., Campbell, I.H., and Faunes, A., 2001, Two ages of porphyry intrusion resolved for the super-giant Chuquicamata copper deposit of northern Chile by ELA-ICP-MS and SHRIMP: Geology, v. 29, p. 383–386.

Barra, F., Ruiz, J., Mathur, R., and Titley, S., 2003, A Re-Os study of sulphide minerals from the Bagdad porphyry Cu-Mo deposit, northern Arizona, USA: Mineralium Deposita, v. 38, p. 585–596.

Bingen, B., and Stein, H., 2003, Molybdenite Re-Os dating of biotite dehydration melting in the Rogaland high-temperature granulites, S. Norway: Earth and Planetary Science Letters, v. 208, p. 181–195.

Bingen, B., Davis, W.J., Hamilton, M.A., Engvik, A.K., Stein, H.J., Skar, O., and Nordgulen, O., 2008, Geochronology of high-grade metamorphism in the Sveconorwegian nelt, S. Norway; U-Pb, Th-Pb, and Re-Os data: Norwegian Journal of Geology, v. 88, p. 12–42.

Brown, S.M., Fletcher, I.R., Stein, H.J., Snee, L.W., and Groves, D.I., 2002, Geochronological constraints on pre-, syn-, and postmineralization events at the world-class Cleo gold deposit, Eastern Goldfields province, Western Australia: Economic Geology, v. 97, p. 541–559.

Creaser, R.A., Papanastassiou, D.A., and Wasserburg, G.J., 1991, Negative thermal ion mass spectrometry of osmium, rhenium, and iridium: Geochimica et Cosmochimica Acta, v. 55, p. 396–401.

Daly, M.C., 1988, Crustal shear zone in central Africa; a kinematic approach to Proterozoic tectonics: Episodes, v. 11, p. 5–11.

Du, A., Wu, S., Sun, D., Wang, S., Qu, W., Markey, R., Stein, H., Morgan, J., and Malinovskiy, D., 2004, Preparation and certification of Re-Os dating reference materials; molybdenites HLP and JDC: Geostandards and Geoanalytical Research, v. 28, p. 41–52.

Ispolatov, V., Lafrance, B., Dubé, B., Creaser, R., and Hamilton, M., 2008, Geologic and structural setting of gold mineralization in the Kirkland Lake-Larder Lake gold belt, Ontario: Economic Geology, v. 103, p. 1309–1340.

Lawley, C.J.M., Richards, J.P., Andersen, R.G., Creaser, R.A., and Heaman, L.M., 2010a, Geochronology and geochemistry of the MAX porphyry Mo deposit and its relationship to Pb-Zn-Ag mineralization, Kootenay arc, southeastern British Columbia, Canada: Economic Geology, v. 105, p. 1113–1142.

Lawley, C.J.M., Selby, D., Condon, D.J., Horstwood, M.S.A., Crowley, Q.G., Imber, J., and MacKenzie, C., 2010b, Geochronology of granites and gold in the Lupa goldfield, southwest Tanzania: Applied Earth Science, v. 119, p. 87.

Mao, J.W., Xie, G.Q., Bierlin, F., Qu, W.J., Du, A.D., Ye, H.S., Pirajino, F., Li, H.M., Guo, B.J., Li, Y.F., and Yang, Z.Q., 2008, Tectonic implications from Re-Os dating of Mesozoic molybdenum deposits in the east Qinling-Dabie orogenic belt: Geochimica et Cosmochimica Acta, v. 72, p. 4607–4626.

Markey, R., Stein, H., and Morgan, J., 1998, Highly precise Re-Os dating for molybdenite using alkaline fusion and NTIMS: Talanta, v. 45, p. 935–946.

Markey, R., Stein, H.J., Hannah, J.L., Zimmerman, A., Selby, D., and Creaser, R.A., 2007, Standardizing Re-Os geochronology; a new molybdenite reference material (Hendersen, USA) and the stoichiometry of Os salts: Chemical Geology, v. 244, p. 74–87.

Neuerburg, G.J., 1961, A method of mineral separation using hydrofluoric acid: The American Mineralogist, v. 46, p. 1498–1501.

Ootes, L., Lentz, D.R., Creaser, R.A., Ketchum, J.W.F., and Falck, H., 2007, Re-Os molybdenite ages from the Archean Yellowknife greenstone belt: Comparison to U-Pb ages and evidence for metal introduction at ~2675 Ma: Economic Geology, v. 102, p. 511–518.

Porter, S.J., and Selby, D., 2010, Rhenium-osmium (Re-Os) molybdenite systematics and geochronology of the Cruchan Granite skarn mineralization, Etive Complex; implications for emplacement chronology: Scottish Journal of Geology, v. 46, p. 17–21.

Selby, D., and Creaser, R.A., 2001, Re-Os geochronology and systematics in molybdenite from the Endako porphyry molybdenum deposit, British Columbia, Canada: Economic Geology, v. 96, p. 197–204.

——2004, Macroscale NTIMS and microscale LA-MC-ICP-MS Re-Os isotopic analysis of molybdenite; testing spatial restrictions for reliable Re-Os age determinations, and implications for the decoupling of Re and Os within molybdenite: Geochimica et Cosmochimica Acta, v. 68, p. 3897–3908.

Selby, D., Creaser, R.A., Hart, C.J.R., Rombach, C.S., Thompson, J.F.H., Smith, M.T., Bakke, A.A., Goldfarb, R.J., 2002, Absolute timing of sulfide and gold mineralization; a comparison of Re-Os molybdenite and Ar-Ar mica methods from the Tintina gold belt, Alaska: Geology, v. 30, p. 791–794.

Selby, D., Creaser, R.A., Stein, H.J., Markey, R.J., and Hannah, J.L., 2007, Assessment of the ^{187}Re decay constant by cross calibration of Re-Os molybdenite and U-Pb zircon chronometers in magmatic ore systems: Geochimica et Cosmochimica Acta, v. 71, p. 1999–2013.

Smoliar, M.I., Walker, R.J., and Morgan, J.W., 1996, Re-Os ages of group IIA, IIIA, IVA, and IVB iron meterorites: Science, v. 271, p. 1099–1102.

Stein, H.J., Markey, R.J., Morgan, J.W., Du, A., and Sun, Y., 1997, Highly precise and accurate Re-Os ages for molybdenite from the East Qinling molybdenum belt, Shaanxi Province, China: Economic Geology, v. 92, p. 827–835.

Stein, H.J., Sundbland, K., Markey, R.J., Morgan, J.W., and Motuza, G., 1998, Re-Os ages for Archean molybdenite and pyrite, Kuittila-Kivisuo, Finland and Proterozoic molybdenite, Kabeliai, Lithuania; testing the chronometer in a metamorphic and metasomatic setting: Mineralium Deposita, v. 33, p. 329–345.

Stein, H.J., Markey, R.J., Morgan, J.W., Hannah, J.L., and Acherstén, A., 2001, The remarkable Re-Os chronometer in molybdenite; how and why it works: Terra Nova, v. 13, p. 479–486.

Stein, H., Schersten, A., Hannah, J., Markey, R., 2003, Subgrain-scale decoupling of Re and ^{187}Os and assessment of laser ablation ICP-MS spot dating in molybdenite: Geochimica et Cosmochimica Acta, v. 67, p. 3673–3686.

Stevenson, J.S., 1940, Molybdenum deposits of British Columbia: Bulletin of the British Columbia Department of Mines, v. 9, 96 p.

Suzuki, K., Feely, M., and O'Reilly, C., 2001, Disturbance of the Re-Os chronometer of molybdenites from the late-Caledonian Galway Granite, Ireland, by hydrothermal fluid circulation: Geochemical Journal, v. 35, p. 29–35.

Takahashi, Y., Uruga, T., Suzuki, K., Tanida, H., Terada, Y., and Hattori, K.H., 2007, An atomic level study of rhenium and radiogenic osmium in molybdenite: Geochimica et Cosmochimica Acta, v. 71, p. 5180–5190.

Völkening, J., Walczyk, T., and Heumann, K.G., 1991, Osmium isotope ratio determinations by negative thermal ionization mass spectrometry: International Journal of Mass Spectrometry and Ion Processes, v. 105, p. 147–159.